UNIVERSITÀ DEGLI STUDI DI PADOVA

Dipartimento di Fisica e Astronomia "Galileo Galilei"

Master Degree in Physics

Final Dissertation

Cosmic Microwave Background Anomalies meet Primordial Non-Gaussianity

Thesis supervisor

Prof. Nicola Bartolo

Candidate

Chiara Zavatto

Academic Year 2022/2023

Table of Contents

Introduction **1**

1 Big Bang Cosmology and Inflation **5**
1.1 The Standard Model of Big Bang Cosmology . . . 5
1.2 Shortcomings of the Standard Big Bang Cosmology . . . 8
1.2.1 The Flatness Problem . . . 8
1.2.2 The Relic Density Problem . . . 9
1.2.3 The Horizon Problem . . . 9
1.3 Inflation . . . 9
1.4 Inflation as driven by a Slowly-rolling Scalar Field . . . 10
1.4.1 Classical Dynamics . . . 12
1.4.2 Slow-roll Parameters . . . 13
1.4.3 Number of e-foldings . . . 13
1.5 Generating Primordial Perturbations during Inflation . . . 14
1.5.1 Quantum Fluctuations of a Scalar Field during a de Sitter Stage . . . 14
1.5.2 Quantum Fluctuations of a Scalar Field in a quasi-de Sitter Stage . . . 18
1.5.3 Correlation Functions and Power Spectrum . . . 18

2 Theory of Cosmological Perturbations **21**
2.1 Perturbing the Metric Tensor . . . 21
2.2 Gauge Dependence . . . 22
2.3 Curvature Perturbation on Spatial Slices of Uniform Density . . . 24
2.3.1 Adiabatic and Entropy Perturbations . . . 25
2.4 Power Spectrum of the Curvature Perturbation . . . 25
2.5 Gravitational Waves from Inflation . . . 27
2.6 The Consistency Relation . . . 28

3 The Cosmic Microwave Background **31**
3.1 Temperature Anisotropies . . . 32
3.2 Polarisation Anisotropies . . . 39
3.3 The `HEALPix` Pixelisation Scheme . . . 42
3.3.1 Conventions . . . 43
3.3.2 The Pixel Window Function . . . 44
3.4 Masking . . . 45

3.5 CMB Surveys . . . 47
3.5.1 The *Planck* Mission and its Full-sky Maps . . . 48
3.5.2 The Next Stage of CMB Research . . . 50

4 The Non-Gaussian Landscape **53**
4.1 Beyond the Power Spectrum . . . 53
4.1.1 The Bispectrum . . . 53
4.1.2 The Trispectrum . . . 56
4.2 Running non-Gaussianity . . . 58
4.3 Non-Gaussianity in the CMB . . . 59
4.3.1 The Angular Bispectrum . . . 60
4.3.2 The Angular Trispectrum . . . 61
4.4 Some (Useful) Analytical Results for the CMB Trispectrum from Inflation . . . 66
4.5 Constraints on Primordial Non-Gaussianity . . . 71

5 Cosmic Microwave Background Anomalies **73**
5.1 Lack of Large-Angle Correlations . . . 74
5.2 Hemispherical Power Asymmetry . . . 77
5.2.1 Dipole Modulation and Directionality . . . 78
5.2.2 Low Variance in the Northern Hemisphere . . . 82
5.3 Alignments of Low Multipole Moments . . . 83
5.4 Point-Parity Asymmetry . . . 85
5.5 The Cold Spot . . . 86
5.6 (Short) Summary of the Findings from *Planck* . . . 87
5.7 The Quest for an Explanation . . . 88
5.7.1 Large-scale Structure Explanations . . . 88
5.7.2 Inflationary Explanations . . . 89

6 CMB Anomalies as Signatures of Non-Gaussianity **91**
6.1 Non-Gaussian Modulation of the Power Spectrum . . . 91
6.1.1 Statistical Anisotropies from Local Non-Gaussian Initial Conditions . . . 91
6.1.2 Generalising the Local Ansatz . . . 98
6.1.3 Beyond the Local Ansatz . . . 101
6.1.4 Statistical Anisotropies from a Scale-Dependent Local Bispectrum . . . 106
6.2 Non-Gaussian Covariance of Statistical Estimators . . . 108
6.2.1 Dipolar Asymmetry from a Scale-dependent Trispectrum . . . 109
6.2.2 Isotropic Power Spectrum Modulation from a Scale-dependent Trispectrum . . . 113
6.3 Searching for Isotropic, Non-Gaussian Phenomenological Toy Models . . . 115
6.3.1 A $g_{\rm NL}$-like Toy Model . . . 116
6.3.2 Reproducing the CMB Anomalous Features . . . 116

7 On the Implications of CMB Anomalies for Early Universe Physics **121**
7.1 Power Asymmetry from a Scale-dependent Inflationary Bispectrum 121
7.1.1 Biasing the 2-point ζ Function by a Long-wavelength Mode 122
7.1.2 Building a Successful Model 124
7.2 *Planck*'s Constraints on Physical Models for CMB Anomalies 129
7.2.1 Models with Suppressed Power at Large Scales 129
7.2.2 Models for Statistical Anisotropy in the Primordial Fluctuations . . . 131

Conclusions **137**

A The Boltzmann Equation **141**
A.1 The Collisionless Boltzmann Equation for Photons 141
A.2 The Boltzmann Equation for Interacting Photons 142
A.3 Free-streaming Solution 143

B Wigner 3-j symbol **147**
B.1 Definition 147
B.2 Symmetries 148
B.3 Orthogonality 148
B.4 Wigner 6-j symbol 149

Introduction

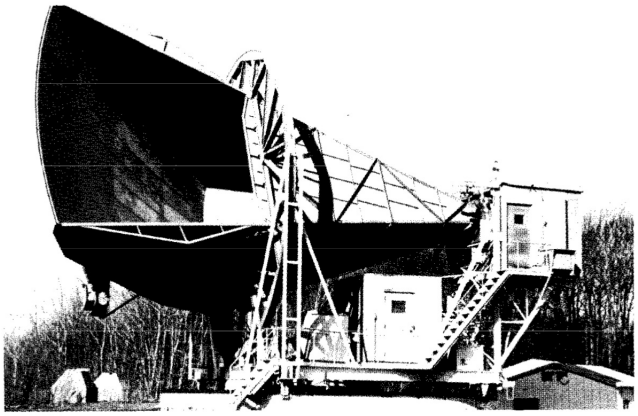

Figure 1. The 20 foot horn-detector that was used to discoverer the CMB radiation.

Modern Cosmology is based on the belief that the place we occupy in the universe is in no way special. This is known in literature as the cosmological principle and it is one of the pillars of the Standard Model of Big Bang Cosmology, also known as the ΛCDM model. In the years, the ΛCDM model has been widely studied and the fundamental parameters that describe it have been constrained through several, different experimental measurements, one of the most powerful being that of the Cosmic Microwave Background (CMB) anisotropies. The first prediction of the CMB dates back to 1948, by Alpher & Hermann [1], and it was serendipitously discovered by Penzias and Wilson in 1964 (see figure 1). Penzias and Wilson, who were set out to measure radio signals from the Milky Way, initially did not understand the nature of what they had measured. Later, Princeton scientists, who were looking for that signal, correctly interpreted the finding of Penzias and Wilson as the CMB. After that, many experiments were designed to look for its characteristics but the real breakthrough came only in the 1990s, when the Cosmic Background Explorer (COBE) satellite [2] made the first measurements of the CMB energy spectrum, showing that it is well described by a black-body function with a mean temperature of ~ 3 K. The COBE data were joined in 2003 by the first results from NASA's Wilkinson Microwave Anisotropy Probe (WMAP) [3], improved upon by analysis of data added every 2 years and culminating in the 9-years results [4]. In 2013 the first results [5] from the third generation CMB satellite, ESA's *Planck* mission, were released and were later followed by the 2015 [6, 7] and the final 2018 *Planck* data release [8, 9]. Even though observations indicates that the properties of the CMB are consistent

with the predictions of the ΛCDM model, enticing evidence of several unexpected statistical features (anomalies) has emerged from both the WMAP and *Planck* full-sky measurements. Given the *a posteriori* nature of their detection, a conservative explanation is that these observed anomalous features are simply statistical flukes of our realisation of the ΛCDM model. However, despite their relative modest statistical significance, their number, the fact that they are not related in a obvious manner and the fact that (almost all of) these features are detected only at the largest angular scales motivate the quest for an underlying physical explanation. One possibility to explain them is that they might be related to local physics effects, namely there is a pernicious foreground that contaminates the CMB and leads to the observed anomalies, but the most exciting possibility is that some or all of these anomalies have a cosmological origin. If that were the case, an understanding of their nature could point us to new physics beyond the Standard Cosmological Model, thus possibly shedding light on the exact mechanism operating during the very first epochs of the Universe. In this Thesis we will explore some of these anomalous features, presenting a description of each of them, along with evidence and methods for detection, aiming to provide an up-to-date review of the main models and explanations proposed in literature, focusing in particular on the possibility that such anomalies are related to non-Gaussian features of the primordial cosmological perturbations arising from inflationary models in the Early Universe.

Thesis Outline

The structure of this Thesis is organised as follows. In Chapter 1 we review the theoretical framework of physical and observational Modern Cosmology, the Standard Model of Big Bang Cosmology. Its short-comings and the elegant solution provided to these puzzles by cosmic inflation, which also provide a compelling mechanism to explain the generation of primordial density fluctuations, are also discussed. Particular attention is devoted to the treatment of single-field models of slow-roll inflation. In Chapter 2 we review the theory of cosmological perturbations, thus setting up the theoretical framework needed to provide a rigorous treatment of primordial density fluctuations. The issue of gauge-dependence is discussed, the definition of gauge-invariant quantities is introduced and the calculations of Chapter 1 are revised. In Chapter 3 we review the treatment of the Cosmic Microwave Background temperature and polarisation anisotropies. The basic methods for the description and simulation of CMB data are also introduced and a brief summary of past, present and upcoming CMB surveys is provided. In Chapter 4 we introduce the concept of primordial non-Gaussianity (PNG). The most well-known and studied types of PNG are discussed and the definitions of inflationary bispectrum and trispectrum are given. The impact of non-Gaussianity on the CMB anisotropies is discussed and some useful analytical results for the CMB trispectrum are reported. In Chapter 5 we explore the CMB large-scale anomalies. A description of some of these anomalies, along with evidence and methods for detection, is provided. A qualitative and non-exhausting summary of some of the cosmological mechanisms related to the large-scale structure or to inflationary physics proposed in the literature to

explain them is also presented. In Chapter 6 we explore the connection between the CMB anomalous features and non-Gaussianity in the primordial fluctuations. In particular, the analytical framework proposed by Adhikari et al. in [10], the results of the subsequent analysis [11] and the phenomenological approach illustrated by Hansen et al. in [12] are discussed. In Chapter 7 we further discuss the implications of the CMB large-scale anomalies for Early Universe physics, focusing in particular on the work of Byrnes et al. who, in [13, 14], report results for a special set of inflationary scenarios that can generate the CMB power asymmetry. For completeness, the results of the analysis on specific physical models for the CMB anomalous features performed by the *Planck* collaboration in [15] using the *Planck* 2018 temperature and polarisation data are also reported. Finally, the main points and results of this Thesis are summarised in the Conclusions.

Chapter 1
Big Bang Cosmology and Inflation

Notation

In this Thesis we will assume for the signature of the metric $g_{\mu\nu}$ the *mostly positive* one i.e. $(-,+,+,+)$. We will also use natural units i.e. $c = \hbar = 1$. Other notation conventions adopted will be introduced when needed.

1.1 The Standard Model of Big Bang Cosmology

The simplest cosmological model which currently fits the experimental observations is the Standard Model of Big Bang Cosmology, also known as the ΛCDM model, based on the theory of General Relativity, presented by A. Einstein in 1915. Its main assumptions are the cosmological principle, which states that the Universe is homogeneous and isotropic on sufficiently large scales; that the Universe was once much hotter and denser and it has been expanding since early times; and that the dynamics is governed by the Einstein's equations. The only geometry compatible with the constraints of homogeneity and isotropy is the one described by the Friedmann-Lamaitre-Robertson-Walker (FLRW) metric, with line-element given by

$$ds^2 = g_{\mu\nu}dx^\mu dx^\nu = -dt^2 + a^2(t)\left[\frac{dr^2}{1-kr^2} + r^2\left(d\theta^2 + \sin^2\theta d\phi^2\right)\right] \tag{1.1}$$

where $g_{\mu\nu}$ is the metric tensor, t is the cosmic time, (r, θ, ϕ) are the comoving spherical coordinates and $a(t)$ is the scale factor. The parameter k is known as the curvature parameter and determines the curvature of 3-dimensional spatial hypersurfaces. It can can normalised to take three possible values corresponding to the possibility that the Universe can be flat ($k = 0$), open ($k = -1$) or closed ($k = +1$). According to the theory of General Relativity, the metric $g_{\mu\nu}$ that describes the Universe satisfies the Einstein's equations:

$$G_{\mu\nu} = R_{\mu\nu} - \frac{1}{2}Rg_{\mu\nu} = 8\pi G T_{\mu\nu} \tag{1.2}$$

where $R_{\mu\nu}$, the Ricci tensor, and $R = g^{\mu\nu}R_{\mu\nu}$, the Ricci scalar, describe the curvature of

the space-time and are collective denoted as $G_{\mu\nu}$, the Einstein tensor. G is the gravitational constant and $T_{\mu\nu}$ is the energy-momentum tensor, which depends on the energy components featuring the Universe. In the case of the FLRW metric, these components are assumed to be perfect fluids and the expression for the energy-momentum tensor is

$$T_{\mu\nu} = (\rho + P)u_\mu u_\nu + P g_{\mu\nu} \tag{1.3}$$

where ρ is the energy density, P the isotropic pressure and u_μ the fluid four-velocity, subjected to the constraint $g^{\mu\nu}u_\mu u_\nu = -1$. Plugging the FLRW metric (1.1) and the expression for the energy-momentum tensor (1.3) into the Einstein equations (1.2) we obtain the evolution equations for the cosmic fluid, known in literature as the Friedmann equations:

$$H^2 = \frac{8\pi G}{3}\rho - \frac{k}{a^2} \tag{1.4}$$

$$\dot{H} + H^2 = -\frac{4\pi G}{3}(\rho + 3P) \tag{1.5}$$

where H is the Hubble expansion rate, defined as

$$H(t) = \frac{\dot{a}}{a} \tag{1.6}$$

and $\rho = \sum_i \rho_i$ and $P = \sum_i P_i$ are, respectively, the total energy density and pressure of the Universe, which include the contributions from all existing cosmological constituents. From the Bianchi identities $D_\mu G^{\mu\nu}$, or by employing energy-momentum conservation, we can then obtain the continuity equation:

$$\dot{\rho} + 3H(\rho + P) = 0 \tag{1.7}$$

from which we can read off the scaling of the energy density with the scale factor, given by

$$\rho(a) = \rho_0 \left(\frac{a}{a_0}\right)^{-3(1+w)} \tag{1.8}$$

Figure 1.1 illustrates the evolution of the energy density during the expansion of the Universe. In the ΛCDM model one assumes the Universe to have five basic components: Dark Energy (DE), responsible for driving the current expansion; Dark Matter (DM), that is pressureless, stable and interacts with regular matter only gravitationally; regular matter, that behaves just like it does on Earth; photons, that we observe as the Cosmic Microwave Background; Neutrinos, that are almost massless and stream as non-interacting, relativistic particles at the time of recombination. At different times, some of these species contribute as relativistic

components, referred to as radiation, with equation of state $w_r = P_r/\rho_r = 1/3$, or as non-relativistic components, referred to as matter, with equation of state $w_M \approx 0$. Many observational clues points towards the DE component being described by an equation of state $w_\Lambda = -1$ with $\rho_\Lambda = constant$ i.e. by a cosmological constant.

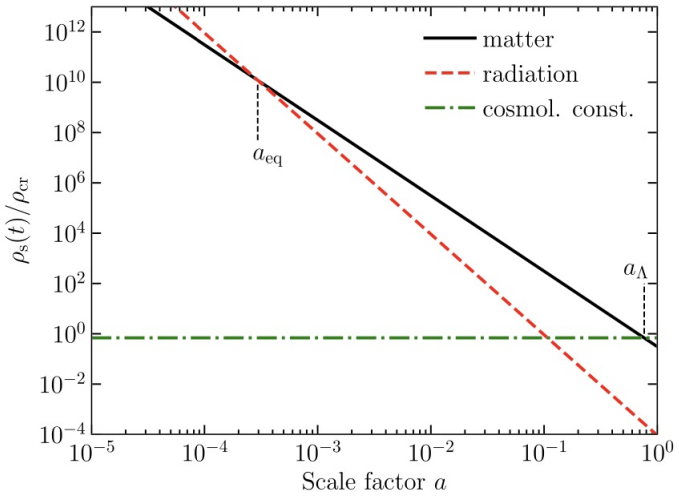

Figure 1.1. Energy density as a function of scale factor for different constituents of the universe: non-relativistic matter ($\propto a^{-3}$), radiation ($\propto a^{-4}$), and a cosmological constant. The epoch at which the energy densities of matter and radiation are equal is a_{eq}, while the epoch at which the densities of matter and cosmological constant match is a_Λ. All are in units of the critical density today.

According to *Planck*, the Universe's predominant constituents today are Dark Matter and Dark Energy which account for, respectively, 26% and 69% of its mass/energy budget, with regular (baryonic) matter contributing to the remaining 5% [16]. Note that it is customary to describe the composition of the Universe introducing dimensionless density parameters:

$$\Omega_i \equiv \frac{\rho_i}{\rho_c} \tag{1.9}$$

where

$$\rho_c = \frac{3H^2(t)}{8\pi G} \tag{1.10}$$

is the critical energy density, defined as the total energy density of a flat Universe at a given time. We can rewrite the first Friedmann equation (1.4) in terms of the density parameters as

$$\sum_i \Omega_i + \Omega_k = 1 \tag{1.11}$$

where the sum is over all the different species in the Universe and $\Omega_k = -\frac{k}{a^2H^2}$ is the curvature

density. From *Planck*'s measurements of the CMB we get the following constraints (at the 68% CL) on the present day values of the density parameters of the main components of the Universe [9]:

$$\begin{aligned} \Omega_B h^2 &= 0.0224 \pm 0.0002 \\ \Omega_{DM} h^2 &= 0.1200 \pm 0.0012 \\ \Omega_\Lambda &= 0.3153 \pm 0.0073 \end{aligned} \tag{1.12}$$

where h is defined such that the Hubble parameter today is given by

$$H_0 = 100h \text{Kms}^{-1}\text{Mpc}^{-1} \tag{1.13}$$

The *Planck* collaboration finds $H_0 = (67.4 \pm 0.5)\text{Kms}^{-1}\text{Mpc}^{-1}$ at 68% CL [9], which is however in tension at about 5σ with the latest local determination by the SH0ES collaboration, which instead finds $H_0 = (73.04 \pm 1.04)\text{Kms}^{-1}\text{Mpc}^{-1}$ at 68% CL [17]. This problem is known in literature as the *Hubble tension* and for an up-to-date review on the topic we refer the reader to [18].

1.2 Shortcomings of the Standard Big Bang Cosmology

The Standard Cosmological Model provides an excellent description of the thermal history of the Universe. It explains, with high accuracy, the Cosmic Microwave Background, the abundaces of light elements and the evolution of the Universe after the Big Bang Nucleosynthesis. There are, however, a few intriguing facts that it fails to provide explanations to.

1.2.1 The Flatness Problem

Several cosmological surveys at different scales and by different probes observe the present Universe to be spatially flat, without being any apparent reason for it to be so. The first Friedmann equation (1.11) implies:

$$\Omega_{tot} - 1 = \frac{k}{a^2 H^2} \tag{1.14}$$

Since in Standard Cosmology the scale factor behaves like $a \propto t^p$ with $p = 1/2$ for radiation and $p = 2/3$ for non-relativistic matter, the comoving Hubble radius $r_H = (aH)^{-1}$ grows with time and, as a consequence, $|\Omega_{tot} - 1|$ must diverge with time. Hence, in the context of the Standard Cosmological Model, explaining the quasi-flatness observed today would require an extreme fine-tuning of Ω_{tot} near 1 in the Early Universe.

1.2.2 The Relic Density Problem

It is believed that very shortly after the Big Bang the Universe was described by Grand Unified Theories (GUTs). In these theories, at very high temperatures, such as those found in the instants after the Universe was created, the strong, weak, and electromagnetic forces were indistinguishable from each other. These theories imply that the very early Universe should produce extremely massive particles, much more massive than any presently known particle, known as magnetic monopoles, and that there should be many such monopoles in the Universe today. However, no one has ever found evidence for such a particle.

1.2.3 The Horizon Problem

The comoving particle horizon $d_H(t)$ is defined as the maximal distance that can be covered by a light-ray in a cosmic time t:

$$\frac{d_H(t)}{a(t)} = \int_0^t \frac{dt'}{a(t')} = \int_0^a \frac{da'}{a'} \frac{1}{aH} \tag{1.15}$$

Since the comoving Hubble radius grows with time, equation (1.15) tells us that, sooner or later, all the scales will enter the horizon. In other words, the fraction of the Universe in causal contact around the observer grows bigger and bigger in time. We observe the Cosmic Microwave Background to exhibit nearly the same statistical properties, in particular the same temperature T, up to very tiny fluctuations, over regions of space that have never been in causal contact before. These regions are indeed separated by distances that are much larger than the largest distance travelled by light in all the history of the Universe.

1.3 Inflation

Inflation consists of a rapid exponential expansion of the Universe at early times that not only provides a solution to the aforementioned problems of the Standard Big Bang Cosmology, but it also provides a compelling mechanism to explain the generation of the primordial density perturbations, which serve as initial conditions to the process of hierarchical structure formation. The key assumption of inflation, as illustrated in Figure 1.2, is that at early times the comoving Hubble radius r_H, instead of increasing, decreases in time. The decreasing of r_H implies that $\dot{r}_H < 0$ and the corresponding condition is that

$$\ddot{a}(t) > 0 \tag{1.16}$$

meaning that the Universe must undergo a phase of accelerated expansion. Equation (1.5) tells us that such a period of accelerated expansion is possible if and only if the cosmic fluid

has a negative pressure, with equation of state:

$$P < -\frac{1}{3}\rho \tag{1.17}$$

An example of such a fluid is the cosmological constant Λ, which has equation of state $P = -\rho$. However, the cosmological constant is not a good candidate to drive inflation since it causes an exponential expansion that never ends. Instead, we want inflation to end at some point, allowing r_H to grow again. This is because if the accelerated expansion were to go on forever, all of the components of the Universe would be extremely diluted, therefore preventing anything to happen.

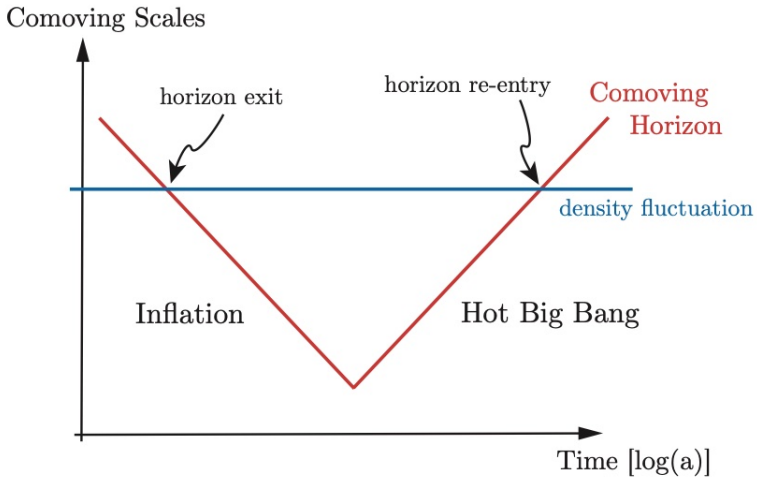

Figure 1.2. Plot of the comoving Hubble radius as a function of time. All scales of cosmological interest were larger than the Hubble radius until $a \simeq 10^{-5}$. However, at sufficiently early times, all scales of interest were smaller than the Hubble radius and thus were causally connected. Similarly, at later times, the scales of cosmological interest are back within the Hubble radius. Figure adapted from [19, 20].

1.4 Inflation as driven by a Slowly-rolling Scalar Field

In most current models of inflation, the exponential expansion is driven by the potential energy density $V(\varphi)$ of a scalar field, φ, called the inflaton, with action:

$$S = \int d^4x\sqrt{-g}\mathcal{L} = \int d^4x\sqrt{-g}\left[-\frac{1}{2}g^{\mu\nu}\partial_\mu\varphi\partial_\nu\varphi - V(\varphi)\right] \tag{1.18}$$

where g is the determinant of the metric tensor $g_{\mu\nu}$. By varying the action with respect to the field φ we obtain the Klein-Gordon equation:

$$\Box\varphi = \frac{\partial V}{\partial\varphi} \tag{1.19}$$

where $\Box$ is the covariant D'Alembert operator:

$$\Box\varphi = \frac{1}{\sqrt{-g}}\partial_\nu\left(\sqrt{-g}g^{\mu\nu}\partial_\mu\varphi\right) \tag{1.20}$$

In a FLRW universe, described by the metric (1.1), the Klein-Gordon equation (1.19) reduces to

$$\ddot{\varphi} + 3H\dot{\varphi} - \frac{\bigtriangledown^2\varphi}{a^2} + V_\varphi(\varphi) = 0 \tag{1.21}$$

where $V_\varphi(\varphi)$ is defined as the derivative of the energy potential with respect to φ. The term $3H\dot{\varphi}$ tells us that due to the expansion of the Universe the scalar field, rolling down its potential, is subjected to a friction. The energy-momentum tensor associated to the scalar field φ is given by

$$T_{\mu\nu} = -\frac{2}{\sqrt{-g}}\frac{\delta S}{\delta g^{\mu\nu}} = \partial_\mu\varphi\partial_\nu\varphi + g_{\mu\nu}\left[-\frac{1}{2}g^{\alpha\beta}\partial_\alpha\varphi\partial_\beta\varphi - V(\varphi)\right] \tag{1.22}$$

Let us now observe that the inflaton field can be split as $\varphi(t,\mathbf{x}) = \varphi_0(t) + \delta\varphi(t,\mathbf{x})$ where φ_0 is the classical background field i.e. the expectation value of the inflaton on the initial homogenous and isotropic state, and $\delta\varphi(t,\mathbf{x})$ are the quantum fluctuations around φ_0. This separation is justified by the fact that the quantum fluctuations are negligible when looking at the classical evolution i.e.

$$\langle\delta\varphi^2(t,\mathbf{x})\rangle \ll \varphi_0^2(t) \tag{1.23}$$

The classical background field φ_0 behaves like a perfect fluid with energy density and isotropic pressure given by

$$\rho_\varphi = \frac{\dot{\varphi}^2}{2} + V(\varphi) \tag{1.24}$$

$$P_\varphi = \frac{\dot{\varphi}^2}{2} - V(\varphi) \tag{1.25}$$

Recalling that inflation requires the pressure being negative, if we assume:

$$V(\varphi) \gg \dot{\varphi}^2 \tag{1.26}$$

we obtain the following condition:

$$P_\varphi \simeq -\rho_\varphi \tag{1.27}$$

This result tells us that indeed a scalar field which energy is dominant in the Universe and which potential energy dominates its kinetic term gives inflation.

1.4.1 Classical Dynamics

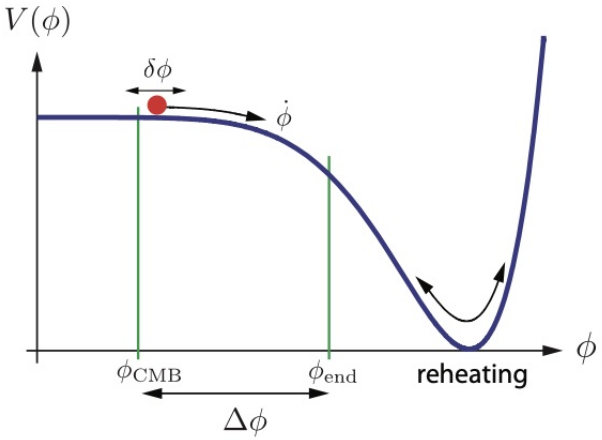

Figure 1.3. Example of a slow-roll inflaton potential. Acceleration occurs when the potential energy of the field, $V(\varphi)$, dominates its kinetic energy, $\frac{1}{2}\dot{\varphi}^2$. Figure adapted from [20].

Let us now focus on the evolution of the classical bagkground field φ_0. The equation of motion (1.21), for an homogeneous field, is given by

$$\ddot{\varphi} + 3H\dot{\varphi} + V_\varphi(\varphi) = 0 \tag{1.28}$$

if we impose the condition (1.26) on equation (1.28), the scalar field slowly rolls down its potential. Such a period of slow-roll can be achieved if the inflaton is in a region where the potential is sufficiently flat (see Figure 1.3). In this case, we expect the $\ddot{\varphi}$ term to be negligible. Assuming the energy density of the universe dominated by the potential energy of the inflaton field, the first Friedmann equation (1.4) becomes:

$$H^2 \simeq \frac{8\pi G}{3} V(\varphi) \tag{1.29}$$

and neglecting the $\ddot{\varphi}$ term, the equation of motion (1.28) reduces to

$$3H\dot{\varphi} = -V_\varphi(\varphi) \tag{1.30}$$

From equation (1.30), using the result (1.29), we read off the flatness conditions:

$$\dot{\varphi}^2 \ll V(\varphi) \Longrightarrow \frac{V_\varphi^2}{V} \ll H^2 \tag{1.31}$$

$$\ddot{\varphi} \ll 3H\dot{\varphi} \Longrightarrow V_{\varphi\varphi} \ll H^2 \tag{1.32}$$

1.4.2 Slow-roll Parameters

In order to give predictions related to specific models and to compare them with each other and with observations, the slow-roll regime dynamics is quantified by means of the so-called slow-roll parameters ϵ and η:

$$\epsilon = -\frac{\dot{H}}{H^2} = \frac{4\pi G\dot{\varphi}^2}{H^2} \simeq \frac{3}{2}\frac{\dot{\varphi}^2}{V(\varphi)} \simeq \frac{1}{16\pi G}\left(\frac{V_\varphi}{V}\right)^2 \tag{1.33}$$

$$\eta = \frac{V_{\varphi\varphi}}{3H^2} \simeq \frac{1}{8\pi G}\frac{V_{\varphi\varphi}}{V} \tag{1.34}$$

A successful period of inflation requires the slow-roll parameters to be $\epsilon, \eta \ll 1$. As soon as these conditions fail, inflation ends. The scalar field will then reach the minimum of the potential and will start to oscillate around it. By this time, any other contribution to the energy density of the Universe has been redshifted away by the expansion. However, we know that the Universe must be repopulated by hot radiation. This is achieved by reheating: the inflaton φ not only starts to oscillate around its minimum but it also begins to decay to lighter relativistic particles, thus allowing us to recover the well established prediction of the Standard Big Bang Model.

1.4.3 Number of e-foldings

Defining inflation as a period of rapid exponential expansion of the Universe is not sufficient to solve the aforementioned problems. We must ensure that inflation lasts long enough that a small, smooth patch of size smaller than the Hubble radius can grow to encompass at least the entire observable Universe. To quantify how much the Universe expands we introduce the number of e-foldings:

$$N = \int_{t_\mathrm{i}}^{t_\mathrm{f}} dt H(t) = \ln\left(\frac{a(t_\mathrm{f})}{a(t_\mathrm{i})}\right) \tag{1.35}$$

where t_i and t_f are, respectively, the time corresponding to when inflation starts and ends. It can be proven that in order to be successful, inflation must last more than about 60 e-foldings.

1.5 Generating Primordial Perturbations during Inflation

We will now discuss the generation and the evolution of the quantum fluctuations of the inflaton field $\delta\varphi(t, \mathbf{x})$. This is extremely important, since these fluctuations are associated to the primordial density perturbations which survive at the end of inflation and provide the initial conditions for the process of hierarchical structure formation. Our current understanding of the origin of structure is that, once the Universe became matter dominated, primeval density inhomogeneities were amplified by gravity and grew into the structures we observe today. For structure formation to occur via gravitational instability, there must have been small, pre-existing fluctuations on scales which entered the Hubble horizon during the radiation and matter-dominated epochs. Inflation provides a causal mechanism to generate these density perturbations since, as we have seen, a key ingredient of inflation is the fact that during the inflationary expansion the Hubble comoving radius instead of increasing decreases with time. As a consequence, soon the wavelength of the quantum fluctuations exceeds the size of the horizon and, due to the expansion, it gets stretched to super-horizon scales. What happens next is that, since causal processes can not happen on super-horizon scales, the quantum fluctuations get frozen to some non-zero value $\delta\varphi$, while their wavelength grows exponentially. Later, when inflation ends and the Hubble comoving radius begins to increase again, the fluctuations eventually re-enter the horizon either during the matter or radiation-dominated epoch, thus providing the initial conditions for the process of structure formation.

1.5.1 Quantum Fluctuations of a Scalar Field during a de Sitter Stage

We begin our discussion considering the case of a scalar field φ (the inflaton) with effective potential $V(\varphi)$ in a pure de Sitter stage, during which the Hubble parameter H is constant. From the equation of motion for the scalar field (1.21), including the perturbations $\delta\varphi$, we obtain, at linear order, the following equation:

$$\ddot{\delta\varphi} + 3H\dot{\delta\varphi} - \frac{\nabla^2\delta\varphi}{a^2} + V_{\varphi\varphi}\delta\varphi = 0 \tag{1.36}$$

It is convenient at this point to switch to the conformal time τ, related to the cosmic time t through $d\tau = dt/a(t)$. The previous equation, switching to conformal time, therefore becomes:

$$\delta\varphi'' + 2\frac{a'}{a}\varphi' - \nabla^2\delta\varphi + a^2 V_{\varphi\varphi}\delta\varphi = 0 \tag{1.37}$$

where prime here denotes the derivative with respect to the conformal time. Redefining now the field $\delta\varphi(\tau, \mathbf{x})$ as

$$\delta\hat{\varphi}(\tau, \mathbf{x}) = a(\tau)\delta\varphi(\tau, \mathbf{x}) \tag{1.38}$$

and introducing the creation and annihilation operators a_k and $a_k^\dagger$, we can promote the field $\delta\hat{\varphi}$ to an operator which can be decomposed as

$$\delta\hat{\varphi}(\tau,\mathbf{x}) = \int \frac{d^3k}{(2\pi)^3}\left[u_k(\tau)\hat{a}_k e^{-i\mathbf{k}\cdot\mathbf{x}} + u_k^*(\tau)\hat{a}_k^\dagger e^{i\mathbf{k}\cdot\mathbf{x}}\right] \tag{1.39}$$

These creation and annihilation operators satisfy the standard commutation relations:

$$[a_k, a_{k'}] = 0, \qquad [a_k, a_{k'}^\dagger] \quad = \delta^{(3)}(\mathbf{k}-\mathbf{k}') \tag{1.40}$$

and the modes $u_k(\tau)$ are normalised so that they satisfy the condition

$$u_k^* u_k^{'} - u_k u_k^{*'} = -i \tag{1.41}$$

From equation (1.37), using the decomposition (1.38), we get that

$$\delta\hat{\varphi}'' - \frac{a''}{a}\delta\hat{\varphi} - \bigtriangledown^2\delta\hat{\varphi} + a^2 V_{\varphi\varphi}\delta\hat{\varphi} = 0 \tag{1.42}$$

from which, going to Fourier space and using that $|\delta\hat{\varphi}_k| = |u_k|$, we read off that the modes $u_k(\tau)$ obey the equation of motion:

$$u_k''(\tau) + \left[k^2 - \frac{a''}{a} + M_\varphi^2 a^2\right] u_k(\tau) = 0 \tag{1.43}$$

where $M_\varphi^2 = V_{\varphi\varphi}$ is the effective mass of the scalar field. This equation is equivalent to the one of an harmonic oscillator with a frequency changing in time due to the expansion of the Universe. Let us observe that, at very short distances, the modes $u_k(\tau)$ must reproduce the form for the ordinary flat space-time quantum field theory. This implies that, well within the horizon, in the limit $k/aH \to \infty$, the modes should approach plane waves of the form:

$$u_k(\tau) \to \frac{\exp^{-ik\tau}}{\sqrt{2k}} \tag{1.44}$$

In the case of a pure de Sitter stage, equation (1.43) has an exact solution. However, before recovering it, let us study its limiting behaviour on super-horizon and sub-horizon scales, considering for simplicity the massless case i.e. $M_\varphi^2 = V_{\varphi\varphi} = 0$. On sub-horizon scales ($k \gg aH$), the k^2 term is the dominant one and equation (1.43) thus reduces to

$$u_k''(\tau) + k^2 u_k(\tau) = 0 \tag{1.45}$$

The solution is simply a plane wave of the form:

$$u_k(\tau) = \frac{e^{-ik\tau}}{\sqrt{2k}} \tag{1.46}$$

This result implies that the field $\delta\varphi_k$, on sub-horizion scales, oscillates with a decreasing amplitude that depends on the inverse of the scale factor $a(\tau)$ as follows:

$$|\delta\varphi_k| = \frac{1}{a(\tau)\sqrt{2k}} \tag{1.47}$$

In the opposite limiting case, on super-horizon scales ($k \ll aH$), the $a^{''}/a$ term is the dominant one. Thus equation (1.43) reduces to

$$u_k^{''}(\tau) - \frac{a^{''}}{a} u_k(\tau) = 0 \tag{1.48}$$

This equation admits two solutions, a growing and a decaying mode:

$$u_k(\tau) = B_+(k)a(\tau) + B_-(k)a^{-2}(\tau) \tag{1.49}$$

As the Universe expands, the decaying mode gets suppressed by the a^{-2} factor and thus can be neglected. The amplitude of the growing mode, $B_+(k)$, can be fixed by matching (the absolute value of) the solution (1.49) to the plane wave solution (1.46) at horizon-crossing i.e. at $k = aH$, obtaining that

$$|B_+(k)| = \frac{1}{a(\tau)\sqrt{2k}} = \frac{H}{\sqrt{2k^3}} \tag{1.50}$$

This result tells us that the quantum fluctuations of the field $\delta\varphi_k$, on super-horizon scales, are constant and with amplitude

$$|\delta\varphi_k| = \frac{|u_k|}{a(\tau)} = \frac{H}{\sqrt{2k^3}} \tag{1.51}$$

Let us now briefly sketch how to derive the exact solution for equation (1.43). It can be proven that in a pure de Sitter stage equation (1.43) can be recast as follows:

$$u_k^{''}(\tau) + \left[k^2 - \frac{\nu^2 - 1/4}{\tau^2}\right] u_k(\tau) = 0 \tag{1.52}$$

where

$$\nu^2 = \left(\frac{9}{4} - \frac{M_\varphi^2}{H}\right) \tag{1.53}$$

Equation (1.52) is a Bessel equation, whose general solution, for real ν, is known to be of the form:

$$u_k(\tau) = \sqrt{-\tau}\left[c_1(k)H_\nu^{(1)}(-k\tau) + c_2(k)H_\nu^{(2)}(-k\tau)\right] \tag{1.54}$$

where $H_\nu^{(1)}$ and $H_\nu^{(2)}$ are, respectively, the Hankel functions of first and second kind. If we now impose that on sub-horizon scales ($-k\tau \gg 1$) the solution matches the plane wave solution expected in a flat space-time, knowing the asymptotic behaviour of the Hankel functions, setting $c_2(k) = 0$ and

$$c_1(k) = \frac{\sqrt{\pi}}{2} e^{i\left(\nu+\frac{1}{2}\right)\frac{\pi}{2}} \tag{1.55}$$

we get that

$$u_k(\tau) = \frac{\sqrt{\pi}}{2} e^{i\left(\nu+\frac{1}{2}\right)\frac{\pi}{2}} \sqrt{-\tau} H_\nu^{(1)}(-k\tau) \tag{1.56}$$

In particular, we are interested in the asymptotic behaviour of the solution when the fluctuation is well outside the horizon ($-k\tau \ll 1$). On super-horizon scales, since

$$H_\nu^{(1)}(-k\tau \ll 1) \sim \sqrt{\frac{2}{\pi}} e^{i\frac{\pi}{2}} 2^{\left(\nu-\frac{3}{2}\right)} \frac{\Gamma(\nu)}{\Gamma(\frac{3}{2})} (-k\tau)^{-\nu} \tag{1.57}$$

we get that the fluctuations of a scalar field $\delta\varphi_k$ with a non-vanishing mass are not exactly constant and have amplitude

$$|\delta\varphi_k| = 2^{\left(\nu-\frac{3}{2}\right)} \frac{\Gamma(\nu)}{\Gamma(\frac{3}{2})} \frac{H}{\sqrt{2k^3}} \left(\frac{k}{aH}\right)^{\frac{3}{2}-\nu} \tag{1.58}$$

Let us notice that the above asymptotic solution is valid for values of the scalar field mass $M_\varphi \leqslant 3/2H$, meaning that fluctuations of the scalar field can be generated on super-horizon scales only if the scalar field is light. This is because it can be shown that for very massive scalar fields the fluctuations of the field remain in the vacuum state and do not produce perturbations on cosmological relevant scales. If the scalar field is very light, remembering the definition for the slow-roll parameter η introduced in the previous sections, we can make

an expansion of the solution (1.58) to lowest order in $\eta = (M_\varphi^2/3H^2) \ll 1$ to find

$$|\delta\varphi_k| = \frac{H}{\sqrt{2k^3}} \left(\frac{k}{aH}\right)^{\frac{3}{2}-\nu} \tag{1.59}$$

with $\frac{3}{2} - \nu \simeq \eta$.

1.5.2 Quantum Fluctuations of a Scalar Field in a quasi-de Sitter Stage

The results we obtained so far, however, are approximate ones. During the inflationary expansion the Hubble rate is not exactly constant, but changes with time as $\dot{H} = -\epsilon H^2$. Therefore, considering a scalar field with a very small effective mass, from the definition of conformal time:

$$a(\tau) \simeq -\frac{1}{H}\frac{1}{\tau(1-\epsilon)} \tag{1.60}$$

where ϵ is the inflationary slow-roll parameter, we get that

$$\frac{a''}{a} = a^2H^2\left(2 + \frac{\dot{H}}{H^2}\right) \simeq \frac{2}{\tau^2}\left(1 + \frac{3}{2}\epsilon\right) \tag{1.61}$$

Plugging this result into equation (1.43) we obtain again a Bessel equation where now ν, to lowest order in the slow-roll parameters, is given by

$$\nu \simeq \frac{3}{2} + \epsilon - \eta \tag{1.62}$$

1.5.3 Correlation Functions and Power Spectrum

To compare theoretical predictions to observations, we need to introduce some observable quantities to characterise the properties of the fluctuations. The fluctuations are described by a quantum field $\delta\varphi(t, \mathbf{x})$, representing the amplitude of the fluctuations in each point of the space-time. Even though the ensemble average of these fluctuations is zero by definition, they are correlated through different points in the space-time. Assuming the perturbations $\delta\varphi(t, \mathbf{x})$ being Gaussian distributed, the 2-point correlation function specifies all the statistical properties of the perturbations. To find the quantities we are looking for, let us therefore begin by considering the 2-point correlation function of the Fourier transform of a generic stochastic field $\delta(t, \mathbf{x})$:

$$\langle\delta(\mathbf{k}_1, t)\delta(\mathbf{k}_2, t)\rangle = (2\pi)^3 P(k)\delta^{(3)}(\mathbf{k}_1 + \mathbf{k}_2) \tag{1.63}$$

Where our convention for the Fourier transform is:

$$\begin{aligned}\delta(\mathbf{x},t) &= \int \frac{d^3\mathbf{k}}{(2\pi)^3} e^{i\mathbf{k}\cdot\mathbf{x}}\delta(\mathbf{k},t) \\ \delta(\mathbf{k},t) &= \int d^3\mathbf{x} e^{-i\mathbf{k}\cdot\mathbf{x}}\delta(\mathbf{x},t)\end{aligned} \tag{1.64}$$

The quantity $P(k)$, defined through equation (1.63), is the power spectrum and it measures the amplitude of the fluctuations at a given scale k. This can be easily proven observing that the mean square value of the stochastic field $\delta(t,\mathbf{x})$, in real space, is given by

$$\langle\delta^2(t,\mathbf{x})\rangle = \int \frac{d^3k}{(2\pi)^3}P(k) = \int \frac{dk}{2\pi^2}k^2P(k) = \int \frac{dk}{k}\mathcal{P}(k) \tag{1.65}$$

where $\mathcal{P}(k)$ is the dimensionless power spectrum, defined by

$$\mathcal{P}(k) = \frac{k^3}{2\pi^2}P(k) \tag{1.66}$$

The slope of the power spectrum is described by its associated spectral index $n(k)$, defined as

$$n(k) - 1 \equiv \frac{d\ln\mathcal{P}(k)}{d\ln k} \tag{1.67}$$

If $n = 1$, we have what is called an Harrison-Zel'dovich spectrum for which the amplitude of the fluctuations does not depend on the cosmological scale k. If instead the spectral index deviates from unity, the power spectrum $\mathcal{P}(k)$ can be written with respect to some pivot scale k_0 as

$$\mathcal{P}(k) = A(k_0)\left(\frac{k}{k_0}\right)^{n-1} \tag{1.68}$$

where A is the amplitude of the perturbations. In the case of the quantum fluctuations of the inflaton field $\delta\varphi(t,\mathbf{x})$, the 2-point correlation function is given by

$$\langle\delta\varphi_{k_1}\delta\varphi^*_{k_2}\rangle = (2\pi)^3|\delta\varphi_k|^2\delta^{(3)}(\mathbf{k}_1+\mathbf{k}_2) \tag{1.69}$$

therefore, by comparing equation (1.69) to equation (1.63), we identify

$$P(k) = |\delta\varphi_k|^2 = \frac{|u_k|^2}{a^2} \quad \longrightarrow \quad \mathcal{P}(k) = \frac{k^3}{2\pi^2}\frac{|u_k|^2}{a^2} \tag{1.70}$$

On super-horizon scales, recalling the result for the amplitude of the fluctuations of the scalar field $\delta\varphi_k$, given by equation (1.59), we get that the dimensionless power spectrum is given by

$$\mathcal{P}(k) = \left(\frac{H}{2\pi}\right)^2 \left(\frac{k}{aH}\right)^{3-2\nu} \tag{1.71}$$

where, a in a quasi-de Sitter stage, $3 - 2\nu \simeq 2\eta - 2\epsilon$.

Chapter 2

Theory of Cosmological Perturbations

In Chapter 1 we have shown how, from the quantum fluctuations of a scalar field, primordial density perturbations are generated during an inflationary period. However, in our computations there is actually an inconsistency: we perturbed our scalar field in an unperturbed space-time. In the case of the inflaton field, taking into account perturbations in the metric tensor is particularly important. The fact that inflaton field drives the inflationary expansion means that it dominates the energy density of the Universe at that time. This entails that any perturbation in the inflaton field $\delta\varphi$ implies a perturbation of the energy-momentum tensor $\delta T_{\mu\nu}$ that, through Einstein's equations, implies a perturbation in the metric tensor $\delta g_{\mu\nu}$. On the other hand, perturbations in the metric tensor affect the evolution of the inflaton field $\delta\varphi$ through the perturbed Klein-Gordon equation (1.19) since

$$\Box\varphi = \frac{1}{\sqrt{-g}}\partial_\nu\left(\sqrt{-g}g^{\mu\nu}\partial_\mu\varphi\right) \tag{2.1}$$

which will then vary the metric again, and so on. Therefore, the following sections will be primarily devoted to set up the framework needed to revise our calculations and thus provide a more rigorous treatment of the primordial density perturbations. Note that unless otherwise specified we will work with conformal time τ.

2.1 Perturbing the Metric Tensor

Let us begin by writing down the perturbations on a spatially flat FLRW background. The components of a perturbed spatially flat FLRW metric can be written as follows:

$$\begin{aligned} g_{00} &= -a^2(\tau)\left[1 + 2\sum_{r=1}^{\infty}\frac{1}{r!}\hat{\Phi}^{(r)}(\tau,\mathbf{x})\right] \\ g_{0i} &= a^2(\tau)\sum_{r=1}^{\infty}\frac{1}{r!}\hat{\omega}_i^{(r)}(\tau,\mathbf{x}) \\ g_{ij} &= a^2(\tau)\left[\left(1 - 2\sum_{r=1}^{\infty}\frac{1}{r!}\hat{\Psi}^{(r)}(\tau,\mathbf{x})\right)\delta_{ij} + \sum_{r=1}^{\infty}\frac{1}{r!}\hat{\chi}_{ij}^{(r)}(\tau,\mathbf{x})\right] \end{aligned} \tag{2.2}$$

where r keeps track of the perturbation order and thus the functions $\hat{\Phi}^{(r)}$, $\hat{\omega}_i^{(r)}$, $\hat{\Psi}^{(r)}$ and $\hat{\chi}_{ij}^{(r)}$ stand for the r-th order perturbations to the metric. These perturbations are usually split according to their transformation properties into their scalar, vector and tensor parts, where the scalar parts are related to a scalar potential, the vector parts are related to transverse vectors and the tensor parts are related to transverse traceless tensors. In particular, the $\hat{\Phi}^{(r)}$ and $\hat{\Psi}^{(r)}$ perturbation functions have only a scalar part and the $\hat{\omega}_i^{(r)}$ and $\hat{\chi}_{ij}^{(r)}$ ones can be decomposed as

$$\hat{\omega}_i^{(r)} = \partial_i \omega_{||}^{(r)} + \omega_{i\perp}^{(r)} \tag{2.3}$$

$$\hat{\chi}_{ij}^{(r)} = D_{ij}\chi_{||}^{(r)} + \partial_i \chi_{j\perp}^{(r)} + \partial_j \chi_{i\perp}^{(r)} + \chi_{ij}^{(r)T} \tag{2.4}$$

where $\omega_{||}^{(r)}$ and $\chi_{||}^{(r)}$ are two scalars, $\omega_{i\perp}^{(r)}$ and $\chi_{i\perp}^{(r)}$ are two transverse vectors i.e. $\partial^i \omega_{i\perp}^{(r)} = \partial^i \chi_{i\perp}^{(r)} = 0$, $\chi_{ij}^{(r)T}$ is a symmetric, transverse and trace-free tensor and

$$D_{ij} = \partial_i \partial_j - \frac{1}{3}\delta_{ij} \bigtriangledown^2 \tag{2.5}$$

is a trace-free operator. Let us observe that, at least at linear order, the scalar, vector and tensor modes are decoupled from each other and thus evolve independently.

2.2 Gauge Dependence

Before proceeding further with our discussion, an important remark is in order. In the perturbation theory of General Relativity one considers a space-time, the *perturbed space-time*, assumed to be close to a simple, symmetric space-time, and the *background space-time*, that in our case of interest is the FLRW space-time. The perturbation δT in a given quantity is then defined as the difference between the physical value of T, computed on the perturbed space-time, and the background unperturbed value T_0. To compare the physical value of T with the reference value T_0, it is necessary to establish a map i.e. a one-to-one correspondence between the perturbed and the background space-time. Such a map represents a gauge choice and a change in the map corresponds to a gauge transformation. From the point of view of a set of coordinates, a change in the gauge means a change of the coordinates and, since General Relativity is a theory based on the freedom of changing locally the system of coordinates, the gauge choice is not unique. This implies that the perturbations δT on the background value T_0 will transform after a change of the coordinates, thus acquiring different values which are nonetheless on equal footing. One possible way to solve this issue of gauge-dependence, which holds at any order of the perturbations, is to choose a gauge and perform our calculations in that gauge. But what does it mean to choose a gauge?

Let us consider an infinitesimal coordinate transformation:

$$\hat{x}^{\mu} = x^{\mu} - \xi^{\mu}_{(r)} \tag{2.6}$$

where $\xi^{\mu}_{(r)}$ is a vector field defining the gauge transformation. In particular, the function $\xi^{0}_{(r)}$ selects constant τ-hypersurfaces i.e. the time-slicing, while the function $\xi^{i}_{(r)}$ selects the space coordinates within these hypersurfaces. These two functions can be decomposed as

$$\begin{aligned} \xi^{0}_{(r)} &= \alpha_{(r)} \\ \xi^{i}_{(r)} &= \partial^{i}\beta_{(r)} + d^{i}_{(r)}, \quad \partial_{i} d^{i}_{(r)} = 0 \end{aligned} \tag{2.7}$$

From a practical point of view choosing a gauge means fixing, order by order, two scalars $\alpha_{(r)}$, $\beta_{(r)}$ and one vector $d^{i}_{(r)}$. If we now expand a generic tensor T, defined in the perturbed space-time, around its background value T_0 as follows:

$$T(\tau, x^{i}) = T_0 + \delta T(\tau, x^{i}) \tag{2.8}$$

then its perturbation δT will transform under a gauge transformation as

$$\widetilde{\delta T} = \delta T + \mathcal{L}_{\xi} T_0 \tag{2.9}$$

where $\mathcal{L}_{\xi}$ is the Lie derivative along the vector ξ^{μ}. Therefore, for example, the perturbation in the energy density $\delta\rho$ would transform as

$$\widetilde{\delta\rho} = \delta\rho + \rho_{0}^{'}\alpha \tag{2.10}$$

Another possible way to circumvent this gauge-dependence problem consists in identifying combinations of perturbations which are gauge-invariant. The first to propose a gauge-invariant treatment of the perturbations at linear order was Bardeen in his seminal work [21]. Central to Bardeen's paper were two scalar potentials, dubbed Bardeen potentials, that govern the evolution of the scalar perturbations and are given by the following combinations:

$$\begin{aligned} \Phi &= \hat{\Phi} + \frac{1}{6}\bigtriangledown^{2}\chi_{||} + \frac{a^{'}}{a}\omega_{||} - \frac{1}{2}\frac{a^{'}}{a}\chi_{||}^{'} \\ \Psi &= \hat{\Psi} + \omega_{||}^{'} + \frac{a^{'}}{a}\omega_{||} - \frac{1}{2}\left(\chi_{||}^{''} + \frac{a^{'}}{a}\chi_{||}^{'}\right) \end{aligned} \tag{2.11}$$

It is interesting to observe that in the Poisson gauge, defined by the two scalar conditions $\omega_{||} = 0$ and $\chi_{||} = 0$ and the vector condition $\chi_{i\perp} = 0$, the expressions for the two Bardeen

potentials reduce to

$$\begin{aligned} \Phi &= \hat{\Phi} \\ \Psi &= \hat{\Psi} \end{aligned} \tag{2.12}$$

In the next section we will give the expression of another relevant gauge-invariant quantity, *the curvature perturbation on spatial slices of uniform energy density*, allowing us to understand how, for example, a gauge-invariant quantity can be found by selecting unambiguously a proper time-slicing.

2.3 Curvature Perturbation on Spatial Slices of Uniform Density

Let us begin by introducing the intrinsic spatial curvature on hypersurfaces of conformal time τ that, for a flat FLRW Universe, is given by

$$^{(3)}R = \frac{4}{a^2} \bigtriangledown^2 \widetilde{\Psi} \tag{2.13}$$

where, for simplicity of notation, we defined

$$\widetilde{\Psi} = \hat{\Psi} + \frac{1}{6} \bigtriangledown^2 \chi \tag{2.14}$$

The combination $\widetilde{\Psi}$ is usually referred to as the *curvature perturbation* but, being defined only on a given slicing, is not a gauge-invariant quantity. Indeed, under a change of the time-slicing $\tau \to \tau + \alpha$, we have that

$$\widetilde{\Psi} \to \widetilde{\Psi} - \mathcal{H}\alpha \tag{2.15}$$

where $\mathcal{H} = a^{'}/a$ is the Hubble parameter in conformal time. If we now consider the slicing of uniform energy density, defined as the slicing where there is no perturbation in the energy density i.e. $\delta\rho = 0$, then from the equation (2.10) we have that

$$\alpha = \frac{\delta\rho}{\rho_0'} \tag{2.16}$$

Therefore, the curvature perturbation $\widetilde{\Psi}$ on uniform density perturbation slices will be given by

$$\widetilde{\Psi}\big|_{\rho} = \widetilde{\Psi} + \mathcal{H}\frac{\delta\rho}{\rho_0'} \tag{2.17}$$

This quantity is clearly gauge-invariant and is usually denoted in literature as follows:

$$-\zeta \equiv \widetilde{\Psi}\big|_{\rho} = \widetilde{\Psi} + \mathcal{H}\frac{\delta\rho}{\rho_0'} \tag{2.18}$$

2.3.1 Adiabatic and Entropy Perturbations

The gauge-invariant curvature perturbation whose expression is given by equation (2.18) was first introduced by Bardeen, Steinhardt and Turner [22] as a conserved quantity on large scales for adiabatic perturbations. Adiabatic perturbations are such that a net perturbation is produced in the energy density and (via the Einstein's equations) also in the intrinsic spatial curvature. Since neither the energy density nor the intrinsic spatial curvature are gauge-invariant, it's straightforward to understand the utility of using the quantity ζ to characterise such perturbations. The notion of adiabaticity thus applies when, in the physical space-time, the properties of a fluid can be described uniquely in terms of its energy density ρ. In the same way, one can define a non-adiabatic (entropy) perturbation of a given quantity T, simply extracting that part of the perturbation that does not depend on the energy density. In general, this can be done considering the value of the perturbation δT on hypersurfaces of uniform energy density:

$$\delta T\big|_{n-ad} \equiv \widetilde{\delta T}\big|_{\rho} \tag{2.19}$$

since, when $T = T(\rho)$, this quantity will vanish for adiabatic perturbations. Given that the entropy perturbations do not induce any inhomogeneities in the energy density and thus on the intrinsic spatial curvature, they are also known in literature as *isocurvature* perturbations.

2.4 Power Spectrum of the Curvature Perturbation

Assuming inflation to be driven by a scalar field, we have already seen how its potential energy will dominate the energy density of the Universe during that time. As we shall see in a moment, the quantum fluctuations of the inflaton field generate adiabatic curvature perturbations and thus our aim in this section will be to calculate the primordial curvature perturbation generated on large scales and its power spectrum. Let us begin our discussion by revising our calculation of the amplitude of the quantum fluctuations of the inflaton, taking this time into account also the perturbations in the metric tensor. With this goal in mind, we introduce a gauge-invariant quantity, the so-called Sasaki-Mukhanov variable, that accounts for both the metric and the inflaton perturbations:

$$Q_{\varphi} = \delta\varphi + \frac{\varphi'}{\mathcal{H}}\widetilde{\Psi} \tag{2.20}$$

In the spatially flat gauge, defined by the requirements that $\hat{\Psi} = 0$ and $\chi = 0$, if one redefines

Q_φ as $\hat{Q}_\varphi = a(\tau)Q_\varphi$, one finds that the Klein-Gordon equation (1.37) in Fourier space reads off [23]:

$$\hat{Q_\varphi}'' + \left[k^2 - \frac{a''}{a} + M^2 a^2\right]\hat{Q_\varphi} = 0 \tag{2.21}$$

where, to lowest order in the slow-roll parameters, the effective mass of the inflaton field is given by

$$M_\varphi^2 = V_{\varphi\varphi} = 3\eta - 6\epsilon \tag{2.22}$$

Since this equation is of the same form of equation (1.43), we can solve it using the same procedure adopted in the previous sections, eventually finding that on super-horizon scales and at lowest order in the slow-roll parameters the amplitude of the quantum fluctuations of the inflaton is given by

$$|Q_\varphi| = \frac{H}{\sqrt{2k^3}}\left(\frac{k}{aH}\right)^{\frac{3}{2}-\nu} \tag{2.23}$$

with $\nu \simeq \frac{3}{2} + 3\epsilon - \eta$. To calculate the curvature perturbation on large scales we can now introduce the *curvature perturbation on comoving hypersurfaces* whose definition, in the case of a scalar field, is given by

$$\mathcal{R} = \tilde{\Psi} + \frac{\mathcal{H}}{\varphi'}\delta\varphi \tag{2.24}$$

It can be proven that the curvature perturbation on comoving hypersurfaces $\mathcal{R}$ and the uniform energy density curvature perturbation $-\zeta$ are simply related by

$$-\zeta = \mathcal{R} + \frac{2\rho}{9(\rho+p)}\left(\frac{k}{aH}\right)^2\hat{\Phi} \tag{2.25}$$

and that in particular, on super-horizon scales, $\mathcal{R} \simeq -\zeta$ [23]. From the definition of the Sasaki-Mukhanov variable (2.20) it is evident that

$$\mathcal{R} = \frac{\mathcal{H}}{\varphi'}Q_\varphi \tag{2.26}$$

Thus, recalling the expression for the dimensionless power spectrum of the quantum fluctuations of the scalar field on super-hozion scales, given by equation (1.71), switching back to cosmic

time t we obtain that the power spectrum for the curvature perturbations on large scales is given by

$$\mathcal{P}_{\mathcal{R}}(k) = \left(\frac{H^2}{2\pi\dot{\varphi}}\right)^2 \left(\frac{k}{aH}\right)^{3-2\nu} \simeq \left(\frac{H^2}{2\pi\dot{\varphi}}\right)^2_* \tag{2.27}$$

where the asterisk denotes quantities evaluated at the epoch a given perturbation mode leaves the horizon during inflation i.e. at horizon crossing $k = aH$. Notice also that this result tells us that, on super-horizon scales, the perturbation mode is constant. In particular, since in the spatially flat gauge $-\zeta = \mathcal{H}(\delta\rho/\rho_0')$, it is clear that the curvature mode allow us to connect the primordial perturbations produced during inflation to observable quantities. We conclude our discussion with the computation of the spectral index of the power spectrum (2.27) which, to lowest order in the slow-roll parameters, in given by

$$n_{\rm s} - 1 = 3 - 2\nu = 2\eta - 6\epsilon \tag{2.28}$$

Current results from CMB data tell us that the spectrum is very close to an Harrison-Zel'dovich one, with $n_{\rm s} = 0.965 \pm 0.004$ at 68% CL [9].

2.5 Gravitational Waves from Inflation

We have seen how the quantum fluctuations of the inflaton field, via the Einstein's equations, induce perturbations in the metric tensor and how these perturbations can be split into their scalar, vector and tensor part according to their transformation properties. Before concluding our discussion we should now spend a few words on the tensor perturbations since these tensor perturbations constitute a stochastic background of Gravitational Waves (GW). A stochastic background of waves is a set of continuous waves, fully characterised by their statistical properties. These GW consist of a signal coming from every direction in the sky and having a whole spectrum in the frequency domain and thus differ from the signal coming from astrophysical sources, which come from a specific direction in the sky and is peaked at a specific frequency at coalescence. Let us begin by considering a generic symmetric three-tensor h_{ij}. In general, a symmetric three-tensor has six degrees of freedom. However, as we have already seen, tensor perturbations are traceless and transverse and thus there remain only two physical degrees of freedom, corresponding to two polarisation states, that are usually denoted as $\lambda = +, \times$. Going to Fourier space and introducing the polarisation tensors ϵ^{λ}_{ij}, having the following properties:

$$\epsilon_{ij} = \epsilon_{ji} \quad , \quad k^i \epsilon_{ij} \quad = 0 \quad , \quad \epsilon^i_{\ i} = 0 \tag{2.29}$$

we can decompose the tensor perturbations h_{ij} as follows:

$$h_{ij}(\mathbf{x},\tau) = \sum_{\lambda} \int \frac{d^3k}{(2\pi)^3} e^{i\mathbf{k}\cdot\mathbf{x}} h_{\lambda}(\mathbf{k},\tau)\epsilon_{ij}^{\lambda}(\mathbf{k}) \tag{2.30}$$

One can prove that the two degrees of freedom of the tensor modes $h_\lambda(\mathbf{k},\tau)$ propagate as two massless, minimally coupled scalar fields φ_λ, with $h_\lambda = \sqrt{32\pi G}\varphi_\lambda$. This implies that h_λ satisfies the equation of motion of a massless scalar field in a FLRW background and thus we can conclude that, on large scales, the amplitude of the tensor modes scales as

$$|h_\lambda| = \sqrt{32\pi G}|\varphi_\lambda| = \sqrt{32\pi G}\frac{H}{\sqrt{2k^3}}\left(\frac{k}{aH}\right)^{\frac{3}{2}-\nu} \tag{2.31}$$

where, to lowest order in the slow-roll parameters, $\frac{3}{2} - \nu \simeq -\epsilon$. On super-horizon scales the fluctuations are constant and, as usual, a way to characterise them is via the calculation of the power spectrum, which is given by

$$\mathcal{P}_{\mathrm{T}}(k) = \left(\frac{k^3}{2\pi^2}\sum_{\lambda}|h_\lambda|^2\right) = \frac{8}{M_{\mathrm{P}}^2}\left(\frac{H}{2\pi}\right)^2\left(\frac{k}{aH}\right)^{-2\epsilon} \tag{2.32}$$

where we introduced the definition of *reduced Planck mass* $M_{\mathrm{P}}^{-2} = 8\pi G$. We can then define the tensor spectral index as

$$n_{\mathrm{T}} \equiv \frac{d\ln\mathcal{P}_{\mathrm{T}}(k)}{d\ln k} = -2\epsilon \tag{2.33}$$

The spectrum of the tensor perturbations is nearly scale-invariant. Furthermore, the amplitude of the tensor modes depends only on the Hubble rate during inflation, which in turn depends only on the energy scale $V^{1/4}$ of the inflaton potential. This means that a detection of a stochastic background of GWs would provide us with a direct measurement of the energy scale of inflation, a crucial piece of information towards our understanding of the Early Universe.

2.6 The Consistency Relation

The results we obtained for the scalar and tensor perturbations induced by single-field slow-roll inflation allow us to predict an important consistency relation for such models. Let us begin by introducing the definition of the so-called tensor-to-scalar ratio, which yields the amplitude of the tensor modes with respect to the scalar ones at some pivot scale k_0:

$$r = \frac{A_{\mathrm{T}}(k_0)}{A_{\mathrm{s}}(k_0)} \tag{2.34}$$

Recalling the expression for the slow-roll parameter ϵ given in equation (1.33), one can easily prove that the amplitude of the scalar perturbations $A_{\rm s}$ can be rewritten as

$$A_{\rm s}(k_0) = \frac{H^2}{M_P^2 \pi \epsilon} \tag{2.35}$$

thus implying that

$$r \simeq 16\epsilon \tag{2.36}$$

From this result, recalling the expression for the tensor spectral index (2.33), we get the following consistency relation:

$$r \simeq -8 n_{\rm T} \tag{2.37}$$

The current datasets provide only upper bounds on the tensor-to-scalar ratio r, with the state-of-the-art on $(r, n_{\rm T})$ represented by the set of bounds obtained by Akrami et al. [15] and Tristam et al. [24] for what regards, respectively, the tensor spectral index $n_{\rm T}$ and the tensor-to-scalar ratio r. In [15], using data from the *Planck* Release 3 (PR3) [25] in the form of the publicly available likelihoods (referred to in Figure 2.1 as "PL18"), in combination to the BICEP2/Keck Array ("BK15") [26] and the "LV15" [27] GWs LIGO-Virgo-KAGRA interferometers datasets, Akrami et al. found the following set of bounds on $(r, n_{\rm T})$: $r_{0.01}$[1] < 0.066 and $-0.76 < n_{\rm T} < 0.52$ at the 95% CL. In [28], Tristam et al. updated the constraint on the tensor-to-scalar ratio r, keeping the tensor spectral index $n_{\rm T}$ fixed to the value predicted from the single-field slow-roll consistency relation (2.37). In particular, they used a combination of the BICEP3/Keck Array ("BK18") B-mode data [29] and the *Planck* Release 4 (PR4) E and B-mode polarisation data [28], finding an upper limit of $r_{0.01} < 0.034$ at the 95% CL, which tightens to $r_{0.01} < 0.032$ when considering also BAO and CMB lensing data. Recently, these results have been updated by Galloni et al., who in [30], considering combinations of different datasets from BICEP/Keck, *Planck* and the LIGO-Virgo-KAGRA collaboration (see Figure 2.1), found the following bounds on the tensor sector, with the one on the tensor-to-scalar ratio being the most stringent one to date: $r_{0.01} < 0.028$ and $-1.37 < n_{\rm T} < 0.42$ at the 95% CL, obtained using a combination of the PR3 and PR4 (referred to in Figure 2.1 as "PL21"), BK18 and the LV21 [31] datasets.

[1] Here the subscript 0.01 denotes the pivot scale, that is $k_0 = 0.01$ Mpc^{-1}.

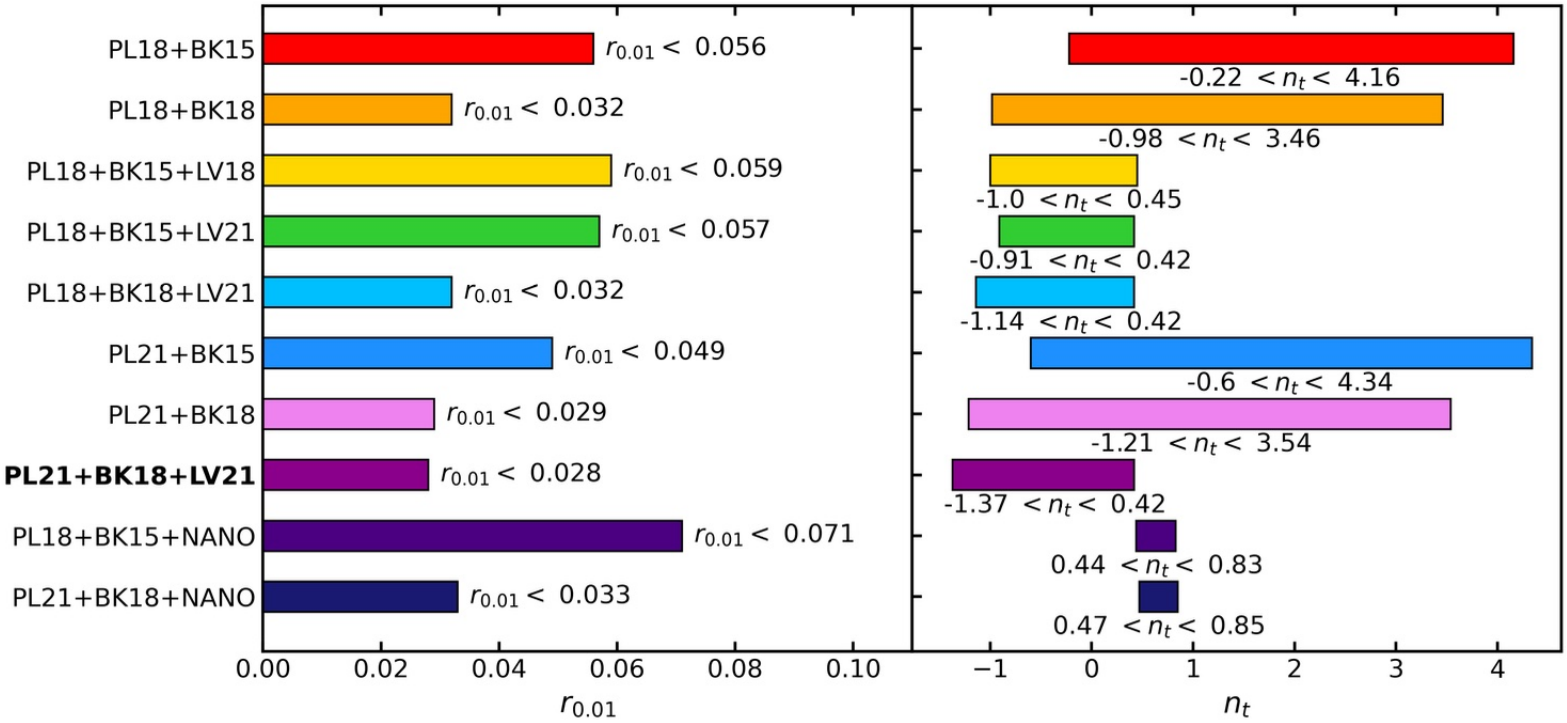

Figure 2.1. Summary of the 95% CL intervals for $r_{0.01}$ and $n_{\rm T}$ obtained by Galloni et al. in [30] considering different combinations of datasets. Figure adapted from [30].

Chapter 3

The Cosmic Microwave Background

At the time of Big Bang Nucleosynthesis, the primordial plasma consisted of photons, free electrons and ionised nuclei (mostly protons). Photons and electrons were tightly coupled by means of Compton scattering:

$$e^- + \gamma \leftrightarrow e^- + \gamma \tag{3.1}$$

In turn, the electrons strongly interacted with the protons via Coulomb scattering:

$$e^- + p^+ \leftrightarrow e^- + p^+ \tag{3.2}$$

Electromagnetic reactions, such as those forming and ionising neutral hydrogen, kept photons and baryons in equilibrium:

$$e^- + p^+ \leftrightarrow H + \gamma \tag{3.3}$$

As the Universe expanded and cooled down, these reactions became less and less efficient, leading to

$$e^- + p^+ \rightarrow H + \gamma \tag{3.4}$$

This process is usually referred to as recombination. By this time, since the electrons were no longer relativistic, the photon-electron scattering was governed by Thomson scattering, with constant cross section σ_T and rate $\Gamma_\gamma \sim n_e \sigma_T$. As the number density of the free electrons n_e dropped, the mean free path of the photons became larger than the size of the horizon. The photons decoupled from matter and the Universe became transparent. This occurred at a temperature $T_{rec} \approx 0.26$ eV, corresponding to a redshift of $z_{rec} \approx 1100$. These photons have since freely streamed through the Universe and we observe them today as the Cosmic Microwave Background (CMB) radiation. Observations show that the CMB is well described by a black-body function having a mean temperature $T_0 = 2.7255 \pm 0.0006$ K [32]

and contains temperature anisotropies at the 10^{-5} level over a wide range of angular scales. These anisotropies are usually split into two types:

- primary anisotropies, due to effects that happened prior or during photon decoupling;
- secondary anisotropies, due to the interactions of the decoupled CMB photons with the content of the Universe during its post-recombination history.

In the following, however, we are going to restrict ourselves only to those anisotropies that come from the fact that during recombination the CMB photons were tightly coupled to the baryons.

3.1 Temperature Anisotropies

The CMB anisotropies are commonly described in terms of small temperature fluctuations $\Theta(\mathbf{x}, \hat{\mathbf{n}}, \tau)$, where $\mathbf{x}$ is the spatial coordinate, $\hat{\mathbf{n}}$ denotes the direction of the incoming photons and τ is the conformal time. It should be noted that, deriving from quantum fluctuations, $\Theta(\mathbf{x}, \hat{\mathbf{n}}, \tau)$ is a random field and thus it can't be predicted in a deterministic way. In other words, what we actually observe is its statistical distribution. Since the temperature fluctuations lie over the surface of a sphere, for which the spherical harmonics define an orthonormal basis, the field $\Theta(\mathbf{x}, \hat{\mathbf{n}}, \tau)$ is usually decomposed as follows:

$$\Theta(\mathbf{x}, \hat{\mathbf{n}}, \tau) = \sum_{\ell=0}^{\infty} \sum_{m=-\ell}^{\ell} a_{\ell m}(\mathbf{x}, \tau) Y_{\ell m}(\hat{\mathbf{n}}) \tag{3.5}$$

Being the spherical harmonics orthogonal, all of the information is encoded in the coefficients $a_{\ell m}$. Using the orthonormality property of the spherical harmonics:

$$\int d\hat{\mathbf{n}} Y_{\ell m}(\hat{\mathbf{n}}) Y^*_{\ell' m'}(\hat{\mathbf{n}}) = \delta_{\ell \ell'} \delta_{m m'} \tag{3.6}$$

we can infer the harmonic coefficients for the temperature field $\Theta(\mathbf{x}, \hat{\mathbf{n}}, \tau)$:

$$a_{\ell m}(\mathbf{x}, \tau) = \int d\Omega_{\hat{\mathbf{n}}} \Theta(\mathbf{x}, \hat{\mathbf{n}}, \tau) Y^*_{\ell m}(\hat{\mathbf{n}}) \tag{3.7}$$

The ΛCDM model makes very simple predictions for the statistical properties of the harmonic coefficients. Assuming the temperature fluctuations being a Gaussian real-valued random field, the coefficients $a_{\ell m}$ are complex Gaussian variables with vanishing mean and non-zero covariance:

$$\langle a_{\ell m} \rangle = 0; \qquad \langle a^*_{\ell' m'} a_{\ell m} \rangle \quad = \delta_{\ell \ell'} \delta_{m m'} C_\ell \tag{3.8}$$

The angled brackets here denote an ensemble average over many different realisations of

the Universe. The quantity C_ℓ is usually referred to as the *angular power spectrum* and it measures how much fluctuation exists on a given angular scale. This is because, assuming the temperature field being Gaussian distributed, all the statistical information on the anisotropies is contained in the variance C_ℓ. Because of statistical isotropy, coefficients $a_{\ell m}$ with the same ℓ but different m are extracted from the Gaussian distribution with the same variance. Therefore, a commonly used estimator for the angular power spectrum is given by

$$C_\ell = \frac{1}{2\ell+1}\sum_m |a_{\ell m}|^2 \tag{3.9}$$

It should be noted, however, that since for each multipole ℓ there are $2\ell+1$ modes to average over, this estimator fails to capture the underlying variance for the largest fluctuations (corresponding to small ℓ). This implies that only for large multipoles ℓ (corresponding to small scales) we have enough statistical power to accurately estimate the angular power spectrum and thus associated to the estimation of the angular power spectrum there is an intrinsic uncertainty. This fundamental uncertainty is referred to as *cosmic variance* and it is quantified by

$$\left(\frac{\Delta C_\ell}{C_\ell}\right)_{cv} = \sqrt{\frac{2}{(2\ell+1)}} \tag{3.10}$$

Note that cosmic variance constitutes a fundamental limitation of cosmological observations and it cannot be overcome by building more precise instruments.

The relevant quantity that we extract from CMB temperature maps is the 2-point temperature correlation function. The angular power spectrum defined in harmonic space can be related to the 2-point CMB correlation function in real space simply by

$$C(\theta) = \langle \Theta(\hat{\mathbf{n}}_1)\Theta(\hat{\mathbf{n}}_2)\rangle = \frac{1}{4\pi}\sum_{\ell=0}^{\infty}(2\ell+1)C_\ell P_\ell(\hat{\mathbf{n}}_1\cdot\hat{\mathbf{n}}_2) \tag{3.11}$$

where $\hat{\mathbf{n}}_1\cdot\hat{\mathbf{n}}_2 = \cos\theta$ and $P_\ell(\cos\theta)$ are the Legendre polynomials of degree ℓ. It remains therefore to discuss how the primordial density fluctuations of the CMB photons at the LSS relate to the observed anisotropies. Let us consider the observed photon perturbation at a given time. In Fourier space, this can be expressed in terms of multipole moments $\Theta_\ell(k,\tau)$:

$$\Theta(\mathbf{x},\hat{\mathbf{p}},\tau) \equiv \int \frac{d^3\mathbf{k}}{(2\pi)^3} e^{i\mathbf{k}\cdot\mathbf{x}} \sum_{\ell=0}^{\infty}(-i)^\ell(2\ell+1)\Theta_\ell(k,\tau)P_\ell(\mu) \tag{3.12}$$

where $\hat{\mathbf{p}}$ denotes the direction of the incoming photons, μ is a variable which denotes the cosine of the angle between the wavevector $\hat{\mathbf{k}}$ and the photon direction $\hat{\mathbf{p}}$. We are now interested in the temperature anisotropies observed today (τ_0) and at our location ($\mathbf{x}_0$) as a function of the direction $\hat{\mathbf{n}}$ in the sky. Since a photon observed in the direction $\hat{\mathbf{n}}$ had to be travelling in

the direction $\hat{\mathbf{p}} = -\hat{\mathbf{n}}$, we have that

$$\Theta(\mathbf{x} = \mathbf{x}_0, \hat{\mathbf{p}} = -\hat{\mathbf{n}}, \tau = \tau_0) = \Theta(\hat{\mathbf{n}}) \equiv \frac{\Delta T}{T_0}(\hat{\mathbf{n}}) \tag{3.13}$$

Introducing now the CMB *radiation transfer function* $g_\ell(k)$, defined such that

$$\Theta_\ell(k, \tau_0) = g_\ell(k)\zeta(k) \tag{3.14}$$

where ζ is the gauge-invariant curvature perturbation we introduced in Chapter 2, we obtain from equation (3.12) the following expression for the observed temperature fluctuation:

$$\Theta(\hat{\mathbf{n}}) = \int \frac{d^3\mathbf{k}}{(2\pi)^3} e^{i\mathbf{k}\cdot\mathbf{x}_0} \sum_{\ell=0}^{\infty} (-i)^\ell (2\ell+1) g_\ell(k)\zeta(k) P_\ell(\mu) \tag{3.15}$$

From the addition theorem for the spherical harmonics it is known that

$$P_\ell(\mu) = \frac{4\pi}{2\ell+1} \sum_{m=-\ell}^{\ell} Y^*_{\ell m}(\hat{\mathbf{k}}) Y_{\ell m}(\hat{\mathbf{n}}) \tag{3.16}$$

Therefore, substituting equation (3.16) into equation (3.15), we get that

$$\Theta(\hat{\mathbf{n}}) = 4\pi \int \frac{d^3\mathbf{k}}{(2\pi)^3} e^{i\mathbf{k}\cdot\mathbf{x}_0} \sum_{\ell=0}^{\infty} (-i)^\ell g_\ell(k)\zeta(k) \sum_{m=-\ell}^{\ell} Y^*_{\ell m}(\hat{\mathbf{k}}) Y_{\ell m}(\hat{\mathbf{n}}) \tag{3.17}$$

Equating equation (3.5) and equation (3.17), we obtain the following definition for the harmonic coefficients of the CMB temperature multipoles:

$$a_{\ell m} = 4\pi(-i)^\ell \int \frac{d^3\mathbf{k}}{(2\pi)^3} e^{i\mathbf{k}\cdot\mathbf{x}_0} g_\ell(k)\zeta(k) Y^*_{\ell m}(\hat{\mathbf{k}}) \tag{3.18}$$

Using equation (3.18) we get that the explicit expression for the 2-point angular correlation function is given by

$$\langle a_{\ell m} a^*_{\ell' m'} \rangle = (4\pi)^2 (-i)^{\ell+\ell'} \int \frac{d^3\mathbf{k}}{(2\pi)^3} \int \frac{d^3\mathbf{k}'}{(2\pi)^3} e^{i(\mathbf{k}+\mathbf{k}')\cdot\mathbf{x}_0} g_\ell(k) g_{\ell'}(k) Y^*_{\ell m}(\hat{\mathbf{k}}) Y_{\ell' m'}(\hat{\mathbf{k}}') \langle \zeta(\mathbf{k})\zeta(\mathbf{k}') \rangle \tag{3.19}$$

Recalling that $\langle \zeta(\mathbf{k})\zeta(\mathbf{k}') \rangle = (2\pi)^3 \delta^{(3)}(\mathbf{k}+\mathbf{k}') P_\zeta(k)$ and exploiting the properties of the Dirac

delta, equation (3.19) becomes:

$$\langle a_{\ell m} a^*_{\ell' m'} \rangle = (4\pi)^2 (-i)^{\ell+\ell'} \int \frac{d^3\mathbf{k}}{(2\pi)^3} P_\zeta(k) g_\ell(k) g_{\ell'}(k) Y^*_{\ell m}(\hat{\mathbf{k}}) Y_{\ell' m'}(\hat{\mathbf{k}}') \tag{3.20}$$

Using now the orthonormality property of the spherical harmonics (3.6) and the second of equation (3.8), we get that

$$\langle a_{\ell m} a^*_{\ell' m'} \rangle = \delta_{\ell\ell'} \delta_{mm'} C_\ell = (-i)^{\ell+\ell'} \frac{2}{\pi} \int dk k^2 P_\zeta(k) g_\ell(k) g_{\ell'}(k) \delta_{\ell\ell'} \delta_{mm'} \tag{3.21}$$

thus obtaining the following key result for the angular power spectrum of the CMB:

$$C_\ell = \frac{2}{\pi} \int dk k^2 P_\zeta(k) g^2_\ell(k) \tag{3.22}$$

This result tells that the radiation transfer function $g_\ell(k)$ provides a map from the primordial density perturbations power spectrum $P_\zeta(k)$ to the angular power spectrum of the observed CMB anisotropies. To compute the explicit expression for the radiation transfer function, we should follow the free-streaming evolution of the CMB photon perturbations from decoupling (τ_{rec}) to today (τ_0). This evolution is described by the Boltzmann equation[1] and by solving it, one finds that the explicit expression for the radiation transfer function is given by

$$\begin{aligned} g_\ell(k) \approx & \left(\Theta_0 + \Phi\right)_{rec} j_\ell\left[k(\tau_0 - \tau_{rec})\right] \\ & + i \left(v_b\right)_{rec} \left(j_{\ell-1}\left[k(\tau_0 - \tau_{rec})\right] - (\ell+1) \frac{j_\ell\left[k(\tau_0 - \tau_{rec})\right]}{k(\tau_0 - \tau_{rec})} \right) \\ & + \int_{\tau_{rec}}^{\tau_0} d\tau e^{-\tau(\tau)} \left(\Psi' + \Phi'\right) j_\ell\left[k(\tau_0 - \tau_{rec})\right] \end{aligned} \tag{3.23}$$

where $(f)_{\tau_{rec}} = f(\mathbf{k}, \tau_{rec})/\zeta(\mathbf{k})$ and $(\tau_0 - \tau_{rec})$ is defined as the conformal distance along the line-of-sight. The $j_\ell\left[k(\tau_0 - \tau_{rec})\right]$ are the spherical Bessel functions, which describe the projection from Fourier space to the harmonic space. Let us now spend a few of words on the physical meaning of the three terms that appear in the expression for the radiation transfer function (3.23). The first one is called the Sachs-Wolfe (SW) term. It gets two contributions: the first captures the intrinsic temperature fluctuations arising from perturbing the thermal distribution of the photons; the second one accounts for the gravitational redshifting that occurs when the photons climb out a potential well at LSS. The second term in equation (3.23) is referred to as the Doppler term. It takes into account the shift in the photons energy due to the fact that the electrons in the photon-baryon fluid are not at rest when the photons scatter off them. Finally, the last term in equation (3.23), dubbed the Integrated

[1] A full treatment of the Boltzmann equation is beyond our scopes, but a sketch of the main results for the free-streaming evolution of the photon perturbations can be found in Appendix A.

Sachs-Wolfe (ISW) term, captures the effect of gravitational redshifting from the evolution of the potentials along the line-of-sight, from recombination until today, and thus it's actually a source of secondary CMB anisotropies. The integrated effect receives two main contributions, referred to as the early ISW effect and the late-time ISW effect. The early ISW effect occurs shortly after recombination, when the photons leave the LSS, and is due to the evolution of the gravitational potentials as the Universe transitions from being radiation-dominated to be matter-dominated. The late-time ISW effect is instead due to the evolution of the gravitational potentials during the Dark Energy epoch at low-redshift ($z \lesssim 1$) and thus it is restricted only to the largest scales. A sketch of how all of these terms contribute to the CMB temperature angular power spectrum is presented in Figure 3.1.

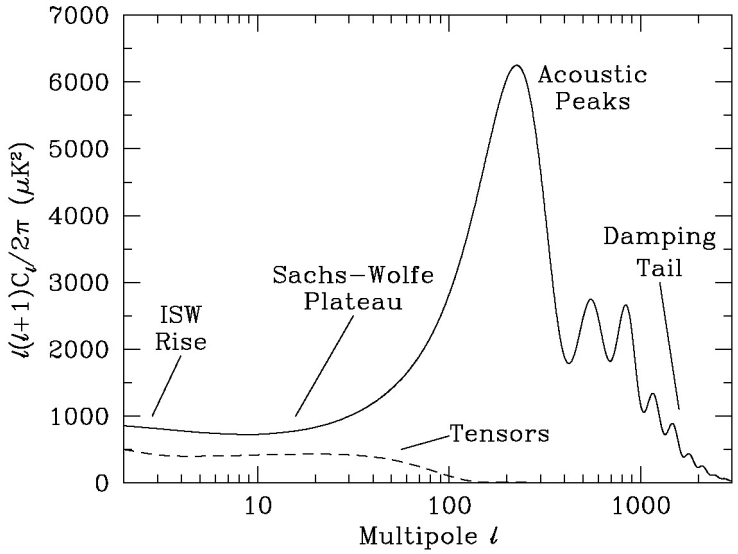

Figure 3.1. Sketch of the different contributions to the CMB temperature angular power spectrum. Also shown is the contribution from tensor perturbations (GW), with an arbitrary normalisation. Figure adapted from [33].

Estimates of the CMB angular power spectrum from a selection of the most recent available experimental results are shown in Figure 3.2. The strongest constraints presently available come from the *Planck* satellite data, although the smaller scale results from the Atacama Cosmology Telescope (ACT) and South Pole Telescope (SPT) experiments are beginning to add meaningful constraining power. Comparison between the datasets show consistency and the band powers shown are in very good agreement with a ΛCDM model. Notice also that one starts measuring the power spectrum at $\ell = 2$. This is because the monopole $\ell = 0$ coincides with the CMB mean temperature T_0 and since all mapping experiments involve difference measurements, they are insensitive to this average level. The dipole $\ell = 1$, with amplitude 3.3621 ± 0.0010 mK [8], is interpreted as due to the Doppler boosting of the monopole, caused by the Solar System motion relative to the nearly isotropic black-body background. Being a frame-dependent quantity, it tells us our velocity with respect to the rest frame of the CMB and it is nowadays routinely used as a primary calibrator for CMB mapping experiments.

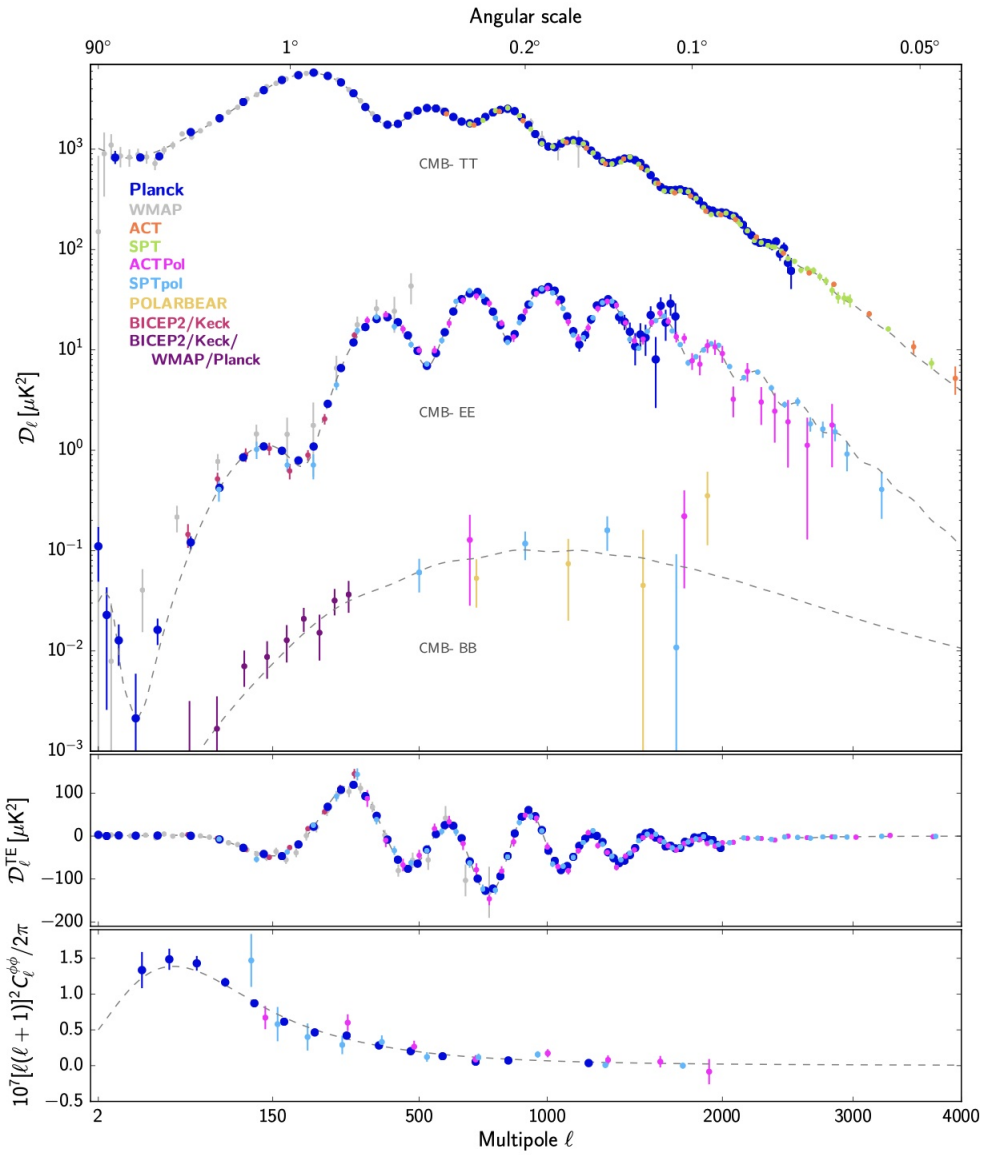

Figure 3.2. Compilation of recent CMB angular power spectrum measurements from which most cosmological inferences are drawn. The upper panel shows the power spectra of the temperature and E-mode and B-mode polarisation signals, the next panel the cross-correlation spectrum between T and E, while the lower panel shows the lensing deflection power spectrum. Different colours correspond to different experiments, each retaining its original binning. For *Planck*, ACTPol, and SPTpol, the EE points with large error bars are not plotted. The dashed line shows the best-fit ΛCDM model to the *Planck* temperature, polarisation, and lensing data. See [8] for details and references. Figure adapted from [8].

From both Figure 3.1 and 3.2, it is clear that we can discuss the underlying physics for the CMB angular power spectrum distinguishing four main regions in ℓ:

- the horizon scale, or more precisely the angle subtended by the Hubble radius at the LSS, corresponds to $\ell \approx 100$. For $10 \lesssim \ell \lesssim 100$ we observe the so-called Sachs-Wolfe plateau: as a result of gravitational redshifting and intrinsic temperature fluctuations at these scales the anisotropies have not evolved significantly and thus directly reflect the

initial conditions. The net effect on the temperature fluctuations is [34]:

$$\Theta(\hat{\mathbf{n}}) = -\frac{1}{3}\Phi_*(\hat{\mathbf{n}}) \quad \longrightarrow \quad \Theta_\ell(k) \quad = -\frac{1}{3}\Phi_*(k) j_\ell(kx_0) \tag{3.24}$$

where Φ is Bardeen's gravitational potential and the '$*$' means that the potential is evaluated at the LSS. Plugging this into equation (3.18) we get that the harmonic coefficients $a_{\ell m}$ become:

$$a_{\ell m} = -\frac{4\pi}{3}(-i)^\ell \int \frac{d^3\mathbf{k}}{(2\pi)^3} e^{i\mathbf{k}\cdot\mathbf{x}_0} j_\ell(kx_0)\Phi_*(k) Y^*_{\ell m}(\hat{\mathbf{k}}) \tag{3.25}$$

Thus, following the same procedure of the previous section, we get that at these scales the angular power spectrum is given by

$$\begin{aligned} \langle a_{\ell m} a^*_{\ell' m'} \rangle &= \frac{2}{9\pi} \int dk k^2 j^2_\ell(kx_0) P_\Phi(k) \delta_{\ell\ell'} \delta_{mm'} \\ C^{SW}_\ell &= \frac{2}{9\pi} \int dk k^2 j^2_\ell(kx_0) P_\Phi(k) \end{aligned} \tag{3.26}$$

where the apex SW means that we are working in the Sachs-Wolfe approximation. Since the power spectrum of Bardeen's gravitational potential is given by $P_\Phi(k) = \frac{A}{k^{4-n_\mathrm{s}}}$ with normalisation A and scalar spectral index n_s, the integral in equation (3.26) can be rewritten as

$$\int dk k^2 j^2_\ell(kx_0) P_\Phi(k) = A \int dk k^{n_\mathrm{s}-2} j_\ell(kx_0) \tag{3.27}$$

This integral admits an analytical solution in terms of Euler Gamma functions:

$$A \int dk k^{n_\mathrm{s}-2} j_\ell(kx_*) = A 2^{n_\mathrm{s}-4} \pi \frac{\Gamma\left(\ell + \frac{n_\mathrm{s}}{2} - \frac{1}{2}\right) \Gamma\left(3 - n_\mathrm{s}\right)}{\Gamma\left(\ell + \frac{5}{2} - \frac{n_\mathrm{s}}{2}\right) \Gamma^2\left(2 - \frac{n_\mathrm{s}}{2}\right)} \tag{3.28}$$

If one assumes that the power spectrum $P_\Phi(k)$ is scale-invariant i.e. $n_\mathrm{s} = 1$, using the properties of the Gamma functions and the particular value $\Gamma\left(\frac{3}{2}\right) = \frac{\sqrt{\pi}}{2}$, one gets for the angular power spectrum in the Sachs-Wolfe approximation the following result:

$$\begin{aligned} C^{SW}_\ell &= \frac{2A}{9\pi}\left[2^{-3}\pi \frac{\Gamma(\ell)}{\Gamma(\ell+2)} \frac{4}{\pi}\right] = \frac{A}{9\pi} \frac{\Gamma(\ell)}{\ell\left(\ell+1\right)\Gamma(\ell)} \\ &= \frac{A}{9\pi} \frac{1}{\ell\left(\ell+1\right)} \end{aligned} \tag{3.29}$$

That is, the quantity $\ell\left(\ell+1\right) C^{SW}_\ell$ is constant. At late times, during the epoch of Dark

Energy dominance, the time variation of the gravitational potentials leads to an upturn in the C_ℓs in the lowest multipoles ($\ell \lesssim 10$), which therefore rise above the SW plateau. Since this effect comes from the line integral of the gravitational potentials, it is referred to as the Integrated Sachs-Wolfe rise. Let us also observe that the tensor perturbations produced during inflation can generate temperature anisotropies through the integrated effect of the locally anisotropic expansion of space. Since tensor modes redshift away when they re-enter the horizon, they contribute only to the largest scales and thus we can assume that a fraction of the low-ℓ signal could also come from a primordial Gravitational Wave contribution (see Figure 3.1);

- at angular scales $100 \lesssim \ell \lesssim 1000$ the structure in the anisotropy spectrum is a consequence of gravity-driven acoustic oscillations occurring before the atoms in the Universe became neutral. Before recombination the CMB photons were tightly coupled to the baryons in the primordial plasma. During that epoch regions of higher density, seeded by the quantum fluctuations produced at the end of inflation, attracted the baryons, further increasing over-densities and decreasing under-densities. However, due to the presence of photons in the plasma, the radiation pressure counteracted the gravitational attraction and the fluid expanded, up until the point where gravity dominated again. This created a pattern of expansion and contraction, thus producing acoustic waves. When recombination happened and the photons decoupled from baryons, the acoustic waves left an imprint in the CMB photons that we observe today as an harmonic series of peaks;

- at scales $\ell \gtrsim 1000$ we observe the so-called damping tail. The spectrum is damped mainly due to residual diffusion of photons, which smooths structures with scales smaller than the photons mean free path (Silk damping). Furthermore, recombination is not instantaneous and the LSS has actually a finite width, leading to further damping of the anisotropies at the highest ℓs, corresponding to scales smaller than the ones subtended by the LSS width.

3.2 Polarisation Anisotropies

Thomson scattering of photons with a quadrupole anisotropy off electrons at the LSS induces a linear polarisation in the CMB radiation (see Figure 3.3) at the 10^{-6} level. From its angular distribution we can get meaningful cosmological information, complementary to the one we extract from the CMB temperature anisotropies. Unlike the temperature (which is a scalar under rotations about $\hat{\mathbf{n}}$), the CMB polarisation is coordinate dependent and therefore it can not be decomposed into spherical harmonics. In particular, the polarisation is a spin-2 field. One way of describing it is by means of the Stokes parameters Q and U, which can be combined into two complex quantities:

$$P(\hat{\mathbf{n}}) = (Q \pm iU)(\hat{\mathbf{n}}) \tag{3.30}$$

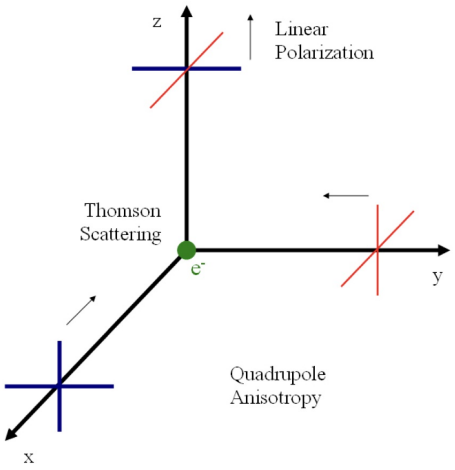

Figure 3.3. Generation of CMB linear polarisation via Thomson scattering. An incoming quadrupole radiation in the $x-y$ plane gets scattered off by an electron in the origin, resulting in a linearly polarised wave in the z-direction.

that transform under rotations around the $\hat{\mathbf{n}}$ axis as spin-2 variables. These quantities can then be decomposed into spin-2 weighted spherical harmonics ${}_{\pm 2}Y_{\ell m}(\hat{\mathbf{n}})$ as follows:

$$(Q \pm iU)(\hat{\mathbf{n}}) = \sum_{lm} a^{(\pm 2)}_{\ell m}\, {}_{\pm 2}Y_{\ell m}(\hat{\mathbf{n}}) \tag{3.31}$$

If we now define

$$\begin{aligned} a^B_{\ell m} &= \frac{i}{2}\left(a^{(2)}_{\ell m} - a^{(-2)}_{\ell m}\right) \\ a^E_{\ell m} &= -\frac{1}{2}\left(a^{(2)}_{\ell m} + a^{(-2)}_{\ell m}\right) \end{aligned} \tag{3.32}$$

we can introduce two independent and invariant quantities, dubbed E-mode and B-mode, that allow us to split the polarisation pattern into a part that comes from a divergence (corresponding to the E-mode) and one with a curl (corresponding to the B-mode), given by

$$E(\hat{\mathbf{n}}) = \sum_{\ell=2}^{\infty} \sum_{m=-\ell}^{\ell} a^E_{\ell m} Y_{\ell m}(\hat{\mathbf{n}}) \tag{3.33}$$

$$B(\hat{\mathbf{n}}) = \sum_{\ell=2}^{\infty} \sum_{m=-\ell}^{\ell} a^B_{\ell m} Y_{\ell m}(\hat{\mathbf{n}}) \tag{3.34}$$

Examples of E-mode and B-mode polarisation patterns that are observed in CMB maps are presented in Figure 3.4.

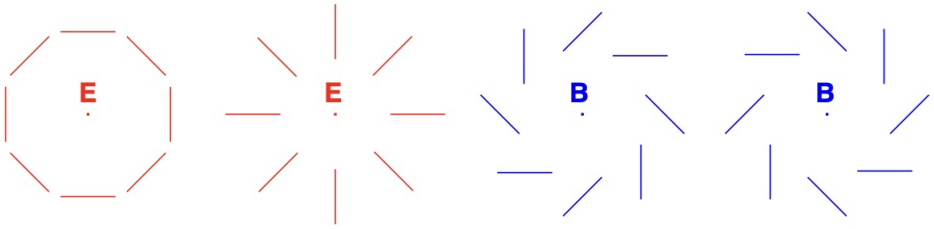

Figure 3.4. Examples of E-mode and B-mode polarisation patterns in CMB maps.

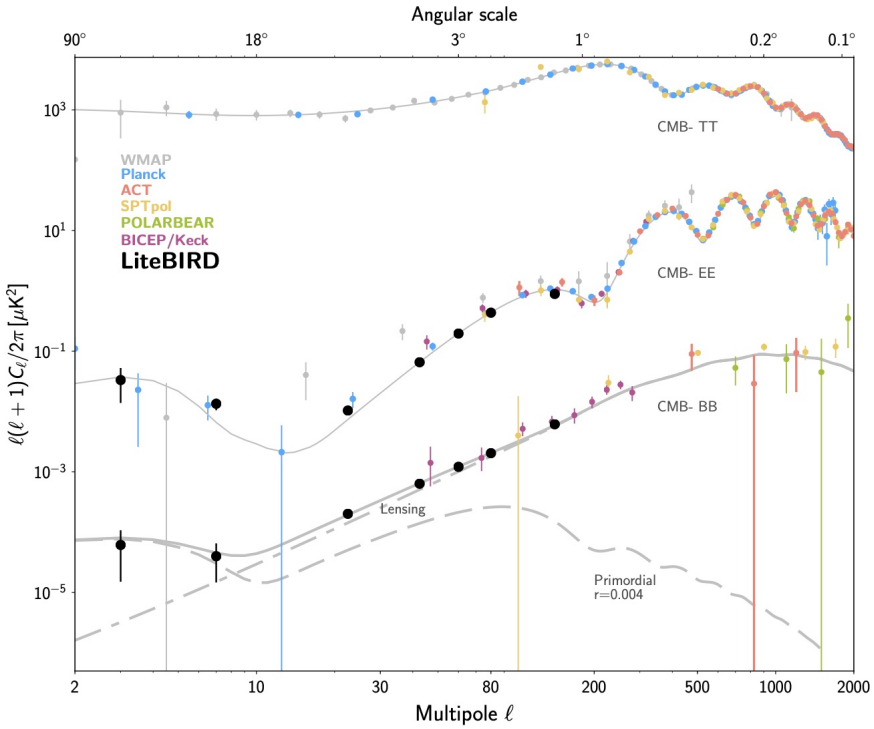

Figure 3.5. CMB power spectra of temperature anisotropy (top), E-mode polarisation (middle) and B-mode polarisation (bottom). The solid lines show the angular power spectra for the best-fit ΛCDM model in the presence of a scale-invariant tensor perturbation with $r = 0.004$. The thin dashed line shows the contribution to the B-mode spectrum from a scale-invariant tensor perturbation with $r = 0.004$. Also shown are a summary of present measurements of CMB power spectra (coloured points) and the expected polarisation sensitivity of LiteBIRD (black points). Figure adapted from [35].

The existence of this linear polarisation of the CMB radiation in principle allows for six different observable power spectra. However, since under parity transformation the temperature T and the E-modes transform differently than the B-modes, the C_ℓ^{TB} and C_ℓ^{EB} power spectra are zero. Therefore we are left with just four observables: C_ℓ^{TT}, C_ℓ^{TE}, C_ℓ^{EE} and C_ℓ^{BB}. In Figure 3.5 we show the theoretical estimates for the CMB power spectra of temperature anisotropy T, E-mode and B-mode polarisation using the best-fitting ΛCDM model from *Planck*. Also shown is the expected polarisation sensitivity of LiteBIRD (see Section 3.5.2). Like with temperature, the polarisation C_ℓs exhibit a series of acoustic peaks generated by

the oscillating photon-baryon fluid. C_ℓ^{EE} has peaks that are out of phase with those in C_ℓ^{TT}. This is because the EE power spectrum is determined by the dipole of the photon distribution (i.e. the fluid velocity), while the TT power spectrum is a combination of the monopole and the dipole, with the monopole being the dominant contribution. Moreover, since the dipole is less affected by the photon diffusion, C_ℓ^{EE} is less damped on small scales than C_ℓ^{TT} is. The TE part of the polarisation and temperature patterns (see middle panel of Figure 3.2) come from correlations between density and velocity perturbations on the LSS, which can be both positive and negative, and is of larger amplitude than the EE signal. There is no polarisation Sachs-Wolfe effect, and hence no large scale plateau. However, scattering during a recent period of reionisation can create a polarisation 'bump' at large angular scales. Reionisation happened long after recombination, at some redshift z_i, and it is characterised by the integrated Thomson scattering optical depth:

$$\tau = \int_0^{z_i} \frac{dt}{dz} dz n_e(z) \sigma_T \tag{3.35}$$

Current measurements [9] set this parameter to $\tau = 0.054 \pm 0.007$. Let us conclude with an important final remark. Since the scalar perturbations have no handedness, the B-modes power spectrum can only be sourced by tensor perturbations. This implies that a determination of a non-zero B-mode signal would allow us to measure the contribution from the primordial Gravitational Waves produced during inflation. However, not only the signal is expected to be rather weak, but the quest for the measurement of a B-mode polarisation signal is further complicated by the fact that the gravitational lensing of CMB photons[2] by the LSS sources B-modes from E-modes.

3.3 The `HEALPix` Pixelisation Scheme

So far we have been discussing the CMB anisotropies from a theoretical point of view. A CMB experiment, however, has a finite resolution which depends on the resolving power of the instrument employed and thus the CMB data have to be represented in a discrete form on the sphere. This is achieved through a discretisation or pixelisation algorithm. The one which stands out as the most used in recent times for CMB studies is `HEALPix`. `HEALPix` [36] is an acronym for Hierarchical Equal Area and isoLatitude pixelisation. Indeed, the requirements on which this pixelisation scheme is built are the following:

1. **the data base must have a hierarchical structure**. To put it simply, this means that the data elements which are nearby in the surface of the sphere are also nearby in the structure of the data base;

[2]The large scale structure between the LSS and the observer gravitationally lenses the temperature and polarisation CMB anisotropies, resulting in the shuffling of the observed locations of the CMB hot and cold spots to slightly different positions. The shuffling of the positions of the E-mode polarisation pattern generates B-modes.

2. **the discrete elements of the partition must have equal areas**. This facilitates any integral discretisation since the area factor can just be factored out;

3. **the discrete area elements on the sphere must have an iso-Latitude distribution**. This property is critical for computational speed of all operations involving evaluation of spherical harmonics.

A `HEALPix` pixel is identified by three variables: its numbering scheme (RING or NESTED), its resolution or size parameter and its pixel index. The RING numbering scheme orders the pixels from the north pole to the south pole along each iso-latitude ring. In the NESTED scheme, instead, pixels that are close in the map are also close in the data. The resolution or size parameter is given by $N_{\rm side} = 2^k$ with k an integer number. The total number of pixels for each map is $N_{\rm pix} = 12N_{\rm side}^2$ and the pixel index p varies from 0 to $N_{\rm pix} - 1$. An orthographic view of the `HEALPix` partition of the sphere is shown in Figure 3.6.

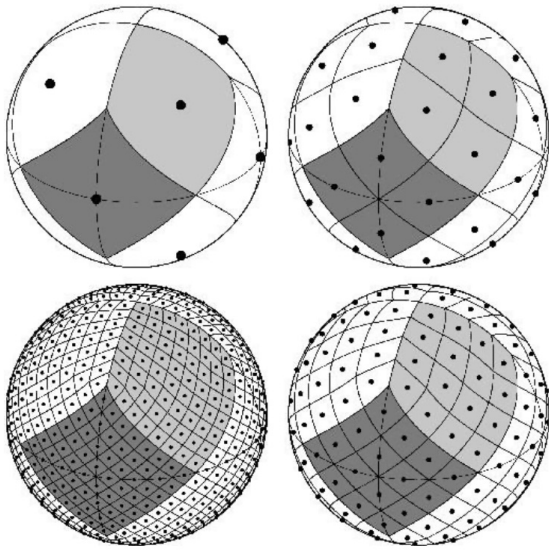

Figure 3.6. Orthographic view of `HEALPix` partition of the sphere. Moving clockwise from the upper left panel the grid is hierarchically subdivided with the grid resolution parameter equal to $N_{\rm side} = 1, 2, 4, 8$, and the total number of pixels equal to $N_{\rm pix} = 12, 48, 192, 768$. All pixel centres are placed on $4 \times N_{\rm side} - 1$ rings of constant latitude and within each panel the areas of all pixels are identical. Figure adapted from [36].

3.3.1 Conventions

Let us consider a band-limited function on the sphere $f(\hat{\mathbf{n}})$, where band-limited means that there is insignificant signal power in the modes $\ell > \ell_{\rm max}$. This function can be decomposed into spherical harmonics $Y_{\ell m}$ as follows:

$$f(\hat{\mathbf{n}}) = \sum_{\ell=0}^{\ell_{\rm max}} \sum_{m=-\ell}^{\ell} a_{\ell m} Y_{\ell m}(\hat{\mathbf{n}}) \quad \text{with} \quad a_{\ell m} = \int d\Omega_{\hat{\mathbf{n}}} f(\hat{\mathbf{n}}) Y^*_{\ell m}(\hat{\mathbf{n}}) \tag{3.36}$$

Representing $f(\hat{\mathbf{n}})$ in the HEALPix pixelisation scheme means sampling it to N_{pix} positions $\hat{\mathbf{n}}_p$, each characterised by its pixel index p. The sampled function values $f(\hat{\mathbf{n}}_p)$ can then be used to create a zero-th order estimator for the harmonic coefficients $a_{\ell m}$, given by

$$\hat{a}_{\ell m} = \frac{4\pi}{N_{\rm pix}} \sum_{p=0}^{N_{\rm pix}-1} f(\hat{\mathbf{n}}_p) Y^*_{\ell m}(\hat{\mathbf{n}}_p) \tag{3.37}$$

where we assume an equal weight $4\pi/N_{\rm pix}$ for each pixel. From these pixelated $\hat{a}_{\ell m}$ we can then define the pixelated angular power spectrum $\hat{C}_\ell$, as usual estimated by

$$\hat{C}_\ell = \frac{1}{2\ell+1} \sum_m |\hat{a}_{\ell m}|^2 \tag{3.38}$$

3.3.2 The Pixel Window Function

In HEALPix the sampled function values $f(\hat{\mathbf{n}}_p)$ are obtained by averaging the field $f(\hat{\mathbf{n}})$ over each pixel. Therefore the field value at each pixel is given by

$$f(\hat{\mathbf{n}}_p) = \int d\Omega_{\hat{\mathbf{n}}} w_p(\hat{\mathbf{n}}) f(\hat{\mathbf{n}}) \tag{3.39}$$

where $w_p(\hat{\mathbf{n}})$ is equal to the inverse of the pixel area within the pixel and 0 outside, so that $\int d\Omega_{\hat{\mathbf{n}}} w_p(\hat{\mathbf{n}}) = 1$. Now we can use the expansion of $f(\hat{\mathbf{n}})$ into spherical harmonics (3.36) to rewrite the sampled function values (3.39) as follows:

$$f(\hat{\mathbf{n}}_p) = \sum_{\ell m} a_{\ell m} w_{\ell m}(\hat{\mathbf{n}}_p) \tag{3.40}$$

where

$$w_{\ell m}(\hat{\mathbf{n}}_p) = \int d\Omega_{\hat{\mathbf{n}}} w_p(\hat{\mathbf{n}}) Y_{\ell m}(\hat{\mathbf{n}}) \tag{3.41}$$

is defined as the spherical harmonic transform of the pixel p. The exact computation of the integral above is in general too difficult to carry out, nonetheless this issue can be circumvented in different ways. One way consists in considering a pixel size such that the pixel is actually small compared to the signal correlation length. With this assumption we can ignore the pixel structure and simply assume that $w_{\ell m}(\hat{\mathbf{n}}_p) = w_\ell(\hat{\mathbf{n}}_p) Y_{\ell m}(\hat{\mathbf{n}}_p)$, where

$$w_\ell(\hat{\mathbf{n}}_p) = \left(\frac{4\pi}{2\ell+1} \sum_{m=-\ell}^{\ell} |w_{\ell m}(\hat{\mathbf{n}}_p)|^2 \right)^{1/2} \tag{3.42}$$

is the m-averaged *window function*, which does not depend on the position of the pixel in the

sky. If we now assume all pixels being identical, we can introduce an effective pixel window function, defined as the average of $w_\ell(\hat{\mathbf{n}}_p)$ over each pixel:

$$w_\ell \equiv \left(\frac{1}{N_{\rm pix}} \sum_{p=0}^{N_{\rm pix}-1} w_\ell^2(\hat{\mathbf{n}}_p) \right)^{1/2} \tag{3.43}$$

With this definition, we can rewrite the expansion into spherical harmonics of the sampled function values as follows:

$$f(\hat{\mathbf{n}}_p) = \sum_{\ell m} a_{\ell m}^{\rm pix} Y_{\ell m}(\hat{\mathbf{n}}_p) \tag{3.44}$$

where the harmonic coefficients $a_{\ell m}^{\rm pix} = a_{\ell m} w_\ell$. This allows us to relate the angular power spectrum associated to the pixelated map $\hat{C}_\ell$ to the one associated the underlying continuous signal C_ℓ as

$$\hat{C}_\ell = w_\ell^2 C_\ell \tag{3.45}$$

This result tells us that, since the power spectrum is modulated by w_ℓ^2, whenever we compare the simulated maps with data it is important to keep track of the pixel window function.

3.4 Masking

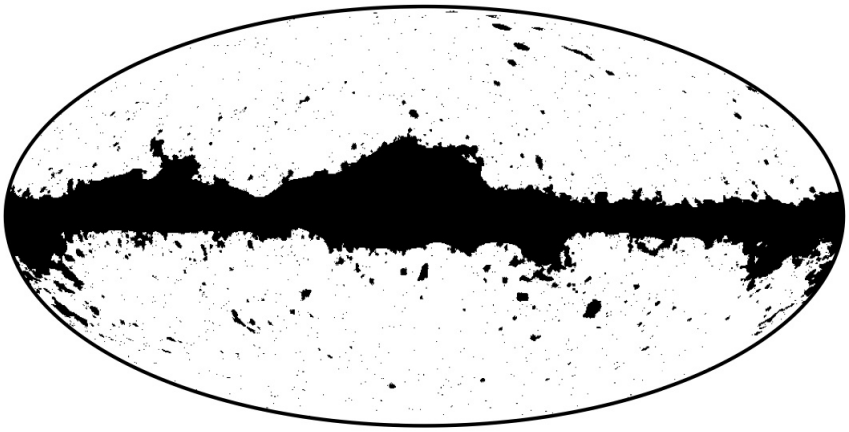

Figure 3.7. *Planck*'s 2018 component separation common mask for temperature data. Figure adapted from [37].

When considering the description and simulation of CMB data, one has to take into account that experimentally, due to foreground effects or lack of complete coverage in the scanning strategy, we can not get data in every direction in the sky. The information about the excluded directions in the sky is encoded in the numerical simulations making use of masks.

Figure 3.7 shows *Planck*'s 2018 common mask for temperature data. In this case, the mask is a binary object which can be mathematically represented by a map, $W(\hat{\mathbf{n}})$, taking pixel values 0 (masked or excluded) and 1 (seen or included) at each position $\hat{\mathbf{n}}_p$. When masking is considered, the temperature fluctuation field can be decomposed into spherical harmonics as

$$W(\hat{\mathbf{n}})\Theta(\hat{\mathbf{n}}) = \sum_{\ell=2}^{\ell_{\max}} \sum_{m=-\ell}^{\ell} \widetilde{a}_{\ell m} Y_{\ell m}(\hat{\mathbf{n}}) \tag{3.46}$$

where the expansion coefficients $\widetilde{a}_{\ell m}$, being the cut-sky representation of the true harmonic coefficients $a_{\ell m}$, are known as pseudo-$a_{\ell m}$ and are defined as follows:

$$\widetilde{a}_{\ell m} = \int d\Omega_{\hat{\mathbf{n}}} W(\hat{\mathbf{n}})\Theta(\hat{\mathbf{n}}) Y^*_{\ell m}(\hat{\mathbf{n}}) \tag{3.47}$$

Using these pseudo-$a_{\ell m}$ we can then generalise the definition of the estimator (3.9) to accommodate for the mask, obtaining the so-called pseudo-C_ℓ:

$$\widetilde{C}_\ell = \frac{1}{2\ell+1} \sum_m |\widetilde{a}_{\ell m}|^2 \tag{3.48}$$

Following [38, 39], it can be shown that the cut-sky 2-point correlation function can be written as

$$C^{\text{cut}}(\theta) = 2\pi A(\theta) \sum_\ell (2\ell+1) \widetilde{C}_\ell P_\ell(\cos\theta) \tag{3.49}$$

where the normalisation coefficient $A(\theta)$ depends on the mask and it may be calculated in harmonic space as

$$A(\theta) = 2\pi \sum_\ell (2\ell+1) w_\ell P_\ell(\cos\theta) \tag{3.50}$$

where

$$w_\ell = \frac{1}{2\ell+1} \sum_m |w_{\ell m}|^2 \tag{3.51}$$

and the $w_{\ell m}$ are defined as harmonic coefficients of the spherical harmonics expansion of the mask:

$$W(\hat{\mathbf{n}}) = \sum_{\ell m} w_{\ell m} Y_{\ell m}(\hat{\mathbf{n}}) \tag{3.52}$$

Finally, since $C^{\text{cut}}(\theta)$ is a function defined on the interval $-1 \leqslant \cos\theta \leqslant 1$, it can be expanded in a Legendre polynomials series as follows:

$$C^{\text{cut}}(\theta) = \sum_{\ell} \frac{2\ell+1}{4\pi} C_{\ell}^{\text{cut}} P_{\ell}(\cos\theta) \tag{3.53}$$

For a statistically isotropic universe, the ensemble averaged of the pseudo-C_ℓ (3.48) is related to the ensemble averaged of the C_ℓ^{cut} through a mode coupling matrix [40]. Therefore, in this case, C_ℓ^{cut} provides an unbiased estimator of the theoretical (full-sky) angular power spectrum (3.9).

3.5 CMB Surveys

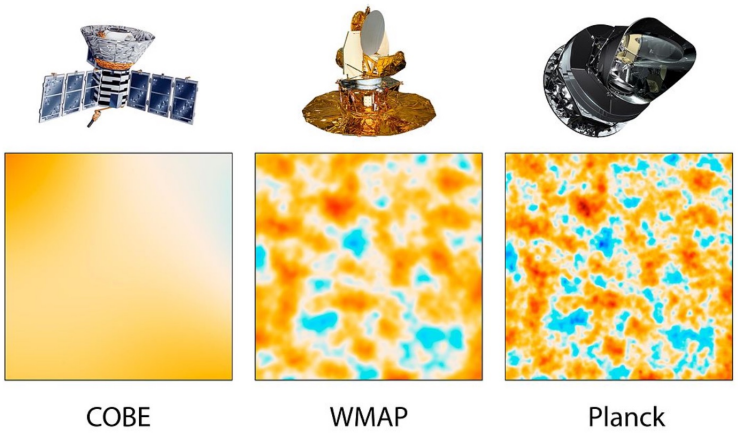

Figure 3.8. Illustration showing the evolution in the precision of full-sky CMB anisotropy measurements comparing COBE, WMAP, and *Planck*. Source https://photojournal.jpl.nasa.gov/catalog/PIA16874.

Many experiments were designed to look for the characteristics of the CMB. The earliest attempts, however, were limited by the sensitivity of the instruments employed. The real breakthrough came only in the 1990s when the Cosmic Background Explorer (COBE) mission made the first measurement of the CMB energy spectrum, showing that the CMB is well described by a black-body function having a mean temperature $T_0 = 2.7255 \pm 0.0006$ K [32]. The COBE satellite was also the first to observe tiny departures from the homogenous black-body temperature T_0 along the line-of-sight. Although the COBE satellite confirmed the predictions of Big Bang Cosmology and provided important insight on the origin of the Universe, it had poor angular sensitivity and resolution. Therefore in 2001 NASA launched a subsequent satellite, WMAP. WMAP had 45 times the sensitivity and 33 times the angular resolution of COBE, leading to results of unprecedented accuracy and precision. A third generation CMB satellite, ESA's *Planck*, was then launched in 2009. After completing seven sky surveys, and upon exhaustion of its helium coolant, it was switched off in 2013. Figure 3.8 illustrates the evolution in the precision of the full-sky CMB anisotropies measurements

from COBE to *Planck*.

3.5.1 The *Planck* Mission and its Full-sky Maps

The main objective of the *Planck* mission, defined in 1995, was to measure the temperature fluctuations in the CMB with an unprecedented accuracy set by fundamental astrophysical limits, thereby aiming to extract all of the cosmological information embedded in the CMB temperature anisotropies [41]. Even though *Planck* was not initially designed to measure to high accuracy also the CMB polarisation anisotropies, during its development it was significantly enhanced in this respect, and nowadays *Planck*'s measurement of both temperature and polarisation anisotropies in the CMB constitutes a cosmological framework that will remain the standard for many years to come. The *Planck* satellite carried two scientific instruments, the High Frequency Instrument (HFI) and the Low Frequency Instrument (LFI), which allowed it to scan the microwave and sub-millimetre sky, producing deep, high-resolution, full-sky maps in nine frequency bands from 30 to 857 GHz. A summary of the principal technical characteristics of the *Planck* mission in comparison to COBE and WMAP is presented in Table 3.1.

Table 3.1. Summary of the principal technical characteristics of the *Planck* mission in comparison to COBE and WMAP.

Mission	Spectral Range [GHz]	Bands	FWHM	$\ell_{\max}$
COBE	$31.5 - 90$	3	420'	30
WMAP	$23 - 94$	5	12'	1000
Planck	$30 - 857$	9	5'	3000

Since in addiction to the primary anisotropies the sky emission contains also several other astrophysical components, which differ by their dependence on frequency as well as their spatial properties, by making measurements at multiple frequency the *Planck* team was able to characterise the foregrounds and thus reduce their contamination of the primary CMB anisotropies. Note that the foregrounds can be divided in two categories: the galactic foreground and the compact sources foreground; the first is responsible for contamination on large scales, while the second dominates small scales. The approaches used to clean the CMB maps from the foreground are four: `Commander`, `NILC`, `SEVEM` and `SMICA`. For details on these methods and how the foreground components are modeled, we refer the reader to [9, 37]. Figure 3.9 shows *Planck* 2018 `SMICA` full-sky CMB anisotropy maps for temperature and polarisation data. Since the polarisation signal is smaller in amplitude than the temperature one, to increase its legibility it is shown with a relatively low angular resolution of 5°. Tests on the *Planck* data shows that even though the primary anisotropies are extremely close to Gaussian-distributed, there are several noteworthy features with a significance of $2 - 3\sigma$ appearing at the largest observed angular scales that seem to indicate that there exists a moderate degree of deviation from the statistical predictions of the standard ΛCDM model

[42, 43, 44]. The existence of these features, the so-called large scale anomalies of the CMB, is uncontested, since they are detected both by WMAP and *Planck*, which have quite different systematics, and thus must be regarded as features of the CMB temperature sky. Nonetheless, given the modest significances at which they deviate from the ΛCDM model and the *a posteriori* nature of their detection, the main question is wether or not this features are unusual enough for physical explanations to be sought. In Chapter 5 we shall return on this topic, aiming to provide a description of some of these anomalies, along with evidence and methods for detection.

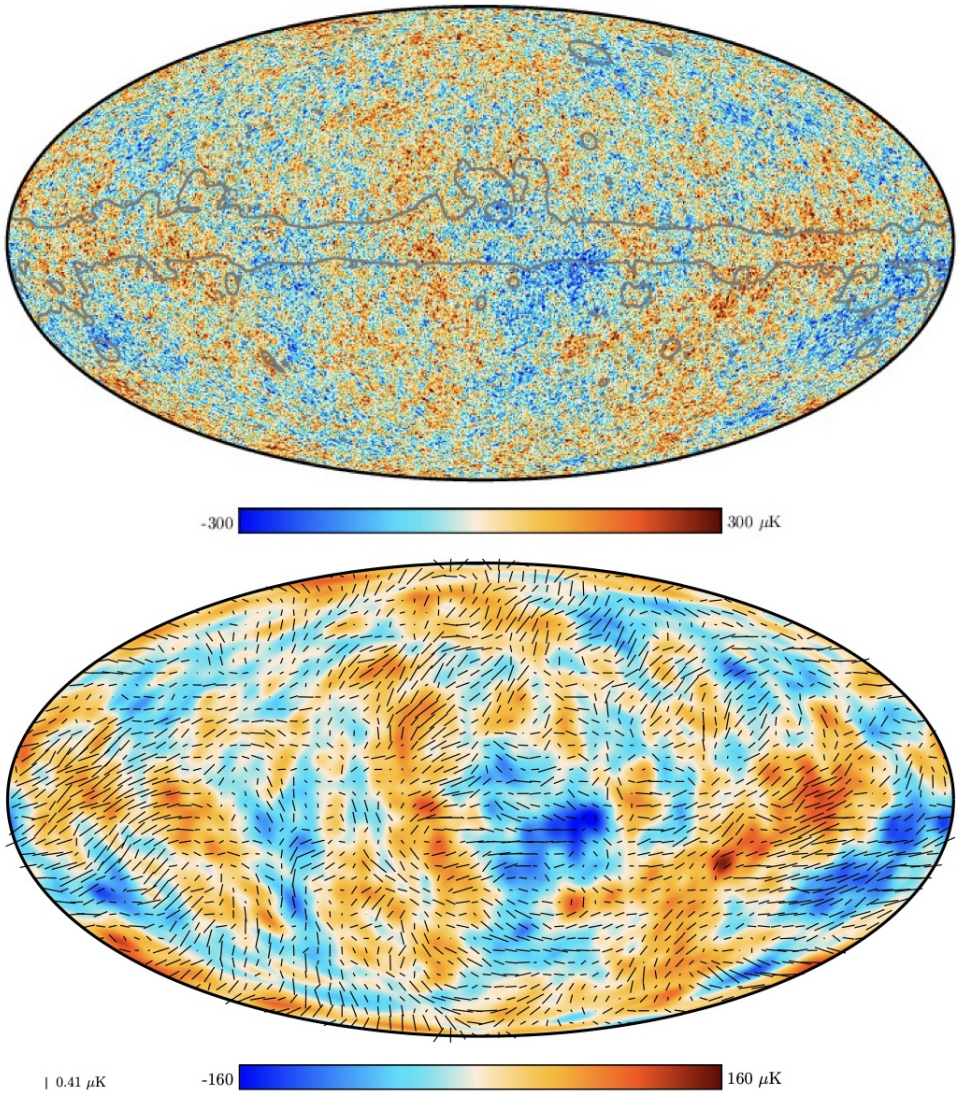

Figure 3.9. *Planck* CMB full-sky maps. The top panel shows the 2018 `SMICA` temperature map. The bottom panel shows the polarisation field as rods of varying length superimposed on the temperature map, both smoothed to 5°. This smoothing is done for visibility purposes. Both CMB maps have been masked and inpainted in regions where residuals from foreground emission are expected to be substantial. This mask, mostly around the Galactic plane, is delineated by a grey line in the full resolution temperature map. Figure adapted from [44].

3.5.2 The Next Stage of CMB Research

The progress in the measurement of the CMB temperature and polarisation anisotropies achieved by *Planck* validated the predictions of the ΛCDM model, providing the most precise estimates to date of its six main cosmological parameters (see Table 3.2) and the tightest constraints on its possible extensions. Nonetheless, many unanswered questions still remain. For example: what is the exact mechanism responsible for the generation of fluctuations in the Early Universe? Assuming inflation to be responsible for the generation of such primordial fluctuations, what are its actual properties and how does it end? What is Dark Matter? Are there additional, light relic particles? What is causing the current accelerated expansion of the Universe? Given the pivotal role of CMB measurements in shaping our understanding of the Universe so far, we do expect further observations of the CMB anisotropies to play a key role in answering those questions as well.

Table 3.2. The 6-parameter ΛCDM model that best fits the combination of data from *Planck* CMB temperature, polarisation and lensing power spectra, and their 68% confidence limits.

Parameter		
Baryon density today	$\Omega_B h^2$	0.0224 ± 0.0002
Cold Dark Matter density today	$\Omega_{DM} h^2$	0.1200 ± 0.0012
Observed angular size of the sound horizon at recombination	$100\theta_{MC}$	1.0409 ± 0.0003
Thomson scattering optical depth	τ	0.0544 ± 0.0073
Initial super-horizon amplitude of curvature perturbations	$\ln(10^{10} A_{\rm s})$	3.044 ± 0.014
Scalar spectral index	$n_{\rm s}$	0.965 ± 0.004

Since *Planck* has effectively mined all relevant information in the primary temperature anisotropies, reaching the cosmic-variance-limit at both large and intermediate angular scales, the focus of CMB research is now turning to precise measurements of polarisation and secondary effects, such as CMB lensing [8]. As far as the field of ground-based CMB experiments is concerned, we are currently in "Stage 3"[3] and transitioning to "Stage 4" experiments (CMB-S4). This next generation of experiments is characterised by a rich and diverse set of scientific goals organised into four major themes: primordial GWs and inflation; the dark Universe; mapping matter in the cosmos; and the time-variable mm-wave sky [45]. An important and unique feature of CMB-S4 is the use of multiple telescopes across multiple sites, namely the geographical South Pole and the Atacama Desert in Chile. Specifically, CMB-S4 is designed to exploit the natural conditions of these two sites: during winter, the lack of daily sunsets and sunrises makes the South Pole's atmosphere extremely stable thus allowing ultra-deep observations of small patches of the sky; due to its high-altitude and dryness, the Atacama Desert site allows instead for ultra-wide and deep survey of up to 80% of the sky. The current experimental efforts at these two sites, namely the POLARBEAR/Simons Array [46] and

[3] Ground-based CMB experiments are classified according to their number of detectors. "Stage 3" experiments have $O(10000)$ detectors. "Stage 4" experiments are designed to have $O(100000)$ detectors.

the BICEP/Keck [47] series of experiments, are already being consolidated into two major precursors of CMB-S4, the Simons Observatory [48] and the South Pole Observatory[4], which are expected to act as pathfinders for "Stage 4" experiments, providing technical and scientific data to continue to inform their design and operation. From space, the LiteBIRD (Lite satellite for the study of B-mode polarisation and Inflation from cosmic background Radiation Detection) mission [35] will map polarisation fluctuations in the CMB over the full-sky to search for the signature of GWs from inflation. Expected to launch in the late 2020s for a 3-year mission, the LiteBIRD satellite is designed to survey the full-sky in 15 frequency bands from 34 to 448 GHz, with a combined polarisation sensitivity of 2μK-arcmin and angular resolution of 31 arc-min (at 140 GHz) [35]. Its capabilities are therefore complementary to those of ground-base experiments: thanks to its broad frequency range, LiteBIRD is expected to provide valuable foreground information to ground-based experiments which, on the other hand, can improve LiteBIRD's observations with high-resolution lensing data. A (tentative) timeline of current, upcoming and proposed ground-based, satellite and sub-orbital CMB experiments from 2020 to 2040 is presented in Figure 3.10.

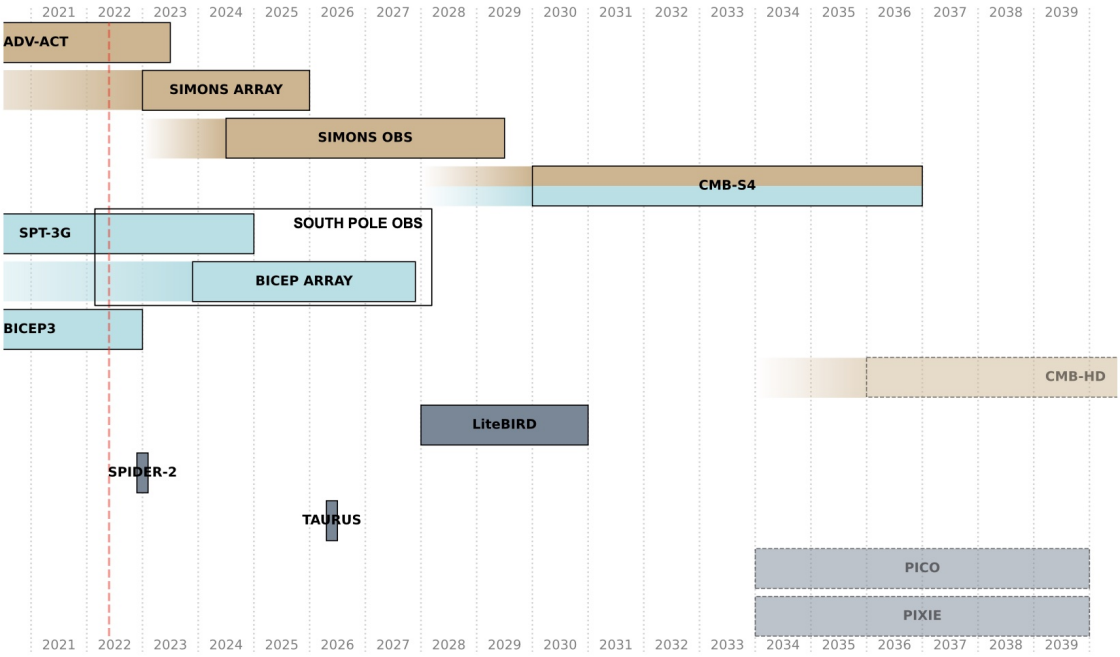

Figure 3.10. Timeline of current, upcoming and proposed ground-based (in brown and light blue), satellite and sub-orbital (in grey) CMB experiments. Figure adapted from [49].

[4]The South Pole Observatory is a coordinated effort between the South Pole Telescope (SPT) and BICEP/Keck collaborations. It will use the synergies of these two experiments to search for a primordial GWs signal in the presence of galactic and gravitational lensing foregrounds with unprecedented sensitivity.

Chapter 4
The Non-Gaussian Landscape

4.1 Beyond the Power Spectrum

Despite evidence that inflation has occurred, rather little is known about its actual properties. Was inflation driven by one or more fields? What form did the potential take? What about the kinetic term? What about the energy scale of inflation? What was the actual mechanism through which the universe became radiation populated at the end of inflation? In the last few years several alternative scenarios to the one provided by the slowly-rolling inflaton field have been proposed. The best way to discriminate between these different classes of models would be to study the statistical properties of the primordial fluctuations they generate during inflation. This is because the simplest model of inflation, where by simplest we mean single-field models of slow-roll inflation, with a canonical kinetic term and a Bunch-Davies choice for the vacuum state, produce perturbations extremely close to Gaussian, with a tiny deviation from Gaussianity of order of the slow-roll parameters [50]. The reason why standard single-field models of slow-roll inflation predicts a tiny level of non-Gaussianity is that, as we have seen in Chapter 1, in order to achieve a period of accelerated expansion, the inflaton potential must be very flat and the flatness of the potential implies a suppression of the inflaton self-interactions, along with any other source of non-linearity, leaving only the inflaton gravitational interactions as a source of non-Gaussianity. This fact allow us to discriminate between the so-called standard scenario of inflation and other classes of inflationary models, which instead produce specific and predictable types of non-Gaussianity [23].

4.1.1 The Bispectrum

The lowest-order statistic that can distinguish Gaussian and non-Gaussian perturbations is the 3-point correlation function, or its harmonic counterpart, the *bispectrum*, defined as follows:

$$\langle \Phi(\mathbf{k}_1)\Phi(\mathbf{k}_2)\Phi(\mathbf{k}_3)\rangle = (2\pi)^3\delta^{(3)}(\mathbf{k}_1+\mathbf{k}_2+\mathbf{k}_3)B_\Phi(k_1,k_2,k_3) \tag{4.1}$$

Here the potential Φ is defined in terms of the comoving curvature perturbation ζ on super-horizon scales by $\Phi \equiv \frac{3}{5}\zeta$, thus corresponding, during the epoch of matter domination, to

Bardeen's gauge-invariant gravitational potential. Indeed, one can prove that, on large scales or during the epoch of matter domination ($w = 0$), the gauge-invariant curvature perturbation ζ and Bardeen's gravitational potential Φ are related by [23]

$$\Phi = -\frac{3+3w}{5+3w}\mathcal{R} = \frac{3+3w}{5+3w}\zeta \tag{4.2}$$

The bispectrum $B_\Phi(k_1, k_2, k_3)$ measures the correlation among three perturbations modes and due to the assumptions of rotational and translational invariance depends only on the magnitudes of the three wavevectors $\mathbf{k}_i$, which satisfy the triangle inequalities. In general, the bispectrum can be written as

$$B_\Phi(k_1, k_2, k_3) = f_{\rm NL} F(k_1, k_2, k_3) \tag{4.3}$$

where $f_{\rm NL}$ is the so-called *non-linearity parameter*, a dimensionless parameter which measures the amplitude of non-Gaussianity, and $F(k_1, k_2, k_3)$ is the so-called *shape function*, which depends on the type of triangle formed by the three wavevectors. Figure 4.1 illustrates possible configurations.

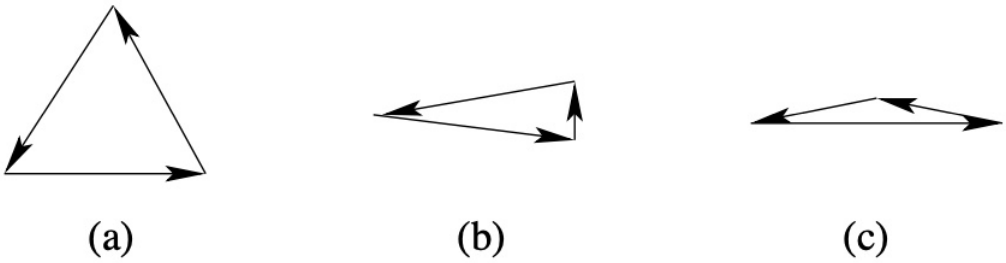

Figure 4.1. Momentum configurations corresponding to (a) equilateral, (b) squeezed, (c) folded triangle shapes. Figure adapted from [51].

Different shapes are linked to different, well motivated classes of inflationary models. For example:

- the so-called *local* non-Gaussianity is characterised by a signal that peaks in *squeezed* triangles with $k_1 \ll k_2 \simeq k_3$ and it is a typical signature of multi-field models of inflation. Such models include the case of *multiple-field inflation*, in which inflation is driven by more than one scalar field, as well as scenarios featuring the presence of additional light degrees of freedom which remain sub-dominant during the inflationary expansion. In these models the non-Gaussianity in the curvature perturbations is generated via a transfer on super-horizon scales of initial isocurvature perturbations to the adiabatic (curvature) perturbations, accompanied by non-linearities in the transfer mechanism

itself. The local bispectrum is given by [52, 53, 54, 55, 56, 57]

$$B_{\Phi}^{\rm local}(k_1,k_2,k_3) = 2f_{\rm NL}^{\rm local}\left[P_{\Phi}(k_1)P_{\Phi}(k_2)+P_{\Phi}(k_1)P_{\Phi}(k_3)+P_{\Phi}(k_2)P_{\Phi}(k_3)\right]$$
$$= 2A_{\rm s}^2 f_{\rm NL}^{\rm local}\left[\frac{1}{k_1^{4-n_{\rm s}}k_2^{4-n_{\rm s}}}+{\rm cycl.}\right] \tag{4.4}$$

where $P_{\Phi}(k) = \frac{A}{k^{4-n_{\rm s}}}$ is the Bardeen's gravitational potential power spectrum with normalisation A and scalar spectral index $n_{\rm s}$. The local form of non-Gaussianity is so-called because a typical example of a curvature perturbation which can generate the bispectrum of equation (4.4) is the standard local form of the gravitational potential [58, 53, 57]:

$$\Phi_{\rm NG}(\mathbf{x}) = \Phi_{\rm L}(\mathbf{x}) + f_{\rm NL}^{\rm local}\left(\Phi_{\rm L}^2(\mathbf{x}) - \langle\Phi_{\rm L}^2(\mathbf{x})\rangle\right) \tag{4.5}$$

where $\Phi_{\rm L}$ is the linear Gaussian gravitational potential and the term $\langle\Phi_{\rm L}^2(\mathbf{x})\rangle$ ensures that the perturbation has zero mean;

- the *equilateral* non-Gaussianity is characterised by a signal that peaks for triangle configurations with $k_1 \simeq k_2 \simeq k_3$. It is typical of single-field models of inflation with a non-canonical kinetic term, models with higher-derivative interactions for the inflaton field or models arising from effective field theories. The equilateral bispectrum is well approximated by the template [59]:

$$B_{\Phi}^{\rm equil}(k_1,k_2,k_3) = 6A_{\rm s}^2 f_{\rm NL}^{\rm equil}\left\{\frac{1}{k_1^{4-n_{\rm s}}k_2^{4-n_{\rm s}}} - \frac{1}{k_2^{4-n_{\rm s}}k_3^{4-n_{\rm s}}} - \frac{1}{k_3^{4-n_{\rm s}}k_1^{4-n_{\rm s}}}\right.$$
$$\left. - \frac{2}{(k_1k_2k_3)^{2(4-n_{\rm s})/3}} + \left[\frac{1}{k_1^{(4-n_{\rm s})/3}k_2^{2(4-n_{\rm s})/3}k_3^{4-n_{\rm s}}} + 5\text{ perms.}\right]\right\} \tag{4.6}$$

- the *orthogonal* non-Gaussianity is characterised by a signal with a positive peak at the equilateral configuration and a negative peak at the folded configuration. It is typical, for example, of single-field models of inflation with a non-canonical kinetic term or with higher-derivative interactions. The orthogonal bispectrum is well approximated by the

template [60]:

$$B_{\Phi}^{\rm ortho}(k_1,k_2,k_3) = 6A_{\rm s}^2 f_{\rm NL}^{\rm ortho} \times \left\{ -\frac{3}{k_1^{4-n_{\rm s}}k_2^{4-n_{\rm s}}} - \frac{3}{k_2^{4-n_{\rm s}}k_3^{4-n_{\rm s}}} - \frac{3}{k_3^{4-n_{\rm s}}k_1^{4-n_{\rm s}}} \right.$$
$$\left. - \frac{8}{(k_1k_2k_3)^{2(4-n_{\rm s})/3}} + \left[\frac{3}{k_1^{(4-n_{\rm s})/3}k_2^{2(4-n_{\rm s})/3}k_3^{4-n_{\rm s}}} + 5 \text{ perms.} \right] \right\} \quad (4.7)$$

- the *folded* (or flattened) non-Gaussianity is characterised by a signal that peaks for triangle configurations with $k_1 + k_2 \simeq k_3$. It is typical of single-field models with a non-Bunch-Davies choice for the vacuum state or models with general higher-derivative interactions. The flattened bispectrum is usually parametrised by the template [61]:

$$B_{\Phi}^{\rm flat}(k_1,k_2,k_3) = 6A_{\rm s}^2 f_{\rm NL}^{\rm flat} \left\{ \frac{1}{k_1^{4-n_{\rm s}}k_2^{4-n_{\rm s}}} + \frac{1}{k_2^{4-n_{\rm s}}k_3^{4-n_{\rm s}}} + \frac{1}{k_3^{4-n_{\rm s}}k_1^{4-n_{\rm s}}} \right.$$
$$\left. + \frac{3}{(k_1k_2k_3)^{2(4-n_{\rm s})/3}} + \left[\frac{1}{k_1^{(4-n_{\rm s})/3}k_2^{2(4-n_{\rm s})/3}k_3^{4-n_{\rm s}}} + 5 \text{ perms.} \right] \right\} \quad (4.8)$$

Al of these inflationary models predict $|f_{\rm NL}| \gg 1$ and thus yield primordial non-Gaussianity with an amplitude much bigger than the one predicted in the simplest models of single-field inflation, for which it has been shown that the level of non-Gaussianity is proportional to the slow-roll parameters i.e. $f_{\rm NL} \sim \mathcal{O}(\eta, \epsilon)$ [62, 50].

4.1.2 The Trispectrum

The 4-point correlation function, or its harmonic counterpart, the *trispectrum*, can also provide information on the mechanism that gave rise to the primordial curvature perturbations. The primordial trispectrum is defined as follows:

$$\langle \Phi(\mathbf{k}_1)\Phi(\mathbf{k}_2)\Phi(\mathbf{k}_3)\Phi(\mathbf{k}_4)\rangle = (2\pi)^3\delta^{(3)}(\mathbf{k}_1+\mathbf{k}_2+\mathbf{k}_3+\mathbf{k}_4)T_{\Phi}(k_1,k_2,k_3,k_4) \quad (4.9)$$

The contributions to the trispectrum are usually described in terms of two non-linearity parameters, $\tau_{\rm NL}$ and $g_{\rm NL}$: $\tau_{\rm NL}$ is often related to $f_{\rm NL}^2$-type contributions, while $g_{\rm NL}$ is interpreted as the amplitude of cubic non-linearities in the primordial gravitational potential. In terms of field interactions $\tau_{\rm NL}$ and $g_{\rm NL}$ correspond, respectively, to a scalar-exchange and a contact interaction term (see Figure 4.2).

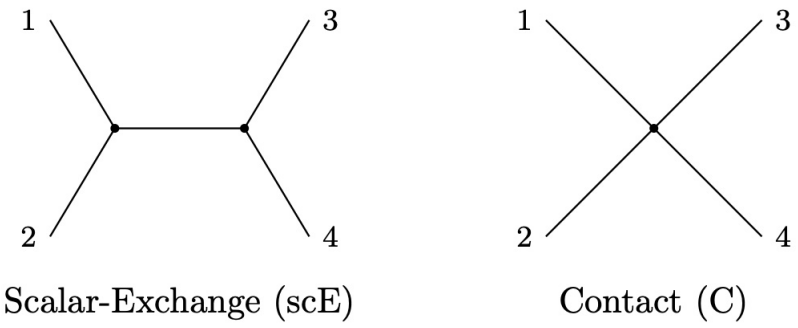

Figure 4.2. Diagrammatic representation of field interactions corresponding, respectively, to the $\tau_{\rm NL}$ and $g_{\rm NL}$ contributions to the trispectrum. Figure adapted from [63].

Similarly to the bispectrum, the local-type trispectrum, which typically arises in multi-field models of inflation, has been extensively studied in literature. The simplest local trispectrum is given by the template:

$$\begin{aligned} T_\Phi^{\rm local}(k_1,k_2,k_3,k_4) = \frac{25}{9}\tau_{\rm NL}^{\rm local}\left[P_\Phi(k_1)P_\Phi(k_2)P_\Phi(k_{13}) + 11 \text{ perms.}\right] \\ + 6g_{\rm NL}^{\rm local}\left[P_\Phi(k_1)P_\Phi(k_2)P_\Phi(k_3) + 3 \text{ perms.}\right] \end{aligned} \tag{4.10}$$

where $k_{ij} \equiv |\mathbf{k}_i + \mathbf{k}_j|$. Note that the local $\tau_{\rm NL}$-trispectrum is characterised by a signal that peaks in quadrilateral configurations with one of the diagonals much smaller than the other side i.e. $K \ll k_1 \simeq k_2 \simeq k_3 \simeq k_4$, usually referred to as the *squeezed-diagonal* or *collapsed* shape; the local $g_{\rm NL}$-trispectrum is instead characterised by a signal that peaks in diagonal configurations with $k_1 \simeq k_2 \ll k_3 \simeq k_4$, usually referred to as the *double-squeezed* shape. One easy way to generate the trispectrum of equation (4.10) is to consider

$$\Phi_{\rm NG}(\mathbf{x}) = \Phi_{\rm L}(\mathbf{x}) + f_{\rm NL}^{\rm local}\left(\Phi_{\rm L}^2(\mathbf{x}) - \langle\Phi_{\rm L}^2(\mathbf{x})\rangle\right) + g_{\rm NL}^{\rm local}\Phi_{\rm L}^3(\mathbf{x}) \tag{4.11}$$

where, as usual, $\Phi_{\rm L}$ is the linear Gaussian gravitational potential. In this case, one has that

$$\tau_{\rm NL} = \left(\frac{6}{5}f_{\rm NL}^{\rm local}\right)^2 \tag{4.12}$$

However, in general, the $\tau_{\rm NL}$-trispectrum amplitude can be larger. Employing the Cauchy-Schwarz identity, Suyama and Yamaguchi proved that in general the following inequality holds [64]:

$$\tau_{\rm NL} \geq \left(\frac{6}{5}f_{\rm NL}^{\rm local}\right)^2 \tag{4.13}$$

It's in the simplest inflationary scenarios that the inequality (4.13) saturates to an equality, thus implying that larger values of $\tau_{\rm NL}$ hint to a more complicated inflationary dynamics.

4.2 Running non-Gaussianity

The non-linearity parameter $f_{\rm NL}$, as defined in equation (4.5), is a constant modulating the second order term of the Bardeen's gravitational potential expansion. Even though this is a good approximation in many models, it is in general not exact. Many inflationary scenarios predict a scale-dependence of the bispectrum, also known in literature as the *running* of the bispectrum (see e.g. [51, 65]), which can arise due to multiple-field effects i.e. from multiple fields contributing to the curvature perturbation, due to non-linearity in the evolution of modes on super-horizon scales or due to a non-trivial field space-time metric. The scale-dependence is often parametrised as a power-law:

$$f_{\rm NL} \longrightarrow f^0_{\rm NL} \left(\frac{K}{k_0}\right)^{n_{f_{\rm NL}}} \tag{4.14}$$

where K is the overall scale corresponding to the triangle configuration, generally defined as the *arithmetic mean* of the three wavenumbers k_i[1], $f^0_{\rm NL}$ is the amplitude of $f_{\rm NL}$ measured at some pivot scale k_0 and $n_{f_{\rm NL}}$ is a constant which, in analogy to the spectral index (1.67), can be defined as

$$n_{f_{\rm NL}} \equiv \frac{d \ln |f_{\rm NL}(k)|}{d \ln k} \tag{4.15}$$

Strictly speaking, being defined with respect to only one scale, this is valid for equilateral configurations only, for which the three momenta $\mathbf{k}_i$ are equal. However, in [65] it has been shown that the scale-dependence of $f_{\rm NL}$ is actually independent on the shape of the triangle configuration it describes, provided one considers variations where all sides of the triangle are rescaled by a same constant factor i.e. $\mathbf{k}_i \to \alpha \mathbf{k}_i$. In [65], Byrnes et al. also studied the running of the trispectrum, computing the scale-dependence of the non-linearity parameters $\tau_{\rm NL}$ and $g_{\rm NL}$. In particular, they showed that for single-source models of inflation the scale-dependencies of $\tau_{\rm NL}$ and $f_{\rm NL}$ are related by

$$n_{\tau_{\rm NL}} = 2 n_{f_{\rm NL}} \tag{4.16}$$

Notice that the above result is analogous to the consistency relation (4.12) and thus it provides a useful consistency check.

[1] In [66], Sefusatti et al. propose an alternative parametrisation of the overall scale K as the *geometric mean* of the three wavenumbers which, due to the separability property of the geometric mean, allows for a much simpler numerical implementation of the associated CMB estimator.

4.3 Non-Gaussianity in the CMB

The observed statistics in the CMB, as we have seen in Chapter 3, are the multipole moments of the temperature and polarisation fields which, at linear order, are related to the underlying primordial fluctuations $\Phi(\mathbf{k})$ as follows[2]:

$$a^x_{\ell m} = 4\pi(-i)^\ell \int \frac{d^3\mathbf{k}}{(2\pi)^3}\Phi(\mathbf{k})g^x_\ell(k)Y^*_{\ell m}(\hat{\mathbf{k}}) \tag{4.17}$$

where $x = T, E$ denote, respectively, the temperature and E-mode polarisation fluctuations and $g^x_\ell(k)$ is the CMB radiation transfer function. Equation (4.17) clearly implies that any non-Gaussianity in the primordial fluctuations gets transferred to the observed CMB anisotropies[3]. The most common way to look for non-Gaussianity in the CMB consists in studying the angular n-point harmonic spectrum, $\langle a_{\ell_1 m_1} a_{\ell_2 m_2} ... a_{\ell_n m_n}\rangle$. However, in reality one cannot actually measure the ensemble average of the angular n-point harmonic spectrum, but only one realisation, $a_{\ell_1 m_1} a_{\ell_2 m_2} ... a_{\ell_n m_n}$, which is very noisy. Therefore one wants to find a way to average it somehow to reduce the noise and, as we shall see in a moment, this can be achieved by simply assuming the Universe to be statistically isotropic. If one requires the CMB temperature and E-mode polarisation fields to be statistically isotropic, one gets that the angular n-point spectrum must obey the following condition:

$$\langle a_{\ell_1 m_1} a_{\ell_2 m_2} ... a_{\ell_n m_n}\rangle = \sum_{\text{all } m'} \langle a_{\ell_1 m'_1} a_{\ell_2 m'_2} ... a_{\ell_n m'_n}\rangle D^{(\ell_1)}_{m'_1 m_1} D^{(\ell_2)}_{m'_2 m_2} ... D^{(\ell_n)}_{m'_n m_n} \tag{4.18}$$

where $D = D(\alpha, \beta, \gamma)$ is the Wigner D-matrix, which describes a rotation for the Euler angles α, β and γ, and thus the matrix element $D^{(\ell)}_{m'm} = \langle \ell', m'|D|\ell, m\rangle$ describes a finite rotation of an initial state represented by ℓ and m into a final state represented by ℓ' and m'. Therefore the condition given by equation (4.18) implies that one can average the angular spectrum over m_i with appropriate weights, that we are going to explicitly evaluate for the angular 3-point and 4-point harmonic spectra following the method illustrated by W. Hu in [67]. The idea in [67] is to seek for a rotationally invariant representation of the angular n-point harmonic spectrum, proceeding as follows. Each pair of rotation matrices $D^{(\ell_a)}_{m'_a m_a} D^{(\ell_b)}_{m'_b m_b}$ is coupled into

[2] From now on we assume that our location $\mathbf{x}_0 \equiv 0$, so that the exponential in equation (3.18) becomes $e^{i\mathbf{k}\cdot\mathbf{x}_0} = 1$.

[3] However, it should be noted that if one were to measure a significant non-Gaussian signature in the CMB, the origin of the signature may not necessarily be primordial, since non-Gaussianity in the CMB can also be generated by secondary sources (e.g. the combined ISW-lensing effect) and/or foreground sources (e.g. extragalactic radio sources) [23].

a single rotation matrix $D^{(L)}_{M'M}$ using the group multiplication property

$$D^{(\ell_a)}_{m'_a m_a} D^{(\ell_b)}_{m'_b m_b} = \sum_L \sum_{M'M} (2L+1)(-1)^{M+M'} D^{(L)}_{M'M} \times \begin{pmatrix} \ell_a & \ell_b & L \\ m_a & m_b & -M \end{pmatrix} \begin{pmatrix} \ell_a & \ell_b & L \\ m'_a & m'_b & -M' \end{pmatrix} \tag{4.19}$$

where the matrix appearing in the right hand side of equation (4.19) is the Wigner 3-j symbol (see appendix B). Once the product $D^{(\ell_1)}_{m'_1 m_1} D^{(\ell_2)}_{m'_2 m_2} ... D^{(\ell_n)}_{m'_n m_n}$ is reduced to the product of a pair of rotation matrices, one seeks the form of the angular n-point harmonic spectrum that reduces this pair of matrices to the orthogonality condition for the Wigner D-matrix, that is:

$$\sum_{m_n} (-1)^{m'_n - m_n} D^{(\ell_n)}_{M m_n} D^{(\ell_n)}_{-m'_n - m_n} = \delta_{M m'_n} \tag{4.20}$$

4.3.1 The Angular Bispectrum

The angular 3-point harmonic spectrum or bispectrum, consists of three harmonic transforms, $a_{\ell_1 m_1} a_{\ell_2 m_2} a_{\ell_3 m_3}$. The requirement of statistical isotropy on the CMB implies that the angular bispectrum must obey the following condition

$$\langle a_{\ell_1 m_1} a_{\ell_2 m_2} a_{\ell_3 m_3} \rangle = \sum_{\text{all } m'} \langle a_{\ell_1 m'_1} a_{\ell_2 m'_2} a_{\ell_3 m'_3} \rangle D^{(\ell_1)}_{m'_1 m_1} D^{(\ell_2)}_{m'_2 m_2} D^{(\ell_3)}_{m'_3 m_3} \tag{4.21}$$

Using the group multiplication property (4.19), equation (4.21) reduces to

$$\langle a_{\ell_1 m_1} a_{\ell_2 m_2} a_{\ell_3 m_3} \rangle = \sum_{\text{all } m'} \langle a_{\ell_1 m'_1} a_{\ell_2 m'_2} a_{\ell_3 m'_3} \rangle \sum_L \sum_{M'M} (2L+1)(-1)^{M+M'} \times \begin{pmatrix} \ell_1 & \ell_2 & L \\ m_1 & m_2 & -M \end{pmatrix} \begin{pmatrix} \ell_1 & \ell_2 & L \\ m'_1 & m'_2 & -M' \end{pmatrix} D^{(L)}_{M'M} D^{(\ell_3)}_{m'_3 m_3} \tag{4.22}$$

To reduce this relation to the orthogonality condition (4.20), one must seek a form for the angular 3-point harmonic spectrum such that the sum over m'_1, m'_2 must be proportional to $\delta_{-M' m'_3} \delta_{L \ell_3}$.

A good guess, as we shall prove in a moment, is [67]:

$$\langle a_{\ell_1 m_1'} a_{\ell_2 m_2'} a_{\ell_3 m_3'} \rangle = \begin{pmatrix} \ell_1 & \ell_2 & \ell_3 \\ m_1' & m_2' & m_3' \end{pmatrix} \langle B_{\ell_1 \ell_2 \ell_3} \rangle \tag{4.23}$$

Substituting equation (4.23) into equation (4.22) and recalling the orthogonality identity of the Wigner 3-j symbol

$$\sum_{m_1 m_2} \begin{pmatrix} \ell_1 & \ell_2 & \ell_3 \\ m_1 & m_2 & m_3 \end{pmatrix} \begin{pmatrix} \ell_1 & \ell_2 & \ell_3' \\ m_1 & m_2 & m_3' \end{pmatrix} = \frac{\delta_{\ell_3 \ell_3'} \delta_{m_3 m_3'}}{2\ell_3 + 1} \tag{4.24}$$

it's straightforward to see that equation (4.22) reduces to

$$\begin{aligned}
&\langle a_{\ell_1 m_1} a_{\ell_2 m_2} a_{\ell_3 m_3} \rangle = \\
&= \langle B_{\ell_1 \ell_2 \ell_3} \rangle \sum_{m_3'} \sum_{L} \sum_{M' M} \begin{pmatrix} \ell_1 & \ell_2 & L \\ m_1 & m_2 & -M \end{pmatrix} \delta_{-M' m_3'} \delta_{L \ell_3} (-1)^{M+M'} D^{(L)}_{M' M} D^{(\ell_3)}_{m_3' m_3} = \\
&= \langle B_{\ell_1 \ell_2 \ell_3} \rangle \sum_{M} \begin{pmatrix} \ell_1 & \ell_2 & \ell_3 \\ m_1 & m_2 & M \end{pmatrix} \sum_{m_3'} (-1)^{M - m_3'} D^{(L)}_{m_3' M} D^{(\ell_3)}_{m_3' m_3} = \\
&= \langle B_{\ell_1 \ell_2 \ell_3} \rangle \sum_{M} \begin{pmatrix} \ell_1 & \ell_2 & \ell_3 \\ m_1 & m_2 & -M \end{pmatrix} \delta_{-M m_3} = \\
&= \langle B_{\ell_1 \ell_2 \ell_3} \rangle \begin{pmatrix} \ell_1 & \ell_2 & \ell_3 \\ m_1 & m_2 & m_3 \end{pmatrix}
\end{aligned} \tag{4.25}$$

thus proving that equation (4.23) is indeed the rotationally invariant solution we are looking for. Note that the Wigner 3-j symbol as defined above describes the coupling of two angular momenta states, (ℓ_1, m_1) and (ℓ_2, m_2), forming a coupled state (ℓ_3, m_3). In particular, ℓ_1, ℓ_2 and ℓ_3 form a triangle, thus implying that $B_{\ell_1 \ell_2 \ell_3}$ must satisfy the triangle condition $|\ell_i - \ell_j| \leq \ell_k \leq \ell_i + \ell_j$ for all permutation indices, with the parity invariance of the angular correlation function also demanding $\ell_1 + \ell_2 + \ell_3 =$ even. The orientation of the triangle formed by ℓ_1, ℓ_2 and ℓ_3 is represented by m_1, m_2 and m_3, with $m_1 + m_2 + m_3 = 0$. Under a rotation of the system, the Wigner 3-j symbol transforms the ms, preserving however the configuration of the triangle. Similarly, the rotational invariance of the angular bispectrum demands that same triangle configurations give the same amplitude for the bispectrum regardless of its orientation. Figure 4.3 sketches one of the possible angular bispectrum configurations.

4.3.2 The Angular Trispectrum

The angular 4-point harmonic spectrum or trispectrum, consists of four harmonic transforms, $a_{\ell_1 m_1} a_{\ell_2 m_2} a_{\ell_3 m_3} a_{\ell_4 m_4}$. The requirement of statistical isotropy implies that:

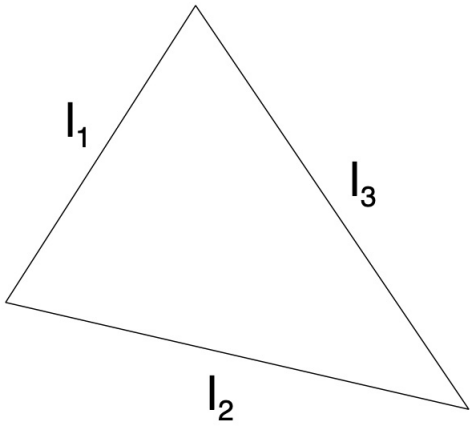

Figure 4.3. Angular bispectrum configuration. Figure adapted from [23].

$$\langle a_{\ell_1 m_1} a_{\ell_2 m_2} a_{\ell_3 m_3} a_{\ell_4 m_4} \rangle = \sum_{\text{all } m'} \langle a_{\ell_1 m_1'} a_{\ell_2 m_2'} a_{\ell_3 m_3'} a_{\ell_4 m_4'} \rangle D^{(\ell_1)}_{m_1' m_1} D^{(\ell_2)}_{m_2' m_2} D^{(\ell_3)}_{m_3' m_3} D^{(\ell_4)}_{m_4' m_4} \tag{4.26}$$

We begin our search for a rotationally invariant representation of the angular 4-point harmonic spectrum by reducing each pair of rotation matrices, $D^{(\ell_1)}_{m_1' m_1} D^{(\ell_2)}_{m_2' m_2}$ and $D^{(\ell_3)}_{m_3' m_3} D^{(\ell_4)}_{m_4' m_4}$, using the group multiplication property (4.19) thus obtaining

$$\begin{aligned}
\langle a_{\ell_1 m_1} a_{\ell_2 m_2} a_{\ell_3 m_3} a_{\ell_4 m_4} \rangle &= \sum_{\text{all } m'} \langle a_{\ell_1 m_1'} a_{\ell_2 m_2'} a_{\ell_3 m_3'} a_{\ell_4 m_4'} \rangle \\
&\times \sum_{L_{12}} \sum_{M_{12}' M_{12}} (2L_{12}+1) \begin{pmatrix} \ell_1 & \ell_2 & L_{12} \\ m_1 & m_2 & -M_{12} \end{pmatrix} \begin{pmatrix} \ell_1 & \ell_2 & L_{12} \\ m_1' & m_2' & -M_{12}' \end{pmatrix} (-1)^{M_{12}+M_{12}'} D^{(L_{12})}_{M_{12}' M_{12}} \\
&\times \sum_{L_{34}} \sum_{M_{34}' M_{34}} (2L_{34}+1) \begin{pmatrix} \ell_3 & \ell_4 & L_{34} \\ m_3 & m_4 & -M_{34} \end{pmatrix} \begin{pmatrix} \ell_3 & \ell_4 & L_{34} \\ m_3' & m_4' & -M_{34}' \end{pmatrix} (-1)^{M_{34}+M_{34}'} D^{(L_{34})}_{M_{34}' M_{34}}
\end{aligned} \tag{4.27}$$

To reduce equation (4.26) to the orthogonality condition (4.20), one must seek a form of the angular trispectrum such that the sum over m_1', m_2' and m_3', m_4' are proportional, respectively, to $\delta_{L_{12} L} \delta_{-M_{12}' - M}$ and $\delta_{L_{34} L} \delta_{-M_{34}' M}$. A good guess, in this case, is [67]:

$$\langle a_{\ell_1 m_1'} a_{\ell_2 m_2'} a_{\ell_3 m_3'} a_{\ell_4 m_4'} \rangle = \sum_{LM} \begin{pmatrix} \ell_1 & \ell_2 & L \\ m_1' & m_2' & -M \end{pmatrix} \begin{pmatrix} \ell_3 & \ell_4 & L \\ m_3' & m_4' & M \end{pmatrix} (-1)^M \langle Q^{\ell_1 \ell_2}_{\ell_3 \ell_4}(L) \rangle \tag{4.28}$$

One can prove that this is indeed the rotationally invariant solution we are looking for by similar calculations to those proving the angular bispectrum (4.23) to be so. Substituting

equation (4.28) into equation (4.27) and using the orthogonality identity of the Wigner 3-j symbol (4.24), it's straightforward to see that equation (4.27) reduces to

$$
\begin{aligned}
&\langle a_{\ell_1 m_1} a_{\ell_2 m_2} a_{\ell_3 m_3} a_{\ell_4 m_4} \rangle = \\
&= \sum_{LM} \sum_{L_{12}} \sum_{M'_{12} M_{12}} \sum_{L_{34}} \sum_{M'_{34} M_{34}} \langle Q^{\ell_1 \ell_2}_{\ell_3 \ell_4}(L) \rangle \begin{pmatrix} \ell_1 & \ell_2 & L_{12} \\ m_1 & m_2 & -M_{12} \end{pmatrix} \begin{pmatrix} \ell_3 & \ell_4 & L_{34} \\ m_3 & m_4 & -M_{34} \end{pmatrix} \\
&\times \delta_{L_{12} L} \delta_{-M'_{12} - M} \delta_{L_{34} L} \delta_{-M'_{34} M} (-1)^{M_{34} + M'_{34}} (-1)^{M_{12} + M'_{12}} (-1)^{M} D^{(L_{12})}_{M'_{12} M_{12}} D^{(L_{34})}_{M'_{34} M_{34}} = \\
&= \sum_{L_{12} M_{12}} \sum_{M_{34}} (-1)^{M_{12}} \langle Q^{\ell_1 \ell_2}_{\ell_3 \ell_4}(L) \rangle \begin{pmatrix} \ell_1 & \ell_2 & L_{34} \\ m_1 & m_2 & -M_{12} \end{pmatrix} \begin{pmatrix} \ell_3 & \ell_4 & L_{34} \\ m_3 & m_4 & -M_{34} \end{pmatrix} \\
&\times \sum_{M} (-1)^{M_{34} + M} D^{(L_{12})}_{M M_{12}} D^{(L_{12})}_{-M M_{34}} = \\
&= \sum_{L_{12} M_{12}} \sum_{M_{34}} (-1)^{M_{12}} \langle Q^{\ell_1 \ell_2}_{\ell_3 \ell_4}(L) \rangle \begin{pmatrix} \ell_1 & \ell_2 & L_{34} \\ m_1 & m_2 & -M_{12} \end{pmatrix} \begin{pmatrix} \ell_3 & \ell_4 & L_{34} \\ m_3 & m_4 & -M_{34} \end{pmatrix} \delta_{M_{12} - M_{34}} = \\
&= \sum_{L_{12} M_{12}} (-1)^{M_{12}} \langle Q^{\ell_1 \ell_2}_{\ell_3 \ell_4}(L) \rangle \begin{pmatrix} \ell_1 & \ell_2 & L_{34} \\ m_1 & m_2 & -M_{12} \end{pmatrix} \begin{pmatrix} \ell_3 & \ell_4 & L_{34} \\ m_3 & m_4 & M_{12} \end{pmatrix}
\end{aligned}
\tag{4.29}
$$

where, to reach the last line, we used the fact that $(-1)^{M_{12}+M} = (-1)^{-M_{12}-M}$. Like the angular 3-point harmonic spectrum, the angular 4-point harmonic spectrum depends on Wigner 3-j symbols, which provide selection rules for the possible configurations of the angular trispectrum. Figure 4.4 sketches one of these possible configurations: by construction ℓ_1, ℓ_2 and L and ℓ_3, ℓ_4 and L form two triangles in a quadrilateral of sides ℓ_1, ℓ_2, ℓ_3 and ℓ_4, with L representing one of its diagonals. If one assumes $\ell_1 \leq \ell_2 \leq \ell_3 \leq \ell_4$, then the value of L lies in $\max(\ell_2 - \ell_1, \ell_4 - \ell 3) \leq L \leq \min(\ell_2 + \ell_1, \ell_4 + \ell 3)$, with the parity invariance of the angular correlation function demanding that $\ell_1 + \ell_2 + L =$ even and $\ell_3 + \ell_4 + L =$ even. Another hint on the fact that the multipoles $(\ell_1, \ell_2, \ell_3, \ell_4)$ must close to form a quadrilateral is given by the m_i: from the first Wigner 3-j symbol we have that $m_1 + m_2 - M = 0$ and similarly from the second one we have that $m_3 + m_4 + M = 0$, thus implying that $m_1 + m_2 + m_3 + m_4 = 0$. Let us also observe that, in general, the averaged angular trispectrum $\langle Q^{\ell_1 \ell_2}_{\ell_3 \ell_4}(L) \rangle$ consists of two parts. The first part is the so-called *non-connected* or *disconnected* one, which describes the contribution from Gaussian fields and is given by [67]

$$
\begin{aligned}
\langle Q^{\ell_1 \ell_2}_{\ell_3 \ell_4}(L) \rangle_{disconnected} = (-1)^{\ell_1 + \ell_3} \sqrt{(2\ell_1 + 1)(2\ell_3 + 1)} \langle C_{\ell_1} \rangle \langle C_{\ell_3} \rangle \delta_{\ell_1 \ell_2} \delta_{\ell_3 \ell_4} \delta_{L0} \\
+ (2L + 1) \langle C_{\ell_1} \rangle \langle C_{\ell_2} \left[(-1)^{\ell_1 + \ell_3 + L} \delta_{\ell_1 \ell_2} \delta_{\ell_3 \ell_4} + \delta_{\ell_1 \ell_4} \delta_{\ell_2 \ell_3} \right]
\end{aligned}
\tag{4.30}
$$

The other part is the so-called *connected* part, whose expectation value is exactly zero for Gaussian fields and thus it's the part sensitive to non-Gaussianity. Note that if $\ell_1 \leq \ell_2 \leq \ell_3 \leq$

ℓ_4, the disconnected part of the trispectrum is non-zero only if $L = 0$ or $\ell_1 = \ell_2 = \ell_3 = \ell_4$. Therefore, when $L \neq 0$ or $\ell_1 \neq \ell_2 \neq \ell_3 \neq \ell_4$, one would expect the angular trispectrum to comprise of the connected part only. However, this is true only if one considers the full sky. This is because on the incomplete sky the disconnected part of the trispectrum leak power to other modes for which all ℓs are different.

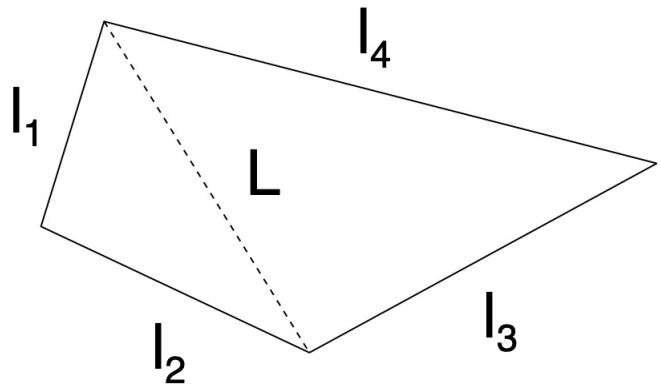

Figure 4.4. Angular trispectrum configuration. Figure adapted from [23].

In [67], W. Hu also illustrates an alternative construction for the angular 4-point harmonic function that automatically enforces on it the desired rotational, permutation and parity symmetries. One begins by observing that the connected part of the angular trispectrum can be written in the following form, which is explicitly symmetric in the three unique pairings, (ℓ_1, ℓ_2), (ℓ_1, ℓ_3) and (ℓ_1, ℓ_4):

$$\begin{aligned}&\langle a_{\ell_1 m_1} a_{\ell_2 m_2} a_{\ell_3 m_3} a_{\ell_4 m_4} \rangle_c = \\ &= \sum_{LM} (-1)^M P^{\ell_1 \ell_2}_{\ell_3 \ell_4}(L) \begin{pmatrix} \ell_1 & \ell_2 & L \\ m_1 & m_2 & -M \end{pmatrix} \begin{pmatrix} \ell_3 & \ell_4 & L \\ m_3 & m_4 & M \end{pmatrix} + (\ell_2 \leftrightarrow \ell_3) + (\ell_2 \leftrightarrow \ell_4)\end{aligned} \tag{4.31}$$

The three unique pairings, (ℓ_1, ℓ_2), (ℓ_1, ℓ_3) and (ℓ_1, ℓ_4) yield alternate representations of the angular 4-point spectrum (4.28). Since each representation is constructed by adding angular momenta, according to the theory of angular momentum each representation is complete and thus they are not independent. In particular, the representations yielded by the pair (ℓ_1, ℓ_3) and (ℓ_1, ℓ_4) can be related to the one yielded by the pair (ℓ_1, ℓ_2) through Wigner 6-j symbols (see appendix B.4) via

$$Q^{\ell_1 \ell_3}_{\ell_2 \ell_4}(L) = \sum_{L'} (-1)^{\ell_1 + \ell_2} \begin{Bmatrix} \ell_1 & \ell_2 & L \\ \ell_3 & \ell_4 & L' \end{Bmatrix} Q^{\ell_1 \ell_2}_{\ell_3 \ell_4}(L') \tag{4.32}$$

$$Q^{\ell_1\ell_4}_{\ell_3\ell_2}(L) = \sum_{L'}(-1)^{L+L'} \begin{Bmatrix} \ell_1 & \ell_2 & L \\ \ell_3 & \ell_4 & L' \end{Bmatrix} Q^{\ell_1\ell_2}_{\ell_3\ell_4}(L') \tag{4.33}$$

Using the relations (4.32) and (4.33), one can therefore project the pairs (ℓ_1, ℓ_3) and (ℓ_1, ℓ_4) in equation (4.31) onto the (ℓ_1, ℓ_2) basis to give:

$$\begin{aligned} T^{\ell_1\ell_2}_{\ell_3\ell_4}(L) = P^{\ell_1\ell_2}_{\ell_3\ell_4}(L) + (2L+1)\sum_{L'}\Bigg[&(-1)^{\ell_2+\ell_3} \begin{Bmatrix} \ell_1 & \ell_2 & L \\ \ell_3 & \ell_4 & L' \end{Bmatrix} P^{\ell_1\ell_3}_{\ell_2\ell_4}(L') \\ &+ (-1)^{L+L'} \begin{Bmatrix} \ell_1 & \ell_2 & L \\ \ell_3 & \ell_4 & L' \end{Bmatrix} P^{\ell_1\ell_4}_{\ell_3\ell_2}(L')\Bigg] \end{aligned} \tag{4.34}$$

where with $T^{\ell_1\ell_2}_{\ell_3\ell_4}(L)$ we denote the connected part of the angular trispectrum, $Q^{\ell_1\ell_2}_{\ell_3\ell_4}(L)$. At this point, one notices that within each unique pair there are four possible permutations of the ordering, but that the quantity $P_{\ell_1\ell_2\ell_3\ell_4}(L)$ is not invariant under $\ell_1 \leftrightarrow \ell_2$ or $\ell_3 \leftrightarrow \ell_4$, since due to the properties of the Wigner 3-j symbol it instead satisfies

$$P^{\ell_1\ell_2}_{\ell_3\ell_4}(L) = (-1)^{\Sigma_U} P^{\ell_2\ell_1}_{\ell_3\ell_4}(L) = (-1)^{\Sigma_L} P^{\ell_1\ell_2}_{\ell_4\ell_3}(L) \tag{4.35}$$

with $\Sigma_U = \ell_1 + \ell_2 + L$ and $\Sigma_L = \ell_3 + \ell_4 + L$. To make it symmetric, one introduces the so-called *reduced trispectrum*, denoted by $\mathcal{T}$, such that $P^{\ell_1\ell_2}_{\ell_3\ell_4}(L)$ can written in the following form:

$$P^{\ell_1\ell_2}_{\ell_3\ell_4}(L) = \mathcal{T}^{\ell_1\ell_2}_{\ell_3\ell_4}(L) + (-1)^{\Sigma_U}\mathcal{T}^{\ell_2\ell_1}_{\ell_3\ell_4}(L) + (-1)^{\Sigma_L}\mathcal{T}^{\ell_1\ell_2}_{\ell_4\ell_3}(L) + (-1)^{\Sigma_U+\Sigma_L}\mathcal{T}^{\ell_2\ell_1}_{\ell_4\ell_3}(L) \tag{4.36}$$

The reduced trispectrum, $\mathcal{T}^{\ell_1\ell_2}_{\ell_3\ell_4}(L)$, is defined as arbitrary function of the angular trispectrum's arguments with the requirement of being invariant under the exchange of its lower and upper indices, that is:

$$\mathcal{T}^{\ell_1\ell_2}_{\ell_3\ell_4}(L) = \mathcal{T}^{\ell_3\ell_4}_{\ell_1\ell_2}(L) \tag{4.37}$$

Parity invariance is then finally enforced on $T^{\ell_1\ell_2}_{\ell_3\ell_4}(L)$ by simply requiring the reduced function to also obey

$$\mathcal{T}^{\ell_1\ell_2}_{\ell_3\ell_4}(L) = \mathcal{T}^{\ell_2\ell_1}_{\ell_4\ell_3}(L) \tag{4.38}$$

4.4 Some (Useful) Analytical Results for the CMB Trispectrum from Inflation

In this section we derive some analytical predictions for the CMB trispectrum from inflation that will come handy later on. Let us begin by computing the explicit expression for the connected part of the angular 4-point correlation function from primordial non-Gaussian initial conditions. Recalling the expression for the multipole moments $a_{\ell m}$ as a function of the primordial perturbation $\Phi(\mathbf{k})$ given by equation (4.17), we get that

$$\begin{aligned}
&\langle a_{\ell_1 m_1} a_{\ell_2 m_2} a_{\ell_3 m_3} a_{\ell_4 m_4} \rangle_c = \\
&= (4\pi)^4 (-i)^{\ell_1+\ell_2+\ell_3+\ell_4} \int \frac{d^3\mathbf{k}_1}{(2\pi)^3} \int \frac{d^3\mathbf{k}_2}{(2\pi)^3} \int \frac{d^3\mathbf{k}_3}{(2\pi)^3} \int \frac{d^3\mathbf{k}_4}{(2\pi)^3} g_{\ell_1}(k) g_{\ell_2}(k) g_{\ell_3}(k) g_{\ell_4}(k) \\
&\times Y^*_{\ell_1 m_1}(\hat{\mathbf{k}}_1) Y^*_{\ell_2 m_2}(\hat{\mathbf{k}}_2) Y^*_{\ell_3 m_3}(\hat{\mathbf{k}}_3) Y^*_{\ell_4 m_4}(\hat{\mathbf{k}}_4) \langle \Phi(\mathbf{k}_1)\Phi(\mathbf{k}_2)\Phi(\mathbf{k}_3)\Phi(\mathbf{k}_4) \rangle_c
\end{aligned} \tag{4.39}$$

In this context, as we shall prove in a moment, instead of using for the connected part of the Φ 4-point correlation function a similar definition to the one given by equation (4.9), it is much more useful to write:

$$\langle \Phi(\mathbf{k}_1)\Phi(\mathbf{k}_2)\Phi(\mathbf{k}_3)\Phi(\mathbf{k}_4) \rangle_c = (2\pi)^3 \int d^3\mathbf{K} \delta^{(3)}(\mathbf{k}_1+\mathbf{k}_2+\mathbf{K}) \delta^{(3)}(\mathbf{k}_3+\mathbf{k}_4-\mathbf{K}) T_\Phi(k_1, k_2, k_3, k_4; K) \tag{4.40}$$

Exploiting the definition (4.40), we get that the connected part of the angular 4-point correlation function relates to the primordial trispectrum via

$$\begin{aligned}
&\langle a_{\ell_1 m_1} a_{\ell_2 m_2} a_{\ell_3 m_3} a_{\ell_4 m_4} \rangle_c = \\
&= (4\pi)^4 (-i)^{\sum_{i=1}^4 \ell_i} \int \prod_{i=1}^4 \left(d^3\mathbf{k}_i g_{\ell_i}(k_i) Y^*_{\ell_i m_i}(\hat{\mathbf{k}}_i) \right) \\
&\times \int d^3\mathbf{K} \delta^{(3)}(\mathbf{k}_1 + \mathbf{k}_2 + \mathbf{K}) \delta^{(3)}(\mathbf{k}_3 + \mathbf{k}_4 - \mathbf{K}) T_\Phi(k_1, k_2, k_3, k_4; K)
\end{aligned} \tag{4.41}$$

Note that equation (4.40) tells us that the wavevectors $(\mathbf{k}_1, \mathbf{k}_2)$ and $\mathbf{K}$ and $(\mathbf{k}_3, \mathbf{k}_4)$ and $\mathbf{K}$ form two triangles in a quadrilateral of sides $\mathbf{k}_1, \mathbf{k}_2, \mathbf{k}_3, \mathbf{k}_4$, with $\mathbf{K}$ representing one of its diagonals (see Figure 4.5). It is however clear that triangles may be formed by using different combinations of the wavevectors. The usefulness of this definition therefore lies in making implicit the fact that the symmetries for exchange of $\Phi(\mathbf{k}_i)$ and $\Phi(\mathbf{k}_j)$ in the Φ 4-point correlation function are identical to the symmetries for exchange of fields in the CMB 4-point correlation function, thus implying that we can follow for the primordial trispectrum a similar

decomposition process to the one used in the previous section for the evaluation of the CMB angular trispectrum, that is we can write for T_Φ the following expression, which is explicitly symmetric under the exchanges $\mathbf{k}_2 \leftrightarrow \mathbf{k}_3$ and $\mathbf{k}_2 \leftrightarrow \mathbf{k}_4$ [68, 69]:

$$\begin{aligned} T_\Phi(k_1, k_2, k_3, k_4; K) = P_\Phi(k_1, k_2, k_3, k_4; K) + \\ + \int d^3\mathbf{K}' \Big[\delta^{(3)}(k_3 - k_2 - \mathbf{K} + \mathbf{K}') P_\Phi(k_1, k_3, k_2, k_4; K') \\ + \delta^{(3)}(k_4 - k_2 - \mathbf{K} + \mathbf{K}') P_\Phi(k_1, k_4, k_3, k_2; K') \Big] \end{aligned} \tag{4.42}$$

where the quantity P_Φ is constructed out of a *reduced* Φ*-trispectrum*, denoted by $\mathcal{T}_\Phi$, as follows:

$$\begin{aligned} P_\Phi(k_1, k_2, k_3, k_4; K) = \mathcal{T}_\Phi(k_1, k_2, k_3, k_4; K) + \mathcal{T}_\Phi(k_2, k_1, k_3, k_4; K) \\ + \mathcal{T}_\Phi(k_1, k_2, k_4, k_3; K) + \mathcal{T}_\Phi(k_2, k_1, k_4, k_3; K) \end{aligned} \tag{4.43}$$

Therefore, we are now going to do, is to compute the reduced trispectrum $\mathcal{T}^{\ell_1\ell_2}_{\ell_3\ell_4}(L)$, which can be obtained from the reduced Φ-trispectrum, $\mathcal{T}_\Phi$, by simply replacing T_Φ in the relation (4.41). It should be noted that it suffices to perform the calculation for one combination of multipoles ℓ_i, corresponding to a given combination of wavevectors $\mathbf{k}_i$, since all the other contributions to the CMB trispectrum can be simply obtained by permuting the symbols.

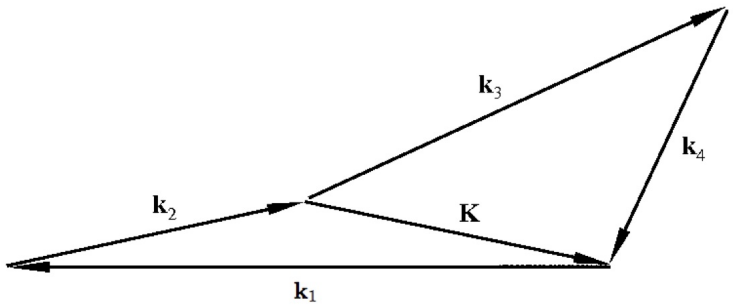

Figure 4.5. Quadrilateral defined by the four wavevectors $\mathbf{k}_i$, with $\mathbf{K}$ representing one of its diagonals. Figure adapted from [69].

To proceed with the calculation, we first of all expand the Dirac delta over spherical harmonics. Using the identities:

$$\begin{aligned}\delta^{(3)}(\mathbf{k}) &= \frac{1}{(2\pi)^3}\int d^3\mathbf{r} e^{i\mathbf{r}\cdot\mathbf{k}} \\ e^{i\mathbf{r}\cdot\mathbf{k}} &= 4\pi\sum_{\ell=0}^{\infty}\sum_{m=-\ell}^{\ell} i^\ell j_\ell(kx)Y^*_{\ell m}(\hat{\mathbf{k}})Y_{\ell m}(\hat{\mathbf{r}})\end{aligned} \tag{4.44}$$

we obtain the following representation for the Dirac delta

$$\delta^{(3)}(\mathbf{k}) = \frac{1}{2\pi^2}\int d^3\mathbf{r}\sum_{\ell=0}^{\infty}\sum_{m=-\ell}^{\ell} i^\ell j_\ell(kx)Y^*_{\ell m}(\hat{\mathbf{k}})Y_{\ell m}(\hat{\mathbf{r}}) \tag{4.45}$$

Therefore, using equation (4.45) and the following properties of the spherical harmonics:

$$\begin{aligned}Y^*_{\ell m}(\hat{\mathbf{n}}) &= (-1)^m Y_{\ell -m}(\hat{\mathbf{n}}) \\ \int d\hat{\mathbf{n}} Y^*_{\ell m}(\hat{\mathbf{n}})Y_{\ell' m'}(\hat{\mathbf{n}}) &= \delta_{\ell\ell'}\delta_{mm'} \\ \int d\hat{\mathbf{n}} Y_{\ell_1 m_1}(\hat{\mathbf{n}})Y_{\ell_2 m_2}(\hat{\mathbf{n}})Y_{\ell_3 m_3}(\hat{\mathbf{n}}) &= \sqrt{\frac{(2\ell_1+1)(2\ell_2+1)(2\ell_3+1)}{4\pi}} \\ &\times \begin{pmatrix}\ell_1 & \ell_2 & \ell_3\\ 0 & 0 & 0\end{pmatrix}\begin{pmatrix}\ell_1 & \ell_2 & \ell_3\\ m_1 & m_2 & m_3\end{pmatrix}\end{aligned} \tag{4.46}$$

we eventually get that equation (4.41) becomes

$$\begin{aligned}&\langle a_{\ell_1 m_1}a_{\ell_2 m_2}a_{\ell_3 m_3}a_{\ell_4 m_4}\rangle_c = \\ &= \left(\frac{2}{\pi}\right)^5\sum_{LM}(-1)^M\int dr_1 r_1^2\int dr_2 r_2^2\int dk_1 ...\int dk_4\int dK\,(k_1k_2k_3k_4K)^2\, j_L(Kr_1)j_L(Kr_2) \\ &\times\left[j_{\ell_1}(k_1r_1)g_{\ell_1}(k_1)\right]\left[j_{\ell_2}(k_2r_1)g_{\ell_2}(k_2)\right]\left[j_{\ell_3}(k_3r_2)g_{\ell_3}(k_3)\right]\left[j_{\ell_4}(k_4r_2)g_{\ell_4}(k_4)\right] \\ &\times\begin{pmatrix}\ell_1 & \ell_2 & L\\ m_1 & m_2 & -M\end{pmatrix}\begin{pmatrix}\ell_3 & \ell_4 & L\\ m_3 & m_4 & M\end{pmatrix}\mathcal{T}_\Phi(k_1,k_2,k_3,k_4;K)h_{\ell_1\ell_2 L}h_{\ell_3\ell_4 L}\end{aligned} \tag{4.47}$$

where we defined

$$h_{\ell_1\ell_2\ell_3} \equiv \sqrt{\frac{(2\ell_1+1)(2\ell_2+1)(2\ell_3+1)}{4\pi}} \begin{pmatrix} \ell_1 & \ell_2 & \ell_3 \\ 0 & 0 & 0 \end{pmatrix} \tag{4.48}$$

Remembering now equation (4.31), we get that

$$\begin{aligned} \mathcal{T}^{\ell_1\ell_2}_{\ell_3\ell_4}(L) = \left(\frac{2}{\pi}\right)^5 \int dr_1 r_1^2 \int dr_2 r_2^2 \int dk_1 ... \int dk_4 \int dK \, (k_1k_2k_3k_4K)^2 \, j_L(Kr_1) j_L(Kr_2) \\ \times \left[j_{\ell_1}(k_1r_1) g_{\ell_1}(k_1)\right] \left[j_{\ell_2}(k_2r_1) g_{\ell_2}(k_2)\right] \left[j_{\ell_3}(k_3r_2) g_{\ell_3}(k_3)\right] \left[j_{\ell_4}(k_4r_2) g_{\ell_4}(k_4)\right] \times \\ \times \mathcal{T}_\Phi(k_1, k_2, k_3, k_4; K) h_{\ell_1\ell_2 L} h_{\ell_3\ell_4 L} \end{aligned} \tag{4.49}$$

This is a very general result, which holds true for any given model of non-Gaussianity. For example, let us consider the simple case of the local non-gaussian initial conditions as given by equation (4.11), that is:

$$\Phi_{\rm NG}(\mathbf{x}) = \Phi_{\rm L}(\mathbf{x}) + f^{\rm local}_{\rm NL} \left(\Phi^2_{\rm L}(\mathbf{x}) - \langle \Phi^2_{\rm L}(\mathbf{x}) \rangle\right) + g^{\rm local}_{\rm NL} \Phi^3_{\rm L}(\mathbf{x}) \tag{4.50}$$

Going to Fourier space, we can decompose $\Phi_{\rm NG}(\mathbf{x})$ into a linear and a nonlinear part, so that

$$\Phi_{\rm NG}(\mathbf{k}) = \Phi_{\rm L}(\mathbf{k}) + \Phi_{\rm NL}(\mathbf{k}) \tag{4.51}$$

where the nonlinear curvature perturbation $\Phi_{\rm NL}(\mathbf{k})$ is defined by

$$\begin{aligned} \Phi_{\rm NL}(\mathbf{k}) &\equiv \Phi_A(\mathbf{k}) + \Phi_B(\mathbf{k}) \\ &= f^{\rm local}_{\rm NL} \left[\int \frac{d^3\mathbf{p}}{(2\pi)^3} \Phi_{\rm L}(\mathbf{k}+\mathbf{p}) \Phi^*_{\rm L}(\mathbf{p}) - (2\pi)^3 \delta^{(3)}(\mathbf{k}) \langle \Phi^2_{\rm L}(\mathbf{x}) \rangle \right] \\ &+ g^{\rm local}_{\rm NL} \int \frac{d^3\mathbf{p}_1}{(2\pi)^3} \frac{d^3\mathbf{p}_2}{(2\pi)^3} \Phi^*_{\rm L}(\mathbf{p}_1) \Phi^*_{\rm L}(\mathbf{p}_2) \Phi_{\rm L}(\mathbf{p}_1 + \mathbf{p}_2 + \mathbf{k}) \end{aligned} \tag{4.52}$$

where

$$\langle \Phi^2_{\rm L}(\mathbf{x}) \rangle = \int \frac{d^3\mathbf{k}}{(2\pi)^3} P_\Phi(k) \tag{4.53}$$

The connected part of the Φ 4-point correlation function receives leading order contributions of the form $\langle \Phi_A(\mathbf{k}_1) \Phi_A(\mathbf{k}_2) \Phi_L(\mathbf{k}_3) \Phi_L(\mathbf{k}_4) \rangle$ and $\langle \Phi_B(\mathbf{k}_1) \Phi_L(\mathbf{k}_2) \Phi_L(\mathbf{k}_3) \Phi_L(\mathbf{k}_4) \rangle$, which give,

respectively, the following leading order contributions to the reduced Φ-trispectrum [68, 69]:

$$\mathcal{T}_{\Phi,A}(k_1,k_2,k_3,k_4;K) = \left(2f_{\rm NL}^{\rm local}\right)^2 P_\Phi(K)P_\Phi(k_1)P_\Phi(k_3) = \frac{25}{9}\tau_{\rm NL}P_\Phi(K)P_\Phi(k_1)P_\Phi(k_3) \tag{4.54}$$

$$\mathcal{T}_{\Phi,B}(k_1,k_2,k_3,k_4;K) = g_{\rm NL}^{\rm local}\left[P_\Phi(k_2)P_\Phi(k_3)P_\Phi(k_4) + P_\Phi(k_1)P_\Phi(k_2)P_\Phi(k_4)\right] \tag{4.55}$$

Substituting the expressions (4.54) and (4.55) into equation (4.49), we get that the reduced CMB trispectrum is given by

$$\mathcal{T}^{\ell_1\ell_2}_{\ell_3\ell_4}(L) = \mathcal{T}_{\rm A}{}^{\ell_1\ell_2}_{\ell_3\ell_4}(L) + \mathcal{T}_{\rm B}{}^{\ell_1\ell_2}_{\ell_3\ell_4}(L) \tag{4.56}$$

with

$$\begin{aligned}
\mathcal{T}_{\rm A}{}^{\ell_1\ell_2}_{\ell_3\ell_4}(L) &= \frac{25}{9}\tau_{\rm NL}\int dr_1 dr_2 r_1^2 r_2^2 F_L(r_1,r_2)\alpha_{\ell_1}(r_1)\beta_{\ell_2}(r_1)\alpha_{\ell_3}(r_2)\beta_{\ell_4}(r_2)h_{\ell_1\ell_2 L}h_{\ell_3\ell_4 L} \\
\mathcal{T}_{\rm B}{}^{\ell_1\ell_2}_{\ell_3\ell_4}(L) &= g_{\rm NL}^{\rm local}\int dr r^2 \beta_{\ell_2}(r)\beta_{\ell_4}(r)\left[\alpha_{\ell_1}(r)\beta_{\ell_3}(r) + \alpha_{\ell_3}(r)\beta_{\ell_1}(r)\right]h_{\ell_1\ell_2 L}h_{\ell_3\ell_4 L}
\end{aligned} \tag{4.57}$$

where

$$\begin{aligned}
F_L(r_1,r_2) &= \frac{2}{\pi}\int dK K^2 P_\Phi(K) j_L(Kr_1)j_L(Kr_2) \\
\alpha_\ell(r) &= \frac{2}{\pi}\int dk k^2 g_\ell(k) j_\ell(kr) \\
\beta_\ell(r) &= \frac{2}{\pi}\int dk k^2 P_\Phi(k) g_\ell(k) j_\ell(kr)
\end{aligned} \tag{4.58}$$

To compute the coefficients $\alpha_\ell(r)$ and $\beta_\ell(r)$ we would need the explicit expressions for the primordial power spectrum $P_\Phi(k)$ and the CMB radiation transfer function $g_\ell(k)$. The computation of both is usually carried out numerically with Boltzmann solvers i.e. codes which solve the system of Boltzmann equations describing the evolution of the perturbations once they re-enter the horizon during the post-inflationary epoch, such as `CAMB` [70] or `CLASS` [71]. Notice that the calculations we just carried out for the case of local non-Gaussian initial conditions as given by equation (4.11) can be easily generalised to the case of running non-Gaussianity: that is, one can prove by similar calculations that the reduced CMB trispectrum can still be written in the form of equation (4.57), with the only difference being in the definition of the $\alpha_\ell(r)$ and/or $\beta_\ell(r)$ coefficients, that get modified to include the scale-dependence of the non-linearity parameters.

4.5 Constraints on Primordial Non-Gaussianity

Planck's measurements of the CMB temperature and E-mode polarisation anisotropies currently provide the most robust constraints on some of most well-known and studied types of primordial non-Gaussianity. It should be noted, however, that in addition to the analysis of the standard local, equilateral, and orthogonal shapes, the *Planck* collaboration analyses also a large number of additional cases, such as scale-dependent feature and resonance bispectra, running $f_{\rm NL}$ models, isocurvature primordial Non-Gaussianity and parity-breaking models [72]. Combining estimates obtained from different bispectrum estimators, the latest *Planck*'s data release provides the following constraints on the local, equilateral and orthogonal bispectrum amplitudes (at the 68% CL) [72]:

$$\begin{aligned} f_{\rm NL}^{\rm local} &= -0.9 \pm 5.1 \\ f_{\rm NL}^{\rm equil} &= -26 \pm 47 \\ f_{\rm NL}^{\rm ortho} &= -38 \pm 24 \end{aligned} \tag{4.59}$$

In [72], making use of the data analysis framework developed by Smith et al. in [73], the *Planck* collaboration also provides updated constraints on different trispectrum shapes. In particular, they provide the following constraint on the local $g_{\rm NL}$-trispectrum amplitude:

$$g_{\rm NL}^{\rm local} = (-5.8 \pm 6.5) \times 10^4 \quad (68\%\ \text{CL}) \tag{4.60}$$

Until recently, the best empirical constraint on the primordial $\tau_{\rm NL}$-trispectrum amplitude came instead from the *Planck* 2013 nominal-mission temperature data. In particular, it was obtained for the collapsed shape [74]:

$$\tau_{\rm NL} < 2.8 \times 10^3 \quad (95\%\ \text{CL}) \tag{4.61}$$

Using the latest *Planck* mission temperature and polarisation data, in [75] Marzouk et al. updated this constraint, finding a significantly tightened one:

$$\tau_{\rm NL} < 1700 \quad (95\%\ \text{CL}) \tag{4.62}$$

Note that since in general local-type non-Gaussianity is most easily understood as a large-scale modulation of small-scale power on the CMB sky, both results were not obtained from a 4-point correlation function estimator but making use of statistical anisotropy estimators (see e.g. [76]).

Chapter 5

Cosmic Microwave Background Anomalies

As we have seen in the Chapter 3, from both WMAP and *Planck* full-sky measurements it has emerged enticing evidence of some features at the largest angular scales that seem to suggest a deviation from the fundamental assumptions of homogeneity and isotropy of our Universe. In this Chapter we are going to explore some of these CMB large-scale anomalies, providing a description of each of them, along with evidence and methods of detection. In particular we are going to discuss:

1. the lack of large-angle correlations;
2. the hemispherical power asymmetry;
3. the alignment of low multipole moments;
4. the point-parity asymmetry;
5. the cold spot.

To quantify any observed departure from the underlying theory, the first step consists in choosing an observable that will serve as indicator of the anomaly. The statistical significance of the anomaly is quantified in terms of the so-called p-value. In statistics, given a null hypothesis (in this case the ΛCDM model), the p-value is defined as the probability with which a certain phenomenon can occur (see Figure 5.1). The smaller the p-value, the greater the statistical significance, since a small p-value tells us that the null hypothesis should be ruled out. The *Planck* collaboration computed the p-values of the chosen observables from the simulation of a large number of random realisations of the CMB temperature map from the probability distribution of the ΛCDM model, so that, for example, if only five simulations out of a thousand lead to a value of the observable which is at least as extreme as the observed value, they would report a p-value of 0.5% for that observation. However, note that since there are many tests that can be performed on the data to assess a violation of statistical isotropy, there is an high probability of finding some spurious signals with a seemingly high significance. This is because even a statistically isotropic CMB sky is a realisation of an underlying statistical process corresponding to many independent random variables. Therefore, when assessing the statistical significance of an anomaly, in order to avoid claiming a false

detection, one needs to take into account also this issue, which is referred to by particle physicists as the "look else-where" effect (LEE).

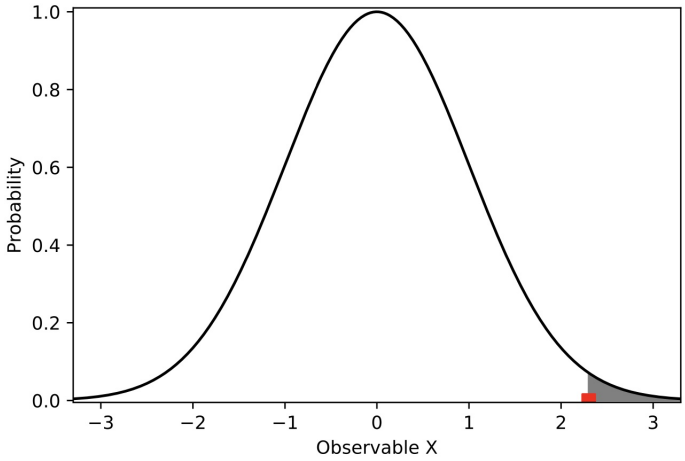

Figure 5.1. An illustration of the concept of p-value. The figure shows the probability distribution of a certain observable X according to the null hypothesis (in black). The value of X actually observed is shown in red. The grey shaded area is the p-value of the observed value of X. Figure adapted from [77].

5.1 Lack of Large-Angle Correlations

Suppressed correlations at the largest observed angular scales, in contrast to what is predicted in the ΛCDM model, were first noticed in the COBE data [78]. Later, both WMAP and *Planck* data confirmed that the 2-point angular correlation function

$$C(\theta) = \langle \Theta(\hat{\mathbf{n}}_1)\Theta(\hat{\mathbf{n}}_2)\rangle \tag{5.1}$$

where the average is over all pairs of pixels with $\hat{\mathbf{n}}_1 \cdot \hat{\mathbf{n}}_2 = \cos\theta$, is very close to zero on scales above $\sim 60°$. Figure 5.2 shows the 2-point correlation function from *Planck* 2013 data, computed in pixel space, for the full-sky and with two masks. The most striking feature of the cut-sky $C(\theta)$ is that all of them are nearly zero for scales above $\sim 60°$, except for some anti-correlation for 180°. This is also true for the full- sky curve, even though less so. To be more quantitative about these observations, in their first year data, the WMAP team [79] introduced the $S_{1/2}$ statistic, which measures the deviation of the 2-point correlation function from zero:

$$S_{1/2} = \int_{-1}^{1/2} [C(\theta)]^2 \, d\,(\cos\theta) \tag{5.2}$$

Depending on the details of the analysis, p-values consistently below 0.5% have been obtained, some even below 0.01%.

The *Planck* team, in their latest results release [44], extended the analysis also to polarisation data, considering the statistic proposed by Copi et al. [80]:

$$S^{XY}(\theta_1, \theta_2) = \int_{\cos\theta_2}^{\cos\theta_1} \left[C^{XY}(\theta)\right]^2 d(\cos\theta) \tag{5.3}$$

where X, Y can denote either the temperature T or the two Stokes parameters U, Q and $C^{XY}(\theta)$ is the corresponding 2-point correlation function. Note that this statistic is a generalisation of the $S_{1/2}$ statistic computed from the temperature correlation function where the considered limits of the separation angle range are $\theta_1 = 60°$ and $\theta_2 = 180°$.

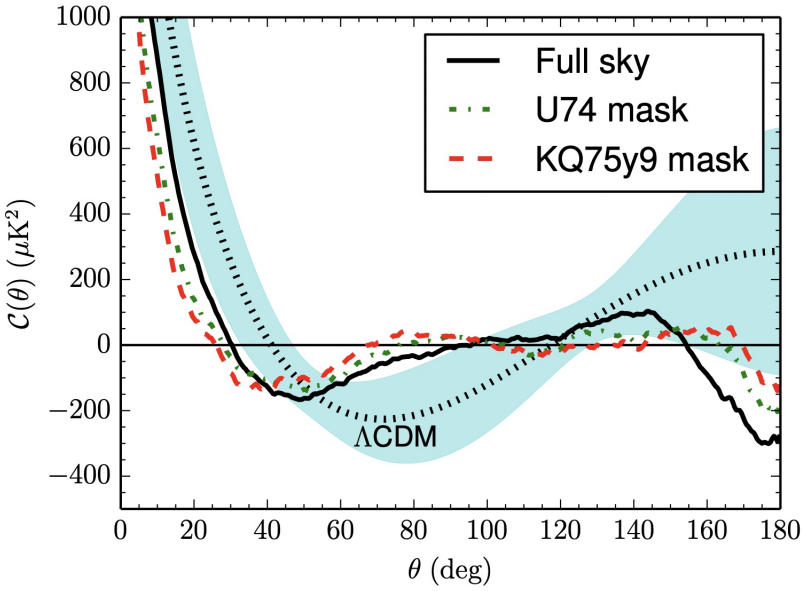

Figure 5.2. 2-point correlation function from *Planck*'s 2013 `SMICA` map, adapted from [39]. The black dotted line represents the best-fitting ΛCDM model. The shaded, cyan region is the 68% cosmic variance confidence interval. Included from the `SMICA` map are the $C(\theta)$ calculated on the full-sky (the black, solid line) and from two cut skies using the U74 mask (the green, dash-dotted line) and the KQ75y9 mask (the red, dashed line).

The values for the $S^{TT}_{1/2}$ statistic for the *Planck* 2018 data with resolution $N_{\text{side}} = 64$ show a lack of correlation on large angular scales with a significance consistent with the one found by Copi et al. for the *Planck* 2015 data [39]. The p-values for the temperature maps are found to be slightly larger than those determined from the 2015 data set, but this can be caused either by changes in the masks or systematic effects in the simulations. The results for the CMB maps estimated using the component separation methods `Commander`, `SMICA`, `NILC` and `SEVEM`, are presented in Table 5.1. Note that the sense of the p-value differs from the one reported in [39].

Table 5.1. Values for the $S^{TT}_{1/2}$ statistic for the *Planck* 2018 data and the associated probabilities of obtaining values for the *Planck* fiducial ΛCDM model at least as large of the ones observed.

Map	$S^{TT}_{1/2}[\mu K^4]$	probability [%]
Planck `Comm.`	1209.2	> 99.9
Planck `SMICA`	1142.4	> 99.9
Planck `NILC`	1156.6	> 99.9
Planck `SEVEM`	1146.2	> 99.9

Since a possible explanation for the lack of correlation in the temperature maps is that is due to the small observed value of the quadrupole, the analysis for the $S^{TT}_{1/2}$ statistic was then repeated after removing the best-fit quadrupole from the temperature maps. The corresponding probabilities, presented in Table 5.2, indicate that the low power in the quadrupole does contribute to the lack of large-angle correlations. However, Copi et al. [81] observe that the lack of correlations cannot be explained by a lack of quadrupole power alone. All modes below $\ell \leqslant 5$ contribute to this, by combining to cancel with each other and with higher order modes.

Table 5.2. Probabilities of obtaining values for the $S^{TT}_{1/2}$ statistic for the *Planck* fiducial ΛCDM model at least as large of the ones observed after removing the best-fit quadrupole from the temperature maps.

Map	probability [%]
Planck `Comm.`	96.0
Planck `SMICA`	96.2
Planck `NILC`	96.1
Planck `SEVEM`	96.1

Copi et al. [80] also pointed out that the cross-correlation between temperature and polarisation data can be used to determine wether or not the lack of large-angle correlations is due to a statistical fluke of the ΛCDM cosmology. Specifically, assuming the statistical fluke hypothesis to be true, given that the temperature and polarisation signal are partially correlated the S^{TQ} statistic would also likely be small on large angular scales. Copi et al. [80] have determined that in 99% of their constrained realisations based on the properties of the WMAP seven-year data, assuming the statistical fluke hypothesis to be true, $S^{TQ}(48°, 120°) \leqslant 1.403\mu K^4$. Therefore a value of the measured statistic exceeding this limit would allow the fluke hypothesis to be ruled out. The values for this statistic for the *Planck* 2018 data and their corresponding p-values are presented in Table 5.3. These results are significantly smaller and thus the statistical fluke hypothesis cannot be ruled out. We conclude our discussion on the lack of large-angle correlations with an important remark. A point that is widely overlooked is that, as reported in [39], the 2-point angular correlation function $C(\theta)$ as discussed above is actually the dipole and monopole subtracted 2-point angular correlation function, $C_{\ell \geqslant 2}(\theta)$. A physical explanation for the smallness of $S_{1/2}$ is likely to predict that $C(\theta)$ is small, not just $C_{\ell \geqslant 2}(\theta)$. However, a cosmological (i.e. non-Doppler) dipole of the size predicted in the best-fit ΛCDM model would completely dominate $S_{1/2}$. Therefore in order to have a small $C(\theta)$, it is required

a constraint on the cosmological contribution $C_1 \lesssim 200\mu K^2 \ll \langle C_1^{\Lambda\mathrm{CDM}} \rangle \simeq 3300\mu K^2$. Since this happens less than 0.5% of the time in the ΛCDM model with standard cosmological parameters, if a low C_1 were observed, that would indeed be compelling evidence of a physical origin for the small value of the $S_{1/2}$ statistic.

Table 5.3. Values for the $S^{TQ}(48°, 120°)$ statistic for the *Planck* 2018 data and the associated probabilities of obtaining values for the *Planck* fiducial ΛCDM model at least as large of the ones observed.

Map	$S^{TQ}(48°, 120°)[\mu K^4]$	probability [%]
Planck `Comm.`	0.20	83.3
Planck `SMICA`	0.07	97.0
Planck `NILC`	0.11	93.3
Planck `SEVEM`	0.26	82.9

5.2 Hemispherical Power Asymmetry

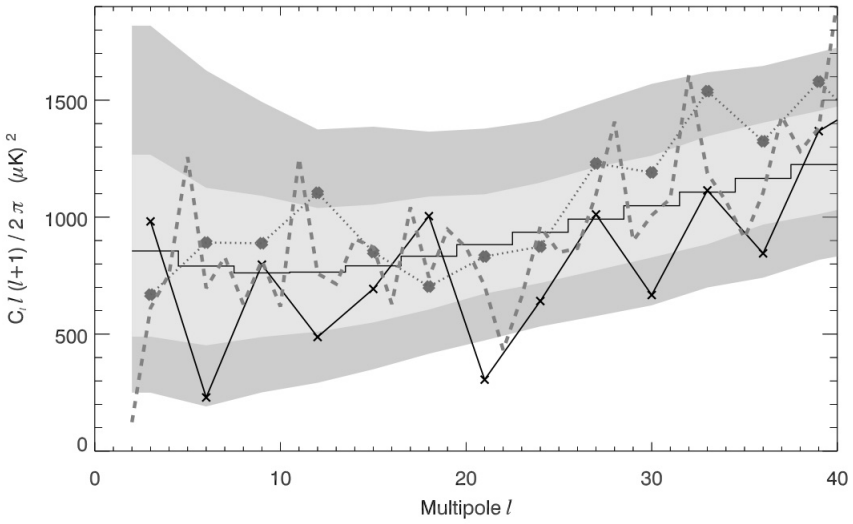

Figure 5.3. Original evidence for the hemispherical power asymmetry, adapted from [82]. The three jagged lines show the binned angular power spectrum computed over the all unmasked sky (dashed line), the northern hemisphere (solid line) and the southern hemisphere (dotted line). Northern and southern hemisphere are defined with respect to the best-fit axis for the WMAP first year data. The histogram and the two grey areas around it denote the mean and the 68% and 95% confidence regions from Gaussian random simulations.

Evidence for an hemispherical power asymmetry emerged in the analysis of WMAP first year data [83, 82]. It was found that the angular power spectrum, when estimated locally at different positions on the sphere, appears not to be isotropic (see Figure 5.3). In particular, the power spectrum calculated for the hemisphere centred at galactic coordinates $(l, b) = (273°, -20°)$ was larger than the one calculated in the opposite hemisphere over the multipole range

$\ell = 2 - 40$, with the axis of maximum asymmetry found to lie close to the ecliptic plane. Eriksen et. al [82] confirmed the asymmetry extending the analysis also to the computation of N-point correlation functions for the northern and southern ecliptic hemispheres, finding that they give indeed different results. In [82] and in subsequent analysis the agreement of the correlation functions of the CMB estimates with the fiducial cosmological model was quantified using a simple χ^2 statistic. Considering that the χ^2 statistic in itself can act as a measure of the fluctuation level, the degree of asymmetry between the two hemispheres was then quantified by a parameter defined as the ratio of the two χ^2 values. In 2013 [42], the *Planck* collaboration repeated this analysis by computing four N-point correlation functions on the northern and southern ecliptic hemispheres for the *Planck* 2013 temperature maps with resolution $N_{\rm side} = 64$, finding results in agreement with those of Eriksen et al. [82]. In particular it was shown that the p-values for the χ^2 statistic for the 3-point and 4-point correlation functions in the northern hemisphere were especially large, with a significance $> 99\%$, exceeding 99.9% for the pseudo-collapse 3-point one. The *Planck* 2015 analysis [43] confirmed these high levels of significance, specifically observing that "the northern hemisphere correlation functions are relatively featureless (both the 3- and 4-point functions lie very close to zero), whereas the southern hemisphere functions exhibit a level of structure consistent with Gaussian simulations". Surprisingly, in their 2018 analysis, the *Planck* collaboration no longer observed the high significance level for the pseudo-collapse 3-point function for the temperature map in the northern hemisphere, as reported in the 2013 and 2015 *Planck* data sets [42, 43]. The *Planck* collaboration states that this discrepancy "may be a consequence of the use of different masks in the various analyses, or of the improved treatment of poorly determined modes in the estimated correlation matrix used for the computation of the χ^2 statistic". However, the fact that the anomaly was consistently observed in both the WMAP data and the two previous *Planck* data releases, strongly suggests that the changes in the mask or the improvement in the analysis might have removed important information in the data, that would instead significantly contribute to the anomaly.

5.2.1 Dipole Modulation and Directionality

A phenomenological model for the hemispherical power asymmetry has been proposed by Gordon et al. [84]. The asymmetry is modeled in terms of a dipole modulation of the temperature field as follows:

$$\Theta(\hat{\mathbf{n}}) = [1 + A\,(\hat{\mathbf{n}} \cdot \hat{\mathbf{p}})]\,\Theta_0(\hat{\mathbf{n}}) \tag{5.4}$$

where $\Theta(\hat{\mathbf{n}})$ and $\Theta_0(\hat{\mathbf{n}})$ are, respectively, the modulated and unmodulated (isotropic) CMB temperature fluctuations, $\hat{\mathbf{n}}$ is an arbitrary direction in the sky and A and $\hat{\mathbf{p}}$ are the dipolar modulation amplitude and direction of maximum asymmetry. This phenomenological model has been tested with both WMAP [85, 86] and *Planck* data [42, 43, 44]. In particular, to assess the level of dipole asymmetry in the CMB sky different analyses relying on different estimators

have been performed. The use of different estimators is crucial, since they are sensitive to different systematics effects and their use allow to probe different regions of parameter space, thus reducing the impact of the *a posteriori* correction.

Pixel-based and QML Likelihood Analyses

A pixel-space likelihood analysis has been performed on the WMAP 3-year [85] and 5-year data [86]. The *Planck* collaboration, in their 2013 [42] and 2015 [43] data releases, performed a similar analysis, considering only large angular scales. The results were found to be all consistent, thus demonstrating also robustness between experiments. In particular, the result for *Planck* 2015 release, using the `Commander` map with resolution $N_{\rm side} = 32$, was $A = 0.066 \pm 0.021$ with $\hat{\mathbf{p}}$ pointing in the direction $(l, b) = (230°, -16°) \pm 24°$. In their 2015 [43] and 2018 [44] releases, the *Planck* collaboration performed also an harmonic-space analysis, using the quadratic maximum likelihood (QML) estimator introduced by Moss et. al [87]. It should be stressed that the QML analysis in multipole space was purely a phenomenological one, with no attempt to connect to any real-space modulation. The technique exploits the fact that the dipole modulation of any cosmological parameter is equivalent to the coupling of ℓ to $\ell \pm 1$ modes in the CMB covariance matrix at leading order. In particular, a scale-invariant modulation from $\ell_{\rm min} = 2$ to a variable maximum multipole $\ell_{\rm max}$ was considered. In the 2015 release, it was observed that the obtained p-values of the fitted modulation amplitude as a function of $\ell_{\rm max}$ for the temperature data showed several peaks, at $\ell_{\rm max} \approx 40$, $\ell_{\rm max} \approx 67$ and $\ell_{\rm max} \approx 240$. The dip at $\ell_{\rm max} \approx 67$, with a p-value $0.9 - 1.0\%$, corresponds to the low-ℓ dipole modulation that has been the focus of most attention in the literature. In 2018 the *Planck* collaboration extended this analysis also to polarisation data, with the temperature data results found to be consistent with previous analyses. The polarisation data results showed a mildly significant asymmetry at $\ell \approx 250$, appearing featureless elsewhere, and seem consistent with statistical isotropy. The results for the amplitude and direction for the low-ℓ dipole-asymmetry signal from the QML analysis for the range $\ell = 2 - 64$ were found consistent between the 2015 and 2018 releases (see Table 5.4).

Table 5.4. Amplitude and direction for the low-ℓ dipole-asymmetry signal from the QML analysis for the range $\ell = 2 - 64$ for *Planck* 2015 and 2018, using the `Commander` temperature maps.

Map	Amplitude	Direction (l, b) [deg]
Planck 2015	$0.063^{+0.025}_{-0.013}$	$(213, -26) \pm 28$
Planck 2018	$0.070^{+0.032}_{-0.015}$	$(221, -22) \pm 31$

Angular Clustering of the Power Distribution

In their analysis of the 5-year WMAP data, Hansen et. al [88] searched for a dipolar power asymmetry performing a simple test in which the power spectrum was computed on a number of discs of various sizes and binned into independent blocks of 100 multipoles, from

$\ell = 2$ to $\ell = 600$. Each block was then used to look for a dipolar asymmetry in the power distribution. The six ℓ ranges considered showed evidence of a consistent dipole direction. This procedure, however, was highly CPU-intensive and thus their 2013 data release [42], the *Planck* collaboration chose to perform a similar test, following the modified approach developed by Axelsson et al. [89] as applied to the 9-year WMAP data. The power spectrum amplitude was estimated on 12 non-overlapping patches of the sky in ℓ-bins of 16 multipoles each, then each block was fitted for a dipolar asymmetry in the power distribution. In particular, the alignment of the dipole directions between the different multipole blocks was used to construct a measure of the power spectrum asymmetry. The significance of the asymmetry was then assessed comparing the clustering of the dipole directions evaluated for the different scales to that observed in simulated maps. They found that the dipole directions at high and low multipoles are strongly correlated up to $\ell \approx 600$, with weakening significance for $\ell > 500$. They also showed that the ratio of the power spectra computed in the two opposite hemispheres defined by the asymmetry axis for $\ell = 2 - 600$ was not statistically anomalous. This same analysis was performed in the *Planck* 2015 data release [43], considering bin sizes between $\Delta\ell = 8$ and $\Delta\ell = 32$ for the multipole range $\ell = 2 - 1500$. In agreement with the results in [42], a large degree of alignment was seen at least up to $\ell_{\rm max} \approx 600$. However, in contrast to the earlier results, the p-values were found to remain low for $\ell_{\rm max} > 750$. Specifically, depending on the bin size and component separation method, they found p-values as low as $< 0.04\%$. Thus, both the 2013 and 2015 results suggest that, beyond a dipole modulation of power on large angular scales, some form of directional asymmetry continues on small scales, and seem to indicate that the directions of dipolar asymmetry are correlated between large and small scales. Since the nature of the asymmetry is unknown, the *Planck* collaboration performed also a Rayleigh statistic (RS) based analysis as a generic test for directionality. An asymmetry was found on scales larger than $\ell_{\rm max} \approx 240$, and the minimum p-value obtained by the data was $0.1 - 0.2\%$, to be compared with the $0.9 - 1.0\%$ obtained for the dipole modulation amplitude at $\ell_{\rm max} \approx 67$. The preferred direction for $\ell_{\rm max} \approx 240$ was found to be $(l, b) = (208°, -29°)$, approximately 20° away from the dipole modulation direction determined by the QML analysis for the multipole range $\ell = 2 - 64$ (see Table 5.4). In the 2018 data release, the *Planck* collaboration extended the analysis also to polarisation data, adopting the same approach for the estimation of the dipole alignment as applied in their 2015 data release [43]. The results for the significance of the temperature alignment as a function of $\ell_{\rm max}$ was found to be consistent with previous analyses up to $\ell_{\rm max} \approx 1000$, with p-values below 1% for all multipoles. The results for the EE polarisation signal seems to indicate the presence of some alignment, beginning at $\ell_{\rm max} \approx 150$, reaching a p-value below 1% and extending up to $\ell_{\rm max} \approx 250$, corresponding to the multipole range where the alignment in temperature also starts to be seen. Furthermore, it was observed that not only the EE and TT dipoles clustered among themselves, but they also appear to be clustered towards the same direction.

Variance Asymmetry

An alternative method for the searching of a dipolar power asymmetry was proposed by Akrami et al. [90], who applied a pixel-space local variance estimator to WMAP 9-year and *Planck* 2013 temperature data. This approach was motivated by its conceptual and implementational simplicity, its directly intuitive interpretation and by the fact that, being defined in pixel space, it provides useful complementarity to other harmonic-based methods. In particular, they measured the local variance of the CMB temperature fluctuations over patches of various sizes and position on the sky. Then, they compared the measured values with the ones obtained from statistically isotropic simulations. For the 2013 *Planck* temperature maps, they found that none of the 1000 available simulations had a larger variance than that estimated from the data. This suggested the presence of an asymmetry at a significance of at least 3.3σ, with a preferred direction $(l, b) = (212°, -13°)$, in good qualitative agreement with other studies. This method was also adopted by the *Planck* collaboration and applied to the 2015 [43] and 2018 [44] temperature maps analyses. In the 2015 analysis it was applied to the full-resolution ($N_{\rm side} = 2048$) temperature maps, finding significantly low p-values, although the significance levels and preferred directions showed slight differences for different disc radii. The highest significance was found for 8° discs, with p-values less than 0.1%. In 2018 the method was applied to both the full and low-resolution ($N_{\rm side} = 64$) temperature maps, extending the analysis also to the scalar E-mode polarisation data. The results for the full-resolution temperature maps were found to be consistent with that of the 2015 analysis. An overall lower level of significance, compared to the one of full-resolution maps, was instead found for the low-resolution ones, with the smallest p-values obtained for the 4° discs. The results obtained from the application of the local variance analysis to the low-resolution E-mode polarisation maps when 4° discs are used are presented in Table 5.5. The preferred directions for the E-mode polarisation data, as shown in Figure 5.4, are found to be intriguingly close to those determined for the temperature data.

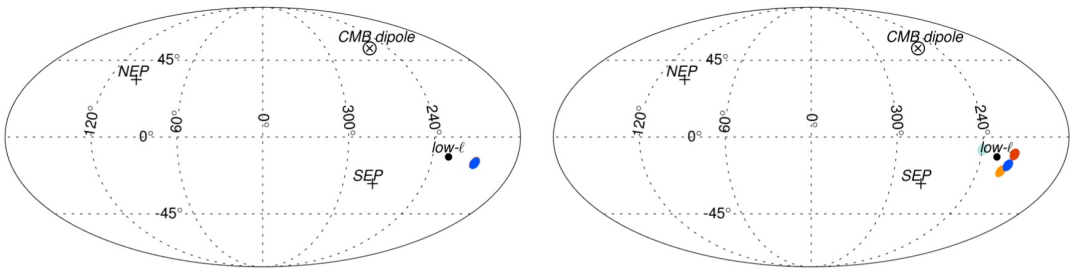

Figure 5.4. Local-variance dipole directions for the low-resolution *Planck* 2018 component-separation temperature (left) and E-polarisation (right) maps `Commander` (red), `NILC` (orange), `SEVEM` (green) and `SMICA` (blue), when 4° discs are used. For reference, the north ecliptic pole (NEP), the south ecliptic pole (SEP) and the preferred dipole modulation axis (labelled as *low-ℓ*) derived from the temperature data through the QML analysis are shown. Figure adapted from [44].

Table 5.5. Local-variance dipole directions and p-values for the variance asymmetry of the four component-separated *Planck* 2018 E-mode polarisation maps with resolution $N_{\rm side} = 64$ when 4° discs are used.

Map	p-value [%]	Direction (l, b) [deg]
Planck `Comm.`	0.7	$(217, -10)$
Planck `SMICA`	5.5	$(219, -19)$
Planck `NILC`	5.8	$(219, -16)$
Planck `SEVEM`	0.4	$(240, -7)$

Peak Distribution Asymmetry

Localised anomalies in the CMB sky can be searched for by testing how the statistical properties of local extrema (or peaks) would vary in patches of the sky as a function of their location. It is indeed expected for the asymmetry measured by the QML estimator to be mirrored by a slight difference in the temperature and polarisation peak distributions in the corresponding positive and negative hemispheres. The peak distributions were therefore analysed by the *Planck* collaboration in both their 2015 [43] and 2018 [44] data releases. In the 2015 analysis, the temperature peaks were selected using a disc of radius 70° centred at $(l, b) = (225°, -18°)$ (corresponding to the dipole modulation found in the `SMICA` temperature map) and its corresponding antipodal disc. For maps filtered with a 40' FWHM GAUSS filter the distribution of the peaks for the positive-direction disc was found in general agreement with the full sky results, while that for the negative-direction was marginally different. In 2018, the same analysis was performed, extending it also to polarisation data. For a 600' filtering scale a marginal difference between the data and the simulations was observed in the negative-direction, consistently with the one observed for the temperature data in the 2015 analysis.

5.2.2 Low Variance in the Northern Hemisphere

A low value for CMB variance was first observed in WMAP data [91]. Since variance is nothing but a weighted sum of the angular power spectrum of the fluctuations over all the multipoles, this feature can be regarded as an indirect signature of a power asymmetry. The WMAP observation was confirmed by the *Planck* collaboration [42, 43], with a p-value of $0.5 - 1.0\%$ for the temperature maps with resolution $N_{\rm side} = 16$, depending wether or not a look-elsewhere effect is considered. In particular, the *Planck* 2013 analysis [42] showed, using both full-resolution ($N_{\rm side} = 2048$) and low-resolution ($N_{\rm side} = 16$) maps, that the low variance was localized in the northern ecliptic hemisphere, with a p-value of $\sim 0.1\%$. No updates on these significance levels have been provided by the 2015 and 2018 *Planck* data releases [43, 44] .

5.3 Alignments of Low Multipole Moments

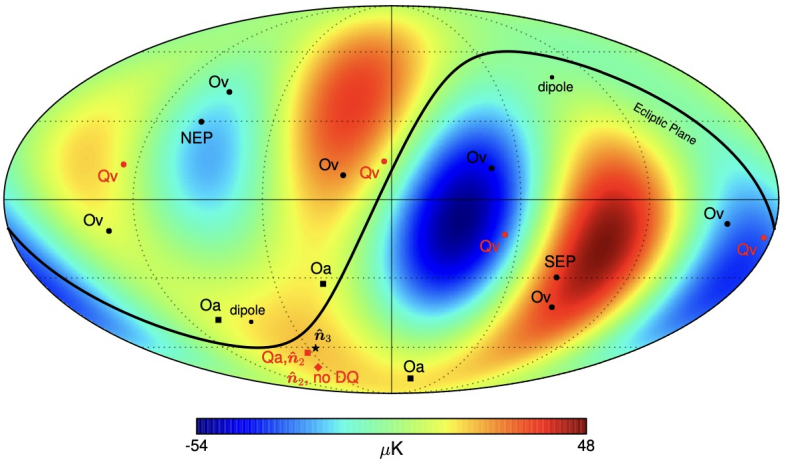

Figure 5.5. Quadrupole and octopole multipole vectors for the DQ corrected *Planck* 2013 SMICA map in the Galactic coordinates, adapted from [92]. The background shows the quadrupole+octopole pattern. The multipole vectors are shown as circles, in red and labelled 'Qv' for the quadrupole and in black and labelled 'Ov' for the octopole. The directions of the oriented-area vectors defined in equation (5.7) $\boldsymbol{w}^{(\ell;i,j)}$ are shown as squares. The quadrupole oriented-area vector, is shown in red and labelled 'Qa', the octopole oriented-area vectors are shown in black and labelled 'Oa'. Since the multipole vectors are only determined up to a sign each vector appears twice in the figure and the oriented-area vectors have only been plotted in the southern hemisphere to avoid cluttering the plot. The maximum angular momentum dispersion direction for the octopole, $\hat{\mathbf{n}}_3$, is shown as the black star. Since $\hat{\mathbf{n}}_2 = \hat{w}^{(2;1,2)}$ it is also represented by the red square. The direction of $\hat{\mathbf{n}}_2$ without the DQ correction is shown as the red diamond. For reference also shown in the figure is the ecliptic plane (black line), the locations of the north (NEP) and south (SEP) ecliptic poles, and the direction of our motion with respect to the CMB (dipole).

A significant alignment between the orientation of the quadrupole ($\ell = 2$) and the octopole ($\ell = 3$) has been first reported by Tegmark et al. [93], who observed it in the WMAP first year temperature data. This is in clearly in contrast with what is predicted by the standard ΛCDM model, according to which the CMB is an isotropic random field and the quadrupole and the octopole are expected to be uncorrelated. The issue of alignment was discussed in greater detail by de Oliveira-Costa et al. [94]. To assess the significance of the alignment, de Oliveira-Costa et al. computed the axis $\hat{\mathbf{n}}_\ell$ around which the angular momentum dispersion, given by

$$[\Delta L(\hat{\mathbf{n}})]^2_\ell = \sum_m m^2 |a_{\ell m}(\hat{\mathbf{n}})|^2 \tag{5.5}$$

was maximised. It should be stressed that in equation (5.5) the $a_{\ell m}(\hat{\mathbf{n}})$ denotes the spherical harmonic coefficient of the CMB map in a rotated coordinate system with the z-axis in the $\hat{\mathbf{n}}$-direction. The alignment was quantified by studying the quantity $|\hat{\mathbf{n}}_2 \cdot \hat{\mathbf{n}}_3|$. The preferred axes for the quadrupole $\hat{\mathbf{n}}_2$ and the octopole $\hat{\mathbf{n}}_3$ were found to be both roughly in the $(l, b) = (-110°, 60°)$ direction, giving $|\hat{\mathbf{n}}_2 \cdot \hat{\mathbf{n}}_3| \approx 0.9838$, corresponding to a separation of 10.3°,

with a p-value of $\approx 1.6\%$. Furthermore, de Oliveira-Costa et al. also found that the quadrupole and the octopole are anomalous on their own. The quadrupole was found surprisingly low, with a significance of about 5%. The octopole was found unusually planar, with roughly the same significance. In [95, 92] Copi et al. proposed an alternative method for studying this alignment based on *multipole vectors*. These multipole vectors form, as the spherical harmonics, an irreducible representation of the rotation group SO(3) and thus they provide a different basis for expanding any scalar function on the sphere. Within this approach, in particular, each multipole order ℓ is represented by ℓ unit vectors, $\{\hat{\boldsymbol{v}}^{(\ell;j)}|j = 1, ..., \ell\}$, pointing in directions on the sky and an overall magnitude $A^{(\ell)} = |\boldsymbol{v}^{(\ell;j)}|$, such that, for example, the dipole $\ell = 1$ would be decomposed as

$$\Theta_1(\hat{\mathbf{n}}) \equiv A^{(1)} \left(\hat{\boldsymbol{v}}^{(1;1)} \cdot \hat{\mathbf{n}} \right) \tag{5.6}$$

The ℓ unit vectors are used to define oriented-area vectors, which define a set of planes:

$$\boldsymbol{w}^{(\ell;i,j)} = \hat{\boldsymbol{v}}^{(\ell;i)} \times \hat{\boldsymbol{v}}^{(\ell;j)} \tag{5.7}$$

The alignment of these planes with a given direction $\hat{\mathbf{n}}$ in the sky is checked by studying the quantity $A_j = |\boldsymbol{w}_j \cdot \hat{\mathbf{n}}|$ and then quantified by the S and T statistics, defined as

$$S = \frac{1}{n} \sum_{j=1}^{n} A_j, \qquad T \ = \frac{1}{n} \sum_{j=1}^{n} (1 - A_j) \tag{5.8}$$

where the sum is over a set of oriented-area vectors and $\boldsymbol{w}_j$ denotes one of the vectors. In [92] Copi et al. searched for alignments in the seven and nine-year WMAP and *Planck* 2013 temperature data. In particular, the WMAP ILC cleaned maps and the *Planck* `SMICA`, `NILC` and `SEVEM` maps were used. In their analysis Copi et al. [92] applied both the multipole vector method they devised and the original approach described by de Oliveira-Costa [94]. They found that the statistics from the maximum angular dispersion and the multipole vectors both showed strong evidence for a mutual alignment of the quadrupole and the octopole, with p-values for at least as much alignment observed occurring in realisations of the ΛCDM model dropping to less than 0.5% once the kinematic (Doppler) quadrupole was removed. They also found that the alignment of the quadrupole and the octopole with the dipole direction appears to be even more robust than their mutual alignment, with p-values of less than 0.4% for all maps and with both the S and T statistics. It was also found the quadrupole and the octopole are jointly perpendicular to the ecliptic plane, with p-values ranging from 2% to 4% depending on the map considered, and to the north galactic pole (NGP), with p-values ranging from 0.8% to 1.6%. Applying the *Planck* Doppler-quadrupole (DQ) corrections to the *Planck* `SMICA`, `NILC` and `SEVEM` cleaned maps lead to results for the alignments even more *unlikely* in the ΛCDM model, thus strengthening the significance of the results. Figure 5.5

provides a visual summary of the observed anomalies and shows the results found for the multipole vectors of the quadrupole and the octopole, the corresponding oriented-area vectors, their maximal angular dispersion directions $\hat{\mathbf{n}}_\ell$ and some special directions.

5.4 Point-Parity Asymmetry

The CMB temperature fluctuation field $\Theta(\hat{\mathbf{n}})$ can be considered as the sum of even and odd parity functions:

$$\Theta(\hat{\mathbf{n}}) = \Theta^+(\hat{\mathbf{n}}) + \Theta^-(\hat{\mathbf{n}}), \qquad \text{with} \quad \Theta^\pm(\hat{\mathbf{n}}) = \frac{\Theta(\hat{\mathbf{n}}) \pm \Theta(-\hat{\mathbf{n}})}{2} \tag{5.9}$$

Using the spherical harmonics decomposition (3.5) and the parity property of the spherical harmonics $Y_{\ell m}(\hat{\mathbf{n}}) = (-1)^\ell Y_{\ell m}(-\hat{\mathbf{n}})$, one can show that

$$\Theta^\pm(\hat{\mathbf{n}}) = \sum_{\ell m} a_{\ell m} Y_{\ell m}(\hat{\mathbf{n}}) \Gamma^\pm(\ell) \tag{5.10}$$

where $\Gamma^+(\ell) = \cos^2(\ell\pi/2)$ and $\Gamma^-(\ell) = \sin^2(\ell\pi/2)$. According to the ΛCDM model, on the largest scales (corresponding to the Sachs-Wolfe plateau in the temperature power spectrum, where $\ell(\ell+1)C_\ell \approx$ constant), the Universe should be parity neutral with no particular parity preference exhibited by the CMB fluctuations. However, an odd point-parity preference was first noted in the WMAP data by Land et al. [96], even though, given their statistical estimator, they found that the statistical significance for this feature was not very high. The point-parity asymmetry analysis was later extended by Kim & Naselsky [97, 98, 99] to the WMAP three, five and seven-year data. To assess the significance of the parity asymmetry Kim & Naselsky proposed the following statistics:

$$g(\ell_{\max}) = \frac{P^+(\ell_{\max})}{P^-(\ell_{\max})} \tag{5.11}$$

where $P^\pm(\ell_{\max})$ are defined as the sum of $C_\ell[\ell(\ell+1)/2\pi]$ over multipoles for the even and the odd maps respectively. The ratio $g(\ell_{\max})$ of WMAP data for various $\ell_{\max}$ is shown in Figure 5.6. In particular, it was found that the parity asymmetry in the WMAP7 data at multipoles $2 \leqslant \ell \leqslant 22$ was the most anomalous, with p-value 0.0031%.

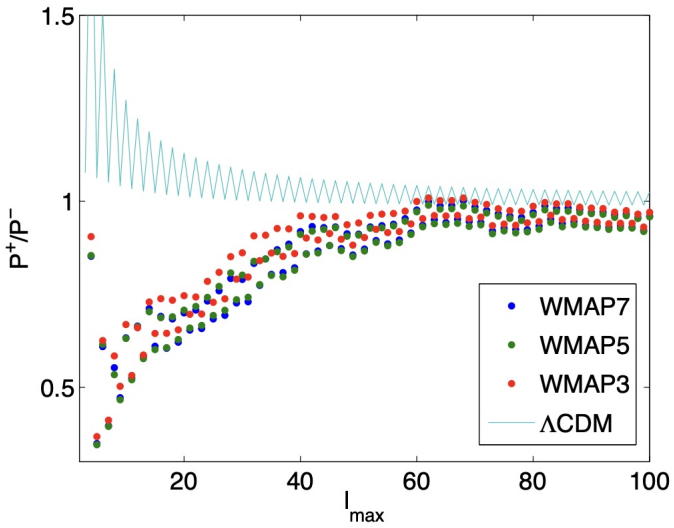

Figure 5.6. The ratio $g(\ell_{\max})$ of WMAP data, adapted from [98].

In a subsequent analysis, Naselsky et al. [100] investigated the directional properties of the CMB parity asymmetry for the WMAP7 data, finding that the direction of maximal (minimal) parity asymmetry, for multipole moments up to $\ell \sim 20$, was parallel (perpendicular) to the direction singled out by the CMB kinematic dipole. Later, the *Planck* collaboration, following the same approach of Kim & Naselsky, investigated the parity asymmetry for the *Planck* 2013 [42], 2015 [43] and 2018 [44] low-resolution ($N_{\rm side} = 32$) temperature maps. The analyses confirmed the results found by Kim & Navelsky [97, 98, 99] for WMAP7 but also found that the significance of the asymmetry depends on the maximum monopole chosen and peaks for $\ell_{\max} \approx 20 - 30$. In their 2018 [44] data release the *Planck* collaboration extended to analysis also to polarisation data, following a similar approach to the one applied to the temperature maps. No significant anomaly was found, but it should be stressed that the low signal-to-noise of the *Planck* polarisation data over the range of scales considered has been a limiting factor for the analysis.

5.5 The Cold Spot

The cold spot is a large region in the CMB map with an angular radius of about $5^\circ - 10^\circ$, centred at Galactic coordinates $(l, b) = (210^\circ, -57^\circ)$. It is characterised by and unusually low temperature with a mean temperature decrease $\Delta T \approx -100$ μK and it is surrounded by an hot ring [101, 102, 103]. It was first detected in the WMAP 1-year data by Vielva et. al [104], who performed a wavelet analysis of the Gaussianity of CMB data applying a technique based on the Spherical Mexican Hat Wavelet (SMHW). In particular, Vielva et al. found that the SMHW coefficients for angular scales of about $\sim 10^\circ$ on the sky presented an excess of kurtosis, while the skewness[1] was consistent with zero. The finding of Vielva et al. was

[1] In statistics, skewness is a measure of the asymmetry of the probability distribution of a real-valued random variable about its mean, while kurtosis is a measure of whether the data are heavy-tailed or light-tailed relative

reassessed in subsequent analyses (see e.g. [105, 106]) and later confirmed in *Planck* data [42, 43, 44]. Its statistical significance, depending on the statistical method applied to assess it (see e.g. [101, 102, 103]) is $2-4\sigma$ and the inconsistency with the CMB Gaussian simulation has a p-value of about 1% [107].

5.6 (Short) Summary of the Findings from *Planck*

The analysis of the temperature maps from WMAP and *Planck* data showed consistent evidence for anomalous features in the CMB, with an overall significance of $2-3\sigma$. The analysis of polarisation data, performed by the *Planck* collaboration on their 2018 data set, showed no evidence for a lack of large-angle correlations, an hemispherical power asymmetry in the N-point correlations functions and peak distributions and for a violation of the point-parity symmetry predicted by the ΛCDM model. However, the searching for a dipolar power asymmetry signature in polarisation data found, using the variance asymmetry estimator, an intriguing alignment of the preferred directions of the E-mode polarisation and temperature data. Due to the low signal-to-noise of the data the *Planck* collaboration was not able to draw firm conclusions on whether or not this alignment might be more than a coincidence and thus related to some underlying physical mechanism. A summary of the findings from the *Planck* satellite data we discussed in the previous sections is presented in Table 5.6.

Table 5.6. Summary of the findings discussed in the previous sections from the *Planck* satellite data. Note that the sense of the p-value differs between some of the analyses.

Feature	p-value	Data	Reference
2-point correlation $S^{TT}_{1/2}$	$\geqslant 99.9\%$	*Planck* 18 `Comm.` map	[44]
2-point correlation $S^{TT}_{1/2}$ (no quadr.)	96.0%	*Planck* 18 `Comm.` map	[44]
hemispherical power asymmetry	$\geqslant 99\%$	*Planck* 13, 15, 18	[42, 43, 44]
hemispherical variance asymmetry	$\leqslant 0.1\%$	*Planck* 15, 18	[43, 44]
low variance in the northern hemisphere	$\leqslant 1\%$	*Planck* 13	[42]
dipolar modulation	$\leqslant 1\%$	*Planck* 13, 15, 18	[42, 43, 44]
quadrupole-octopole alignment	$\leqslant 0.5\%$	*Planck* 13	[92]
$\ell = 1, 2, 3$ alignment	$\leqslant 0.4\%$	*Planck* 13	[92]
odd parity preference $\ell_{\max} \approx 20-30$	$\leqslant 1\%$	*Planck* 18	[44]
odd parity preference $\ell_{\max} = 27$	$\leqslant 0.3\%$	*Planck* 18 with 15 common mask	[44]
cold spot	$\leqslant 1\%$	*Planck* 15	[43]

to a normal distribution.

5.7 The Quest for an Explanation

Given the *a posteriori* nature of their detection, a conservative explanation is that the observed CMB anomalous features are due to a statistical fluke of our realisation of the ΛCDM model. However, despite their relative modest statistical significance, the number of these features, the fact that they are not related in a obvious manner and the fact that (almost all of them) are detected only at the largest angular scales, motivate the quest for an underlying physical explanation. One possibility to explain the CMB anomalous features is that they might be related to local physics effects, namely there is a pernicious foreground that contaminates the CMB and leads to the observed anomalies. In particular, physical well motivated foregrounds that might effect or even be the cause of the anomalies are the Solar System (see e.g. [108, 109]) and the Milky Way (see e.g. [110]). Recently, Luparello et al. [111] reported the finding of new CMB foreground associated with extended galactic haloes and the extent to which this foreground may impact the CMB fluctuations and be responsible for the observed large-scale anomalies has been studied by Hansen et al. in [112]. However, the fact that the CMB anomalous features show up at more or less the same statistical significance in both *Planck* and WMAP foreground cleaned maps[2] constitutes in general a major argument against a foreground-related explanation. Another possibility is that the observed anomalies have a cosmological origin. This possibility is the most exciting, because it implies new physics beyond the standard ΛCDM model. Therefore, in the following sections, we will provide a short and non-exhaustive qualitative summary of some of the cosmological mechanisms that have been proposed to explain the CMB large-scale anomalies.

5.7.1 Large-scale Structure Explanations

In principle the local structure of the Universe i.e. over/under-densities in the dark matter distribution within tens or hundred of Megaparsecs from our location, could be responsible for some of the alignments. In particular, one possibility is that the observed alignments are induced by the Integrated Sachs-Wolfe (ISW) or, in the non-linear regime, the Rees-Sciama effect. As we have seen in Chapter 3, the ISW effect is one of the contributions to the Cosmic Microwave Background temperature fluctuations and it arises from the time-dependance of the gravitational potentials as the photons propagate from the last scattering surface to us. The same mechanism responsible for the ISW effect is referred to as the Rees-Sciama (RS) effect when considering the non-linear evolution of the gravitational potentials. Rakić et al. [113] explored the possibility that the local RS effect could induce a correlation between the dipole and higher multipoles, assuming for the local superstructure spherical symmetry. They found, as they expected, some alignments among the low multipoles. However, they also found that these alignments are not in agreement with those observed in the data. In [114], Inoue & Silk explored instead the possibility that the Cosmic Microwave Background is affected by the RS effect for local voids at redshift $z \lesssim 1$, finding that not only such a structure can account

[2] WMAP and *Planck* missions not only have different observational strategies, but use also different data reduction methods.

for both the planarity of the octopole and the alignment of the quadrupole and the octopole, but also the cold spot in the Galactic southern hemisphere can be explained by such a large void at redshift $z \sim 1$. An argument against explaining the observed alignments via a ISW or RS effect is that it is simply unlikely that this effect could match the signal and the pattern of the primordial CMB [92]. The idea that the cold spot could be due to an anomalously large spherical under-dense region of unknown origin, on the line of sight between us and the LSS, has also been repeatedly revised in literature. Rudnick et al. [115] have claimed that there is a cold spot in the NRAO VLA Sky Survey (NVSS) which is statistically significant and aligned with the cold spot found in both WMAP and *Planck*. However, after including systematic effects and carefully accounting for the effect of *a posteriori* choices when assessing the statistical significance, no evidence was found for an NVSS cold spot [116]. Recently, using the data from the WISE-2MASS survey, a low density (supervoid) region centred at redshift $z \sim 0.2$ and lying in the direction of the CMB cold spot has been detected [117, 118]. In particular, it has been claimed that this supervoid is capable of accounting for the cold spot temperature profile through the RS effect [118]. This claim has been however refuted by Nadathur et al. [102], who argue that the maximum temperature effect that this void could produce on the CMB is not sufficient to cause the observed cold spot.

5.7.2 Inflationary Explanations

The high-precision measurements of CMB anisotropies from both WMAP and *Planck* are in agreement with the predictions of single-field models of inflation. However, the anomalous features consistently observed at the largest angular scales pose a challenge to such models, which in order to generate them should be either modified or rejected. Within the class of single-field models of inflation one possibility to generate some of these features consists in briefly modifying the slow-roll dynamics of the inflaton field to accommodate for a breaking of scale invariance. This can be achieved either by introducing a step in the inflaton potential (see e.g. [119, 120, 121, 122]), allowing an inflection point in the potential (see e.g. [123, 124, 125]) or by imposing kinetic/fast slow-roll initial conditions for the dynamical evolution of the inflaton field (see e.g. [126, 127, 128, 129]). Even though all of these approaches give rise to localised features in the primordial power spectrum, which usually provide an improved quality of fit to the observations, a generic problem related to an explanation for the CMB anomalies along this line is that some of these models introduce a new fine tuning. Another possibility to generate some of the anomalous CMB features consists in considering models violating statistical isotropy. The most common strategy for incorporating the breaking of statistical isotropy into inflation is to consider some form of multi-field inflation, using one of the directions orthogonal to the direction of slow-roll as a modulating field. In the specific case of the dipolar asymmetry, however, there are a number of aspects which make an explanation along this line difficult and thus must be taken into account when attempting model building. Since most extra fields in multi-field models of inflation become disordered in a nearly scale-invariant way, obtaining the required modulation is usually problematic. Moreover, to respect

the constraints on the non-Gaussian parameter $f_{\rm NL}$, one must avoid that the modulating field leave a direct imprint on the temperature anisotropies. Finally, the measured amplitude for the dipolar asymmetry exhibits a strong scale-dependence. It is also interesting to point out that the apparent breaking of statistical isotropy suggested by the anomalous CMB features can also be an artefact of primordial non-Gaussianity. Along this line, relevant is the work of Schmidt & Hui [130], Byrnes et al. [14, 13] and Adhikari et al. [10, 11], who proposed non-Gaussian models (based on the early proposals by Gordon et al. [84], Erickcek et al. [131] and Dvorkin et al. [132]) to explain the power asymmetry, and Hansen et al. [12], who assume for six of the most extensively studied CMB anomalous features to have a common cosmological origin and look for toy models that can naturally reproduce them. In particular, Schmidt & Hui [130] have shown that the coupling between a long-wavelength mode a shorter one, induced by non-Gaussianity, could manifest in the observation of a preferred direction in the sky. However, the model proposed by Schmidt & Hui fails to actually reproduce the observed asymmetry: this is because the (modulated) power spectrum which arises in their model depends on the direction of $\mathbf{k}$ because the long-wavelength modes in our particular realisation of the Universe statistically pick out certain directions and, as pointed out in [133, 134], the asymmetry can not arise due to a preferred direction in $P(k)$ but must be attributed to a spatial modulation of power across the observable Universe[3]. In [10], Adhikari et al. performed a systematic study of the power asymmetry expected in the CMB if the primordial fluctuations are non-Gaussian and exist on scales larger than we can observe, showing that scale-dependent modulations are a generic feature of non-Gaussian models and that such modulations can naturally reproduce the observed power asymmetry. Subsequently, in [11], Adhikari et al. shown that a large-scale power asymmetry may also arise in models with local trispectra and strong scale-dependent $\tau_{\rm NL}$ amplitudes. In [14, 13], Byrnes et al. extended previous calculations, which were restricted only to one or two-source scenarios, computing the response of the 2-point correlation function to a long-wavelength perturbation in models characterised by a near-local bispectrum, showing that the amplitude and scale-dependence of the observed power asymmetry are actually sourced by a combination of response functions. Finally, in [12], inspired by the additional non-linear terms in the gravitational potential that appear in models of inflation, Hansen et al. search for isotropic but non-Gaussian models, where the non-Gaussianity is the origin of the apparent deviations from statistical isotropy seen in the data, aiming to phenomenologically determine the properties that a physical model able to explain them should exhibit. The connection between primordial non-Gaussianity and the CMB large-scale anomalies, along with the possible implications of these anomalous features for Early Universe physics, will be further explored in the next two Chapters.

[3]This point will be further clarified in Chapter 6.

Chapter 6

CMB Anomalies as Signatures of Non-Gaussianity

6.1 Non-Gaussian Modulation of the Power Spectrum

When one has access only to a finite volume of the Universe, isotropy and Gaussianity are not really two independent criteria for the statistics of the primordial fluctuations [135], thus implying that if one assumes non-Gaussianity for fluctuations of wavelengths much bigger than the size of the observable Universe, then one expects some level of statistical anisotropy to naturally arise in the observed sky. The analytical framework proposed by Adhikari et al. in [10], which is going to be the subject of the next few sections, allows us to calculate, through a cosmic-variance analysis, the distribution of expected deviations from isotropy in any isotropic, non-Gaussian model. An interesting point is that this framework incorporates the most successful proposals to explain the power asymmetry, even those that were not initially formulated as non-Gaussian models. This is because, if one assumes to maintain the hypothesis of statistical isotropy, then the power asymmetry can be modeled by a fluctuation in some long-wavelength modulating field coupled to some primordial cosmological parameter [134] and, in a way, this is a sort of non-Gaussianity, since it implies the coupling of a long-wavelength fluctuation to short-wavelength ones.

6.1.1 Statistical Anisotropies from Local Non-Gaussian Initial Conditions

In an homogenous and statistically isotropic Universe, as we have already seen in Chapter 1, the 2-point correlation function of a generic stochastic Gaussian field $\phi(x)$ depends only on the magnitude of the separation between the two points and is defined as the Fourier transform of the power spectrum:

$$\left\langle \phi\left(\mathbf{x}-\frac{\mathbf{r}}{2}\right)\phi\left(\mathbf{x}+\frac{\mathbf{r}}{2}\right)\right\rangle \equiv \int \frac{d^3\mathbf{k}}{(2\pi)^3} e^{i\mathbf{k}\cdot\mathbf{r}} P_\phi(k) \tag{6.1}$$

However, as pointed out in [133, 134], an hemispherical power asymmetry cannot arise by simply dropping the assumption of isotropy, which would result for the power spectrum in a dependence on the direction of $\mathbf{k}$. This is because, being the fluctuations real, the Fourier modes of $\mathbf{k}$ and $-\mathbf{k}$ are related in such a way that the only multipole moments ℓ giving contributions

to the modulation would be even, thus forbidding a dipole modulation for the temperature field. The arising of the asymmetry must therefore be attributed to a *spatial modulation* of power across the observable Universe, that we can model introducing a position dependence in the power spectrum i.e. $P_\phi(k) \to P_\phi(k, \mathbf{x})$, which allows for contributions from both even and odd multipole moments. We will now proceed to prove that such an inhomogeneous power spectrum naturally arises in non-Gaussian models where short-wavelength modes are coupled to long-wavelength ones. Let us begin our discussion by assuming that at some early time, after reheating but prior to the decoupling of photons from the primordial plasma, a large volume of the Universe $V_{\rm L}$ is filled with adiabatic (curvature) fluctuations, described by an isotropic but non-Gaussian statistics. For the sake of simplicity, in the following we will assume that the fluctuations are described by the standard local form of the gravitational potential with constant non-linearity parameter $f_{\rm NL}$ given by equation (4.5):

$$\Phi(\mathbf{x}) = \phi(\mathbf{x}) + f_{\rm NL}\left(\phi^2(\mathbf{x}) - \langle\phi^2(\mathbf{x})\rangle\right) \tag{6.2}$$

where $\Phi(\mathbf{x})$ is Bardeen's gravitational potential and $\phi(\mathbf{x})$ is a random Gaussian field. Going to Fourier space, the *convolution theorem* tells us that the Fourier transform of a product of functions is the Fourier transform of the convolution of the functions, thus implying that the Fourier modes of the non-Gaussian field are related to those of the Gaussian field by

$$\Phi(\mathbf{k}) = \phi(\mathbf{k}) + f_{\rm NL}\int \frac{d^3\mathbf{q}}{(2\pi)^3}\left[\phi(\mathbf{k}-\mathbf{q})\phi(\mathbf{q}) - \langle\phi(\mathbf{k}-\mathbf{q})\phi(\mathbf{q})\rangle\right] \tag{6.3}$$

The 2-point correlation function of the non-Gaussian field is therefore given by

$$\begin{aligned}\left\langle \Phi\left(\mathbf{x}-\frac{\mathbf{r}}{2}\right)\Phi\left(\mathbf{x}+\frac{\mathbf{r}}{2}\right)\right\rangle &= \int\frac{d^3\mathbf{k}}{(2\pi)^3}\int\frac{d^3\mathbf{k}'}{(2\pi)^3}\langle\Phi(\mathbf{k})\Phi(\mathbf{k}')\rangle e^{i(\mathbf{k}+\mathbf{k}')\cdot\mathbf{x}}e^{i(\mathbf{k}-\mathbf{k}')\cdot\frac{\mathbf{r}}{2}} \\ &= Z_1 + f_{\rm NL}Z_2 + f_{\rm NL}^2 Z_3\end{aligned} \tag{6.4}$$

The integral Z_1 simply gives the following contribution:

$$\begin{aligned}Z_1 &= \int\frac{d^3\mathbf{k}}{(2\pi)^3}\int\frac{d^3\mathbf{k}'}{(2\pi)^3}\langle\phi(\mathbf{k})\phi(\mathbf{k}')\rangle e^{i(\mathbf{k}+\mathbf{k}')\cdot\mathbf{x}}e^{i(\mathbf{k}-\mathbf{k}')\cdot\frac{\mathbf{r}}{2}} \\ &= \int\frac{d^3\mathbf{k}}{(2\pi)^3}\int\frac{d^3\mathbf{k}'}{(2\pi)^3}\left[(2\pi)^3 P_\phi(k)\delta^{(3)}(\mathbf{k}+\mathbf{k}')\right]e^{i(\mathbf{k}+\mathbf{k}')\cdot\mathbf{x}}e^{i(\mathbf{k}-\mathbf{k}')\cdot\frac{\mathbf{r}}{2}} \\ &= \int\frac{d^3\mathbf{k}}{(2\pi)^3}P_\phi(k)e^{i\mathbf{k}\cdot\mathbf{r}}\end{aligned} \tag{6.5}$$

The integral Z_2, instead, reads off:

$$\begin{aligned}
Z_2 = &\int \frac{d^3\mathbf{k}}{(2\pi)^3}\int \frac{d^3\mathbf{k}'}{(2\pi)^3} e^{i\left(\mathbf{k}+\mathbf{k}'\right)\cdot\mathbf{x}} e^{i\left(\mathbf{k}-\mathbf{k}'\right)\cdot\frac{\mathbf{r}}{2}} \\
&\times \left[\int \frac{d^3\mathbf{q}'}{(2\pi)^3}\langle\phi(\mathbf{k})\phi(\mathbf{k}'-\mathbf{q}')\phi(\mathbf{q}')-\phi(\mathbf{k})\langle\phi(\mathbf{k}'-\mathbf{q}')\phi(\mathbf{q}')\rangle\rangle\right. \\
&\left.+\int \frac{d^3\mathbf{q}}{(2\pi)^3}\langle\phi(\mathbf{k}-\mathbf{q})\phi(\mathbf{q})\phi(\mathbf{k}')-\langle\phi(\mathbf{k}-\mathbf{q})\phi(\mathbf{q})\rangle\phi(\mathbf{k}')\rangle\right] \\
= &\int \frac{d^3\mathbf{k}}{(2\pi)^3}\int \frac{d^3\mathbf{k}'}{(2\pi)^3} e^{i\left(\mathbf{k}+\mathbf{k}'\right)\cdot\mathbf{x}} e^{i\left(\mathbf{k}-\mathbf{k}'\right)\cdot\frac{\mathbf{r}}{2}} \\
&\times \left[\int \frac{d^3\mathbf{q}'}{(2\pi)^3}\langle\phi(\mathbf{k})\phi(\mathbf{k}'-\mathbf{q}')\phi(\mathbf{q}')\rangle+\int \frac{d^3\mathbf{q}}{(2\pi)^3}\langle\phi(\mathbf{k}-\mathbf{q})\phi(\mathbf{q})\phi(\mathbf{k}')\rangle\right]
\end{aligned} \tag{6.6}$$

where we used that

$$\langle\phi(\mathbf{k})\langle\phi(\mathbf{k}'-\mathbf{q}')\phi(\mathbf{q}')\rangle\rangle = \langle\phi(\mathbf{k})\rangle\langle\phi(\mathbf{k}'-\mathbf{q}')\phi(\mathbf{q}')\rangle = 0 \tag{6.7}$$

since $\langle\phi(\mathbf{k})\rangle = 0$. Similarly, the Z_3 integral gives:

$$\begin{aligned}
Z_3 = &\int \frac{d^3\mathbf{k}}{(2\pi)^3}\int \frac{d^3\mathbf{k}'}{(2\pi)^3} e^{i\left(\mathbf{k}+\mathbf{k}'\right)\cdot\mathbf{x}} e^{i\left(\mathbf{k}-\mathbf{k}'\right)\cdot\frac{\mathbf{r}}{2}} \\
&\times \int \frac{d^3\mathbf{q}'}{(2\pi)^3}\int \frac{d^3\mathbf{q}}{(2\pi)^3}\left[\langle\phi(\mathbf{k}-\mathbf{q})\phi(\mathbf{q})\phi(\mathbf{k}'-\mathbf{q}')\phi(\mathbf{q}')\rangle\right. \\
&\left.-\langle\phi(\mathbf{k}-\mathbf{q})\phi(\mathbf{q})\rangle\langle\phi(\mathbf{k}'-\mathbf{q}')\phi(\mathbf{q}')\rangle\right]
\end{aligned} \tag{6.8}$$

When we consider the statistics in a volume $V_{\rm L}\to\infty$, being ϕ a random Gaussian field, the contribution from Z_2 to the 2-point correlation function vanishes and thus, in that case, the power spectrum is corrected just by the term proportional to $f_{\rm NL}^2$ which, if the non-Gaussianity is weak, is small. However, if we instead consider the statistics in a finite sub-volume $V_{\rm S}\ll V_{\rm L}$, corresponding in size to our observable Hubble volume, then we have that if the mode $\mathbf{q}$ corresponds to a long-wavelength mode and the modes $\mathbf{k}$ and $\mathbf{k}'$ are well within the sub-volume $V_{\rm S}$, then

$$\langle\phi(\mathbf{q})\phi(\mathbf{k})\phi(\mathbf{k}')\rangle|_{V_{\rm S}} = \phi(\mathbf{q})\langle\phi(\mathbf{k})\phi(\mathbf{k}')\rangle|_{V_{\rm S}} \neq 0 \tag{6.9}$$

that is, while $\phi(\mathbf{k})$ and $\phi(\mathbf{k}')$ remains randomly distributed in the sub-volume $V_{\rm S}$, $\phi(\mathbf{q})$ is no longer stochastic and takes a particular value, corresponding to a particular realisation of the field that constitutes the background of a particular Hubble volume. Therefore, assuming

the Fourier mode $\phi(\mathbf{q})$ to be stochastic only if $|\mathbf{q}| > k_{\rm min} = \pi/r_{\rm CMB}$ with $r_{\rm CMB}$ defined as the comoving distance to the last scattering surface, we get that the integrals Z_2 and Z_3 reduce to:

$$\begin{aligned} Z_2 &= \int_{|\mathbf{k}|>k_{\rm min}} \frac{d^3\mathbf{k}}{(2\pi)^3} P_\phi(k) e^{i\mathbf{k}\cdot\mathbf{r}} \int_{|\mathbf{q}|<k_{\rm min}} \frac{d^3\mathbf{q}}{(2\pi)^3}\phi(\mathbf{q}) \left[e^{i\mathbf{q}\cdot\left(\mathbf{x}+\frac{\mathbf{r}}{2}\right)} + e^{i\mathbf{q}\cdot\left(\mathbf{x}-\frac{\mathbf{r}}{2}\right)}\right] \\ &= 2\int_{|\mathbf{k}|>k_{\rm min}} \frac{d^3\mathbf{k}}{(2\pi)^3} P_\phi(k) e^{i\mathbf{k}\cdot\mathbf{r}} \int_{|\mathbf{q}|<k_{\rm min}} \frac{d^3\mathbf{q}}{(2\pi)^3}\phi(\mathbf{q}) \cos\left(\frac{\mathbf{q}\cdot\mathbf{r}}{2}\right) e^{i\mathbf{q}\cdot\mathbf{x}} \end{aligned} \tag{6.10}$$

$$\begin{aligned} Z_3 &= \int_{|\mathbf{k}|>k_{\rm min}} \frac{d^3\mathbf{k}}{(2\pi)^3} P_\phi(k) e^{i\mathbf{k}\cdot\mathbf{r}} \left\{\int_{|\mathbf{q}|<k_{\rm min}} \frac{d^3\mathbf{q}}{(2\pi)^3}\phi(\mathbf{q}) \left[e^{i\mathbf{q}\cdot\left(\mathbf{x}+\frac{\mathbf{r}}{2}\right)} + e^{i\mathbf{q}\cdot\left(\mathbf{x}-\frac{\mathbf{r}}{2}\right)}\right]\right\}^2 \\ &= 4\int_{|\mathbf{k}|>k_{\rm min}} \frac{d^3\mathbf{k}}{(2\pi)^3} P_\phi(k) e^{i\mathbf{k}\cdot\mathbf{r}} \left\{\int_{|\mathbf{q}|<k_{\rm min}} \frac{d^3\mathbf{q}}{(2\pi)^3}\phi(\mathbf{q}) \cos\left(\frac{\mathbf{q}\cdot\mathbf{r}}{2}\right) e^{i\mathbf{q}\cdot\mathbf{x}}\right\}^2 \end{aligned} \tag{6.11}$$

These results tells us that the position dependence of the power spectrum arises from the factor $e^{i\mathbf{q}\cdot\mathbf{x}}$, thus implying that the inhomogeneous power spectrum $P_{\Phi,V_{\rm S}}(k,\mathbf{x})$ will be nearly constant on scales that are well within $V_{\rm S}$ i.e. on scales shorter than $1/|\mathbf{q}|$. Therefore, if we restrict the 2-point correlation function to separations such that $\mathbf{q}\cdot\mathbf{r} \ll 1$, in which case the term $\cos(\mathbf{q}\cdot\mathbf{r}/2) \sim 1$, we get that the inhomogeneous power spectrum $P_{\Phi,V_{\rm S}}(k,\mathbf{x})$ is given by

$$P_{\Phi,V_{\rm S}}(k,\mathbf{x}) = P_\phi(k)\left[1 + 4\bar{f}_{\rm NL}\int_{|\mathbf{q}|<k_{\rm min}} \frac{d^3\mathbf{q}}{(2\pi)^3}\phi(\mathbf{q}) e^{i\mathbf{q}\cdot\mathbf{x}}\right] \tag{6.12}$$

where the locally observed non-linearity parameter, $\bar{f}_{\rm NL}$, is given by

$$\bar{f}_{\rm NL} = f_{\rm NL} + f_{\rm NL}^2 \int_{|\mathbf{q}'|<k_{\rm min}} \frac{d^3\mathbf{q}'}{(2\pi)^3}\phi(\mathbf{q}') e^{i\mathbf{q}'\cdot\mathbf{x}} \tag{6.13}$$

Notice that for $f_{\rm NL} > 0$ and a positive background fluctuation, the net effect of the correction arising from the 4-point ϕ-function is to make the statistics in any finite sub-volume $V_{\rm S} \ll V_{\rm L}$ appear *less* Gaussian than they are in the large volume $V_{\rm L}$; conversely, a negative $f_{\rm NL}$ and background fluctuation would make the statistics in the smaller volume appear *more* Gaussian. The imprint of the inhomogeneous power spectrum (6.12) on the CMB can be described in terms of a multipole expansion as follows:

$$P_{\Phi,V_{\rm S}}(k,\hat{\mathbf{n}}) = P_\phi(k)\left[1 + \bar{f}_{\rm NL}\sum_{\ell=0}^{\infty}\sum_{m=-\ell}^{\ell} g_{\ell m} Y_{\ell m}(\hat{\mathbf{n}})\right] \tag{6.14}$$

where $Y_{\ell m}$ are the spherical harmonics and $\hat{\mathbf{n}}$ denotes the direction of observation of the

incoming photons. To find the explicit expression for the harmonic coefficients $g_{\ell m}$ we make use of the expansion of the exponential $e^{i\mathbf{q}\cdot\mathbf{x}}$ into spherical harmonics, given by

$$e^{i\mathbf{q}\cdot\mathbf{x}} = 4\pi \sum_{\ell=0}^{\infty} \sum_{m=-\ell}^{\ell} i^{\ell} j_{\ell}(qx) Y^{*}_{\ell m}(\hat{\mathbf{q}}) Y_{\ell m}(\hat{\mathbf{n}}) \tag{6.15}$$

where $j_\ell(qx)$ are the Bessel functions and $\mathbf{x} = x\hat{\mathbf{n}}$ specifies the position of the observed fluctuation. Substituting equation (6.15) into equation (6.12) and neglecting the correction arising from the 4-point function we get that the harmonic coefficients $g_{\ell m}$ are given by

$$g_{\ell m} = 16\pi i^{\ell} \int_{|\mathbf{q}|<k_{\min}} \frac{d^3\mathbf{q}}{(2\pi)^3} j_{\ell}(qx) \phi(\mathbf{q}) Y^{*}_{\ell m}(\hat{\mathbf{q}}) \tag{6.16}$$

Even though the quantity $g_{\ell m}$ has a fixed value in any single sub-volume V_{S}, when averaged over all the sub-volumes in the larger volume V_{L}, $\langle g_{\ell m} \rangle|_{V_{\mathrm{L}}} = 0$. On the other hand, the expected covariance in the large volume V_{L} is non-zero:

$$\begin{aligned} \langle g_{\ell m} g^{*}_{\ell' m'} \rangle|_{V_{\mathrm{L}}} &= 256\pi^2 (-i)^{\ell'} i^{\ell} \int_{|\mathbf{q}|<k_{\min}} \frac{d^3\mathbf{q}}{(2\pi)^3} j_{\ell}(qx) j_{\ell'}(qx) P_{\phi}(q) Y^{*}_{\ell m}(\hat{\mathbf{q}}) Y_{\ell' m'}(\hat{\mathbf{q}}) \\ &= \frac{32}{\pi} \int_{|\mathbf{q}|<k_{\min}} dq q^2 j^2_{\ell}(qx) P_{\phi}(q) \delta_{\ell\ell'} \delta_{mm'} \end{aligned} \tag{6.17}$$

At this point it is straightforward to study the monopole ($\ell = 0$) and dipole ($\ell = 1$) contributions to the power spectrum in the parametrisation of equation (6.14). The monopole contribution is given by

$$A_0 = f_{\mathrm{NL}} g_{00} Y_{00}(\hat{\mathbf{n}}) = f_{\mathrm{NL}} \frac{g_{00}}{2\sqrt{\pi}} \tag{6.18}$$

For a constant f_{NL}, the effect of the monopole contribution A_0 is to shift the amplitude of the isotropic power spectrum $P_\phi(k)$ on all scales and thus it's not observationally distinguishable. The dipole contribution to the power spectrum in the parametrisation of equation (6.14) is instead given by

$$A_1 = f_{\mathrm{NL}} \sum_{m=-1,0,1} g_{1m} Y_{1m}(\hat{\mathbf{n}}) \tag{6.19}$$

where the g_{1m} coefficients are Gaussian distributed with zero mean and expected covariance

$$\langle g_{1m} g^{*}_{1m} \rangle = 64\pi \int_{|\mathbf{q}|<k_{\min}} \frac{dq}{q} \left[\frac{\sin(qx)}{(qx)^2} - \frac{\cos(qx)}{qx} \right]^2 \mathcal{P}_{\phi}(q) \tag{6.20}$$

Since what we are actually interested in is the dipole modulation of the observed power spectrum in the CMB sky, we absorb the unobservable monopole contribution into the isotropic power spectrum redefining

$$P_\phi(k) \to P_\phi^{\rm obs}(k) = P_\phi(k)\left[1 + f_{\rm NL}\frac{g_{00}}{2\sqrt{\pi}}\right] \tag{6.21}$$

and thus we get that the observed modulated power spectrum in the parametrisation of equation (6.14) is given by

$$P^{\rm obs}_{\Phi,V_{\rm S}}(k,\mathbf{n}) = P_\phi^{\rm obs}(k)\left[1 + f_{\rm NL}^{\rm obs}\sum_{m=-1,0,1} g_{1m}Y_{1m}(\hat{\mathbf{n}})\right] \tag{6.22}$$

where

$$f_{\rm NL}^{\rm obs} \equiv \frac{f_{\rm NL}}{1 + f_{\rm NL}\frac{g_{00}}{2\sqrt{\pi}}} \tag{6.23}$$

is defined as the observed amplitude of local non-Gaussianity within our Hubble volume[1]. Now, when we consider the power asymmetry generated by the random realisation of super-horizon perturbations, we have no *a priori* choice for the preferred direction of modulation. Therefore, in this case observations of the dipole power modulations are reported in terms of the amplitude of dipole modulation in the direction of maximum asymmetry. Let us therefore consider the decomposition of such a direction into any three orthonormal directions $(\mathbf{d}_1, \mathbf{d}_2, \mathbf{d}_3)$ on the CMB sky, each corresponding to a particular realisation of the coefficients g_{1m}, and measure the dipole modulation amplitude A_i as seen in the selected orthonormal direction for each sky, such that the observed power spectrum of equation (6.22) rewrites as:

$$P^{\rm obs}_{\Phi,V_{\rm S}}(k,\mathbf{n}) = P_\phi^{\rm obs}(k)\left[1 + 2A_i\cos\theta\right] \tag{6.25}$$

where $\cos\theta = \mathbf{d}_i \cdot \hat{\mathbf{n}}$. Each contribution to the dipole modulation from the non-Gaussianity is given by

$$A_i = \frac{1}{4}\sqrt{\frac{3}{\pi}} f_{\rm NL}^{\rm obs} g_{10} \tag{6.26}$$

[1]The shift in the isotropic power spectrum due to the monopole contribution induces also a shift in the value of the non-linearity parameter $f_{\rm NL}$ as defined from the bispectrum template of equation (4.4)

$$\begin{aligned} B_\Phi^{\text{local, obs}}(k_1,k_2,k_3) &= 2f_{\rm NL}^{\rm obs}\left[P_\Phi^{\rm obs}(k_1)P_\Phi^{\rm obs}(k_2) + 2 \text{ perm.}\right] \\ &= 2f_{\rm NL}\left[1 + f_{\rm NL}\frac{g_{00}}{2\sqrt{\pi}}\right]\left[P_\phi^{\rm obs}(k_1)P_\phi^{\rm obs}(k_2) + 2 \text{ perm.}\right] \end{aligned} \tag{6.24}$$

and is normally distributed, with zero mean and standard deviation

$$\sigma_{f_{\rm NL}^{\rm obs}} = \frac{1}{4}\sqrt{\frac{3}{\pi}} f_{\rm NL}^{\rm obs} \langle g_{10} g_{10}^{*} \rangle^{1/2} \tag{6.27}$$

The total modulation amplitude A for the observed (or simulated) CMB sky is then given by

$$A = \sqrt{A_1^2 + A_2^2 + A_3^2} \tag{6.28}$$

The probability distribution function (pdf) of A is the χ distribution with three degrees of freedom (also known as the *Maxwell distribution*):

$$p_\chi(A, \sigma) = \sqrt{\frac{2}{\pi}} \frac{A^3}{\sigma^3} e^{-\frac{A^2}{2\sigma^2}} \tag{6.29}$$

where $\sigma = \left(\sigma^2_{f_{\rm NL}^{\rm obs}} + \sigma^2_{\rm G}\right)^{\frac{1}{2}}$ and the quantity $\sigma^2_{\rm G}$, defined as the variance of the A_i in Gaussian CMB maps, is measured from numerical realisations of Gaussian Sachs-Wolfe CMB maps. The variance $\sigma^2_{f_{\rm NL}^{\rm obs}}$ is instead given by equation (6.27), from which it is directly computed for a given value of $f_{\rm NL}$. Figure 6.1 shows that the distribution of the asymmetry amplitudes obtained from the CMB realisations are in good agreement with the χ distribution given by equation (6.29).

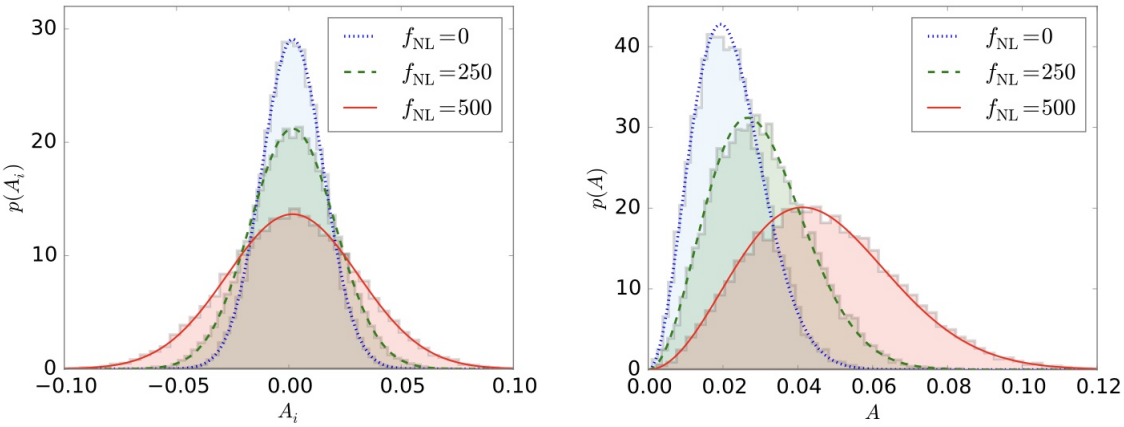

Figure 6.1. Left panel: distribution of power asymmetry A_i (in a particular direction $\mathbf{d}_i$) measured in 10000 simulated CMB sky as described in the text. Right panel: distribution of the amplitude of power asymmetry A from the simulated Gaussian and non-Gaussian maps. Figure adapted from [10].

But how do the predictions of this simple non-Gaussian model compare to the observed power asymmetry in the CMB sky? Adhikari et al. point out that it's not possible to directly compare the amplitudes obtained for their Sachs-Wolfe realisations with the observed values of the power asymmetry. The only way to make a connection is by using the p-value of the asymmetry. For a given measurement of A and the normalised pdf for A, given by equation

(6.29), the p-value is simply defined as [10]

$$\int_A^\infty dA' p_\chi(A', \sigma) \tag{6.30}$$

i.e. as the probability that the observed value of the asymmetry amplitude is greater than some threshold value A. What was found is that an asymmetry amplitude of $A = 0.055$ is approximately 3.3σ i.e. it has a p-value of 0.001 with respect to the distribution of A obtained in the simulated Gaussian Sachs-Wolfe CMB maps (see Figure (6.2)), result which is approximately equal to the more recent reports on the power asymmetry [43, 44].

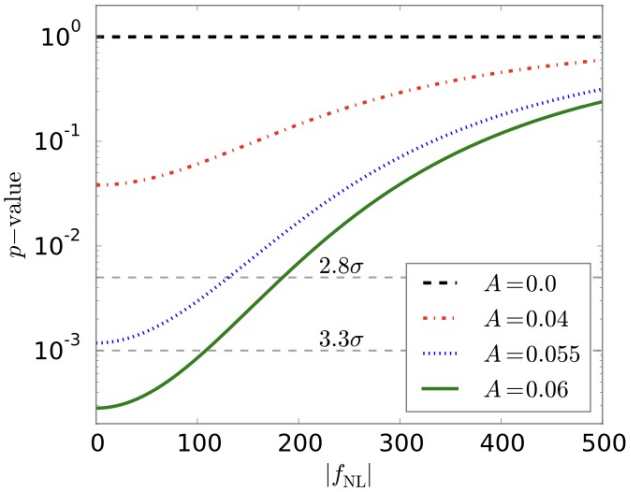

Figure 6.2. The p-value for different values of the asymmetry amplitudes A in a local non-Gaussian model as a function of the value of $|f_{\rm NL}^{\rm obs}|$. Figure adapted from [10].

6.1.2 Generalising the Local Ansatz

The results obtained in the previous section for single-source non-Gaussian models can be easily generalised to the case of two-field models. Let us therefore consider a two-field extension of equation (6.2):

$$\Phi(\mathbf{x}) = \phi(\mathbf{x}) + \sigma(\mathbf{x}) + f_{\rm NL}^{\sigma}\left(\sigma^2(\mathbf{x}) - \langle\sigma^2(\mathbf{x})\rangle\right) \tag{6.31}$$

where $\phi(\mathbf{x})$ and $\sigma(\mathbf{x})$ are two random and uncorrelated Gaussian fields and one assumes that only the field $\sigma(\mathbf{x})$ has local-type non-Gaussianity. Going to Fourier space, the modes of the non-Gaussian field Φ are related to those of the two Gaussian fields by

$$\Phi(\mathbf{k}) = \phi(\mathbf{k}) + \sigma(\mathbf{k}) + f_{\rm NL}^{\sigma}\int \frac{d^3\mathbf{q}}{(2\pi)^3}\left[\sigma(\mathbf{k}-\mathbf{q})\sigma(\mathbf{q}) - \langle\sigma(\mathbf{k}-\mathbf{q})\sigma(\mathbf{q})\rangle\right] \tag{6.32}$$

Following the same procedure as illustrated in the previous section, we eventually get that the 2-point correlation function of the non-Gaussian field in a finite sub-volume $V_{\rm S}$, neglecting the correction arising from the 4-point σ-function, is given by

$$\begin{aligned}
&\left\langle \Phi\left(\mathbf{x}-\frac{\mathbf{r}}{2}\right)\Phi\left(\mathbf{x}+\frac{\mathbf{r}}{2}\right)\right\rangle\Big|_{V_{\rm S}} \approx \\
&\approx \int_{|\mathbf{k}|>k_{\rm min}} \frac{d^3\mathbf{k}}{(2\pi)^3} P_\phi(k) e^{i\mathbf{k}\cdot\mathbf{r}} + \int_{|\mathbf{k}|>k_{\rm min}} \frac{d^3\mathbf{k}}{(2\pi)^3} P_\sigma(k) e^{i\mathbf{k}\cdot\mathbf{r}} \\
&+ 4 f_{\rm NL}^\sigma \int_{|\mathbf{k}|>k_{\rm min}} \frac{d^3\mathbf{k}}{(2\pi)^3} P_\sigma(k) e^{i\mathbf{k}\cdot\mathbf{r}} \int_{|\mathbf{q}|<k_{\rm min}} \frac{d^3\mathbf{q}}{(2\pi)^3} \sigma(\mathbf{q}) \cos\left(\frac{\mathbf{q}\cdot\mathbf{r}}{2}\right) e^{i\mathbf{q}\cdot\mathbf{x}}\Bigg]
\end{aligned} \tag{6.33}$$

Restricting the 2-point correlation function to separations such that $\mathbf{q}\cdot\mathbf{r} \ll 1$, we get that the inhomogeneous power spectrum $P_{\Phi,V_{\rm S}}(k,\mathbf{x})$ is given by

$$P_{\Phi,V_{\rm S}}(k,\mathbf{x}) = P_{\phi,\sigma}(k)\left[1 + 4\xi f_{\rm NL}^\sigma \int_{|\mathbf{q}|<k_{\rm min}} \frac{d^3\mathbf{q}}{(2\pi)^3}\sigma(\mathbf{q}) e^{i\mathbf{q}\cdot\mathbf{x}}\right] \tag{6.34}$$

where $P_{\phi,\sigma}(k) = P_\phi(k) + P_\sigma(k)$ is the mean power spectrum in the larger volume $V_{\rm L}$ and the quantity ξ is defined as the fraction of power in the field σ i.e.

$$\xi \equiv \frac{P_\sigma}{P_{\phi,\sigma}} \tag{6.35}$$

In this model, the non-linearity parameter $f_{\rm NL}^\sigma$ relates to the non-Gaussian amplitude defined from the local bispectrum template of equation (4.4) as $f_{\rm NL}^\sigma = f_{\rm NL}/\xi^2$ [136]. Therefore, equation (6.34) can be also rewritten as:

$$P_{\Phi,V_{\rm S}}(k,\mathbf{x}) = P_{\phi,\sigma}(k)\left[1 + 4\frac{f_{\rm NL}}{\xi} \int_{|\mathbf{q}|<k_{\rm min}} \frac{d^3\mathbf{q}}{(2\pi)^3}\sigma(\mathbf{q}) e^{i\mathbf{q}\cdot\mathbf{x}}\right] \tag{6.36}$$

As seen in the previous section, the imprint of this inhomogeneous power spectrum on the CMB can be described in terms of a multipole expansion:

$$P_{\Phi,V_{\rm S}}(k,\hat{\mathbf{n}}) = P_{\phi,\sigma}(k)\left[1 + f_{\rm NL}\sum_{l=0}^{\infty}\sum_{m=-\ell}^{\ell} g_{\ell m}^\sigma Y_{\ell m}(\hat{\mathbf{n}})\right] \tag{6.37}$$

where the harmonic coefficients $g_{\ell m}^\sigma$ are given by

$$g_{\ell m}^\sigma = \frac{16\pi}{\xi} i^\ell \int_{|\mathbf{q}|<k_{\rm min}} \frac{d^3\mathbf{q}}{(2\pi)^3} j_\ell(qx)\sigma(\mathbf{q}) Y_{\ell m}^*(\hat{\mathbf{q}}) \tag{6.38}$$

As in the case of the single-source model, the quantity $g^{\sigma}_{\ell m}$ has a fixed value in any single sub-volume $V_{\rm S}$ and when averaged over all the sub-volumes in the larger volume $V_{\rm L}$, $\langle g^{\sigma}_{\ell m}\rangle|_{V_{\rm L}} = 0$. The expected covariance in the large volume $V_{\rm L}$ is non-zero and given by

$$\begin{aligned}\langle g^{\sigma}_{\ell m} g^{\sigma,*}_{\ell' m'}\rangle|_{V_{\rm L}} &= \frac{256\pi^2}{\xi^2}(-i)^{\ell'} i^{\ell} \int_{|\mathbf{q}|<k_{\rm min}} \frac{d^3\mathbf{q}}{(2\pi)^3} j_{\ell}(qx) j_{\ell'}(qx) P_{\sigma}(q) Y^{*}_{\ell m}(\hat{\mathbf{q}}) Y_{\ell' m'}(\hat{\mathbf{q}}) \\ &= \frac{32}{\pi}\frac{1}{\xi^2}\int_{|\mathbf{q}|<k_{\rm min}} dq q^2 j^2_{\ell}(qx) P_{\sigma}(q)\delta_{\ell\ell'}\delta_{mm'} \\ &= \frac{1}{\xi}\langle g_{\ell m} g_{\ell' m'}\rangle|_{V_{\rm L},\xi=1}\end{aligned} \tag{6.39}$$

that is, for the same amplitude of non-Gaussianity observed in the Φ field, the expected covariance of the non-Gaussian modulations in the two-field scenario increases by a factor of $1/\xi$ compared to the single-source ($\xi = 1$) one. As in the single-source scenario, the monopole ($\ell = 0$) contribution to the inhomogeneous power spectrum in the parametrisation of equation (6.37) is not observationally distinguishable and thus can be absorbed in the definition of the isotropic (mean) power spectrum $P_{\phi,\sigma}$, that is:

$$P_{\phi,\sigma}(k) \longrightarrow P^{\rm obs}_{\phi,\sigma}(k) = P_{\phi,\sigma}(k)\left[1 + f_{\rm NL}\frac{g^{\sigma}_{00}}{2\sqrt{\pi}}\right] \tag{6.40}$$

and thus the observed modulated power spectrum can be written as:

$$P^{\rm obs}_{\Phi,V_{\rm S}}(k,\hat{\mathbf{n}}) = P^{\rm obs}_{\phi,\sigma}(k)\left[1 + f^{{\rm obs},\sigma}_{\rm NL}\sum_{m=-1,0,1} g^{\sigma}_{1m} Y_{1m}(\hat{\mathbf{n}})\right] \tag{6.41}$$

where we defined

$$f^{{\rm obs},\sigma}_{\rm NL} \equiv \frac{f_{\rm NL}}{1 + f_{\rm NL}\frac{g^{\sigma}_{00}}{2\sqrt{\pi}}} \tag{6.42}$$

What we argued in the previous section on the power asymmetry arising from random realisations of super-horizon perturbations applies also in the case of the generalised local model given by equation (6.31). Thus, considering again the decomposition of the direction of maximum asymmetry in any three orthonormal directions $(\mathbf{d}_1, \mathbf{d}_2, \mathbf{d}_3)$ on the CMB sky and measuring the dipole amplitude A^{σ}_i as seen in the selected orthonormal direction for each sky such that the observed power spectrum can be rewritten as

$$P^{\rm obs}_{\Phi,V_{\rm S}}(k,\hat{\mathbf{n}}) = P^{\rm obs}_{\phi,\sigma}(k)\left[1 + 2A^{\sigma}_i\cos\theta\right] \tag{6.43}$$

one gets that each contribution to the dipole modulation from the non-Gaussianity in the

two-field scenario is given by

$$A_i^\sigma = \frac{1}{4}\sqrt{\frac{3}{\pi}} f_{\rm NL}^{{\rm obs},\sigma} g_{10}^\sigma \tag{6.44}$$

and the amplitude A_i^σ is normal distributed, with zero mean and standard deviation

$$\begin{aligned} \sigma_{f_{\rm NL}^{{\rm obs},\sigma}} &= \frac{1}{4}\sqrt{\frac{3}{\pi}} |f_{\rm NL}^{{\rm obs},\sigma}| \langle g_{10}^\sigma g_{10}^{\sigma,*} \rangle^{1/2} \\ &= \frac{1}{\sqrt{\xi}} \left[\sigma_{f_{\rm NL}^{\rm obs}}\right]_{\xi=1} \end{aligned} \tag{6.45}$$

This result tells us that if one considers scenarios such that $\xi < 1$, then it's easier to generate the observed hemispherical power asymmetry for smaller values of $f_{\rm NL}^{\rm obs}$.

6.1.3 Beyond the Local Ansatz

In the previous sections we have demonstrated that a dipolar asymmetry is to be expected in models with local-type non-Gaussianity. The scenarios we considered, however, can reproduce the observed asymmetry only if we restrict to the largest scales. Indeed, in order to get a power asymmetry compatible with the data, both the amplitude of the asymmetry and the amplitude of the non-Gaussianity must sharply decrease on smaller scales. In particular, the fact that the asymmetry falls off on small scales implies that shorter scales are more weakly coupled to super-horizon scales than larger scales are. In the generalised local scenario as given by equation (6.31) one could generate a scale-dependent asymmetry simply considering a scale-dependent power fraction i.e. $\xi \to \xi(k)$ since, as can be deduced from the power spectrum in the parametrisation of equation (6.34), a decreasing value of $\xi(k)$ for large k would imply for the modulation of the power spectrum to decrease as well. The question now is whether or not there exist a different non-Gaussian model that could reproduce the observed asymmetry. The answer, as we shall see, turns out to be positive and the plan for this section is to demonstrate first of all that scale-dependent modulations are a generic feature of non-Gaussian models. In order to do that, in the following we will consider the model proposed by Baytaş et al. in [137]. The idea in [137] is to build the non-Gaussian field $\Phi(\mathbf{x})$ from a series of non-local functionals of a Gaussian random field $\phi(\mathbf{x})$ such that in Fourier space the modes of the non-Gaussian field are related to those of Gaussian one by

$$\Phi(\mathbf{k}) = \phi(\mathbf{k}) + f_{\rm NL}\Phi_2(\mathbf{k}) + g_{\rm NL}\Phi_3(\mathbf{k}) + ... \tag{6.46}$$

where $\Phi_2(\mathbf{k})$ and $\Phi_3(\mathbf{k})$ are given by

$$
\begin{aligned}
\Phi_2(\mathbf{k}) &= \frac{1}{2!(2\pi)^3}\int d^3\mathbf{q}_1 \int d^3\mathbf{q}_2\,[\phi(\mathbf{q}_1)\phi(\mathbf{q}_2) - \langle\phi(\mathbf{q}_1)\phi(\mathbf{q}_2)\rangle] \\
&\quad \times N_2(\mathbf{q}_1,\mathbf{q}_2,\mathbf{k})\delta^{(3)}(\mathbf{k}-\mathbf{q}_1-\mathbf{q}_2) \\
\Phi_3(\mathbf{k}) &= \frac{1}{3!(2\pi)^6}\prod_{i=1}^{3}\int d^3\mathbf{q}_i \left[\phi(\mathbf{q}_1)\phi(\mathbf{q}_2)\phi(\mathbf{q}_3) - \sum_{\substack{i=1\\ k\neq j\neq i}}^{3}\phi(\mathbf{q}_i)\langle\phi(\mathbf{q}_j)\phi(\mathbf{q}_k)\rangle\right] \\
&\quad \times N_3(\mathbf{q}_1,\mathbf{q}_2,\mathbf{q}_3,\mathbf{k})\delta^{(3)}(\mathbf{k}-\mathbf{q}_1-\mathbf{q}_2-\mathbf{q}_3)
\end{aligned}
\tag{6.47}
$$

and the n-th order term in the expansion (6.46) is defined by

$$
\begin{aligned}
\Phi_n(\mathbf{k}) &= \frac{(2\pi)^3}{n!}\prod_{i=1}^{n}\int \frac{d^3\mathbf{q}_i}{(2\pi)^3}\,[\phi(\mathbf{q}_1)...\phi(\mathbf{q}_n) - \mathcal{F}(\phi(\mathbf{q}_1)...\phi(\mathbf{q}_n))] \\
&\quad \times N_n(\mathbf{q}_1,...,\mathbf{q}_n,\mathbf{k})\delta^{(3)}(\mathbf{k}-\mathbf{q}_1-...-\mathbf{q}_n)
\end{aligned}
\tag{6.48}
$$

The structure of the subtracted functions $\mathcal{F}(\phi(\mathbf{q}_1)...\phi(\mathbf{q}_n))$ in the above expressions ensures that the mean of $\Phi_n(\mathbf{k})$ is zero, that is $\langle\Phi_n(\mathbf{k})\rangle = 0$, and that from each term we only get contributions to the connected part of the (tree-level) n-point correlation function. The kernels $N_n(\mathbf{q}_1,...,\mathbf{q}_n,\mathbf{k})$ are symmetric in their n entries $\mathbf{q}_n$ and can be chosen to reproduce any (tree-level) $(n+1)$-point correlation function. To study how the level of isotropy breaking is enhanced in such a model when we consider the statistics in a given sub-volume V_S, we can split the Fourier space modes into long ($k_l < k_{min}$) and short-wavelength ($k_s \gtrsim k_{min}$) ones [137, 138]. That is, we can write each of the integrals in equation (6.46) as:

$$
\int \frac{d^3\mathbf{q}}{(2\pi)^3} \longrightarrow \int_{|\mathbf{q}|<k_{min}} \frac{d^3\mathbf{q}}{(2\pi)^3} + \int_{|\mathbf{q}|\gtrsim k_{min}} \frac{d^3\mathbf{q}}{(2\pi)^3}
\tag{6.49}
$$

For example, the integrals in the $\Phi_2(\mathbf{k})$ term in equation (6.46) are split as follows:

$$
\begin{aligned}
\Phi_2(\mathbf{k}) \longrightarrow &\int_{|\mathbf{q}_1|<k_{min}} \frac{d^3\mathbf{q}_1}{(2\pi)^3}\int_{|\mathbf{q}_2|<k_{min}} \frac{d^3\mathbf{q}_2}{(2\pi)^3} \\
&+ \int_{|\mathbf{q}_1|<k_{min}} \frac{d^3\mathbf{q}_1}{(2\pi)^3}\int_{|\mathbf{q}_2|\gtrsim k_{min}} \frac{d^3\mathbf{q}_2}{(2\pi)^3} + (\mathbf{q}_1 \leftrightarrow \mathbf{q}_2) \\
&+ \int_{|\mathbf{q}_1|\gtrsim k_{min}} \frac{d^3\mathbf{q}_1}{(2\pi)^3}\int_{|\mathbf{q}_2|\gtrsim k_{min}} \frac{d^3\mathbf{q}_2}{(2\pi)^3}
\end{aligned}
\tag{6.50}
$$

When considering the statistics in any finite sub-volume V_S the long-long term in the above expansion is just a constant. Therefore, when we write down the full expression for the modes

of the non-Gaussian field well within the sub-volume, we can drop all of the terms of this kind, meaning that the only terms of interest are the long-short and short-short ones. With this in mind, performing the long-short mode split for each of the integrals in all of the $\Phi_n(\mathbf{k})$ terms in equation (6.46), we can write the following expression for the modes of the non-Gaussian field as observed in the sub-volume V_S:

$$\begin{aligned}\Phi^{\rm obs}(\mathbf{k}) = \phi(\mathbf{k}) &\left[1 + 2f_{\rm NL}Z_2^{(1)}(\mathbf{k}) + 3g_{\rm NL}Z_3^{(2)}(\mathbf{k}) + ...\right] \\ &+ \left[f_{\rm NL}Z_2^{(0)} + 3g_{\rm NL}Z_3^{(1)}(\mathbf{k}) + ...\right] \\ &+ \left[g_{\rm NL}Z_3^{(0)}(\mathbf{k}) + ...\right] + ...\end{aligned} \tag{6.51}$$

where the quantity $Z_n^{(i)}(\mathbf{k})$ corresponds to a Φ_n term with i integrals over super-horizon modes, that is:

$$\begin{aligned}Z_n^{(i)}(\mathbf{k}) = \frac{(2\pi)^3}{n!}\prod_{\ell=1}^{n-i}\left(\int_{|\mathbf{q}_\ell|\gtrsim k_{\rm min}}\frac{d^3\mathbf{q}_\ell}{(2\pi)^3}\right)\prod_{\ell=n-i+1}^{n}\left(\int_{|\mathbf{q}_\ell|<k_{\rm min}}\frac{d^3\mathbf{q}_\ell}{(2\pi)^3}\right)N_n(\mathbf{q}_1,...,\mathbf{q}_n,\mathbf{k}) \\ \times\left[\phi(\mathbf{q}_1)...\phi(\mathbf{q}_n) - \mathcal{F}(\phi(\mathbf{q}_1)...\phi(\mathbf{q}_n))\right]\delta^{(3)}(\mathbf{k}-\mathbf{q}_1-...-\mathbf{q}_n)\end{aligned} \tag{6.52}$$

and the numerical pre-factors account for the fact that the integrals in $\Phi_n(\mathbf{k})$ are symmetric in the $\mathbf{q}_n$, so that equal contributions come from choosing any of the momenta to be the long-wavelength ones. From equation (6.51) it's clear that the statistics in the sub-volume depend on parameters that control the size of all higher-order, tree-level correlations. Therefore, in general, the observed anisotropy is probing features of both the bispectrum and the trispectrum, and possibly beyond [11].

Statistical Anisotropies from General Bispectra

The statistical shift to the small-volume power spectrum is given by the linear term in equation (6.51), which regroups all the terms with a single integral over a sub-horizon mode. Following the same procedure as in the case of the local and generalised local ansatz, we get that the 2-point correlation function of the non-Gaussian field in a finite sub-volume V_S, taking into account for the moment only the correction arising from the 3-point function and restricting ourselves to separations such that $\mathbf{q}\cdot\mathbf{r} \ll 1$, gives that

$$P_{\Phi,V_S}(k,\mathbf{x}) \approx P_\phi(k)\left[1 + 2f_{\rm NL}\int_{|\mathbf{q}|<k_{\rm min}}\frac{d^3\mathbf{q}}{(2\pi)^3}\phi(\mathbf{q})N_2(\mathbf{q},-\mathbf{k},\mathbf{q}-\mathbf{k})e^{i\mathbf{q}\cdot\mathbf{x}}\right] \tag{6.53}$$

It is clear from the above result that scale-dependent power modulations are indeed a generic feature of non-Gaussian models beyond the local ansatz, being the k-dependence encoded in

the kernel N_2. In particular, the quadratic kernels for the local, equilateral and orthogonal bispectrum templates given, respectively, by equations (4.4), (4.6) and (4.7), are given by [137]

$$\begin{aligned} N_2^{\rm local} &= 2 \\ N_2^{\rm equil} &= \frac{4q^2 - 2kq}{k^2} \\ N_2^{\rm ortho} &= \frac{2q^2}{k^2} \end{aligned} \tag{6.54}$$

The imprint of the inhomogeneous power spectrum (6.53) on the CMB can be described, as usual, in terms of a multipole expansion with harmonic coefficients $g_{\ell m}$ given in this case by

$$g_{\ell m}(k) = 8\pi i^\ell \int_{|\mathbf{q}|<k_{\rm min}} \frac{d^3\mathbf{q}}{(2\pi)^3} j_\ell(qx)\phi(\mathbf{q})N_2(\mathbf{q}, -\mathbf{k}, \mathbf{q}-\mathbf{k})Y^*_{\ell m}(\mathbf{q}) \tag{6.55}$$

As in the case of the local and generalised local models discussed in the previous sections, the quantity $g_{\ell m}$ has a fixed value in any single sub-volume $V_{\rm S}$ and when averaged over all the sub-volumes in the larger volume $V_{\rm L}$, $\langle g_{\ell m}\rangle|_{V_{\rm L}} = 0$. The expected covariance in the large volume $V_{\rm L}$ is non-zero and given by

$$\langle g_{\ell m} g^*_{\ell' m'}\rangle|_{V_{\rm L}} = \frac{8}{\pi}\int_{|\mathbf{q}|<k_{\rm min}} dq q^2 j^2_\ell(qx) P_\phi(q) \left[N_2(\mathbf{q}, -\mathbf{k}, \mathbf{q}-\mathbf{k})\right]^2 \delta_{\ell\ell'}\delta_{mm'} \tag{6.56}$$

If we consider either the kernel for equilateral or orthogonal-type non-Gaussianity it is straightforward to see that both the monopole ($\ell = 0$) and the dipole ($\ell = 1$) contributions to the modulated power spectrum are observable. For example, Figure 6.3 shows the expected dipolar modulation of the power spectrum for large amplitude local, equilateral and orthogonal-type non-Gaussianity: the magnitudes of the modulations are smaller compared to the local case and thus for the effect to be interesting a very large amplitude of $f_{\rm NL}^{\rm equil}$ or $f_{\rm NL}^{\rm ortho}$ is required.

Statistical Anisotropies from a Large Collapsed-limit Trispectrum

What would now happen if we were to take into account also the contribution from higher-order correlation functions? In general, the presence of correlations beyond the bispectrum can alter the shape of lower-order functions in any finite sub-volume [137, 138]. As pointed out by Adhikari et al. in [11], particularly relevant for the observed power asymmetry is the case of non-Gaussian models where the collapsed limit of the 4-point function, parametrised by $\tau_{\rm NL}$, is larger than it would be from the simple local ansatz given by equation (6.2). An interesting example of this type, that naturally gives a scale-dependent dipolar asymmetry, is that of the

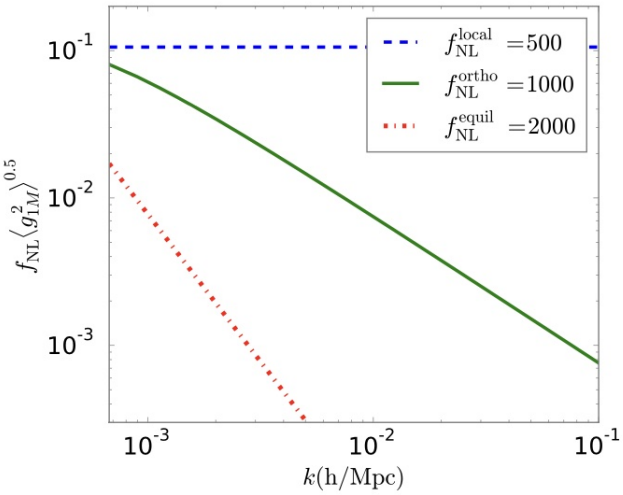

Figure 6.3. The expected dipolar modulation of the power spectrum for large amplitude local, equilateral and orthogonal-type non-Gaussianity. Figure adapted from [10].

quasi-single field inflationary model [139] which features a massless inflaton φ field weakly coupled to a massive extra scalar field σ. The collapsed-limit trispectrum of quasi-single field models of inflation has the form [140]:

$$T_\Phi(k_1,k_2,k_3,k_4) = 4\tau_{\rm NL}P_\Phi(k_1)P_\Phi(k_3)P_\Phi(k_{12})\left(\frac{k_{12}}{\sqrt{k_1k_3}}\right)^{3-2\nu} + \text{ perms.} \tag{6.57}$$

with $\nu \equiv (9/4 - m_\sigma^2/H^2)^{1/2}$, where m_σ is the mass of the additional scalar field, which determines the scaling of the collapsed-limit trispectrum, and H is the Hubble rate during inflation. In the language of the model (6.51), such an example would require us to consider an additional cubic kernel N_3 to subtract-off the sub-leading contribution from the quadratic kernel N_2 and add back the same shape, but with an appropriately scaled coefficient [138]. By doing that, we would eventually get that for such a non-Gaussian model the shift to the small-volume power spectrum is given by [141]

$$P_{\Phi,V_{\rm S}} \approx P_\phi(k)\left[1 + 4\sqrt{\tau_{\rm NL}}\int \frac{d^3\mathbf{q}}{(2\pi)^3}\phi(\mathbf{q})\left(\frac{\mathbf{q}}{\sqrt{\mathbf{k}}}\right)^{\frac{3}{2}-\nu} e^{i\mathbf{q}\cdot\mathbf{x}}\right] \tag{6.58}$$

The imprint of this inhomogeneous power spectrum on the CMB fluctuations can be described, as usual, in terms of a multipole expansion with harmonic coefficients and expected variance in the larger volume in this case given by

$$\begin{aligned} g_{\ell m}(k) &= 16\pi i^{\ell}\sqrt{\tau_{\rm NL}}\int \frac{d^3\mathbf{q}}{(2\pi)^3} j_{\ell}(qx)\phi(\mathbf{q})\left(\frac{\mathbf{q}}{\sqrt{\mathbf{k}}}\right)^{\frac{3}{2}-\nu} Y^*_{\ell m}(\hat{\mathbf{q}}) \\ \langle g_{\ell m} g^*_{\ell' m'}\rangle &= \frac{32}{\pi}\tau_{\rm NL}\int dq q^2 j^2_{\ell}(qx) P_{\phi}(q)\left(\frac{\mathbf{q}}{\sqrt{\mathbf{k}}}\right)^{3-2\nu} \delta_{\ell'\ell}\delta_{m'm} \end{aligned} \tag{6.59}$$

Figure 6.4 shows the expected dipolar ($\ell = 1$) and quadrupolar ($\ell = 2$) modulations of the power spectrum for such a non-Gaussian model choosing the trispectrum amplitude to be $\tau_{\rm NL} = 10^5$ and assuming $m_\sigma = 0.9H$ i.e. $\nu = 1.2$.

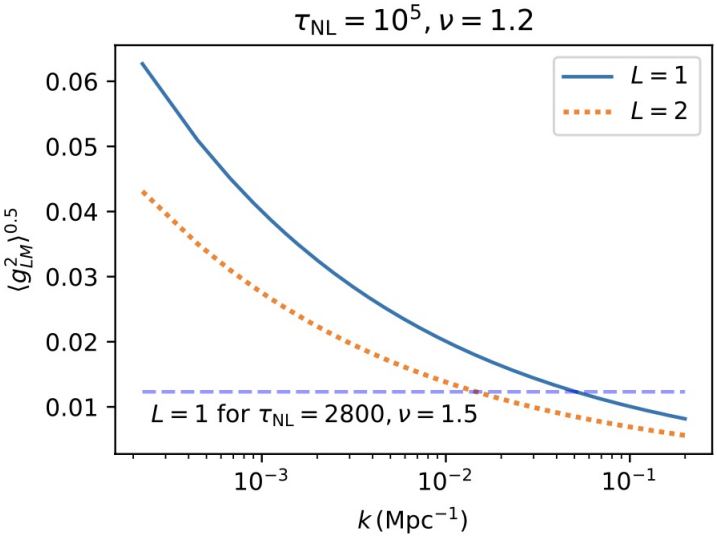

Figure 6.4. Expected dipolar ($\ell = 1$) and quadrupolar ($\ell = 2$) modulations of the power spectrum for a non-Gaussian model characterised by a large trispectrum in the collapsed limit. Also shown is the expected dipolar modulation for the same model with a massless σ (i.e. $\nu = 1.5$) and assuming for the $\tau_{\rm NL}$-amplitude the empirical constraint from *Planck* 13 nominal-mission temperature data [74]. Figure adapted from [141].

6.1.4 Statistical Anisotropies from a Scale-Dependent Local Bispectrum

Now that we have demonstrated that scale-dependent modulations are a generic feature of non-Gaussian models we will attempt to construct a scenario more likely to be preferred by the data starting from the results we obtained in Section 6.1.1. To match the scale dependence of the observed power asymmetry, we first of all require the strength of the coupling between sub-horizon and long-wavelength background modes to be scale-dependent.

This scale-dependence can be parametrised by introducing two bispectral indices, such that the inhomogeneous power spectrum observed in our sky can be written as:

$$P_{\Phi,V_{\rm S}}(k,\mathbf{x}) = P_{\phi}(k)\left[1+4f_{\rm NL}(k_0)\left(\frac{k}{k_0}\right)^{n_{\rm f}}\int_{|\mathbf{q}|<k_{\rm min}}\frac{d^3\mathbf{q}}{(2\pi)^3}\left(\frac{q}{k_0}\right)^{\alpha}\phi(\mathbf{q})e^{i\mathbf{q}\cdot\mathbf{x}}\right] \tag{6.60}$$

Here the parameter $n_{\rm f}$ captures the scale-dependence in our observed sub-volume $V_{\rm S}$ and the parameter α captures the scale-dependence of the coupling strength to the long-wavelength modes. In particular, $n_{\rm f} < 0$ turns off the power asymmetry on short scales, whilst the parameter $\alpha < 0$ results in an enhancement of the sensitivity of the model to infrared modes. Notice that even though we used $f_{\rm NL}$ to denote the coefficient in equation (6.60) a similar expression can be derived from higher-order correlation functions. Since to constrain both the parameters in equation (6.60) we would need more than one additional measurement[2] and here we consider only the large-scale power suppression in the temperature data, we restrict ourselves to the case with just one additional parameter, setting $\alpha = 0$. Let us then consider the case of a local-type bispectrum with amplitude depending on the scale of the short-wavelength mode k as:

$$f_{\rm NL}(k) = f^0_{\rm NL}\left(\frac{k}{k_0}\right)^{n_{f_{\rm NL}}} \tag{6.61}$$

where, as we have already seen in the Chapter 4, $f^0_{\rm NL}$ is the amplitude of $f_{\rm NL}$ measured at some pivot scale k_0 and $n_{f_{\rm NL}}$ is a constant, which in the parametrisation of equation (6.60) coincides with the parameter $n_{\rm f}$. Following the procedure illustrated in the previous sections, it is straightforward to see that such a scale-dependent local-type non-Gaussian model not only gives rise to a scale-dependent power asymmetry, but it also generates a scale-dependent modulation of the power spectrum amplitude that can provide a possible explanation to an anomalous power deficit in the low-ℓ ($\ell < 40$) multipoles range observed in both WMAP and *Planck* temperature data with a significance of $2-3\sigma$ (see e.g. [145, 42]). Figure 6.5 shows the effects of such a simple scale-dependent non-Gaussian model in the bispectrum (top panel), the power asymmetry amplitude (middle panel) and the modulation of the isotropic power spectrum amplitude (bottom panel).

[2]For example, one could get additional data from large-scale polarisation measurements [142], from galaxy surveys [143] or from 21-cm fluctuations [144].

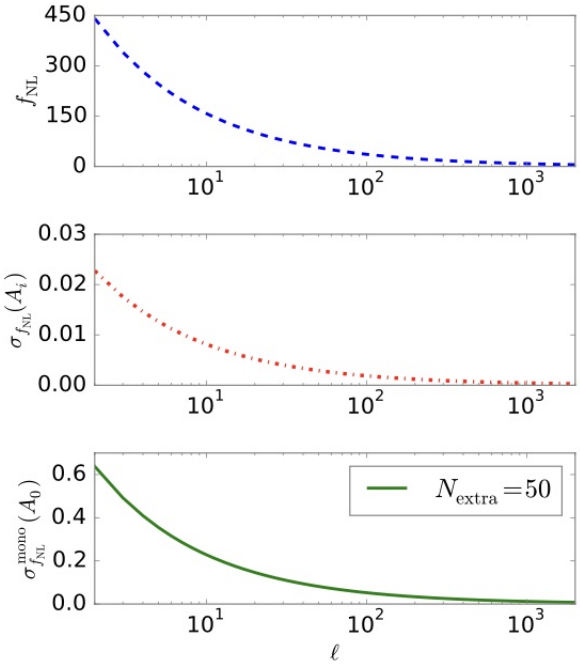

Figure 6.5. Plot of $f_{\rm NL}$, $\sigma_{f_{\rm NL}}(A_i)$ and $\sigma^{mono}_{f_{\rm NL}}(A_0)$ for a number of super-horizon e-folds of $N_{\rm extra} = 50$ as a function of the multipole number ℓ for a simple non-Gaussian model given by $f_{\rm NL}(\ell) = 50(\ell/60)^{-0.64}$. A different choice for $f^0_{\rm NL}$ only rescales the lines above. Figure adapted from [10].

We conclude by observing that the scale-dependent modulation generated by the scale-dependent local-type non-Gaussian model as given by equation (6.61) can also be interpreted in terms of an asymmetry in the spectral index of the observed power spectrum $P_{\Phi,V_{\rm S}}$, that is:

$$\left.\frac{d\ln P_{\Phi,V_{\rm S}}}{d\ln k}\right|_{k_0} = (n_{\rm s}-1)_\phi + n_{f_{\rm NL}}\frac{\Delta P(k_0,\mathbf{x})}{1+\Delta P(k_0,\mathbf{x})} \tag{6.62}$$

where $(n_{\rm s}-1)_\phi$ is the (scalar) spectral index of the Gaussian field ϕ and

$$\Delta P(k_0,\mathbf{x}) = 4f^0_{\rm NL}\int_{|\mathbf{q}|<k_{\rm min}}\frac{d^3\mathbf{q}}{(2\pi)^3}\phi(\mathbf{q})e^{i\mathbf{q}\cdot\mathbf{x}} \tag{6.63}$$

is the super cosmic variance contribution.

6.2 Non-Gaussian Covariance of Statistical Estimators

In [11], Adhikari et al. extend their analysis on the modulation effect of scale-dependent primordial non-Gaussianity in the CMB fluctuations to non-Gaussian models with scale-dependent local-type trispectra and a large collapsed-limit signal, and they do so by computing covariances of statistical estimators of 2-point functions. This approach, whilst in a way

similar to the one introduced in [10] and discussed in the previous sections[3], is more general, since it allows to simultaneously consider the effect on the modulations expected in the CMB polarisation and forecast the improvement in trispectrum constraints when adding polarisation data.

6.2.1 Dipolar Asymmetry from a Scale-dependent Trispectrum

The role of polarisation data in helping pin down whether or not the observed dipolar asymmetry is of primordial origin has been previously discussed in literature: in [142], for example, Contreras et al. attempt to construct position- or k-space models that naturally give a scale-dependent dipolar asymmetry, making use of a statistical estimator to extract the modulation parameters for a given model from data or simulations. Somewhat similarly, in [11] Adhikari et al. write down the general expressions for the covariances of dipole modulation estimators in presence of a trispectrum and use them to generate realisations of the estimators and study the expected constraints by using *Planck* 2015 temperature and E-mode polarisation data. As we have already seen in Section 5.2.1, the statistics of the observed power asymmetry in a finite volume can be modeled as a spatial modulation of the observed CMB temperature fluctuations. That is, one can write the temperature fluctuation field as follows:

$$\Theta(\hat{\mathbf{n}}) = \left[1 + A\,(\hat{\mathbf{n}} \cdot \hat{\mathbf{p}})\right] \Theta_0(\hat{\mathbf{n}}) \tag{6.64}$$

where $\hat{\mathbf{n}}$ is the direction of observation, $\hat{\mathbf{p}}$ is the direction of the asymmetry and A is the amplitude. The dipole dependence on the direction can be expressed in terms of $\ell = 1$ spherical harmonics as follows [146]:

$$A\,(\hat{\mathbf{n}} \cdot \hat{\mathbf{p}}) = 2\sqrt{\frac{\pi}{3}}\left(A_{+}Y_{1-1}(\hat{\mathbf{n}}) - A_{-}Y_{1+1}(\hat{\mathbf{n}}) + A_{z}Y_{10}(\hat{\mathbf{n}})\right) \tag{6.65}$$

where $A_{\pm} \equiv (A_x \pm iA_y)/\sqrt{2}$. Exploiting the fact that in harmonic space a dipole modulation is equivalent to the coupling of ℓ to $\ell \pm 1$ modes, one can then define the following dipole modulation estimators [11]:

$$\begin{aligned}
\Delta\hat{X}_0^{wx}(\ell) &= \frac{1}{(2\ell+1)\sqrt{C_\ell^{ww}C_{\ell+1}^{xx}}} \sum_{m=-\ell}^{\ell} a_{\ell m}^{w,*} a_{\ell+1,m}^{x} \\
\Delta\hat{X}_1^{wx}(\ell) &= \frac{1}{(2\ell+1)\sqrt{C_\ell^{ww}C_{\ell+1}^{xx}}} \sum_{m=-\ell}^{\ell} a_{\ell m}^{w,*} a_{\ell+1,m+1}^{x}
\end{aligned} \tag{6.66}$$

[3] In [11], Adhikari et al. use a framework where the observed power asymmetry arises spontaneously as the result of looking at a sub-volume of a larger space whose fluctuations are described by an isotropic but non-Gaussian statistics, exactly as in [10].

where w, x can either be T, E, describing the temperature and E-mode fluctuations respectively, and the C_ℓs are the CMB angular power spectra of the best-fit Cosmology. For models in which a CMB power asymmetry is generated by explicitly changing the power spectrum, the mean of the estimators $\Delta\hat{X}_M$, with $M = 0, 1$, is non-zero i.e. $\langle\Delta\hat{X}_M\rangle \neq 0$. On the other hand, in models characterised by a significant level of non-Gaussianity in the primordial fluctuations, it is possible for the assumption of global statistical isotropy to hold i.e. $\langle\Delta\hat{X}_M\rangle = 0$, with the expected cosmic variance of the CMB dipolar modulation enhanced by correlations between modes having different wavelengths [10]. Note that the $\Delta\hat{X}_0(\ell)$ are real, whilst the $\Delta\hat{X}_1(\ell)$ are complex, with $\Delta\hat{X}_{-1}(\ell) = -\Delta\hat{X}_1^*(\ell)$, and thus among the two estimators there are three degrees of freedom determining the amplitude and the direction of the dipole modulation. Furthermore, to map the definitions (6.66) to the Cartesian components of the dipole modulation parameter A, as defined in equation (6.65), one has to take into account additional ℓ-dependent factors. For large ℓ, these factors approach constant values, such that [11]:

$$A_x \approx 2\mathrm{Re}\Delta\hat{X}_1, \quad A_y \approx 2\mathrm{Im}\Delta\hat{X}_1, \quad A_z \approx \frac{5}{4}\Delta\hat{X}_0 \tag{6.67}$$

Assuming the primordial fluctuations to be Gaussian distributed, the covariance of the dipole modulation estimators is given by

$$\langle\Delta\hat{X}_M^{wx}(\ell)\Delta\hat{X}_{M'}^{yz}(\ell')\rangle = \frac{\delta_{MM'}\delta_{\ell\ell'}}{2\ell+1}\frac{C_\ell^{yz}C_{\ell+1}^{xz}}{\sqrt{C_\ell^{ww}C_{\ell+1}^{xx}C_{\ell'}^{yy}C_{\ell'+1}^{zz}}} \tag{6.68}$$

If the fluctuations are non-Gaussian, the covariance of the dipole modulation estimators depends instead on a particular configuration of the CMB trispectrum, that is

$$\langle\Delta\hat{X}_M^{wx}(\ell)\Delta\hat{X}_{M'}^{yz}(\ell')\rangle|_{\mathrm{NG}} = \delta_{MM'}\frac{\sum_{m,m'=-\ell}^{\ell}\langle a_{\ell m}^w a_{\ell+1,m+M}^{x,*} a_{\ell' m'}^{y,*} a_{\ell'+1,m'+M'}^z\rangle_c}{(2\ell+1)(2\ell'+1)\sqrt{C_\ell^{ww}C_{\ell+1}^{xx}C_{\ell'}^{yy}C_{\ell'+1}^{zz}}} \tag{6.69}$$

where the subscript c denotes the *connected* part of the CMB trispectrum. To compute the CMB trispectrum, we now follow one of the methods illustrated by W. Hu in [67] and already introduced in Chapter 4: that is, we construct the CMB trispectrum from a "reduced function" which automatically enforces on the angular 4-point harmonic spectrum the desired rotational, permutation and parity symmetries, and whose explicit expression depends on the specific model of the primordial trispectrum. In [11], Adhikari et al. consider a scale-dependent local τ_{NL}-trispectrum of the form [65]:

$$T_\Phi(k_1, k_2, k_3, k_4) = \tau_{\mathrm{NL}}^0\left(\frac{k_2 k_4}{k_0}\right)^n [P_\Phi(k_1)P_\Phi(k_3)P_\Phi(k_{13}) + 11 \quad \text{perms.}] \tag{6.70}$$

where $k_{ij} = |\mathbf{k}_i + \mathbf{k}_j|$, n describes the scale-dependence of the trispectrum amplitude and

$\tau_{\rm NL}^0$ is the amplitude at some pivot scale k_0, assumed to be $k_0 = 0.05$ Mpc^{-1}. Similar to the calculations carried out in Section 4.4 for the simple case of the local non-Gaussian initial conditions as given by equation (4.11), we get that the reduced trispectrum in this case is given by

$$\mathcal{T}_{\ell_3\ell_4}^{\ell_1\ell_2}(L) = \tau_{\rm NL}^0 \int dr_1 dr_2 r_1^2 r_2^2 F_L(r_1, r_2) \alpha_{\ell_1}^w(r_1, n) \beta_{\ell_2}^x(r_1) \alpha_{\ell_3}^y(r_2, n) \beta_{\ell_4}^z(r_2) h_{\ell_1\ell_2 L} h_{\ell_3\ell_4 L} \tag{6.71}$$

where

$$\begin{aligned} F_L(r_1, r_2) &= 4\pi \int \frac{dK}{K} P_\Phi(K) j_L(Kr_1) j_L(Kr_2) \\ \alpha_\ell^w(r, n) &= \frac{2}{\pi} \int dk k^2 \left(\frac{k}{k_0}\right)^n g_\ell^w(k) j_\ell(kr) \\ \beta_\ell^x(r) &= 4\pi \int \frac{dk}{k} \mathcal{P}_\Phi(k) g_\ell^x(k) j_\ell(kr) \end{aligned} \tag{6.72}$$

where $g_\ell^x(k)$ is the CMB radiation transfer function and $j_\ell(kr)$ are the spherical Bessel functions. Note that the angular power spectrum C_ℓ^{wx} can also be written as an integral over the comoving distance r, using the quantities $\alpha_\ell(r, n)$ and $\beta_\ell(r)$ as defined above:

$$C_\ell^{wx} = \int dr r^2 \alpha_\ell^w(r, 0) \beta_\ell^x(r) \tag{6.73}$$

Numerically evaluating the reduced trispectrum of equation (6.71) using `CAMB` [70] to obtain the explicit expression for the CMB transfer functions $g_\ell(k)$, Adhikari et al. computed the non-Gaussian covariances for the dipole estimators (6.69). Then, they proceeded to use the full covariance matrix for the dipole modulation estimators to generate realisations of the modulation estimators $\Delta\hat{X}_M$ for various values of $\tau_{\rm NL}$ and n. The full covariance matrix (including the $f_{\rm sky}$ scaling for partial sky coverage and the noise power spectra) is given by

$$\begin{aligned} \mathbf{C} &= \langle \Delta\hat{X}_M^{wx}(\ell) \Delta\hat{X}_{M'}^{yz}(\ell') \rangle \\ &= \frac{1}{(2\ell+1) f_{\rm sky}} \frac{\delta_{MM'}}{\sqrt{C_\ell^{ww} C_{\ell+1}^{xx} C_{\ell'}^{yy} C_{\ell'+1}^{zz}}} \\ &\times \left[\delta_{\ell\ell'} \tilde{C}_\ell^{wy} \tilde{C}_{\ell+1}^{xz} + \frac{1}{2\ell'+1} \sum_{m,m'=-\ell}^{\ell} \langle a_{\ell m}^w a_{\ell+1, m+M}^{x,*} a_{\ell' m'}^{y,*} a_{\ell'+1, m'+M'}^z \rangle_c \right] \end{aligned} \tag{6.74}$$

where $M, M' = 0, 1$, w, x, y, z can be T, E, and $\tilde{C}_\ell^{wy} = C_{\ell,\rm CMB}^{wy} + C_{\ell,\rm noise}^{wy}$, with the noise power

spectrum for *Planck* is approximated using the specifications for two channels as in [147], assuming $f_{\rm sky} = 0.65$. Making use of the realisations of the modulation estimators $\Delta\hat{X}_M$ they obtained from equation (6.74), Adhikari et al. measured the best-fit dipole amplitude and scale-dependence, (A, n), by fitting to a phenomenological ℓ-dependent model given by

$$A(\ell) = A(\ell_0)\left(\frac{\ell}{\ell_0}\right)^n \tag{6.75}$$

where they choose $\ell_0 = 300$. Based on the distribution of (A, n) they obtained, they choose their fiducial scale-dependent trispectrum parameters values to be $\tau_{\rm NL} = 2\times10^4$ and $n = -0.68$.

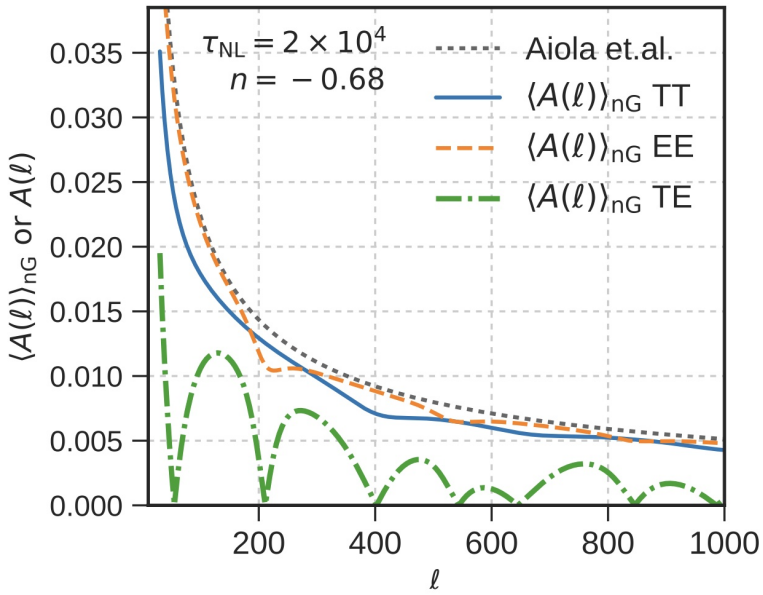

Figure 6.6. Expected ℓ-dependent amplitude of dipole modulation for a scale-dependent trispectrum as given by equation (6.70) for the chosen fiducial parameters values: $\tau_{\rm NL} = 2 \times 10^4$ and $n = -0.68$. For reference, it is also plotted the best-fit ℓ-dependent dipole modulation amplitude obtained by Aiola et al. in [146], by fitting the *Planck* 2013 temperature data to the phenomenological model (6.75). Figure adapted from [11].

Figure 6.6 shows the expectation value of the non-Gaussian contribution to the dipole modulation amplitude, given by

$$\langle A(\ell)\rangle|_{NG} \equiv \sqrt{\langle A_x^2(\ell)\rangle|_{NG} + \langle A_y^2(\ell)\rangle|_{NG} + \langle A_z^2(\ell)\rangle|_{NG}} \tag{6.76}$$

using the fiducial $(\tau_{\rm NL}, n)$ values. Note that here $A(\ell)$ corresponds to the dipole modulation amplitude as given by equation (6.65). From Figure 6.6 we can see that a scale-dependent trispectrum can generate a scale-depedent dipole modulation of the CMB temperature fluctuations similar to the best- fit values found by [146]. Furthermore, we can see that in general the polarisation asymmetry amplitude is larger than that of the temperature: the

reason is that temperature multipoles get contribution from a wider range of scales, and each modulation multipole roughly traces the average level of modulation over this range of scales. However, if one were to postulate a scale-dependence of the modulation amplitude which increases at smaller scales (i.e. $n > 0$), the temperature modulation amplitudes on average would be larger than the polarisation modulation amplitudes [11].

6.2.2 Isotropic Power Spectrum Modulation from a Scale-dependent Trispectrum

In [11], Adhikari et al. observe that a scale-dependent trispectrum with a large collapsed-limit has also other interesting modulating effects on the temperature and polarisation fluctuations than the one discussed in the previous section, since it also modulates the isotropic angular power spectrum of the CMB. In particular, the presence of a non-zero connected trispectrum induces a covariance between measured angular power spectra at widely separated multipoles:

$$\mathbf{C}(\hat{C}_\ell, \hat{C}_{\ell'}) = \frac{2C_\ell^2}{2\ell+1}\delta_{\ell\ell'} + \frac{1}{(2\ell+1)(2\ell'+1)} \sum_{m,m'=-\ell}^{\ell} \langle a_{\ell m} a_{\ell -m} a_{\ell' m'} a_{\ell' -m'} \rangle_c \tag{6.77}$$

where

$$\hat{C}_\ell = \frac{1}{2\ell+1} \sum_{m=-\ell}^{\ell} a_{\ell m}^* a_{\ell m} \tag{6.78}$$

Let us consider again the scale-depedent $\tau_{\rm NL}$-trispectrum as given by equation (6.70): the isotropic power modulation, given by the second term in equation (6.77), that arises from such a trispectrum is infrared-divergent, because the integral

$$F_{L=0}(r) \propto \int \frac{dK}{K} P_\Phi(K) j_0^2(Kr) \tag{6.79}$$

receives contributions from arbitrary large wavelength modes. Therefore, in order to study any possible modulations of the isotropic power spectrum arising from the scale-dependent trispectrum (6.70) we need to assume an infrared cut-off $K_{\rm min}$. Furthermore, we also need to assume a form for the primordial power spectrum $P_\Phi(K)$ at large scales. Assuming the near scale-invariant form (i.e. $n_{\rm s} \approx 1$) of the primordial power spectrum to be valid at all scales $K \gtrsim K_{\rm min}$, we get that for $K_{\rm min} r \ll 1$ the integral (6.79) can by approximated as follows [11]:

$$F_{L=0}(r) \approx 4\pi A_\Phi \int_{K_{\rm min}}^{\infty} \frac{dK}{K} j_0^2(Kr) \approx 4\pi A_\Phi \ln\left(\frac{1}{K_{\rm min} r}\right) \tag{6.80}$$

With this approximation, we obtain that for $\ell, \ell' \gg 2$ the non-Gaussian covariance term in equation (6.77) is given by [11]

$$\mathbf{C}_{\rm NG}(\hat{C}_\ell, \hat{C}_{\ell'}) \approx \tau_{\rm NL} \frac{A_\Phi \mathcal{N}}{\pi} \int dr_1 r_1^2 \alpha_\ell(r_1, n)\beta_\ell(r_1) \int dr_2 r_2^2 \alpha_{\ell'}(r_2, n)\beta_{\ell'}(r_2) \tag{6.81}$$

where

$$\mathcal{N} = \ln\left(\frac{1}{K_{\rm min} r_{\rm CMB}}\right) \tag{6.82}$$

with $r_{\rm CMB}$ defined as the comoving distance to the last scattering surface. Figure 6.7 shows the fractional non-Gaussian contribution to the power spectrum covariance (6.77) for $(\tau_{\rm NL}, n) = (2 \times 10^4, n = -0.68)$ and a chosen value of $\mathcal{N}$.

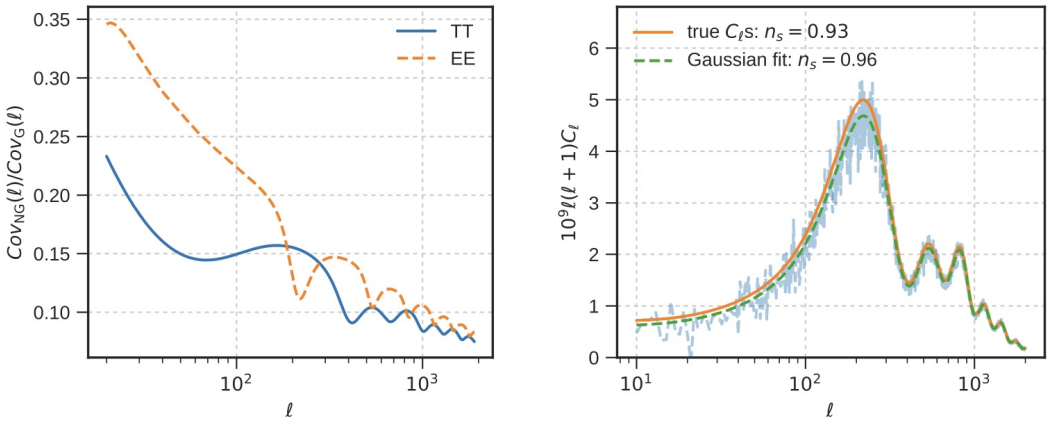

Figure 6.7. Left panel: Diagonal component of the non-Gaussian term in the power spectrum covariance (6.77) as a fraction of the Gaussian term for $(\tau_{\rm NL}, n) = (2 \times 10^4, n = -0.68)$ and $\mathcal{N} = 40$. Right panel: Example of how the inferred spectral index $n_{\rm s}$ can be significantly biased high if the observed power deficit at large scales is due to a scale-depedent trispectrum and the non-Gaussian covariance term (6.81) is ignored in the CMB analysis. For details on the analysis we refer the reader to [11]. Figure adapted from [11].

In standard cosmological analyses, where one assumes the primordial fluctuations to be Gaussian distributed, the second term in equation (6.77) is ignored. However, in [11] Adhikari et al. point out that in the case that the primordial fluctuations do have a scale-dependent trispectrum but one follows the standard cosmological analysis, ignoring the non-Gaussian covariance term in equation (6.77) results in the inference of cosmological parameters that are significantly biased. This is exemplified in the right panel of Figure 6.7: an increasing correlation between the angular power spectra C_ℓ can explain the anomalous power deficit in the low-ℓ multipoles range observed in the CMB temperature data. If one assumes the low-ℓ power deficit to be due to a scale-dependent trispectrum with $(\tau_{\rm NL}, n) = (2 \times 10^4, n = -0.68)$, the decreasing strength of the correlations at larger multipoles means that the inferred value of the spectral index $n_{\rm s}$ is shifted higher than its true value. In particular, Figure 6.7 shows that

realisations of the C_ℓ for the non-Gaussian model (6.70) with $(\tau_{\rm NL}, n) = (2 \times 10^4, n = -0.68)$ and the additional parameter $\mathcal{N} = 40$ can have large-scale power lower than the true value and that, in that case, a CMB analysis ignoring the non-Gaussian covariance term (6.81) produces a biased high estimate of the spectral index $n_{\rm s}$.

6.3 Searching for Isotropic, Non-Gaussian Phenomenological Toy Models

In [12] Hansen et al. propose an alternative approach to the one illustrated by Adhikari et al. in [10, 11]. Whilst the approach of Adhikari et al. relies on the assumption that the observed power asymmetry can be modeled in terms of a dipolar modulation and arises spontaneously as the result of looking at a sub-volume of a larger volume, filled with fluctuations described by an isotropic but non-Gaussian statistics, the approach of Hansen et al. does not relay in the presence of any long-wavelength field. The authors assume that six of the most extensively studied CMB anomalous features, namely:

1. the hemispherical power asymmetry which, as we have seen, has been modeled in terms of a dipole modulation of an isotropic sky and it is detected by *Planck* at scales $\ell < 60$ with a significance of $2 - 3\sigma$;

2. the fact that despite the dipolar modulation being detected only on large scales, it has been shown that the spatial distribution of power on the sky is correlated over a wider range of multipoles i.e. some form of directional asymmetry continues on small scales, with the preferred directions of the dipolar power distribution appearing to be aligned between multipoles;

3. the cold spot, a large, cold region in the CMB map with an angular radius of about $5^\circ - 10^\circ$, centred at Galactic coordinates $(l, b) = (210^\circ, -57^\circ)$ and surrounded by an hot ring, which has been detected with a significance of $2 - 4\sigma$;

4. the anomalous power deficit in the low-ℓ ($\ell < 40$) multipoles range observed in both WMAP and *Planck* temperature data with a significance of $2 - 3\sigma$;

5. the significant alignment between the orientation of the quadrupole ($\ell = 2$) and the octopole ($\ell = 3$) multipole moments;

6. the point-parity asymmetry, that is the fact that on large angular scales, the C_ℓ values for the even multipoles have been found to be consistently lower than those for odd multipoles.

have a common cosmological origin and search for a class of isotropic, non-Gaussian phenomenological toy models, where the non-Gaussianity is responsible for the apparent deviation from statistical isotropy observed in the data, that are able to reproduce them. It should be stressed that Hansen et al. do not attempt to derive a physical model that can be fitted to

the data. Their scope is to guide the theoretical research effort by proposing a general form for a non-Gaussian term that might be the origin of the observed CMB anomalies.

6.3.1 A $g_{\rm NL}$-like Toy Model

In general, as we have seen in Chapter 4, inflationary models may have second-order (i.e. $f_{\rm NL}$-like) and third-order (i.e. $g_{\rm NL}$-like) terms in the primordial gravitational potential. However, Hansen et al. observe that despite the fact that scale-dependent $f_{\rm NL}$ and $\tau_{\rm NL}$ models may reproduce some of the anomalous features listed above (for example, as it has been shown by Adhikari et al. in [10, 11], they can reproduce the anomalies 1. and 4.), they would not generally reproduce also the other anomalies, since in order to do that an enhancement of the original Gaussian fluctuations would be required. This is not easily achievable in either models: for $f_{\rm NL}$-like models, whilst positive fluctuations would be enhanced, the negative ones would be erased, and thus, for example, it would be difficult to reproduce the anomalies 5. and 6. Furthermore, models with a second-order $f_{\rm NL}$ term would give rise to an excess skewness and not the excess kurtosis observed in the CMB anomalous cold spot; in the case of $\tau_{\rm NL}$ models, the enhancement required to reproduce anomalies other than the large-scale power asymmetry is instead difficult due to the fact in such models the non-Gaussian term is strongly influenced by a second, uncorrelated field. Therefore, in [12], Hansen et al. consider the case of scale-dependent $g_{\rm NL}$-like models, proposing the following phenomenological toy model to reproduce the anomalies:

$$\begin{aligned} T(\theta,\phi) &= T_G(\theta,\phi) + \beta \left[T_G(\theta,\phi)\, T_F^2(\theta,\phi) \right]^{\rm filtered} \\ &= T_G(\theta,\phi) + \beta \sum_{\ell m} g_\ell Y_{\ell m}(\theta,\phi) \int d\Omega' Y^*_{\ell m}(\theta',\phi') T_G(\theta',\phi') T_F^2(\theta',\phi') \end{aligned} \tag{6.83}$$

where $T_G(\theta,\phi)$ is an isotropic Gaussian CMB realisation, β is the modulation amplitude, w_ℓ and g_ℓ are two filter functions, corresponding to specific scale-dependences of the primordial $g_{\rm NL}$-trispectrum, and

$$T_F(\theta',\phi') = \sum_{\ell m} w_\ell Y_{\ell m}(\theta,\phi) \int d\Omega' Y^*_{\ell m}(\theta',\phi') T_G(\theta',\phi') \tag{6.84}$$

6.3.2 Reproducing the CMB Anomalous Features

The extent to which the anomalies are present in simulations of the toy model (6.83) is determined by the filters w_ℓ and g_ℓ and the amplitude β, which can be tuned to test whether or not the CMB anomalous features can be reproduced. Hansen et al. observe that not all simulations will reproduce all of the anomalies, with some simulations not showing any sign of anomalous features at all. Nonetheless, in their analysis, Hansen et al. show that a $g_{\rm NL}$-like non-Gaussian term of the form (6.83) can indeed reproduce anomalies from 1. to 6.

For example, Figure 6.8 shows the mean power spectrum of their simulated toy model CMB maps (in green) compared to the *Planck* best-fit theoretical ΛCDM model [7] (in red): one can clearly see how the phenomenological toy model (6.83) reproduces the anomaly 4. (i.e. the low-ℓ power deficit) and the anomaly 6. (i.e. the point-parity asymmetry) for the lowest multipoles, corresponding to the largest angular scales.

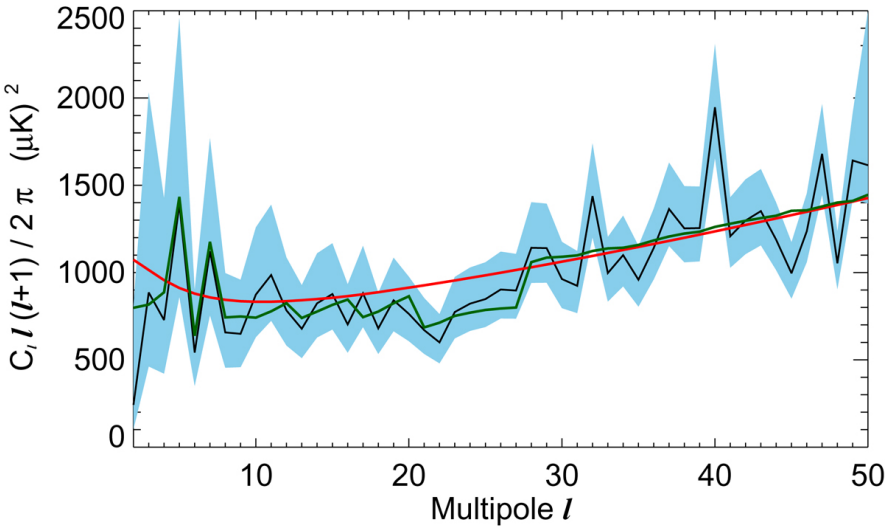

Figure 6.8. Angular power spectrum estimated from *Planck* data (in black) [148]; mean power spectrum of 1000 non-Gaussian simulations (in green); angular power spectrum of *Planck* best-fit ΛCDM model [7] (in red). The blue, shaded area represents the 2σ error bars from [148]. Figure adapted from [12].

Figure 6.9 shows the filters functions w_ℓ and g_ℓ (solid black line) that are used for the majority of the results in [12]. Also shown are additional examples of filters that can reproduce most (or all) of the anomalies. In particular, the black line filters are constructed from a combination of step functions to obtain the following general properties:

- the oscillations in the lowest multipoles of w_ℓ reproduce the point-parity asymmetry for the largest scales; the filter w_ℓ then incrementally rises up to a plateau around $\ell = 21$, allowing the model to reproduce the large trough observed in the power spectrum at this scale. Since for $\ell > 27$ the observed power spectrum is no longer anomalously low with respect to the one of the best-fit model, the filter w_ℓ can be zero for all higher multipoles;

- for the lowest multipoles (that is, up to $\ell = 27$) the filter g_ℓ is negative in order to suppress the power at the largest scales; furthermore, a strong negative value at $\ell = 2$ is not only required to ensure a small quadrupole but also to generate correlations with the octopole, thus reproducing the anomaly 5. At $\ell = 27$, the filter suddenly becomes positive, and in order to reproduce the anomaly 2., it needs to be non-zero up to $\ell \sim 1500$.

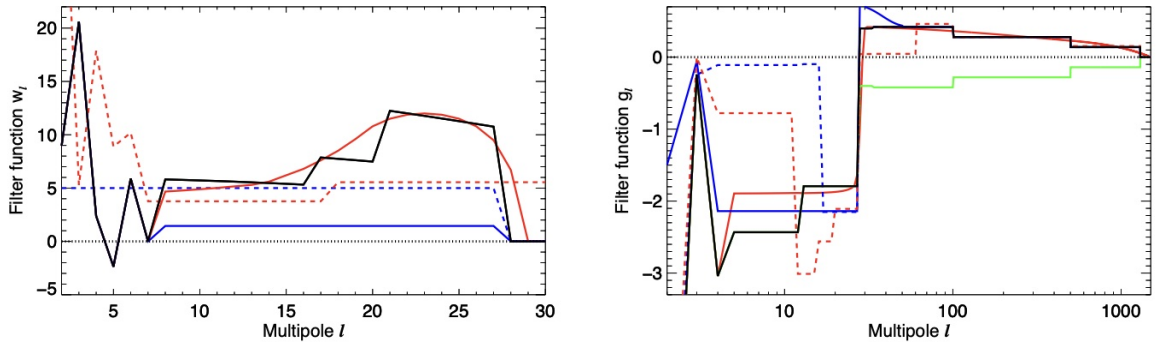

Figure 6.9. The filters w_ℓ (left panel) and g_ℓ (right panel), shown as a solid black line, used in the majority of the results in [12]. Also shown are additional examples of filters that can reproduce most or all of the anomalies. Figure adapted from [12].

The actual process of reproducing the anomalies in the simulated toy model maps can then be summarised as follows:

1. one must apply the filter w_ℓ to the original (simulated) Gaussian map;
2. then, the filtered CMB map just obtained must be squared;
3. the original Gaussian map is then modulated by means of the squared filtered CMB map, thus generating the non-Gaussian term;
4. the g_ℓ filter is then applied to the non-Gaussian term, so that it is ensured that the anomaly 2. does not become too pronounced at small scales;
5. finally, the non-Gaussian term is added to the original Gaussian CMB map to obtain the non-Gaussian CMB map.

Hansen et al. observe that the spectrum used for generating the original Gaussian map is unimportant, since the anomalous CMB features can be reproduced using either a Sachs-Wolfe or pure white noise spectrum. Figure 6.10 shows the non-Gaussian term (middle panel) obtained for a simulated Gaussian map (top panel) with more large-scale power in the northern hemisphere, using a dimensionless[4] amplitude $\beta_{\text{dimensionless}} = 4.4 \times 10^6$ and the black filter functions of Figure 6.9. Also shown is the non-Gaussian map (bottom panel) resulting from the addition of the non-Gaussian term to the original Gaussian map: notice, in particular, the presence of a cold spot surrounded by an hot ring (highlighted in the figure by a black circle).

[4]With *dimensionless* amplitude, Hansen et al. refer to the amplitude β determined when the maps are made dimensionless after dividing equation (6.83) by 2.73 K.

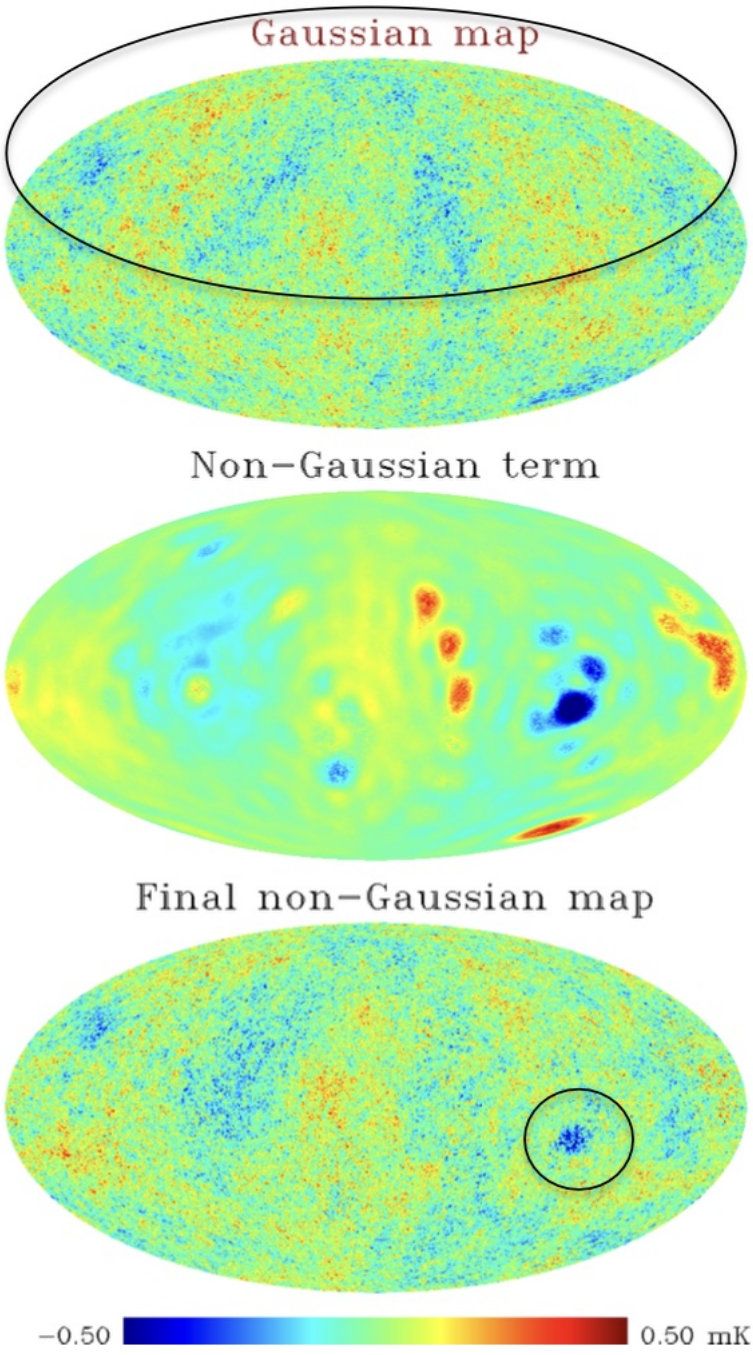

Figure 6.10. Top panel: example of simulated Gaussian map, with the circle denoting the hemisphere with the most large-scale power; middle panel: the non-Gaussian term obtained for said Gaussian map following the procedure described in the text; bottom panel: the non-Gaussian map resulting from the addition of the non-Gaussian term to the original Gaussian map. Figure adapted from [12].

Chapter 7

On the Implications of CMB Anomalies for Early Universe Physics

When we introduced the CMB large-scale anomalies, back in Chapter 5, we provided a brief summary of some of the cosmological mechanisms related to Early Universe physics that have been proposed in literature to explain them, discussing also the difficulties that such proposals have encountered. In this last Chapter we are going to spend a few words more on the topic, focusing in particular on the work of Byrnes et al. who, in the Letter [13] that accompanies the paper [14], report results for a special set of inflationary scenarios that can generate the CMB power asymmetry. We will then conclude our discussion by reporting results from the *Planck* collaboration who, in [15], test specific physical models for the CMB anomalous features using the *Planck* 2018 temperature and polarisation data.

7.1 Power Asymmetry from a Scale-dependent Inflationary Bispectrum

The starting point of the analysis of Byrnes et al. in [13, 14] is the work of Aiola et al. who, using the *Planck* 2013 temperature data, demonstrated that the observed power asymmetry can be approximately fit by a position-dependent power spectrum at the last scattering surface of the form [146]:

$$\mathcal{P}^{\rm obs}(k) \approx \frac{k^3 P(k)}{2\pi^2}\left(1 + 2A(k)\hat{\mathbf{n}}\cdot\hat{\mathbf{p}} + ...\right) \tag{7.1}$$

where $\hat{\mathbf{p}}$ is the direction of maximum asymmetry, $\hat{\mathbf{n}}$ is an arbitrary direction in the sky and $A(k)$ is the asymmetry amplitude which Aiola et al. found to roughly scale as $k^{-0.5}$. One of the interesting inflationary scenarios proposed to account for this anomaly is the one proposed by Erickcek et al. in [131]. In [131], Erickcek et al. observe that single-field models of slow-roll inflation can not generate the observed asymmetry without violating constraints to the homogeneity of the Universe and that, on the other hand, multi-field models of inflation can produce the anomaly without violating the homogeneity constraints. In particular, they suggest that the modulation (7.1) could be generated during an inflationary epoch if the

small-scale 2-point ζ function at wavenumber k is modulated by perturbations of much longer wavelength via local-type non-Gaussianity. In the last decade, many efforts have been made to quantify this effect, with Kanno et al. [149], Lyth [150] and Kobayashi et al. [151] showing that, if one ignores the expected scale-dependence of the bispectrum suggested by the strong scaling of $A(k)$, an inflationary origin of the observed asymmetry would require:

$$\frac{|a_{20}|}{6.9\times10^{-6}}\frac{|f_{\rm NL}|}{10}\simeq 6\left(\frac{A}{0.07}\right)^2\beta \tag{7.2}$$

where a_{20} is the quadrupole of the CMB temperature anisotropy, measured at $|a_{20}|\approx 6.9\times10^{-6}$, and the parameter β is a model-dependent number, which would typically be rather larger than one. This result suggests that the idea of an inflationary origin, at least if produced by the mechanism suggested by Erickcek et al., should be abandoned since it would require $|f_{\rm NL}|\gtrsim 60$, which is clearly in tension with observations. To evade this, equation (7.2) could be weakened by tuning our position on the long-wavelength background to reduce the parameter β. However, Byrnes et al. observe that this approach would introduce a fine-tuning even less likely than the anomaly it seeks to explain. An alternative way out of this lies instead in the requirement that $A(k)$ varies with scales. It could happen that the bispectrum amplitude is large on long-wavelengths but runs small at shorter ones, so that equation (7.2) might then apply only for a small number of wavelength configurations. Therefore, what Byrnes et al. aim to in [13], is to provide an analysis of the CMB temperature bispectrum generated by a scale-dependent inflationary bispectrum compatible with the modulation $A(k)$. In particular, they do so by constructing an explicit model that can be contrived to match all current observations and also serves as a useful example to explain why it is so difficult to built a viable inflationary model.

7.1.1 Biasing the 2-point ζ Function by a Long-wavelength Mode

To generate the observed asymmetry Byrnes et al. focus on the simplest possibility that the non-Gaussian fluctuations are present just in one species, dubbed σ. The first question Byrnes et al. ask themselves in [13] is thus how, within a given volume $V_{\rm S}$ enclosed inside a larger volume $V_{\rm L}\gg V_{\rm S}$ filled with statistically isotropic and homogenous fluctuations, the 2-point ζ function would respond to the presence of a large-amplitude long-wavelength background of σ modes, $\delta\sigma(\mathbf{x})$, with wavenumber $k_{\rm L}\ll k_{\rm S}\propto 1/\lambda_{\rm S}$. To address this they make use of the operator product expansion (OPE), a general method that can be used to study the biasing of any n-point function. Neglecting all gradient-suppressed terms in the expansion, Byrnes et al. found that if the power spectrum $P(k)$ within the larger volume $V_{\rm L}$ satisfies the following relation:

$$\langle\zeta(\mathbf{k}_1)\zeta(\mathbf{k}_2)\rangle|_{\rm L}=(2\pi)^3\delta^{(3)}(\mathbf{k}_1+\mathbf{k}_2)P(k) \tag{7.3}$$

then, within the smaller volume $V_{\rm S}$, it is possible to write [14]:

$$P(k,\mathbf{x})|_{\rm S} = P(k)\left(1+\delta\sigma(\mathbf{x})\rho_\sigma(k)+...\right) \tag{7.4}$$

where they introduce the *linear response function* ρ_σ, defined as follows [13]:

$$\rho_\sigma(k) \equiv \frac{1}{P(k)}\frac{d\ln P(k)}{d\sigma} \tag{7.5}$$

In particular, they found that the OPE gives that [14]:

$$\rho_\sigma(k) \approx \frac{1}{P(k)}\left[\Sigma^{-1}(k_{\rm L})\right]_{\sigma\sigma} B^\sigma(k,k,k_L) \quad \text{if} \quad k \gg k_L \tag{7.6}$$

where $\Sigma^{\sigma\sigma}$ is the power spectrum of the σ fluctuations computed within the larger volume, that is:

$$\langle\sigma(\mathbf{k})\sigma(\mathbf{k}')\rangle|_{\rm L} = (2\pi)^3\delta^{(3)}(\mathbf{k}+\mathbf{k})\Sigma^{\sigma\sigma}(k) \tag{7.7}$$

and B^σ is the bispectrum of the mixed correlation function defined by:

$$\langle\sigma(\mathbf{k}_3)\zeta(\mathbf{k}_1)\zeta(\mathbf{k}_2)\rangle|_{\rm L} = (2\pi)^3\delta^{(3)}(\mathbf{k}_1+\mathbf{k}_2+\mathbf{k}_3)B^\sigma(k_1,k_2,k_3) \tag{7.8}$$

The spatial variation of the long-wavelength background fluctuations can then be modeled as follows [14]:

$$\delta\sigma(\mathbf{x}) \approx E\mathcal{P}_\sigma^{1/2}(k_{\rm L})\cos\left(\mathbf{k}_{\rm L}\cdot\mathbf{x}+\vartheta\right) \tag{7.9}$$

where $\mathcal{P}_\sigma$ is the dimensionless σ power spectrum, the factor E labels the "exceptionality" of the amplitude, with $E=1$ being typical and $E \gg 1$ being substantially larger than typical, and the phase ϑ varies between realisations. As we have seen in Chapter 3, at the largest angular scales the anisotropies in the CMB angular power spectrum are due to the Sachs-Wolfe effect and directly reflects the conditions at the last scattering surface (LSS). Therefore, in order to reproduce these anisotropies, the smaller volume $V_{\rm S}$ must be located on the LSS. In other words, $V_{\rm S}$ must be located at a comoving distance $x_{\rm LSS}$, for which $\mathbf{x} = x_{\rm LSS}\hat{\mathbf{n}}$. If we now parametrise the wavenumber $\mathrm{k_L}$ as:

$$\mathrm{k_L} = \frac{2\pi}{x_{\rm LSS}}\alpha\hat{\mathbf{p}} \tag{7.10}$$

where $\hat{\mathbf{p}}$ is a unit vector and the parameter α is taken to be less than one, so that the walenght

associated to $k_{\rm L}$ is somewhat longer than $x_{\rm LSS}$, then equation (7.4) gives [13]:

$$P(k,\mathbf{x})|_{\rm S} = P(k)\left(1 - C(k) - 2A(k)\frac{\hat{\mathbf{p}}\cdot\mathbf{x}}{x_{\rm LSS}} + ...\right) \tag{7.11}$$

where the quantities $A(k)$ and $C(k)$, are defined by [13]:

$$\begin{aligned} A(k) &= \pi\alpha E\mathcal{P}_\sigma^{1/2}(k_{\rm L})\rho_\sigma(k)\sin\vartheta \\ C(k) &= -E\mathcal{P}_\sigma^{1/2}(k_{\rm L})\rho_\sigma(k)\cos\vartheta = -\frac{A(k)}{\pi\alpha}\cot\vartheta \end{aligned} \tag{7.12}$$

Lyth [152, 150] and Kobayashi et al. [151], who studied the biasing of the 2-point ζ function in the special case of single-source models of slow-roll inflation, obtained results equivalent to equation (7.12) with $\mathcal{P}_\sigma(k)$ replaced by the amplitude of the ζ fluctuations and [13]

$$\rho_\sigma(k) = \frac{12}{5}f_{\rm NL}(k,k,k_{\rm L}) \quad \text{if} \quad k \gg k_L \tag{7.13}$$

Here $f_{\rm NL}(k_1,k_3,k_3)$ is the reduced bispectrum of the 3-point ζ function, given by:

$$\frac{6}{5}f_{\rm NL}(k_1,k_2,k_3) = \frac{B(k_1,k_2,k_3)}{P(k_1)P(k_2) + 2 \text{ cycl. perms.}} \tag{7.14}$$

which in the squeezed limit ($k \sim k_1 \sim k_2 \gg k_L = k_3$) reduces to:

$$\frac{6}{5}f_{\rm NL}(k,k,k_{\rm L}) \approx \frac{B(k,k,k_{\rm L})}{2P(k_{\rm L})P(k)} \tag{7.15}$$

Furthermore, in [152, 150] Lyth suggested that the quantity $C(k)$ could be used to explain another anomalous CMB feature, namely the lack of power on the largest angular scales. This would be particularly desirable since a viable explanation for the CMB power asymmetry should also explain at least another anomaly [153]. However, if that were the case, one would have to ensure that $C(k)$ does not depress power too strongly at small ℓ by imposing a stringent constraint on α which would clearly be an obstacle for construction of viable models.

7.1.2 Building a Successful Model

Once resolved the question of how the 2-point ζ function responds to the presence of a long-wavelength background of σ modes, Byrnes et al. proceed to consider different inflationary scenarios, aiming to construct an explicit model that can produce a ρ_σ function with suitable amplitude and scale-dependence. The first case they consider is that of single-source scenarios, for which the bispectrum in squeezed and equilateral configurations is equal [154, 155] and

thus the response function reduces to:

$$\rho_\sigma = \frac{12}{5} f_{\rm NL}(k,k,k) \tag{7.16}$$

Since in the single-source scenario the asymmetry is independent of the scaling of the σ power spectrum, one has that:

$$A(k) \sim f_{\rm NL}(k,k,k) \tag{7.17}$$

In [65] Byrnes et al. showed that, if the scaling is not too large, the scale-dependence of the reduced bispectrum can be computed as follows:

$$\frac{d\ln A(k)}{d\ln k} \sim \frac{d\ln |f_{\rm NL}(k,k,k)|}{d\ln k} = \frac{5}{6 f_{\rm NL}} \sqrt{\frac{r}{8}} \frac{M_{\rm P}^2 V'''}{3H^2} \tag{7.18}$$

where r is the tensor-to-scalar ratio, $M_{\rm P}^2 = (8\pi G)^{-1/2}$ is the reduced Planck mass and H is the Hubble expansion rate. Therefore, to achieve in such a scenario the required strong scaling of the asymmetry amplitude $A(k)$, Byrnes et al. postulate that $M_{\rm P}^2 V'''/3H^2 \gg 1$. However, within a few e-folds, this requirement would typically result in an unacceptably large slow-roll η_σ parameter, as usual defined by:

$$\eta_\sigma = \frac{V_{\sigma\sigma}}{3H^2} \tag{7.19}$$

that would spoil the observed near scale-invariance of the power spectrum. Furthermore, as pointed out by Byrnes & Tarrant [156], who studied the scale-dependence of $f_{\rm NL}$ in the specific case of a self–interacting curvaton scenario, this would also give rise to many other difficulties. These difficulties include a logarithmic running of the reduced bispectrum with k, which is not an acceptable fit to the scale-dependent modulation of $A(k)$ found by Aiola et al. in [146], and the fact that since equation (7.18) is only large when $f_{\rm NL}$ is suppressed below its natural value, both the amplitude of the $g_{\rm NL}$-trispectrum and the quadrupolar modulation of the small-scale ζ power spectrum would be too large. Therefore, in light of these difficulties, Byrnes et al. choose not to pursue single-source scenarios further and instead proceed to consider the case of multiple-source scenarios, for which a large slow-roll η_σ parameter does not necessarily spoils the scale-invariance of the power spectrum. In particular, they consider the case of multiple-source scenarios in which a single source dominates the 3-point ζ function. In this scenario the response function reads off [14]:

$$\rho_\sigma(k) \sim f_{\rm NL}(k,k,k_{\rm L}) \sim f_{\rm NL}^{1/2}(k,k,k) \sim \frac{\mathcal{P}_\sigma(k)}{\mathcal{P}(k)} \tag{7.20}$$

Therefore, the scale-dependence of the asymmetry is given by [13]:

$$\frac{d\ln A(k)}{d\ln k} \sim \frac{1}{2}\frac{d\ln|f_{\rm NL}(k,k,k)|}{d\ln k} \sim \frac{d\ln}{d\ln k}\left(\frac{\mathcal{P}_\sigma(k)}{\mathcal{P}(k)}\right) \approx 2\eta_\sigma - (n_{\rm s}-1) \tag{7.21}$$

where $\mathcal{P}(k)$ is the small-scale dimensionless ζ power spectrum, $(n_{\rm s}-1)$ is the observed scalar spectral index and η_σ is the slow-roll parameter defined by equation (7.19). Byrnes et al. observe that if one could achieve a constant $\eta_\sigma \approx -0.25$ during the inflationary expansion, then it would be possible to produce an acceptable power law for the asymmetry amplitude. This possibility is throughly explored in [14], where Byrnes et al. consider the following potential with a narrow hilltop at $\sigma = 0$:

$$V(\varphi,\sigma) = V(\varphi)\left(1 - \frac{1}{2}\frac{m_\sigma^2\sigma^2(N)}{M_{\rm P}^2}\right) \tag{7.22}$$

where the inflaton φ is taken to dominate the energy density and thus drives the inflationary expansion. The σ field is assumed to initially lie near the hilltop so that its kinetic energy is subdominant. As inflation goes on, the σ field will roll down the hill and, assuming η_σ to be a constant, its evolution will be described by:

$$\sigma(N) \approx \sigma_* e^{-\eta_\sigma N} \tag{7.23}$$

where '$*$' means that a quantity is evaluated at the initial time and N measures the number of subsequent e-folds. To ensure that the kinetic energy of σ remains subdominant one must prevent it rolling to large field values. This implies that σ_* must be chosen very close (but not too much close) to the hilltop, where its evolution is dominated by quantum diffusion rather than classical evolution. To ensure that σ_* stays outside the diffusion regime, it suffices to require that the classical motion in a single e-fold dominates the quantum motion i.e. $|d\sigma/dN| \gg \delta\sigma/\delta N \sim H_*/(2\pi)$. This, in combination with the requirement that σ must remain subdominant during inflation, gives that:

$$|\sigma_*| \gtrsim \sqrt{\epsilon_\varphi^*\mathcal{P}(k)}\frac{M_{\rm P}}{\eta_\sigma} \tag{7.24}$$

where ϵ_φ is the first slow-roll parameter of the inflaton field, as usual defined by:

$$\epsilon_\varphi = \frac{M_{\rm P}^2}{2}\left(\frac{V_\varphi}{V}\right)^2 \tag{7.25}$$

However, if one considers typical values of $\epsilon \sim \mathcal{O}(10^{-2})$ and imposes $\eta_\sigma = -0.25$, equation (7.24) gives that at inflationary exit $|\sigma(60)| \gtrsim 100 M_{\rm P}$ which is way too large. One could try to solve this problem by tuning the value of ϵ. However, since σ does contribute to ϵ during the

inflationary expansion, this approach would result in a reduction of the bispectrum amplitude to a tiny value and/or in σ to contaminate the power spectrum, thus spoiling scale-invariance. To avoid these issues, Byrnes et al. allow a step in the inflationary potential, so that η_σ can evolve. In particular, they consider the potential [14]:

$$V(\varphi,\sigma) = V_0\left(1+\frac{1}{2}\eta_\varphi\frac{\varphi^2}{M_{\rm P}^2}\right)\left(1+\frac{1}{2}\eta_\sigma(N)\frac{\sigma^2}{M_{\rm P}^2}\right) \tag{7.26}$$

where the scale V_0 should be chosen to match the normalisation of the ζ power spectrum and $\eta_\sigma(N)$ is parametrised as follows:

$$\eta_\sigma(N) = \frac{\eta_2-\eta_1}{2}\tanh\left(\frac{\sigma-\sigma_c}{\sigma_{\rm step}}\right) + \frac{\eta_1+\eta_2}{2} - \frac{\sigma_c}{\sigma_{\rm step}}\frac{\eta_2-\eta_1}{2}\left[1+\tanh\left(\frac{\sigma-\sigma_c}{\sigma_{\rm step}}\right)\right] \tag{7.27}$$

The step in the potential, centred at $\sigma=\sigma_c$ and assumed to have a small characteristic width $\sigma_{\rm step}$, allows the η_σ parameter to rapidly interpolate between two different values, dubbed η_1 and η_2, chosen by Byrnes et al. to be, respectively, $\eta_1=-0.25$ and $\eta_2=-0.08$. In their numerical computations Byrnes et al. take $V_0\approx 10^{-14}M_{\rm P}^4$ and work in a regime where the fluctuations of the φ field dominate the Gaussian part of the primordial perturbations. To make sure of obtaining an acceptable value of the scalar spectral index $n_{\rm s}$, they fix $\eta_\varphi\approx -0.02$. The chosen initial conditions at $N=0$ are $\varphi_*=0.01M_{\rm P}$ and $\sigma_*=8.94427\times10^{-8}M_{\rm P}$. Finally, the η_σ transition is taken to occur at $\sigma_c=3.445\times10^{-6}M_{\rm P}$ with width $\sigma_{\rm step}=10^{-10}M_{\rm P}$, roughly corresponding to 15 e-folds. Using this set of parameters, Byrnes et al. compute estimates of the response functions on isosceles configurations with squeezing $k_3/k_t<0.1$, where $k_t\equiv k_1+k_2+k_3$. In particular, they do so by combining equation (7.6) with numerical computations for the 2-point and 3-point correlation functions of the model (7.26). Their results are plotted in Figure 7.1. The φ response function is reasonably close to scale-invariance, while the σ response function exhibits a strong scale-dependence that can be approximately fit by the power law [14]:

$$\rho_\sigma(k)\approx 5600\left(\frac{k}{k_{\ell=1}}\right)^{-0.405} \tag{7.28}$$

where $k_{\ell=1}=1/1400$ Mpc^{-1} corresponds to $\ell\approx 1$. Equation (7.28) exhibits a scale-dependence that is a roughly acceptable match to the one of the asymmetry amplitude $A(k)$. The reduced bispectrum $f_{\rm NL}(k_1,k_2,k_3)$ computed on the same configurations used to estimate the response functions (also shown in Figure (7.1)) exhibits a similar scaling behaviour, with spectral index -0.404 [14]. What now remains to be checked is whether of not the bispectrum amplitude is compatible with the observational constraints reported by the *Planck* collaboration. It should be stressed, however, that these constraints are limits on the amplitude of scale-independent templates averaged over many configurations and thus can not be related directly

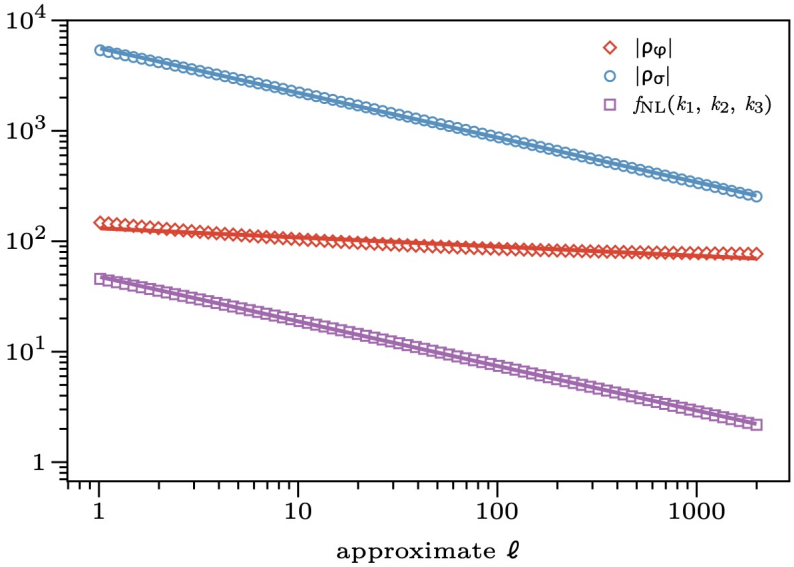

Figure 7.1. The ρ_φ (in red) and ρ_σ (in blue) response functions computed for the step model (7.26) as a function of the approximate multipole $\ell = 1400k$ Mpc, corresponding to the wavenumber k. Also shown is the reduced bispectrum amplitude $f_{\rm NL}(k_1, k_2, k_3)$ (in purple) computed on the same configurations used to estimate the response functions. Figure adapted from [14].

to a bispectrum with a strong scale-dependence [14]. To assess how the estimator for local, equilateral and orthogonal non-Gaussian amplitudes would respond to the bispectrum produced by the model (7.26), Byrnes et al. construct a Fisher matrix estimate. They numerically compute $\sim 5 \times 10^6$ bispectrum configurations covering the multipole range $\ell \sim 1 - 7000$ and use them to predict the observed angular temperature power spectrum. What they found is that the amplitudes that would be measured for a bispectrum generated by the model (7.26) (with the aforementioned choices for the values of its parameters) are of order unity. In particular, they obtain the following estimates [14]:

$$f_{\rm NL}^{\rm local} = 0.25, \quad f_{\rm NL}^{\rm equil} = 0.6, \quad f_{\rm NL}^{\rm ortho} = -1.0 \tag{7.29}$$

which are well within the observational limits reported in Section 4.5. Byrnes et al. conclude their discussion by observing that although the bispectrum used in their analysis to obtain the results (7.29) strictly applies for the model (7.26), they believe it to be a good proxy for any inflationary explanation of the power asymmetry that uses a large η parameter to generate the observed scale-dependence. Finally, it should be stressed that having being successful in constructing a model that gives a response function with an acceptable amplitude and scale-dependence for the asymmetry $A(k)$ doesn't mean that an inflationary explanation should automatically be attractive. To make the model successful, Byrnes et al. have been forced to make a number of arbitrary choices on the initial and final values of the effective σ mass, $\eta_\sigma(N)$, and on the location and the rapidity of the transition it undergoes. Furthermore,

it's also unclear whether or not the model (7.26) can be embedded within a viable Early Universe scenario.

7.2 *Planck*'s Constraints on Physical Models for CMB Anomalies

Having now reached the end of our discussion on the topic of the CMB large-scale anomalies as signatures of non-Gaussianity, in this last section we report (for completeness of information) results from the *Planck* collaboration who, in [15], test specific physical models for the CMB anomalous features using the *Planck* 2018 temperature and polarisation data.

7.2.1 Models with Suppressed Power at Large Scales

The anomalous power deficit in the low-ℓ ($\ell < 40$) multipoles range observed in the temperature data might be explained by models with suppressed primordial perturbations below a given cut-off scale k_c. In particular, this effect may be due to fluctuations at the largest observable scales being generated at the onset of inflation after a prior era of kinetic or radiation domination, or due to the presence of some feature (such as a kink) in the inflaton potential. Within these scenarios, the (dimensionless) primordial power spectrum can be analytically approximated as follows [15]:

$$\ln \mathcal{P}_{\mathcal{R}}(k) = \ln \mathcal{P}_0(k) + \ln \mathcal{Y}(y) \tag{7.30}$$

where $y = k/k_c$ and $\mathcal{Y}(y)$ is a function with $\ln \mathcal{Y}(y) \to 0$ in the limit $k \gg k_c$ that describes the shape of the cut-off and the transition to a power-law spectrum at smaller scales. To compute the CMB angular power spectra for feature models, the *Planck* collaboration employs a modified version of `CAMB`. For all combinations of feature models and data, the parameter space is then sampled using a nested sampling algorithm as implemented in `MultiNest` [157]. The improvement in the fit due to the introduction of a feature is quantified by the effective $\Delta\chi^2 \equiv -2(\ln \mathcal{L}_{\Lambda\mathrm{CDM}} - \ln \mathcal{L}_{\mathrm{feature}})$. The Bayesian evidence [158] against the base ΛCDM model is also computed.

Model 1: Pre-inflationary Kinetic Domination (KD)

If the inflationary phase is preceded by a fast rolling stage, we have that the cut-off function reads off [126]:

$$\mathcal{Y}_{\mathrm{KD}}(y) = \frac{\pi}{16} y |C(y) - D(y)|^2 \tag{7.31}$$

where

$$C(y) = e^{-iy}\left[H_0^{(2)}\left(\frac{y}{2}\right) - \left(\frac{1}{y} + i\right) H_1^{(2)}\left(\frac{y}{2}\right)\right]$$
$$D(y) = e^{iy}\left[H_0^{(2)}\left(\frac{y}{2}\right) - \left(\frac{1}{y} - i\right) H_1^{(2)}\left(\frac{y}{2}\right)\right] \tag{7.32}$$

with $H_0^{(2)}$ and $H_1^{(2)}$ denoting, respectively, the Hankel function of the second kind with order 0 and 1. The best-fit effective $\Delta\chi^2$ and logarithm of the Bayes factors with respect to a featureless power spectrum obtained by the *Planck* collaboration for the KD cut-off model are reported in Table 7.1.

Table 7.1. Best-fit effective $\Delta\chi^2$ and logarithm of the Bayes factors with respect to a featureless power spectrum obtained by the *Planck* collaboration for the KD cut-off model.

	TT	EE	TT,TE,EE
$\Delta\chi^2$	-1.2	0.0	-0.9
$\ln B$	0.0	-0.2	0.0
$\ln_{10}(k_c)$	-3.70	-4.98	-3.72

Model 2: Pre-inflationary Radiation Domination (RD)

If the inflationary phase is preceded by a radiation-dominated phase, we have that the cut-off function reads off [159]:

$$\mathcal{Y}_{\rm RD}(y) = \frac{1}{4y^4}\left|e^{-2iy}(1+2iy) - 1 - 2y^2\right|^2 \tag{7.33}$$

The best-fit effective $\Delta\chi^2$ and logarithm of the Bayes factors with respect to a featureless power spectrum obtained by the *Planck* collaboration for the RD cut-off model are reported in Table 7.2.

Table 7.2. Best-fit effective $\Delta\chi^2$ and logarithm of the Bayes factors with respect to a featureless power spectrum obtained by the *Planck* collaboration for the RD cut-off model.

	TT	EE	TT,TE,EE
$\Delta\chi^2$	-0.2	-4.7	0.0
$\ln B$	-0.8	0.0	-0.7
$\ln_{10}(k_c)$	-4.87	-3.48	-4.86

Model 3: Strobinsky

A kink in the inflaton potential lead to a cut-off function approximately given by [160]:

$$\begin{aligned}\mathcal{Y}_{\rm kink}(y) = 1 - (3R-1)\frac{1}{y}\left[\left(1-\frac{1}{y^2}\sin 2y + \frac{2}{y}\cos 2y\right)\right] \\ + \frac{9}{2}(R-1)^2\frac{1}{y^2}\left(1+\frac{1}{y^2}\right)\left[1+\frac{1}{y^2}+\left(1-\frac{1}{y^2}\right)\cos 2y - \frac{2}{y}\sin 2y\right]\end{aligned} \tag{7.34}$$

where the parameter R denotes the the ratio of the slopes of the inflaton potential before and after the kink. The best-fit effective $\Delta\chi^2$ and logarithm of the Bayes factors with respect to a featureless power spectrum obtained by the *Planck* collaboration for the kink cut-off model are reported in Table 7.3.

Table 7.3. Best-fit effective $\Delta\chi^2$ and logarithm of the Bayes factors with respect to a featureless power spectrum obtained by the *Planck* collaboration for the kink cut-off model.

	TT	EE	TT,TE,EE
$\Delta\chi^2$	-2.1	-7.4	-1.1
$\ln B$	-0.4	0.1	-0.4
$\ln_{10}(k_c)$	-3.05	-3.48	-3.91
R	-0.02	0.33	-0.22

Conclusions

Of note are the relatively high values of the RD and kink cut-off models for polarisation-only data. However, the *Planck* collaboration shows that the best-fit parameters and spectra do not match their counterparts in the temperature data at all, thus strongly suggesting that this is not a physical effect (see Figure 30 in [15]). The Bayesian evidence for all combinations of models and data lies between *barely worth mentioning* $(0-0.5)$ and *substantial* $(0.5-1)$ evidence against the feature models on the Jeffreys scale [161]. This implies that the *Planck* 2018 data do not show a preference for the feature models here considered.

7.2.2 Models for Statistical Anisotropy in the Primordial Fluctuations

In the simplest models violating statistical isotropy, some of the CMB anomalies, such as the power asymmetry, are modeled in terms of a modulation of the temperature field:

$$\Theta(\hat{\mathbf{n}}) = [1 + f(\hat{\mathbf{n}})]\,\Theta_0(\hat{\mathbf{n}}) \tag{7.35}$$

where $\Theta(\hat{\mathbf{n}})$ and $\Theta_0(\hat{\mathbf{n}})$ are, respectively, the modulated and unmodulated (isotropic) CMB temperature fluctuations, $\hat{\mathbf{n}}$ is an arbitrary direction in the sky and $f(\hat{\mathbf{n}})$ denotes the modulating field. If $f(\hat{\mathbf{n}}) = A(\hat{\mathbf{n}}\cdot\hat{\mathbf{p}})$, we have the case of a dipolar modulation with amplitude A and

direction $\hat{\mathbf{p}}$. However, we can also consider higher-order modulations (e.g. a quadrupolar modulation[1]), or mixed modulations (e.g. modulations by a scale-invariant field). Alternatively, we can consider modulations of the position or k-space fluctuations.

Case 1: Curvaton Modulation Model

To explain the observed power asymmetry, the modulated curvaton model [163] employs a gradient in a background curvaton field. In particular, within this scenario, the curvaton field, via a coupling κ, produces nearly scale-invariant CDM isocurvature (CDI) fluctuations as well as a fraction ξ of adiabatic (curvature) fluctuations, with ξ also providing a measure of the amplitude of dipolar modulation. The fraction of CDI fluctuations can be written in terms of these two parameters as follows [163]:

$$\beta_{CDI} = \frac{9\kappa^2\xi}{1+9\kappa^2\xi} \tag{7.36}$$

Using the dipolar asymmetry estimators defined in [164], the *Planck* collaboration finds the posteriors for the modulation parameters κ and ξ. Their results are shown (in red) in Figure 7.2. Also shown (in blue) are the isotropic constraints i.e. constraints from the power spectra via equation (7.36), as well as joined constraints (in black). Despite a substantial amount of the asymmetry (as measured by the parameter ξ) can be captured by the model, the asymmetry and the isotropic posteriors only weakly overlap. Furthermore, no evidence for asymmetry (i.e. no preference for $\xi > 0$) is exhibited by the joint constraints, which treat the isotropic and asymmetry data as independent.

Case 2: Position or k-space Modulation Models

As discussed in [142], position or k-space models that generate a scale-dependent dipolar asymmetry can be constructed employing the formalism introduced in [165]. The idea is to take a portion of the primordial adiabatic fluctuations, dubbed $\widetilde{\mathcal{R}}^{\rm lo}(\mathbf{x})$ and restricted mainly to large scales, to be spatially linearly modulated [165]:

$$\widetilde{\mathcal{R}}^{\rm lo}(\mathbf{x}) = \mathcal{R}^{\rm lo}(\mathbf{x})\left(1 + A\frac{\mathbf{x}\cdot\hat{\mathbf{p}}}{x_{\rm LSS}}\right) \tag{7.37}$$

where $\mathcal{R}^{\rm lo}(\mathbf{x})$ is statistically isotropic with power spectrum $\mathcal{P}^{\rm lo}_{\mathcal{R}}(k)$, A is the modulation amplitude, $\hat{\mathbf{p}}$ is the direction of the modulation and $x_{\rm LSS}$ is the comoving distance to the LSS. This leads to a covariance of the total temperature or polarisation anisotropy multipoles given, to first order in the modulation amplitude, by [165]:

$$\langle a_{\ell m} a^*_{\ell' m'}\rangle = C_\ell \delta_{\ell\ell'}\delta_{mm'} + \frac{\delta C_{\ell\ell'}}{2}\sum_M \Delta X_M \xi^M_{\ell m \ell' m'} \tag{7.38}$$

[1]Such a modulation can be used, for example, to explain the observed alignment of the quadrupole and the octopole [162, 84].

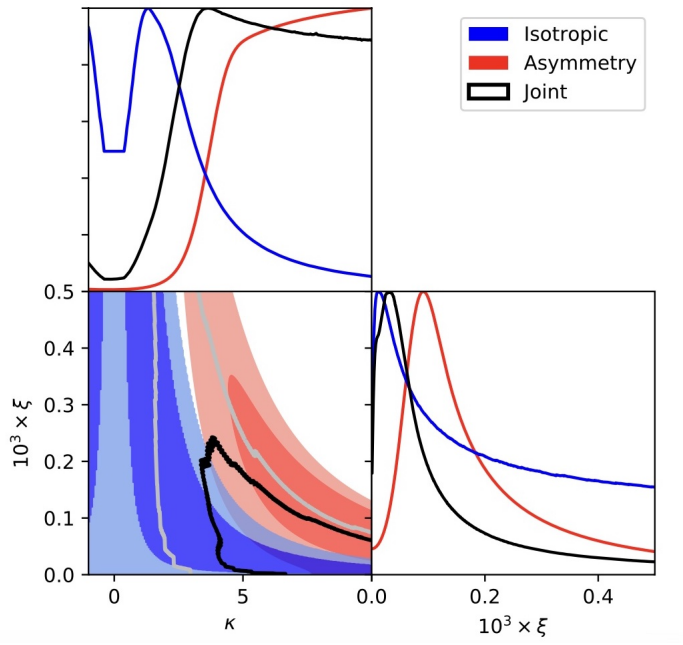

Figure 7.2. Posteriors for the curvaton modulation model parameters κ and ξ. Contours enclose 68% and 95% of the posteriors. Figure adapted from [15].

where $\delta C_{\ell\ell'} \equiv 2(C_\ell^{\rm lo} + C_{\ell'}^{\rm lo})$, ΔX_M denotes the multipole decomposition of $A(\hat{\mathbf{n}} \cdot \hat{\mathbf{p}})$ and the coupling coefficients $\xi^M_{\ell m \ell' m'}$ are defined by:

$$\xi^M_{\ell m \ell' m'} \equiv \sqrt{\frac{4\pi}{3}} \int d\Omega_{\hat{\mathbf{n}}} Y_{\ell' m'}(\hat{\mathbf{n}}) Y_{1M}(\hat{\mathbf{n}}) Y^*_{\ell m}(\hat{\mathbf{n}}) \tag{7.39}$$

For the scale-dependence of the asymmetry spectrum $\mathcal{P}^{\rm lo}_{\mathcal{R}}(k)$, in [15] three phenomenological forms are considered:

1. a tanh model whose asymmetry spectrum, on scales larger than a given cut-off scale k_c, approaches that of the ΛCDM model, $\mathcal{P}^0_{\mathcal{R}}(k)$:

$$\mathcal{P}^{\rm lo}_{\mathcal{R}}(k) = \frac{1}{2}\mathcal{P}^0_{\mathcal{R}}(k)\left[1 - \tanh\left(\frac{\ln k - \ln k_c}{\Delta \ln k}\right)\right] \tag{7.40}$$

2. a power-law model:

$$\mathcal{P}^{\rm lo}_{\mathcal{R}}(k) = \mathcal{P}^0_{\mathcal{R}}(k)\left(\frac{k}{k_0^{\rm lo}}\right)^{n_{\rm s}^{\rm lo}-1} \tag{7.41}$$

   where $n_{\rm s}^{\rm lo}$ and $k_0^{\rm lo}$ are, respectively, the tilt and pivot scale of the modulation. In particular, the *Planck* collaboration consider the case $n_{\rm s}^{\rm lo} \leq n_{\rm s}$ and takes $k_0^{\rm lo} = 1.5 \times 10^{-4}$ Mpc^{-1};

3. a model with a linear gradient in the scalar tilt $n_{\rm s}$:

$$C_\ell^{\rm lo} = -\frac{\Delta n_{\rm s}}{2}\frac{dC_\ell}{dn_{\rm s}} \tag{7.42}$$

Using the maximum likelihood estimators for the modulation defined in [164], the *Planck* collaboration analyses the quantity $\hat{O}_{j0}$, defined as the ratio of the maximum likelihood for a given modulation model j to that of the ΛCDM model. What they found is that, for the models considered, the *Planck* 2018 temperature and polarisation data do not help to decide wether or not we have a physical modulation, with p-values of 30%, 43% and 57% for, respectively, the tanh, power-law and $n_{\rm s}$-gradient models, relative to statistically isotropic polarisation simulations.

Case 3: Quadrupole Modulation Models

In general, for models that give a quadrupolar direction dependence in the primordial power spectrum we have that [15]:

$$\mathcal{P}_\mathcal{R}(k) = \mathcal{P}^0_\mathcal{R}(k)\left[1 + g(k)\left(\hat{\mathbf{k}}\cdot\hat{\mathbf{p}}\right)^2\right] \tag{7.43}$$

which can be rewritten as follows:

$$\mathcal{P}_\mathcal{R}(k) = \mathcal{P}^0_\mathcal{R}(k)\left[1 + \frac{1}{3}g(k) + \sum_m g_{2m}(k)Y_{2m}(\hat{\mathbf{k}})\right] \tag{7.44}$$

where

$$g_{2m}(k) \equiv \frac{8\pi}{15}g(k)Y^*_{2m}(\hat{\mathbf{p}}) \tag{7.45}$$

with $g_{2m}(k)$ satisfying $g_{2,-m}(k) = (-1)^m g^*_{2m}(k)$. In their analysis, the *Planck* collaboration parametrises the scale-dependence of the modulation as a power law with pivot scale $k_* = 0.05\ \text{Mpc}^{-1}$ and spectral index q, that is:

$$g(k) = g_*\left(\frac{k}{k_*}\right)^q \tag{7.46}$$

Constraints on the modulation parameters are obtained by forming quadratic maximum-likelihood estimates, $\hat{g}_{2m}$, for the data and simulations (for details on the analysis refer to [164, 15]). The same analysis is then performed for a completely general form of quadrupolar modulation [15]:

$$\mathcal{P}_\mathcal{R}(k) = \mathcal{P}^0_\mathcal{R}(k)\left[1 + \sum_m g_{2m}\left(\frac{k}{k_*}\right)^q Y_{2m}(\hat{\mathbf{k}})\right] \tag{7.47}$$

The g_* values for the model (7.44), obtained by minimising the χ^2, are reported in Table 7.4. Also shown are the associated p-values, defined as the fraction of isotropic simulations with larger $|g_*|$ than the data. For the model (7.47), results for the quantity $g_2 \equiv \sqrt{\sum_m |g_{2m}|^2/5}$, as well as the associated p-values, are reported in Table 7.5. For brevity, the only results shown are those obtained from SMICA foreground-cleaned maps. In all cases, as quantified by the p-values, there is no significant detection of a quadrupolar modulation and the data are consistent with cosmic variance in a statistically isotropic sky.

Table 7.4. Minimum-χ^2 g_* values and p-values for the quadrupolar modulation (7.44) determined from the SMICA foreground-cleaned maps. The TT results use the multipole range $\ell = 2 - 1200$, while the EE use $\ell = 2 - 850$.

	TT		EE		TT + EE	
q	g_*	p value [%]	g_*	p value [%]	g_*	p value [%]
-2	-6.83×10^{-5}	75.7	1.23×10^{-4}	54.7	-6.90×10^{-5}	75.0
-1	-8.56×10^{-3}	64.7	1.44×10^{-2}	30.0	-6.15×10^{-3}	86.0
0	1.08×10^{-2}	82.7	3.17×10^{-2}	55.3	1.07×10^{-2}	83.0
1	7.77×10^{-3}	82.7	5.09×10^{-2}	24.0	7.75×10^{-3}	82.3
2	4.92×10^{-3}	78.3	5.62×10^{-2}	17.0	4.92×10^{-3}	78.7

Table 7.5. As Table 7.4, but for the quantity $g_2 \equiv \sqrt{\sum_m |g_{2m}|^2/5}$ for the quadrupolar model (7.47).

	TT		EE		TT + EE	
q	g_2	p value [%]	g_2	p value [%]	g_2	p value [%]
-2	3.30×10^{-5}	82.3	9.00×10^{-5}	27.0	3.32×10^{-5}	81.0
-1	4.34×10^{-3}	66.0	6.81×10^{-3}	40.0	3.24×10^{-3}	87.0
0	7.65×10^{-3}	51.7	1.79×10^{-2}	45.7	7.62×10^{-3}	51.7
1	5.39×10^{-3}	58.0	2.95×10^{-2}	12.7	5.38×10^{-3}	58.3
2	3.15×10^{-3}	58.7	3.39×10^{-2}	6.0	3.15×10^{-3}	58.7

Conclusions

The Standard Cosmological Model, also known as the ΛCDM model, currently provides the best-fit theoretical framework of physical and observational Modern Cosmology. In the years, its six main cosmological parameters (see Table 3.2) have been constrained through several, different experimental measurements, one of the most powerful being that of the Cosmic Microwave Background (CMB) temperature and polarisation anisotropies. Even though observations show that the statistical properties of the CMB are consistent with the predictions of the ΛCDM model, both WMAP and *Planck* have detected some features (anomalies) at the largest angular scales that seem to suggest a deviation from the fundamental assumptions of global statistical isotropy and Gaussianity of the ΛCDM model. Our first objective in this Thesis was to explore some of these anomalous features, namely:

- the lack of large-angle correlations i.e. the fact that the temperature 2-point angular correlation function averaged over the complete sky

$$C(\theta) = \langle \Theta(\hat{\mathbf{n}}_1)\Theta(\hat{\mathbf{n}}_2)\rangle, \quad \hat{\mathbf{n}}_1 \cdot \hat{\mathbf{n}}_2 = \cos\theta \tag{7.48}$$

  is found to be smaller than expected on scales above $\sim 60°$;

- the hemispherical power asymmetry i.e. the fact that the CMB angular power spectrum, when estimated locally at different positions on the sky, appears not to be isotropic. This asymmetry has been modeled in terms of a dipole modulation of the temperature field [84]:

$$\Theta(\hat{\mathbf{n}}) = [1 + A\,(\hat{\mathbf{n}} \cdot \hat{\mathbf{p}})]\,\Theta_0(\hat{\mathbf{n}}) \tag{7.49}$$

  where $\Theta(\hat{\mathbf{n}})$ and $\Theta_0(\hat{\mathbf{n}})$ are, respectively, the modulated and unmodulated (isotropic) CMB temperature fluctuations, A is the dipolar modulation amplitude and $\hat{\mathbf{p}}$ is the direction of maximum asymmetry;

- the alignment of low multipole moments i.e. the fact that the orientation of the quadrupole ($\ell = 2$) and the octopole ($\ell = 3$) of the CMB are found to be significantly aligned;

- the point-parity asymmetry i.e. the fact that on large angular scales, the values for the

CMB angular power spectrum for even multipoles have been found to be consistently lower than those for odd multipoles;

- the cold spot i.e. the presence in the CMB sky map of a large region, centred at Galactic coordinates $(l, b) = (210°, -57°)$ and with an angular radius of about $5° - 10°$, characterised by an usually low temperature $\Delta T \approx -100$ μK and surrounded by an hot ring.

For each of these anomalous features in Chapter 5 we reported a summary of all evidence, from the earliest analyses performed on WMAP temperature data to the latest results from the *Planck* collaboration who, in [44], presented a first comprehensive attempt at assessing the isotropy of the Universe via an analysis of the *Planck* 2018 full-sky polarisation data. Despite not finding any evidence in the polarisation data for a lack of large-angle correlations, an hemispherical power asymmetry and a violation of point-parity symmetry, the searching for a dipolar asymmetry signature found an intriguing alignment between the preferred directions of the E-mode polarisation and temperature data (see Figure 5.4). Given the *a posteriori* nature of the detection of these features, the most conservative explanation for them is that they are simply statistical flukes of our realisation of the ΛCDM model. However, despite the fact that none of them reaches individually a significance of 5σ (regarded in particle physics as the discovery threshold), their number and their (almost) exclusive occurrence at the largest angular scales motivate the quest for a possible underlying physical explanation, the most exciting possibility being that some of all of these features have a cosmological origin. Our second objective in this Thesis was therefore to provide an up-to-date review of some of the main cosmological mechanisms that have been proposed in literature to explain them. With this goal in mind in Chapter 5 we also provided a brief, qualitative summary of some of these proposals and the difficulties they have encountered, focusing in particular on the following proposals:

- mechanisms related to the local structure of our Universe e.g. the Integrated Sachs-Wolfe or (in the non-linear regime) the Rees-Sciama effect [113, 114];

- mechanisms which entail a breaking of scale-invariance during inflation e.g. single-field models of inflation with kinetic/fast slow-roll initial conditions [126] or a step [119] in the potential;

- mechanisms which entail a breaking of statistical isotropy during inflation due e.g. to some stochastic modulating field or primordial non-Gaussianity.

The possibility that the (apparent) breaking of statistical isotropy suggested by the CMB anomalous features may be an artefact of non-Gaussianity in the primordial perturbations (PNG) is particularly enticing and was throughly explored in Chapter 6. As we have seen in Chapter 4, where we first introduced the concept of PNG, the definition of *bispectrum* and *trispectrum*, the most-well known and studied types of PNG and discussed its impact on the CMB temperature and polarisation anisotropies, different classes of inflationary models

produce specific and predictable types of non-Gaussianity. Therefore, if we were to measure a significant non-Gaussian signature in the CMB, we may be able to discriminate among competing inflationary scenarios[2] thus possibly shedding light on the exact mechanism at work during the very first epochs of the Universe. On the topic of CMB anomalies as signatures of PNG relevant is the work of Schmidt & Hui [130] and Adhikari et al. [10, 11], who proposed models for the CMB power asymmetry, and Hansen et al. [12], who assumed for six of most extensively studied anomalies to have a common, cosmological origin and searched for a class of toy models that can naturally reproduce them. In particular, Schmidt & Hui [130] showed that the coupling between a long-wavelength mode a shorter one, induced by non-Gaussianity, could manifest in the observation of a preferred direction in the sky[3]. In [10], Adhikari et al. performed a systematic study of the power asymmetry expected in the CMB if the primordial fluctuations are non-Gaussian and exist on scales larger than we can observe, showing that scale-dependent modulations are a generic feature of non-Gaussian models and that such modulations can naturally reproduce the observed power asymmetry. Subsequently, in [11], Adhikari et al. showed that a large-scale power asymmetry may also arise in models with local trispectra and strong scale-dependent $\tau_{\rm NL}$ amplitudes. Finally, in [12], inspired by the additional non-linear terms in the gravitational potential that appear in models of inflation, Hansen et al. searched for isotropic but non-Gaussian models, where the non-Gaussianity is the origin of the apparent deviations from statistical isotropy seen in the data, aiming to phenomenologically determine the properties that a physical model able to explain them should exhibit. However, none of these proposals address the issue of finding a physical model that can be fitted to the data. In this regard relevant is the work of Byrnes et al. [14, 13] who extended previous calculations, which were restricted only to one or two-source scenarios, computing the response of the 2-point correlation function to a long-wavelength perturbation in models characterised by a near-local bispectrum. In particular, Byrnes et al. showed that the amplitude and scale-dependence of the observed power asymmetry are actually sourced by a combination of response functions and attempted to construct an explicit model that could produce a response with suitable amplitude and scale-dependence to match current observations. Despite being successful in this ordeal (see Section 7.1.2), Byrnes et al. observe that this doesn't mean that an inflationary explanation for the CMB power asymmetry should automatically be attractive since to construct a successful model they were forced to make several arbitrary choices and whether or not their model could actually be embedded within a viable Early Universe scenario still remains to be seen. To conclude our discussion, in Section 7.2 we reported results from the *Planck* collaboration who, in [15], tested physical models for the CMB anomalous features using the *Planck* 2018 temperature and polarisation data. No statistically significant evidence was found in favour of any of the scenarios considered over the ΛCDM model, but that doesn't mean that one should give up on the possibility that the

[2]We *may* be able to do so because, as we have seen in Chapter 4, if we were to measure such a signature the origin of the signature may not necessarily be primordial.

[3]The model proposed by Schmidt & Hui, however, induces a dependence on the direction of $\mathbf{k}$ in the primordial power spectrum $P(k)$, from which the observed asymmetry can not arise [133, 134]. In light of this issue, we didn't spend more than a few words discussing it.

observed CMB large-scale anomalies may have a primordial origin. Our expectation for the future is that upcoming precision measurements of the CMB polarisation (see Section 3.5.2), along with other observations, such as large scale structure surveys and the analysis of other potential CMB foregrounds, will provide us with the tools to eventually solve the puzzle of these anomalous features.

Appendix A
The Boltzmann Equation

To study the formation and evolution of CMB fluctuations we have to follow a complicated set of interactions between different species. The main tool used to do that is the Boltzmann equation. For each species a there is a Boltzmann equation that describes the evolution of its distribution function f_a and that can be written in the following abstract form

$$\frac{df_a}{dt} = C\left[\{f_b\}\right] \tag{A.1}$$

Equation (A.1) contains a collisionless part, df_a/dt, which accounts for the effect of gravity on the distribution function f_a, and a collision term, $C\left[\{f_b\}\right]$, which accounts for interactions with other species in the universe. In the following we are going to focus only on the evolution of the distribution function for photons f_γ. Since the photons most strongly interact with electrons, the Boltzmann equation we will be interested in is

$$\frac{df_\gamma}{dt} = C\left[\{f_\gamma, f_e\}\right] \tag{A.2}$$

Let us observe that, since the electrons are strongly coupled to the baryons, it actually makes no difference thinking of the right-hand side of the Boltzmann equation (A.2) as the photon-electron or photon-baryon coupling.

A.1 The Collisionless Boltzmann Equation for Photons

The ultimate source of spatial fluctuations in the photon distribution is gravity. Its effects are described by the collisionless Boltzmann (or Liouville) equation which controls the evolution of the distribution function f_γ as the photons stream along their geodesics. In a relativistic space-time $f_\gamma = f_\gamma(x^\mu, p^\mu)$ with $p^\mu = dx^\mu/d\lambda$ and the collisionless Boltzmann equation reads

$$\frac{df_\gamma}{d\lambda} = p^\mu \frac{\partial f_\gamma}{\partial x^\mu} - \Gamma^\mu_{\alpha\beta} p^\alpha p^\beta \frac{\partial f_\gamma}{\partial p^\mu} = 0 \tag{A.3}$$

where $\Gamma^\mu_{\alpha\beta}$ is the Christoffel symbol. In a FLRW the distribution function simplifies to

$f_\gamma = f_\gamma(E,t)$ and equation (A.3) reduces to

$$\frac{df_\gamma}{d\lambda} = E\frac{\partial f_\gamma}{\partial t} - \frac{\dot{a}}{a}|\hat{\mathbf{p}}|^2\frac{\partial f_\gamma}{\partial E} \tag{A.4}$$

Let us now consider small perturbations in the metric and introduce in the photon distribution function a direction and position dependent temperature perturbation $\Theta(\mathbf{x},\hat{\mathbf{p}},t)$

$$f_\gamma(\mathbf{x},p,\hat{\mathbf{p}},t) = \left\{\exp\left[\frac{p}{T(t)\left(1+\Theta(\mathbf{x},\hat{\mathbf{p}},t)\right)}\right] - 1\right\}^{-1} \tag{A.5}$$

Then at linear order, in the Poisson gauge, after performing some calculations, the Boltzmann equation (A.4) will read

$$\left.\frac{df_\gamma}{d\lambda}\right|_{(1)} = -p\frac{\partial f_\gamma^{(0)}}{\partial t}\left[\frac{\partial\Theta}{\partial t} + \frac{\hat{p}^i}{a}\frac{\partial\Theta}{\partial x^i} - \frac{\partial\Psi}{\partial t} + \frac{\hat{p}^i}{a}\frac{\partial\Phi}{\partial x^i}\right] \tag{A.6}$$

where $f_\gamma^{(0)}$ is the zero-th order distribution function, given by

$$f_\gamma^{(0)} = \left[\exp\left\{\frac{p}{T}\right\} - 1\right]^{-1} \tag{A.7}$$

A.2 The Boltzmann Equation for Interacting Photons

Photons as the LSS interacted with the no longer relativistic electrons via Thomson scattering

$$e^-(\mathbf{q}) + \gamma(\mathbf{p}) \leftrightarrow e^-(\mathbf{q}') + \gamma(\mathbf{p}') \tag{A.8}$$

The collision term for this interaction reads

$$C\left[f_\gamma(\mathbf{p})\right] = -p\frac{\partial f_\gamma^{(0)}}{\partial t} n_e\sigma_T\left[\Theta_0 - \Theta(\hat{\mathbf{p}}) + \hat{\mathbf{p}}\cdot\mathbf{v}_b\right] \tag{A.9}$$

where $\mathbf{v}_b$ is the baryon velocity, which tells us how fast the electrons, that are tightly coupled to the baryons, are moving; n_e is the free electrons number density; σ_T is the Thomson scattering cross section and Θ_0 is *monopole* moment of the photon distribution, defined as the integral of the photon perturbation at any given point over all photon directions

$$\Theta_0 \equiv \frac{1}{4\pi}\int d\Omega_{\hat{\mathbf{p}}}\Theta(\mathbf{x},\hat{\mathbf{p}},t) \tag{A.10}$$

Equating now equations (A.6) and (A.9), we get that the Boltzmann equation for the interacting photons is given by

$$\dot{\Theta} + \frac{\hat{p}^i}{a}\frac{\partial \Theta}{\partial x^i} - \dot{\Psi} + \frac{\hat{p}^i}{a}\frac{\partial \Phi}{\partial x^i} = n_e \sigma_T \left[\Theta_0 - \Theta(\hat{\mathbf{p}}) + \hat{\mathbf{p}} \cdot \mathbf{v}_b\right] \tag{A.11}$$

At this point it is convenient to switch to the conformal time τ, in terms of which the above equation is rewritten

$$\Theta^{'} + \hat{p}^i \frac{\partial \Theta}{\partial x^i} - \Psi^{'} + \hat{p}^i \frac{\partial \Phi}{\partial x^i} = n_e \sigma_T a \left[\Theta_0 - \Theta + \hat{\mathbf{p}} \cdot \mathbf{v}_b\right] \tag{A.12}$$

where the prime as usual denotes the time derivative with respect to the conformal time. A partial differential equation of this form is usually solved in Fourier space. Before going to Fourier space, let us however introduce a new variable, that we denote as $\mu = \hat{\mathbf{k}} \cdot \hat{\mathbf{p}}$, defined as the cosine of the angle between the wavevector $\hat{\mathbf{k}}$ and the photon direction $\hat{\mathbf{p}}$. Let us also observe that, in general, in Cosmology the velocities all point in the same direction of the wavevector, meaning that $\hat{\mathbf{p}} \cdot \mathbf{v}_b \equiv \mu v_b$, and introduce the definition of *optical depth*

$$\tau(\tau) \equiv \int_{\tau}^{\tau_0} d\tau^{'} n_e \sigma_T a \tag{A.13}$$

With these definitions, going to Fourier space, the Boltzmann equation for the interacting photons reads

$$\Theta^{'} + ik\mu\Theta - \Psi^{'} + ik\mu\Phi = -\tau^{'} \left[\Theta_0 - \Theta + \mu v_b\right] \tag{A.14}$$

Note that we choose not to employ a different notation for the Fourier-space fields. The appearance of μ automatically means that the equation is written in Fourier space.

A.3 Free-streaming Solution

In the previous section we have found convenient to introduce the monopole moment of the photon distribution Θ_0. Analogously, we can introduce an ℓth multipole moment for the temperature perturbation field, defined as

$$\Theta_\ell(k, \tau) = \frac{1}{(-i)^\ell} \int_{-\mu}^{\mu} \frac{d\mu}{2} P_\ell(\mu) \Theta(k, \mu, \tau) \tag{A.15}$$

where $P_\ell(\mu)$ is the Legendre polynomial of order ℓ. In this way, the photon perturbations can then be described either in terms of $\Theta(k, \mu, \tau)$ or by a hierarchy of multipole moments $\Theta_\ell(k, \tau)$. Our objective will now be to sketch the derivation of the solution for the photon multipole moments today, $\Theta_\ell(k, \tau_0)$, at recombination.

By subtracting $\tau^{'}\Theta$ from both sides of equation (A.14), and introducing the so-called *source* function $\hat{S}$, defined as

$$\hat{S} \equiv \Psi^{'} - ik\mu\Phi - \tau^{'}\left[\Theta_0 + \mu v_b\right] \tag{A.16}$$

we obtain the following equation

$$\Theta^{'}\left(ik\mu - \tau^{'}\right)\Theta = \hat{S} \tag{A.17}$$

By performing some manipulations, one can prove that the solution for the photon anisotropies today is

$$\Theta(k,\mu,\tau_0) = \int_0^{\tau_0} d\tau \hat{S}(k,\mu,\tau) e^{ik\mu(\tau-\tau_0)-\tau(\tau)} \tag{A.18}$$

This solution can easily be turned into an equation for each multipole $\Theta_\ell(k,\tau)$: it suffices to multiply both sides by the Legendre polynomial P_ℓ and then integrate over μ, giving

$$\Theta_\ell(k,\tau_0) = (-1)^\ell \int_0^{\tau_0} d\tau \hat{S}(k,\tau) e^{-\tau(\tau)} j_\ell\left[k(\tau-\tau_0)\right] \tag{A.19}$$

where $j_\ell\left[k(\tau-\tau_0)\right]$ are the Bessel functions. It is now useful to introduce the *visibility function*

$$g(\tau) = -\tau^{'}(\tau) e^{-\tau(\tau)} \tag{A.20}$$

defined such that $\int d\tau g(\tau) = 1$, so it can be thought of as the probability that a photon last scattered at the time τ. In terms of the visibility function, the source function reads

$$\hat{S}(k,\tau) \approx g(\tau)\left[\Theta_0(k,\tau) + \Phi(k,\tau)\right] + \frac{i}{k}\frac{d}{d\tau}\left[v_b g(\tau)\right] + e^{-\tau(\tau)}\left[\Psi^{'}(k,\tau) + \Phi^{'}(k,\tau)\right] \tag{A.21}$$

Being the optical depth τ very large early on, this probability, due to the exponential $e^{-\tau(\tau)}$, is zero for τ before recombination. After recombination, the prefactor $-\tau^{'}(\tau)$, corresponding to the scattering rate, drops and thus this probability becomes again very small. Hence, we can consider the visibility function as a Dirac delta peaked on some time instant τ_*. Substituting the expression for the source function (A.21) into equation (A.19), introducing the above approximation for the visibility function and integrating over the Dirac delta and using that

$v_b \equiv -3i\Theta$ at τ_*, we get the following result for the multipole moments today $\Theta_\ell(k, \tau_0)$:

$$\begin{aligned}\Theta_\ell(k,\tau_0) \approx & \left(\Theta_0(k,\tau_*) + \Phi(k,\tau_*)\right) j_\ell\left[k(\tau_0-\tau_*)\right] \\ & + 3\Theta_1(k,\tau_*)\left(j_{\ell-1}\left[k(\tau_0-\tau_*)\right] - (\ell+1)\frac{j_\ell\left[k(\tau_0-\tau_*)\right]}{k(\tau_0-\tau_*)}\right) \\ & + \int_0^{\tau_0} d\tau e^{-\tau(\tau)}\left(\Psi' + \Phi'\right) j_\ell\left[k(\tau_0-\tau_*)\right]\end{aligned} \tag{A.22}$$

Appendix B

Wigner 3-j symbol

B.1 Definition

The Wigner 3-j symbol, given by

$$\begin{pmatrix} \ell_1 & \ell_2 & \ell_3 \\ m_1 & m_2 & m_3 \end{pmatrix} \tag{B.1}$$

is related to the Clebsh–Gordan coefficients which describe coupling of two angular momenta in quantum mechanics. In quantum mechanics, ℓ is the eigenvalue of the angular momentum operator $\mathbf{L} = \mathbf{r} \times \mathbf{p}$, that is $\mathbf{L}^2 Y_{\ell m} = \ell(\ell+1) Y_{\ell m}$, while m is the eigeinvalue of the z-direction component of the angular momentum, that is $L_z Y_{\ell m} = m Y_{\ell m}$. In particular, the Wigner 3-j symbol as defined in equation (B.1) describes a set of three angular momenta $\mathbf{L}_1$, $\mathbf{L}_2$ and $\mathbf{L}_3$ forming a triangle, meaning that $\mathbf{L}_1 + \mathbf{L}_2 + \mathbf{L}_3 = 0$. Since the three angular momenta form a triangle, they have to satisfy triangle conditions i.e.

$$|L_i - L_j| \leq L_k \leq L_i + L_j \tag{B.2}$$

where $L_i = |\mathbf{L}_i|$. The triangle conditions (B.2) also imply the following selection rules on ℓ_1, ℓ_2, ℓ_3 and m_1, m_2, m_3:

$$\begin{aligned} &|\ell_i - \ell_j| \leq \ell_k \leq \ell_i + \ell_j \\ &m_1 + m_2 + m_3 = 0 \end{aligned} \tag{B.3}$$

B.2 Symmetries

The Wigner 3-j symbol (B.1) is invariant under even permutations, meaning that

$$\begin{pmatrix} \ell_1 & \ell_2 & \ell_3 \\ m_1 & m_2 & m_3 \end{pmatrix} = \begin{pmatrix} \ell_3 & \ell_1 & \ell_2 \\ m_3 & m_1 & m_2 \end{pmatrix} = \begin{pmatrix} \ell_2 & \ell_3 & \ell_1 \\ m_2 & m_3 & m_1 \end{pmatrix} \tag{B.4}$$

whilst, if $\ell_1 + \ell_2 + \ell_3 = \text{odd}$, it changes phase for odd permutations, e.g.

$$(-1)^{\ell_1+\ell_2+\ell_3} \begin{pmatrix} \ell_1 & \ell_2 & \ell_3 \\ m_1 & m_2 & m_3 \end{pmatrix} = \begin{pmatrix} \ell_2 & \ell_1 & \ell_3 \\ m_2 & m_1 & m_3 \end{pmatrix} \tag{B.5}$$

furthermore, if $\ell_1+\ell_2+\ell_3 = \text{odd}$, the phase also changes under a transformation $m_1+m_2+m_3 \to -(m_1 + m_2 + m_3)$, that is

$$\begin{pmatrix} \ell_1 & \ell_2 & \ell_3 \\ -m_1 & -m_2 & -m_3 \end{pmatrix} = (-1)^{\ell_1+\ell_2+\ell_3} \begin{pmatrix} \ell_1 & \ell_2 & \ell_3 \\ m_1 & m_2 & m_3 \end{pmatrix} \tag{B.6}$$

This last property implies that if there is no z-direction component of the angular momentum in the system i.e. $m_i = 0$, then the Wigner 3-j symbol

$$\begin{pmatrix} \ell_1 & \ell_2 & \ell_3 \\ 0 & 0 & 0 \end{pmatrix} \tag{B.7}$$

is non-zero only if $\ell_1 + \ell_2 + \ell_3 = \text{even}$.

B.3 Orthogonality

The Wigner 3-j symbol has the following orthogonality properties which, by definition, are consistent with the orthonormality of the angular momentum eigenstate vectors and the unitarity of the Clebsh-Gordon coefficients:

$$\sum_{\text{all } m} \begin{pmatrix} \ell_1 & \ell_2 & \ell_3 \\ m_1 & m_2 & m_3 \end{pmatrix}^2 = 1 \tag{B.8}$$

$$\sum_{\ell_3 m_3} (2\ell_3 + 1) \begin{pmatrix} \ell_1 & \ell_2 & \ell_3 \\ m_1 & m_2 & m_3 \end{pmatrix} \begin{pmatrix} \ell_1 & \ell_2 & \ell_3 \\ m_1' & m_2' & m_3 \end{pmatrix} = \delta_{m_1 m_1'} \delta_{m_2 m_2'} \tag{B.9}$$

$$\sum_{m_1 m_2} \begin{pmatrix} \ell_1 & \ell_2 & \ell_3 \\ m_1 & m_2 & m_3 \end{pmatrix} \begin{pmatrix} \ell_1 & \ell_2 & \ell_3' \\ m_1 & m_2 & m_3' \end{pmatrix} = \frac{\delta_{\ell_3 \ell_3'} \delta_{m_3 m_3'}}{2\ell_3 + 1} \tag{B.10}$$

B.4 Wigner 6-j symbol

The Wigner 6-j symbol, given by

$$\begin{Bmatrix} \ell_1 & \ell_2 & \ell_3 \\ \ell_1' & \ell_2' & \ell_3' \end{Bmatrix} \tag{B.11}$$

describes the coupling of three angular momenta and it is related to the Wigner 3-j symbol (B.1) through

$$\begin{aligned}(-1)^{\ell_1'+\ell_2'+\ell_3'} \begin{Bmatrix} \ell_1 & \ell_2 & \ell_3 \\ \ell_1' & \ell_2' & \ell_3' \end{Bmatrix} \begin{pmatrix} \ell_1 & \ell_2 & \ell_3 \\ m_1 & m_2 & m_3 \end{pmatrix} = \sum_{\text{all } m'} (-1)^{m_1'+m_2'+m_3'} \begin{pmatrix} \ell_1 & \ell_2' & \ell_3' \\ m_1 & m_2' & -m_3' \end{pmatrix} \\ \times \begin{pmatrix} \ell_1' & \ell_2 & \ell_3' \\ -m_1' & m_2 & m_3' \end{pmatrix} \begin{pmatrix} \ell_1' & \ell_2' & \ell_3 \\ -m_1' & -m_2' & m_3 \end{pmatrix}\end{aligned} \tag{B.12}$$

By using the orthogonality condition (B.8) one also has the following relation:

$$\begin{aligned}(-1)^{\ell_1'+\ell_2'+\ell_3'} \begin{Bmatrix} \ell_1 & \ell_2 & \ell_3 \\ \ell_1' & \ell_2' & \ell_3' \end{Bmatrix} = \sum_{\text{all } mm'} (-1)^{m_1'+m_2'+m_3'} \\ \times \begin{pmatrix} \ell_1 & \ell_2 & \ell_3 \\ m_1 & m_2 & m_3 \end{pmatrix} \begin{pmatrix} \ell_1 & \ell_2' & \ell_3' \\ m_1 & m_2' & -m_3' \end{pmatrix} \\ \times \begin{pmatrix} \ell_1' & \ell_2 & \ell_3' \\ -m_1' & m_2 & m_3' \end{pmatrix} \begin{pmatrix} \ell_1' & \ell_2' & \ell_3 \\ -m_1' & -m_2' & m_3 \end{pmatrix}\end{aligned} \tag{B.13}$$

Bibliography

[1] Ralph A Alpher and Robert Herman. "Evolution of the Universe". In: *Nature* 162.4124 (1948), pp. 774–775.

[2] George F Smoot et al. "Structure in the COBE differential microwave radiometer first-year maps". In: *The Astrophysical Journal* 396 (1992), pp. L1–L5.

[3] WMAP collaboration et al. "First year Wilkinson Microwave Anisotropy Probe (WMAP) observations: Preliminary maps and basic results". In: *Astrophys. J. Suppl* 148.1 (2003).

[4] Gary Hinshaw et al. "Nine-year Wilkinson Microwave Anisotropy Probe (WMAP) observations: cosmological parameter results". In: *The Astrophysical Journal Supplement Series* 208.2 (2013), p. 19.

[5] Peter AR Ade et al. "Planck 2013 results. XVI. Cosmological parameters". In: *Astronomy & Astrophysics* 571 (2014), A16.

[6] Rémi Adam et al. "Planck 2015 results-I. Overview of products and scientific results". In: *Astronomy & Astrophysics* 594 (2016), A1.

[7] Peter AR Ade et al. "Planck 2015 results-XIII. cosmological parameters". In: *Astronomy & Astrophysics* 594 (2016), A13.

[8] Nabila Aghanim et al. "Planck 2018 results-I. Overview and the cosmological legacy of Planck". In: *Astronomy & Astrophysics* 641 (2020), A1.

[9] Nabila Aghanim et al. "Planck 2018 results-VI. Cosmological parameters". In: *Astronomy & Astrophysics* 641 (2020), A6.

[10] Saroj Adhikari, Sarah Shandera, and Adrienne L Erickcek. "Large-scale anomalies in the cosmic microwave background as signatures of non-Gaussianity". In: *Physical Review D* 93.2 (2016), p. 023524.

[11] Saroj Adhikari, Anne-Sylvie Deutsch, and Sarah Shandera. "Statistical anisotropies in temperature and polarization fluctuations from a scale-dependent trispectrum". In: *Physical Review D* 98.2 (2018), p. 023520.

[12] Frode Kristian Hansen et al. "Isotropic non-Gaussian g_{NL}-like toy models that reproduce cosmic microwave background anomalies". In: *Astronomy & Astrophysics* 626 (2019), A13.

[13] Christian T Byrnes et al. "Implications of the cosmic microwave background power asymmetry for the early universe". In: *Physical Review D* 93.12 (2016), p. 123003.

[14] Christian T Byrnes et al. “The hemispherical asymmetry from a scale-dependent inflationary bispectrum”. In: *Journal of Cosmology and Astroparticle Physics* 2016.06 (2016), p. 025.

[15] Yashar Akrami et al. “Planck 2018 results-X. Constraints on inflation”. In: *Astronomy & Astrophysics* 641 (2020), A10.

[16] https://sci.esa.int/web/euclid/-/cosmic-energy-budget.

[17] Adam G Riess et al. “A comprehensive measurement of the local value of the Hubble constant with 1 km s- 1 mpc- 1 uncertainty from the Hubble space telescope and the sh0es team”. In: *The Astrophysical Journal Letters* 934.1 (2022), p. L7.

[18] Elcio Abdalla et al. “Cosmology intertwined: A review of the particle physics, astrophysics, and cosmology associated with the cosmological tensions and anomalies”. In: *Journal of High Energy Astrophysics* (2022).

[19] Peter Coles and Francesco Lucchin. *Cosmology: The origin and evolution of cosmic structure*. John Wiley & Sons, 2003.

[20] Daniel Baumann. “TASI lectures on inflation”. In: (2012). arXiv: 0907.5424 [hep-th].

[21] James M. Bardeen. “Gauge-invariant cosmological perturbations”. In: *Phys. Rev. D* 22 (8 1980), pp. 1882–1905.

[22] James M Bardeen, Paul J Steinhardt, and Michael S Turner. “Spontaneous creation of almost scale-free density perturbations in an inflationary universe”. In: *Physical Review D* 28.4 (1983), p. 679.

[23] Nicola Bartolo et al. “Non-Gaussianity from inflation: Theory and observations”. In: *Physics Reports* 402.3-4 (2004), pp. 103–266.

[24] Matthieu Tristram et al. “Improved limits on the tensor-to-scalar ratio using BICEP and P l a n c k data”. In: *Physical Review D* 105.8 (2022), p. 083524.

[25] Nabila Aghanim et al. “Planck 2018 results-V. CMB power spectra and likelihoods”. In: *Astronomy & Astrophysics* 641 (2020), A5.

[26] PAR Ade et al. “Constraints on Primordial Gravitational Waves Using Planck, WMAP, and New BICEP2/Keck Observations through the 2015 Season”. In: *Physical review letters* 121.22 (2018), p. 221301.

[27] Benjamin P Abbott et al. “Upper limits on the stochastic gravitational-wave background from Advanced LIGO’s first observing run”. In: *Physical review letters* 118.12 (2017), p. 121101.

[28] Matthieu Tristram et al. “Planck constraints on the tensor-to-scalar ratio”. In: *Astronomy & Astrophysics* 647 (2021), A128.

[29] PAR Ade et al. “Improved constraints on primordial gravitational waves using Planck, WMAP, and BICEP/Keck observations through the 2018 observing season”. In: *Physical review letters* 127.15 (2021), p. 151301.

[30] Giacomo Galloni et al. “Updated constraints on amplitude and tilt of the tensor primordial spectrum”. In: *Journal of Cosmology and Astroparticle Physics* 2023.04 (2023), p. 062.

[31] Ryan Abbott et al. “Upper limits on the isotropic gravitational-wave background from Advanced LIGO and Advanced Virgo’s third observing run”. In: *Physical Review D* 104.2 (2021), p. 022004.

[32] DJ Fixsen. “The temperature of the cosmic microwave background”. In: *The Astrophysical Journal* 707.2 (2009), p. 916.

[33] KG Hayes et al. “Review of particle physics”. In: *Physics letters B* 592.1-4 (2004), pp. 1–5.

[34] Martin White and Wayne Hu. “The Sachs-Wolfe effect”. In: *Astronomy and Astrophysics* 321 (1997), pp. 8–9.

[35] Collaboration LiteBIRD et al. “Probing cosmic inflation with the LiteBIRD cosmic microwave background polarization survey”. In: *Progress of Theoretical and Experimental Physics* 2023.4 (2023), 042F01.

[36] Krzysztof M Gorski et al. “The healpix primer”. In: (1999). arXiv: astro-ph/9905275 [astro-ph].

[37] Yashar Akrami et al. “Planck 2018 results-IV. Diffuse component separation”. In: *Astronomy & Astrophysics* 641 (2020), A4.

[38] Gayoung Chon et al. “Fast estimation of polarization power spectra using correlation functions”. In: *Monthly Notices of the Royal Astronomical Society* 350.3 (2004), pp. 914–926.

[39] Craig J Copi et al. “Lack of large-angle TT correlations persists in WMAP and Planck”. In: *Monthly Notices of the Royal Astronomical Society* 451.3 (2015), pp. 2978–2985.

[40] MG Hauser and PJE Peebles. “Statistical analysis of catalogs of extragalactic objects. II. The Abell catalog of rich clusters”. In: *The Astrophysical Journal* 185 (1973), pp. 757–786.

[41] Planck Collaboration et al. “The Scientific programme of Planck”. In: (2006). arXiv: astro-ph/0604069 [astro-ph].

[42] Peter AR Ade et al. “Planck 2013 results. XXIII. Isotropy and statistics of the CMB”. In: *Astronomy & Astrophysics* 571 (2014), A23.

[43] PAR Ade et al. “Planck 2015 results-XVI. Isotropy and statistics of the CMB”. In: *Astronomy & Astrophysics* 594 (2016), A16.

[44] Yashar Akrami et al. “Planck 2018 results-VII. Isotropy and statistics of the CMB”. In: *Astronomy & Astrophysics* 641 (2020), A7.

[45] Kevork Abazajian et al. “Snowmass 2021 CMB-S4 White Paper”. In: (2022). arXiv: 2203.08024 [astro-ph.CO].

[46] S Adachi et al. “Improved upper limit on degree-scale CMB B-mode polarization power from the 670 square-degree POLARBEAR survey”. In: *The Astrophysical Journal* 931.2 (2022), p. 101.

[47] PAR Ade et al. “Bicep/Keck XV: The Bicep3 cosmic microwave background polarimeter and the first three-year data set”. In: *The Astrophysical Journal* 927.1 (2022), p. 77.

[48] Peter Ade et al. “The Simons Observatory: science goals and forecasts”. In: *Journal of Cosmology and Astroparticle Physics* 2019.02 (2019), p. 056.

[49] Clarence L Chang et al. “Snowmass2021 Cosmic Frontier: Cosmic Microwave Background Measurements White Paper”. In: (2022). arXiv: 2203.07638 [astro-ph.CO].

[50] Juan Maldacena. “Non-Gaussian features of primordial fluctuations in single field inflationary models”. In: *Journal of High Energy Physics* 2003.05 (2003), p. 013.

[51] Xingang Chen. “Primordial non-Gaussianities from inflation models”. In: *Advances in Astronomy* 2010 (2010).

[52] Toby Falk, Raghavan Rangarajan, and Mark Srednicki. “The angular dependence of the three-point correlation function of the cosmic microwave background radiation as predicted by inflationary cosmologies”. In: *The Astrophysical journal* 403.1 (1993), pp. L1–L3.

[53] Alejandro Gangui et al. “The Three–Point Correlation Function of the Cosmic Microwave Background in Inflationary Models”. In: *The Astrophysical Journal* 430 (1994), pp. 447–457.

[54] Alejandro Gangui and Jérôme Martin. “Cosmic microwave background bispectrum and slow-roll inflation”. In: *Monthly Notices of the Royal Astronomical Society* 313.2 (2000), pp. 323–330.

[55] Licia Verde et al. “Large-scale structure, the cosmic microwave background and primordial non-Gaussianity”. In: *Monthly Notices of the Royal Astronomical Society* 313.1 (2000), pp. 141–147.

[56] Limin Wang and Marc Kamionkowski. “Cosmic microwave background bispectrum and inflation”. In: *Physical Review D* 61.6 (2000), p. 063504.

[57] Eiichiro Komatsu and David N Spergel. “Acoustic signatures in the primary microwave background bispectrum”. In: *Physical Review D* 63.6 (2001), p. 063002.

[58] DS Salopek and JR Bond. “Nonlinear evolution of long-wavelength metric fluctuations in inflationary models”. In: *Physical Review D* 42.12 (1990), p. 3936.

[59] Paolo Creminelli et al. “Limits on non-Gaussianities from WMAP data”. In: *Journal of Cosmology and Astroparticle Physics* 2006.05 (2006), p. 004.

[60] Leonardo Senatore, Kendrick M Smith, and Matias Zaldarriaga. “Non-Gaussianities in single field inflation and their optimal limits from the WMAP 5-year data”. In: *Journal of Cosmology and Astroparticle Physics* 2010.01 (2010), p. 028.

[61] P Daniel Meerburg, Jan Pieter Van Der Schaar, and Pier Stefano Corasaniti. “Signatures of initial state modifications on bispectrum statistics”. In: *Journal of Cosmology and Astroparticle Physics* 2009.05 (2009), p. 018.

[62] Viviana Acquaviva et al. “Second-order cosmological perturbations from inflation”. In: *Nuclear Physics B* 667.1-2 (2002), pp. 119–148.

[63] Hayden Lee and Cora Dvorkin. “Cosmological angular trispectra and non-Gaussian covariance”. In: *Journal of Cosmology and Astroparticle Physics* 2020.05 (2020), p. 044.

[64] Teruaki Suyama and Masahide Yamaguchi. “Non-Gaussianity in the modulated reheating scenario”. In: *Physical Review D* 77.2 (2008), p. 023505.

[65] Christian T Byrnes et al. “Scale-dependent non-Gaussianity probes inflationary physics”. In: *Journal of Cosmology and Astroparticle Physics* 2010.10 (2010), p. 004.

[66] Emiliano Sefusatti et al. “Constraining running non-Gaussianity”. In: *Journal of Cosmology and Astroparticle Physics* 2009.12 (2009), p. 022.

[67] Wayne Hu. “Angular trispectrum of the cosmic microwave background”. In: *Physical Review D* 64.8 (2001), p. 083005.

[68] Takemi Okamoto and Wayne Hu. “Angular trispectra of CMB temperature and polarization”. In: *Physical Review D* 66.6 (2002).

[69] DM Regan, EPS Shellard, and JR Fergusson. “General CMB and primordial trispectrum estimation”. In: *Physical Review D* 82.2 (2010), p. 023520.

[70] https://camb.info.

[71] https://class-code.net.

[72] Y Akrami et al. “Planck 2018 results-IX. Constraints on primordial non-Gaussianity”. In: *Astronomy & Astrophysics* 641 (2020), A9.

[73] Kendrick M Smith, Leonardo Senatore, and Matias Zaldarriaga. “Optimal analysis of the CMB trispectrum”. In: (2015). arXiv: 1502.00635 [astro-ph.CO].

[74] Peter AR Ade et al. “Planck 2013 results. XXIV. Constraints on primordial non-Gaussianity”. In: *Astronomy & Astrophysics* 571 (2014), A24.

[75] Kareem Marzouk, Antony Lewis, and Julien Carron. “Constraints on $\tau_{\rm NL}$ from Planck temperature and polarization”. In: *Journal of Cosmology and Astroparticle Physics* 2022.08 (2022), p. 015.

[76] Duncan Hanson and Antony Lewis. “Estimators for CMB statistical anisotropy”. In: *Physical Review D* 80.6 (2009), p. 063004.

[77] Ivan Agullo, Dimitrios Kranas, and V Sreenath. “Anomalies in the Cosmic Microwave Background and Their Non-Gaussian Origin in Loop Quantum Cosmology”. In: *Frontiers in Astronomy and Space Sciences* (2021), p. 130.

[78] G Hinshaw et al. “Two-Point Correlations in the COBE* DMR Four-Year Anisotropy Maps”. In: *The Astrophysical Journal* 464.1 (1996), p. L25.

[79] David N Spergel et al. “First-year Wilkinson Microwave Anisotropy Probe (WMAP)* observations: determination of cosmological parameters”. In: *The Astrophysical Journal Supplement Series* 148.1 (2003), p. 175.

[80] Craig J Copi et al. “Large-angle cosmic microwave background suppression and polarization predictions”. In: *Monthly Notices of the Royal Astronomical Society* 434.4 (2013), pp. 3590–3596.

[81] Craig J Copi et al. “No large-angle correlations on the non-Galactic microwave sky”. In: *Monthly Notices of the Royal Astronomical Society* 399.1 (2009), pp. 295–303.

[82] Hans K Eriksen et al. “Asymmetries in the Cosmic Microwave Background anisotropy field”. In: *The Astrophysical Journal* 605.1 (2004), p. 14.

[83] Frode K Hansen, AJ Banday, and KM Górski. “Testing the cosmological principle of isotropy: local power-spectrum estimates of the WMAP data”. In: *Monthly Notices of the Royal Astronomical Society* 354.3 (2004), pp. 641–665.

[84] Christopher Gordon et al. “Spontaneous isotropy breaking: a mechanism for CMB multipole alignments”. In: *Physical Review D* 72.10 (2005), p. 103002.

[85] Hans K Eriksen et al. “Hemispherical power asymmetry in the third-year Wilkinson Microwave Anisotropy Probe sky maps”. In: *The Astrophysical Journal* 660.2 (2007), p. L81.

[86] J Hoftuft et al. “Increasing evidence for hemispherical power asymmetry in the five-year WMAP data”. In: *The Astrophysical Journal* 699.2 (2009), p. 985.

[87] Adam Moss et al. “Tilted physics: A cosmologically dipole-modulated sky”. In: *Physical Review D* 84.2 (2011), p. 023014.

[88] FK Hansen et al. “Power asymmetry in cosmic microwave background fluctuations from full sky to sub-degree scales: is the universe isotropic?” In: *The Astrophysical Journal* 704.2 (2009), p. 1448.

[89] M Axelsson et al. “Directional dependence of ΛCDM cosmological parameters”. In: *The Astrophysical Journal Letters* 773.1 (2013), p. L3.

[90] Y Akrami et al. “Power asymmetry in WMAP and Planck temperature sky maps as measured by a local variance estimator”. In: *The Astrophysical Journal Letters* 784.2 (2014), p. L42.

[91] C Monteserin et al. “A low CMB variance in the WMAP data”. In: *Monthly Notices of the Royal Astronomical Society* 387 (2008), pp. 209–219.

[92] Craig J Copi et al. “Large-scale alignments from WMAP and Planck”. In: *Monthly Notices of the Royal Astronomical Society* 449.4 (2015), pp. 3458–3470.

[93] Max Tegmark, Angelica de Oliveira-Costa, and Andrew JS Hamilton. “High resolution foreground cleaned CMB map from WMAP”. In: *Physical Review D* 68.12 (2003), p. 123523.

[94] Angelica de Oliveira-Costa et al. “Significance of the largest scale CMB fluctuations in WMAP”. In: *Physical Review D* 69.6 (2004), p. 063516.

[95] Craig J Copi, Dragan Huterer, and Glenn D Starkman. “Multipole vectors: A new representation of the CMB sky and evidence for statistical anisotropy or non-Gaussianity at $2 \leqslant l \leqslant 8$”. In: *Physical Review D* 70.4 (2004), p. 043515.

[96] Kate Land and Joao Magueijo. “Is the Universe odd?” In: *Physical Review D* 72.10 (2005), p. 101302.

[97] Jaiseung Kim and Pavel Naselsky. “Anomalous parity asymmetry of the Wilkinson Microwave Anisotropy Probe power spectrum data at low multipoles”. In: *The Astrophysical Journal Letters* 714.2 (2010), p. L265.

[98] Jaiseung Kim and Pavel Naselsky. “Anomalous parity asymmetry of WMAP 7-year power spectrum data at low multipoles: is it cosmological or systematics?” In: *Physical Review D* 82.6 (2010), p. 063002.

[99] Jaiseung Kim and Pavel Naselsky. “Lack of angular correlation and odd-parity preference in cosmic microwave background data”. In: *The Astrophysical Journal* 739.2 (2011), p. 79.

[100] P Naselsky et al. “Is the Cosmic Microwave Background Asymmetry due to the Kinematic Dipole?” In: *The Astrophysical Journal* 749.1 (2012), p. 31.

[101] Ray Zhang and Dragan Huterer. "Disks in the sky: A reassessment of the WMAP "cold spot"". In: *Astroparticle Physics* 33.2 (2010), pp. 69–74.

[102] Seshadri Nadathur et al. "Can a supervoid explain the cold spot?" In: *Physical Review D* 90.10 (2014), p. 103510.

[103] András Kovács. "The part and the whole: voids, super voids, and their ISW imprint". In: *Monthly Notices of the Royal Astronomical Society* 475.2 (2018), pp. 1777–1790.

[104] Patricio Vielva et al. "Detection of non-Gaussianity in the Wilkinson microwave anisotropy probe first-year data using spherical wavelets". In: *The Astrophysical Journal* 609.1 (2004), p. 22.

[105] M Cruz et al. "The non-Gaussian cold spot in Wilkinson Microwave Anisotropy Probe: significance, morphology and foreground contribution". In: *Monthly Notices of the Royal Astronomical Society* 369.1 (2006), pp. 57–67.

[106] Marcos Cruz et al. "The non-gaussian cold spot in the 3 year Wilkinson microwave anisotropy probe data". In: *The Astrophysical Journal* 655.1 (2007), p. 11.

[107] M Cruz, E Martinez-Gonzalez, and P Vielva. "The WMAP Cold Spot". In: (2010), pp. 275–275.

[108] M Hansen et al. "Can residuals of the Solar System foreground explain low multipole anomalies of the CMB?" In: *Journal of Cosmology and Astroparticle Physics* 2012.10 (2012), p. 059.

[109] Priscilla C Frisch. "Tentative Identification of Interstellar Dust in the Nose of the Heliosphere". In: *LPI Contributions* 1280 (2005), p. 49.

[110] PAR Ade et al. "Planck 2015 results-XXV. Diffuse low-frequency Galactic foregrounds". In: *Astronomy & Astrophysics* 594 (2016), A25.

[111] Heliana E Luparello et al. "The cosmic shallows I: Interaction of CMB photons in extended galaxy halos". In: *Monthly Notices of the Royal Astronomical Society* 518.4 (2023), pp. 5643–5652.

[112] Frode K Hansen et al. "Cosmic Microwave Background anomalies explained: a strong impact of nearby galaxies on observed CMB large scale fluctuations". In: (2023). arXiv: 2305.00268 [astro-ph.CO].

[113] Aleksandar Rakić, Syksy Räsänen, and Dominik J Schwarz. "The microwave sky and the local Rees—Sciama effect". In: *Monthly Notices of the Royal Astronomical Society: Letters* 369.1 (2006), pp. L27–L31.

[114] Kaiki Taro Inoue and Joseph Silk. "Local voids as the origin of large-angle cosmic microwave background anomalies. I." In: *The Astrophysical Journal* 648.1 (2006), p. 23.

[115] Lawrence Rudnick, Shea Brown, and Liliya R Williams. "Extragalactic radio sources and the WMAP cold spot". In: *The Astrophysical Journal* 671.1 (2007), p. 40.

[116] Kendrick M Smith and Dragan Huterer. "No evidence for the cold spot in the NVSS radio survey". In: *Monthly Notices of the Royal Astronomical Society* 403.1 (2010), pp. 2–8.

[117] István Szapudi et al. “Detection of a supervoid aligned with the cold spot of the cosmic microwave background”. In: *Monthly Notices of the Royal Astronomical Society* 450.1 (2015), pp. 288–294.

[118] Fabio Finelli et al. “Supervoids in the WISE–2MASS catalogue imprinting cold spots in the cosmic microwave background”. In: *Monthly Notices of the Royal Astronomical Society* 455.2 (2016), pp. 1246–1256.

[119] Jennifer Adams, Bevan Cresswell, and Richard Easther. “Inflationary perturbations from a potential with a step”. In: *Physical Review D* 64.12 (2001), p. 123514.

[120] Laura Covi et al. “Inflation and WMAP three year data: Features have a future!” In: *Phys. Rev. D* 74 (Oct. 2006).

[121] Dhiraj Kumar Hazra et al. “Primordial features due to a step in the inflaton potential”. In: *Journal of Cosmology and Astroparticle Physics* 2010.10 (2010), p. 008.

[122] I Dalianis et al. “Spectrum oscillations from features in the potential of single-field inflation”. In: *Physical Review D* 104.10 (2021), p. 103510.

[123] Rajeev Kumar Jain, Pravabati Chingangbam, and L Sriramkumar. “On the evolution of tachyonic perturbations at super-Hubble scales”. In: *Journal of Cosmology and Astroparticle Physics* 2007.10 (2007), p. 003.

[124] Rajeev Kumar Jain et al. “Punctuated inflation and the low CMB multipoles”. In: *Journal of Cosmology and Astroparticle Physics* 2009.01 (2009), p. 009.

[125] Mussadiq H Qureshi et al. “Low-ℓ power suppression in punctuated inflation”. In: *Journal of Cosmology and Astroparticle Physics* 2017.04 (2017), p. 013.

[126] Carlo R Contaldi et al. “Suppressing the lower multipoles in the CMB anisotropies”. In: *Journal of Cosmology and Astroparticle Physics* 2003.07 (2003), p. 002.

[127] Gavin Nicholson and Carlo R Contaldi. “The large scale cosmic microwave background cut-off and the tensor-to-scalar ratio”. In: *Journal of Cosmology and Astroparticle Physics* 2008.01 (2008), p. 002.

[128] LT Hergt et al. “Case for kinetically dominated initial conditions for inflation”. In: *Physical Review D* 100.2 (2019), p. 023502.

[129] HV Ragavendra, Debika Chowdhury, and L Sriramkumar. “Suppression of scalar power on large scales and associated bispectra”. In: *Physical Review D* 106.4 (2022), p. 043535.

[130] Fabian Schmidt and Lam Hui. “Cosmic microwave background power asymmetry from non-Gaussian modulation”. In: *Physical Review Letters* 110.1 (2013), p. 011301.

[131] Adrienne L Erickcek, Marc Kamionkowski, and Sean M Carroll. “A hemispherical power asymmetry from inflation”. In: *Physical Review D* 78.12 (2008), p. 123520.

[132] Cora Dvorkin, Hiranya V Peiris, and Wayne Hu. “Testable polarization predictions for models of CMB isotropy anomalies”. In: *Physical Review D* 77.6 (2008), p. 063008.

[133] Anthony R Pullen and Marc Kamionkowski. “Cosmic microwave background statistics for a direction-dependent primordial power spectrum”. In: *Physical Review D* 76.10 (2007), p. 103529.

[134] Liang Dai et al. “The pesky power asymmetry”. In: *Physical Review D* 87.12 (2013), p. 123005.

[135] Pedro G Ferreira and Joao Magueijo. "Closet non-Gaussianity of anisotropic Gaussian fluctuations". In: *Physical Review D* 56.8 (1997), p. 4578.

[136] Dmitriy Tseliakhovich, Christopher Hirata, and Anže Slosar. "Non-Gaussianity and large-scale structure in a two-field inflationary model". In: *Physical Review D* 82.4 (2010), p. 043531.

[137] Bekir Baytaş et al. "Nonlocal bispectra from super cosmic variance". In: *Physical Review D* 91.8 (2015), p. 083518.

[138] Béatrice Bonga et al. "Cosmic variance in inflation with two light scalars". In: *Journal of Cosmology and Astroparticle Physics* 2016.05 (2016), p. 018.

[139] Xingang Chen and Yi Wang. "Quasi-single field inflation and non-Gaussianities". In: *Journal of Cosmology and Astroparticle Physics* 2010.04 (2010), p. 027.

[140] Valentin Assassi, Daniel Baumann, and Daniel Green. "On soft limits of inflationary correlation functions". In: *Journal of Cosmology and Astroparticle Physics* 2012.11 (2012), p. 047.

[141] https://tevpa2017.osu.edu/talks/Wednesday/Spartan/BeforeBreak/3_Adhikari.pdf.

[142] D Contreras et al. "Testing physical models for dipolar asymmetry with CMB polarization". In: *Physical Review D* 96.12 (2017), p. 123522.

[143] Zhongxu Zhai and Michael R Blanton. "A forecast for the detection of the power asymmetry from galaxy surveys". In: *The Astrophysical Journal* 850.1 (2017), p. 41.

[144] Maresuke Shiraishi et al. "Violation of statistical isotropy and homogeneity in the 21-cm power spectrum". In: *Physical Review D* 93.10 (2016), p. 103506.

[145] CL Bennett et al. "Seven-year wilkinson microwave anisotropy probe (WMAP*) observations: Are there cosmic microwave background anomalies?" In: *The Astrophysical journal supplement series* 192.2 (2011), p. 17.

[146] Simone Aiola et al. "Microwave background correlations from dipole anisotropy modulation". In: *Physical Review D* 92.6 (2015), p. 063008.

[147] Silvia Galli et al. "CMB Polarization can constrain cosmology better than CMB temperature". In: *Physical Review D* 90.6 (2014), p. 063504.

[148] Nabila Aghanim et al. "Planck 2015 results-XI. CMB power spectra, likelihoods, and robustness of parameters". In: *Astronomy & Astrophysics* 594 (2016), A11.

[149] Sugumi Kanno, Misao Sasaki, and Takahiro Tanaka. "A viable explanation of the CMB dipolar statistical anisotropy". In: *Progress of Theoretical and Experimental Physics* 2013.11 (2013), 111E01.

[150] David H Lyth. "Generating $f_{\rm NL}$ at $\ell \lesssim 60$". In: *Journal of Cosmology and Astroparticle Physics* 2015.04 (2015), p. 039.

[151] Takeshi Kobayashi, Marina Cortês, and Andrew R Liddle. "A separate universe view of the asymmetric sky". In: *Journal of Cosmology and Astroparticle Physics* 2015.05 (2015), p. 029.

[152] David H Lyth. "The CMB modulation from inflation". In: *Journal of Cosmology and Astroparticle Physics* 2013.08 (2013), p. 007.

[153] Dominik J Schwarz et al. “CMB anomalies after Planck”. In: *Classical and Quantum Gravity* 33.18 (2016), p. 184001.

[154] Mafalda Dias, Raquel H Ribeiro, and David Seery. “Scale-dependent bias from multiple-field inflation”. In: *Physical Review D* 87.10 (2013), p. 107301.

[155] Zachary Kenton and David J Mulryne. “The squeezed limit of the bispectrum in multi-field inflation”. In: *Journal of Cosmology and Astroparticle Physics* 2015.10 (2015), p. 018.

[156] Christian T Byrnes and Ewan RM Tarrant. “Scale-dependent non-Gaussianity and the CMB Power Asymmetry”. In: *Journal of Cosmology and Astroparticle Physics* 2015.07 (2015), p. 007.

[157] Farhan Feroz, MP Hobson, and Michael Bridges. “MultiNest: an efficient and robust Bayesian inference tool for cosmology and particle physics”. In: *Monthly Notices of the Royal Astronomical Society* 398.4 (2009), pp. 1601–1614.

[158] Roberto Trotta. “Applications of Bayesian model selection to cosmological parameters”. In: *Monthly Notices of the Royal Astronomical Society* 378.1 (2007), pp. 72–82.

[159] Alexander Vilenkin and Lawrence H Ford. “Gravitational effects upon cosmological phase transitions”. In: *Physical Review D* 26.6 (1982), p. 1231.

[160] AA Starobinskij. “Spectrum of adiabatic perturbations in the universe when there are singularities in the inflationary potential.” In: *Soviet Journal of Experimental and Theoretical Physics Letters* 55.9 (1992), pp. 489–494.

[161] Harold Jeffreys. *The theory of probability*. OuP Oxford, 1998.

[162] Angé lica de Oliveira-Costa et al. “Significance of the largest scale CMB fluctuations in WMAP”. In: *Physical Review D* 69.6 (2004).

[163] Adrienne L Erickcek, Christopher M Hirata, and Marc Kamionkowski. “A scale-dependent power asymmetry from isocurvature perturbations”. In: *Physical Review D* 80.8 (2009), p. 083507.

[164] PAR Ade et al. “Planck 2015 results-XX. Constraints on inflation”. In: *Astronomy & Astrophysics* 594 (2016), A20.

[165] JP Zibin and D Contreras. “Testing physical models for dipolar asymmetry: from temperature to k space to lensing”. In: *Physical Review D* 95.6 (2017), p. 063011.